RUPRECHT-KARLS-UNIVERSITÄT HEIDELBERG

DOCTORAL THESIS

Stellar Imaging and Spectroscopy for the Discovery of Extrasolar Planets

---

Author:
Stefan Sebastian BREMS

Supervisors:
Prof. Dr. Andreas QUIRRENBACH
PD Dr. Sabine REFFERT
Dr. Wolfgang BRANDNER

Referees:
Prof. Dr. Andreas QUIRRENBACH
Apl. Prof. Dr. Hubert KLAHR

A thesis submitted in fulfillment of the requirements
for the degree of Doctor of Natural Sciences

in the

Extrasolar Planet Research Group at the Landessternwarte
Zentrum für Astronomie der Universität Heidelberg
Combined Faculties of the Natural Sciences and Mathematics

Oral Examination: July 3rd, 2019

Dissertation

submitted to the
Combined Faculties of the Natural Sciences and Mathematics
of the Ruperto-Carola-University of Heidelberg. Germany
for the degree of

Doctor of Natural Sciences

Put forward by

Stefan Sebastian BREMS
born in: Tübingen, Germany

Oral examination: July 3rd, 2019

Stellar Imaging and Spectroscopy for the Discovery of Extrasolar Planets

Referees: Prof. Dr. Andreas QUIRRENBACH
Apl. Prof. Dr. Hubert KLAHR

“There is no planet B!”

#FridaysForFuture

RUPRECHT-KARLS-UNIVERSITÄT HEIDELBERG

Zusammenfassung | *Abstract*

Entdeckung Extrasolarer Planeten
durch Abbilden und Spektroskopieren von Sternen

von Stefan Sebastian BREMS

Wenn man verstehen möchte wie sich Planeten entwickeln, ist es notwendig, diese auch während ihrer Entstehungsphase zu untersuchen. Dies ist jedoch sehr schwierig und in der vorliegenden Arbeit beschreibe ich meine Beiträge zu diversen Forschungsprojekten, welche mittels direkter Abbildungen oder im Falle von RVSPY mittels Radialgeschwindigkeitsmessungen versuchen, genau dies zu tun. Ich erläutere meine Beiträge bei der Auswahl geeigneter Sterne, der Datenanalyse sowie der Kalibration der Instrumente. Der Fokus richtet sich hierbei auf die Beobachtungsprojekte NaCo-ISPY und RVSPY. In der Arbeit stelle ich stellare Systeme des NaCo-ISPY Projektes vor, die zu Beginn vielversprechend aussahen. Eine genauere Analyse zeigte jedoch, dass die Signale höchstwahrscheinlich nicht von Begleitern verursacht wurden – mit Ausnahme des Sterns HD 101412: Dieser scheint von zwei Braunen Zwergen oder masserarmen Sternen ($\lesssim 0.1 M_\odot$) umkreist zu werden. Ich erkläre, warum wir dies denken und wie wir in Zukunft vorgehen werden, um uns hierüber Gewissheit zu verschaffen. Außerdem stelle ich den gegenwärtigen Stand sowie erste Ergebnisse von RVSPY vor.

Des Weiteren präsentiere ich die Ergebnisse meiner Arbeit zur Charakterisierung von Fluktuationen in Radialgeschwindigkeitsdaten, welche durch stellare Aktivität induziert werden. Das Hauptergebnis dieser Analyse ist eine stärker als exponentielle Abnahme der Stärke der Fluktuationen mit zunehmendem Alter des Sterns. Außerdem verstärken sich die Fluktuationen ungefähr um einen Faktor zwei, wenn man Beobachtungsreihen auf Zeitskalen von Jahren statt Stunden oder Tagen .

Stellar Imaging and Spectroscopy for
the Discovery of Extrasolar Planets

Observing planets during their formation is a challenging, but also important task if one wants to learn about their evolution. In this thesis I explain how I have contributed to various direct imaging surveys, as well as the RVSPY radial velocity survey, which aim at finding planets around young stars. The contributions include appropriate target selection, data analysis and calibration of the instruments, in particular for the NaCo-ISPY and RVSPY surveys. I present systems I analyzed throughout the course of the NaCo-ISPY direct imaging survey which showed promising signals. Further investigation showed that all signals are most likely not caused by physical companions – with the exception of HD 101412, which is a good candidate for a system composed of a star orbited by two brown dwarfs or low mass stellar objects ($\lesssim 0.1\,M_\odot$). I explain what makes us believe this and what are our next steps to conclude on the system's nature. Further I present the current status as well as some early results of the recent RVSPY survey.

I also present results from the analysis of stellar radial velocity jitter as function of age and observational timescale. The main result is a greater than exponential decrease of the radial velocity jitter with increasing stellar age. Additionally the radial velocity jitter increases by about a factor of two when probing timescales of years instead of hours or days.

Contents

1 Introduction **1**

1.1 A brief History of Exoplanets . . . 1

1.2 Planet and Star Formation . . . 4

1.2.1 Star Formation . . . 4

1.2.2 Planet Formation and Planet Disk Interaction . . . 7

1.3 Direct Imaging of Exoplanets . . . 12

1.3.1 Introduction . . . 12

1.3.2 Observational Challenges . . . 14

Atmospheric Turbulence and Adaptive Optics . . . 14

Coronagraphy . . . 17

1.3.3 Data Analysis Methods . . . 21

1.3.4 Instruments: NaCo, GPI and SPHERE . . . 23

1.4 Detection of Exoplanets using the Radial Velocity Method . . . 26

1.4.1 Data Analysis Methods . . . 28

1.5 Other Methods to Detect Exoplanets . . . 32

1.5.1 Microlensing . . . 32

1.5.2 Astrometric Detection of Exoplanets . . . 34

1.5.3 Exoplanetary Transit Detections . . . 34

1.6 Direct Imaging Surveys . . . 35

1.6.1 NaCo Imaging Survey for Planets around Young stars . . . 35

Introduction . . . 35

Target Selection . . . 36

Standard Setup . . . 37

Results . . . 38

1.6.2 LBTI Exozodi Exoplanets Common Hunt . . . 39

Target Selection . . . 40

Observations . . . 41

Data Reduction . . . 41

Results . . . 42

1.6.3 L-band Imaging Survey to find Exoplanets in the North . . . 43

Introduction and Target Selection . . . 43

Observations . . . 44

Results . . . 44

2 Astrometric Calibration **47**

2.1 Introduction . . . 47

2.2 Observations . . . 47

2.3 Method . . . 51

2.3.1 Rough Sky Position . . . 51
2.3.2 Fine Overall Positioning . . . 52
2.3.3 Source Matching and Refined Positions . . . 53
2.3.4 Repeating the Process on Individual Images . . . 54
2.3.5 Calculating the Platescale and True North . . . 54
2.4 Results . . . 55
2.5 Discussion . . . 56

3 Individual Systems of the NaCo-ISPY Survey 59
3.1 Two Companions around HD 101412? . . . 60
3.1.1 Introduction . . . 60
3.1.2 Follow up with NaCo . . . 62
3.1.3 Observations . . . 64
NaCo-ISPY Observations . . . 65
GPI observations . . . 66
3.1.4 Background Statistics . . . 69
3.1.5 Summary and Conclusion . . . 73
3.2 SPHERE's and NaCo's View of HD 191849 . . . 74
3.2.1 Introduction . . . 74
3.2.2 Observations . . . 75
3.2.3 Data Reduction . . . 76
3.2.4 Results . . . 79
3.2.5 Conclusion . . . 80
3.3 Does HD 58647 have a Companion? . . . 81
3.3.1 Observations and Data Reduction . . . 81
3.3.2 Results . . . 82
3.3.3 Conclusion . . . 85
3.4 A foreground Object to HD 98922 . . . 85
3.4.1 Introduction . . . 85
3.4.2 Observations and data reduction . . . 85
3.4.3 Common Proper Motion Analysis . . . 87
3.5 A background Object to HD 97048 . . . 89
3.5.1 Observations and Data Reduction . . . 89
SPHERE reduction . . . 90
HST Reduction . . . 90
NICI Reduction . . . 91
3.5.2 Common Proper Motion Analysis . . . 92

4 Radial Velocity Survey for Planets around Young stars 97
4.1 Motivation and Previous Work . . . 97
4.2 Target Selection . . . 99
4.3 Observing Strategy . . . 101
4.3.1 Feasibility Study . . . 101
4.3.2 Conclusion . . . 104
4.4 Data Reduction . . . 104
4.5 Early Results . . . 107

5 Radial Velocity Jitter of Stars 113

5.1 Introduction . . . 113
5.2 Target sample . . . 114
5.3 Method . . . 119
5.3.1 Models . . . 119
5.3.2 Block Sizes . . . 120
5.3.3 Activity Modeling . . . 121
5.3.4 Uncertainty Estimation . . . 122
5.4 Results . . . 122
5.5 Discussion . . . 126
5.6 Conclusions . . . 127

6 Summary and Outlook **129**
6.1 Summary . . . 129
6.2 Outlook . . . 130

A Individual measurements of the Astrometric Correction **133**

B Cross Correlation Function Time Series of RVSPY 80 **141**

C Supplementary Material of Chapter 5 **145**
C.1 Analytic description of the PV . . . 145
C.2 Analytic PV of sinusoids . . . 146
C.3 Radial Velocity Data . . . 146
C.4 Pooled Variance fits . . . 149

Bibliography **150**

Bibliography of own Publications **163**

List of Figures **165**

List of Tables **169**

List of Acronyms **171**

Acknowledgements **175**

Declaration of Authorship **177**

Chapter 1

Introduction

This introduction serves as an overview for anybody new to the field of extrasolar planets (exoplanets) and to understand the content of this thesis and is not complete by any means. For a more complete overview I recommend e.g. Seager et al. (2010) or Perryman (2018).

1.1 A brief History of Exoplanets

Even after Nicolas Kopernikus published his work *De revolutionibus orbium coelestium* (Copernicus, 1543), it was unknown whether our home planet, Earth, is the center of the universe or not. But when Johannes Kepler published his laws predicting the planetry orbits using ellipsoids and Isaac Newton could explain those using a simple law of mass attraction in the end of the 17th century, this was generally accepted. As we know now, the Sun is orbited by at least[1] eight planets, the question arose whether other stars are also host to (multiple) planets. After an initial discovery in 1991 had to be rejected (Lyne & Bailes, 1992), it was only in 1992 that the first planet outside our solar system was identified: Wolszczan & Frail (1992) measured Pulsar timing variations of the millisecond pulsar PSR 1257+12 to indirectly infer to the presence of two planets orbiting this dead star. However, the first exoplanet orbiting a (pre-)main sequence star still had to be found. Being motivated by our own solar system's architecture, most surveys looked out for planets with orbital periods of a few months at least. It were Mayor & Queloz (1995) who first scanned their Radial Velocity (RV) data for planets with orbits of a few days only and announced the discovery of 51 Pegasi b (later also named *Dimidium*) orbiting the G2 IV star 51 Pegasi.

The next huge step in exoplanetary science was the first image of an exoplanet: 2M 1207 b, a 5 ± 2 M_{Jup} planet orbiting a Brown Dwarf (BD) was imaged by Chauvin et al. (2004) using the Naos Conica (NaCo) instrument at the Very Large Telescope (VLT), see Fig. 1.1. Since then more and more planets were discovered every year, see Fig. 1.2. Outstanding are the years 2014 and 2016 with about 1000 planet discoveries each. Those detections are owed mainly to the Kepler spacecraft data and

[1] Batygin & Brown (2016) proposed to explain orbits of distant Kuiper Belt objects by an additional Giant Planet (GP) and retake Pluto's spot as ninth planet.

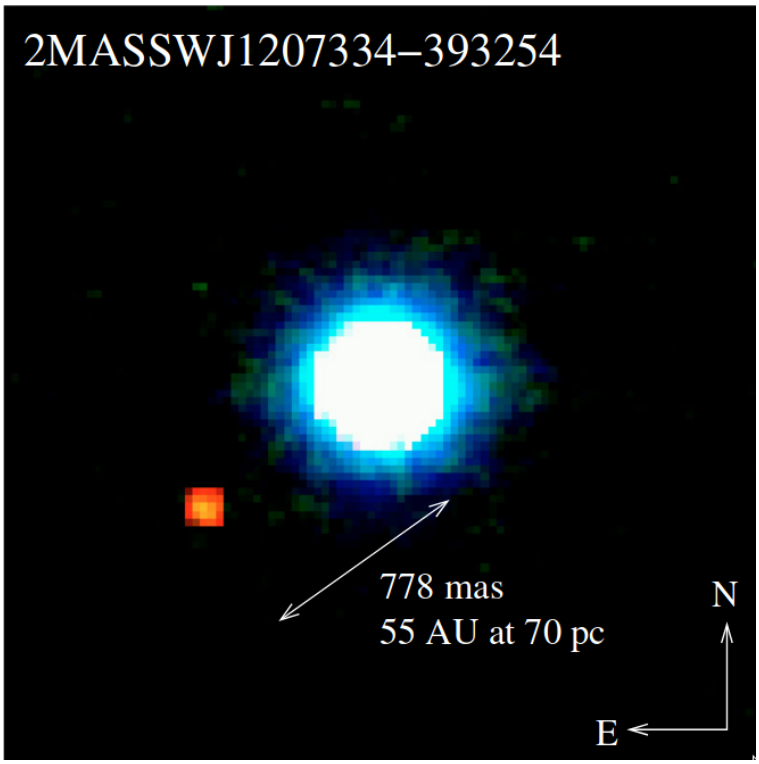

Figure 1.1: Discovery image of 2M 1207 b and its brown dwarf host. The image is a composite image with the H-band in blue, K-band in green and L'-band in red. Credit: Chauvin et al. (2004).

a new analysis method of this data in 2016. So today we know of 3924 planets[2] with 657 multiplanetary systems, where the vast majority was discovered using the transit and RV discovery methods. Fig. 1.3 shows the distribution of those planets as function of mass and semi-major axis, color coded with the detection method. Due to microlensing surveys, we now know that there are more planets than stars in our home galaxy (Cassan et al., 2012). And if one was interested in e.g. the search for life, one can even put constraints on the occurrence rates for planets in the habitable zone around FGK main sequence stars: It is $0.24^{+0.11}_{-0.10}$, where the habitable zone translates to periods between 237 days and 500 days (Hsu et al., 2019)[3].

But even though a lot of progress has been made, large areas of the detection space remain unexplored. E.g. from our own Solar system, if any at all, probably only Jupiter would have been detected if we were to observe it from another stellar system. But this knowledge is crucial if we also want to understand our home, our own Solar system: Is it always there are only gas giants beyond a few astronomical units (AU)? What are other systems' planets' composed of? How did Earth end up where it is now? And of course: Are we alone? These questions can hardly be answered with our current knowledge. And one part of the path to answer those

[2] According to `https://exoplanetarchive.ipac.caltech.edu/index.html` as on March 10th, 2019

[3] It also needs to be said that only the upper limit can be robust. And further this result is also only true for planets with sizes of 1-1.75 $R_\oplus$.

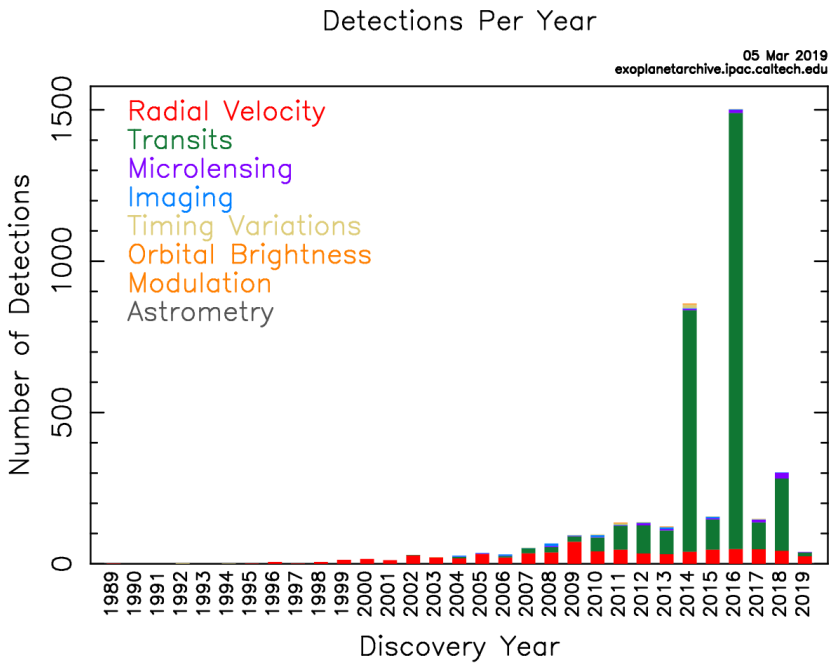

Figure 1.2: Detections of exoplanets per year with the detection method color coded. The peak in 2014 comes from detections using data the Kepler spacecraft, which unfortunately could not continue staring at its intended position after 2013 since a second gyroscope broke. The peak in 2016 than was a result of an new False Positive Probability (FPP) based analysis of the Kepler data, leading to 1284 new exoplanets at once (Morton et al., 2016).
Credit: NASA exoplanets archive.

questions is to explore the unexplored regions of Fig. 1.3. Other immediate goals are to observe planets during their formation, to determine their atmospheric composition and to get a complete census of at least a few planetary systems, at least down to a few earth masses.

Fortunately we live in the golden era of astronomy and upcoming missions such as the recently launched GAIA (Gaia Collaboration et al., 2016)[4] and Transiting Exoplanet Survey Satellite (TESS) (Ricker et al., 2014)[5] missions, the upcoming James Webb Space Telescope (JWST) (Gardner et al., 2006)[6] or the European Extremely Large Telescope (E-ELT) (de Zeeuw et al., 2014)[7] will help us answering those immediate questions. In particular when it comes to the atmospheric characterization of exoplanets, the JWST with its coronagraphic Direct Imaging (DI) and transit sensitivity capabilities will revolutionize what we know of the atmospheric compositions of (exo)planets today (Danielski et al., 2018, Sect. 1.3.2).

[4] http://sci.esa.int/gaia/
[5] https://heasarc.gsfc.nasa.gov/docs/tess
[6] https://www.jwst.nasa.gov
[7] https://www.eso.org/sci/facilities/eelt

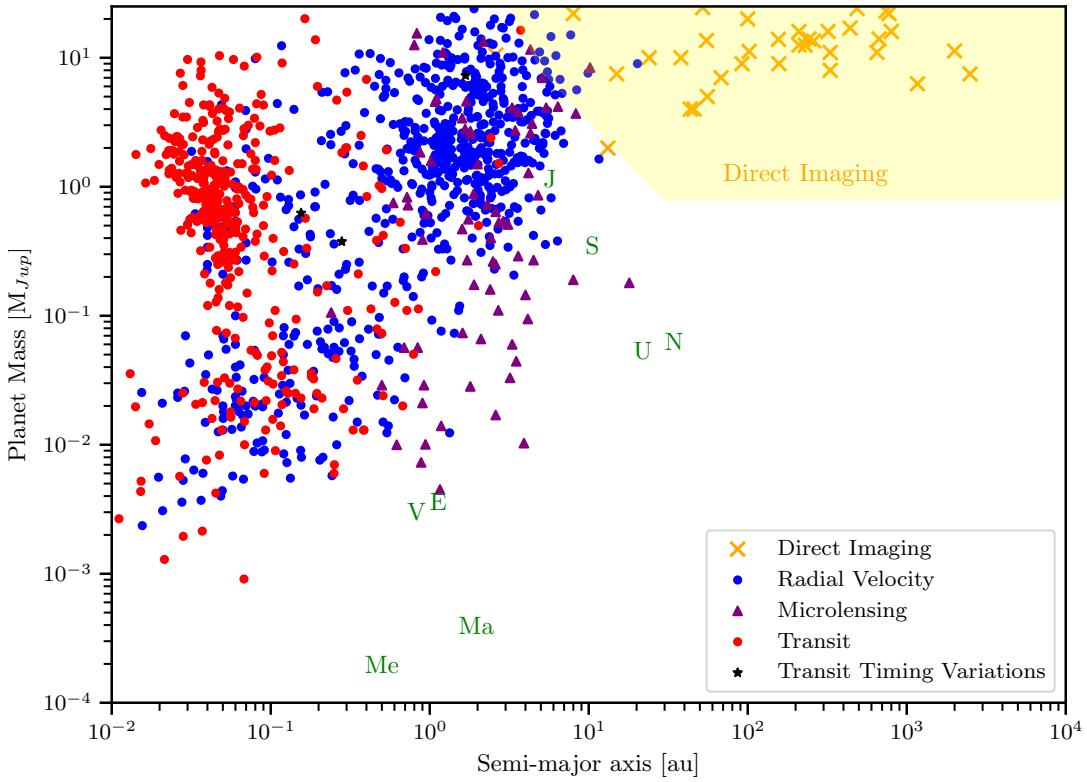

Figure 1.3: Diagram of all known exoplanets as a function of their planetary mass and semi-major axis, as of January 2019[2]. The yellow area roughly marks the detection space probed by NaCo-ISPY. The detection space of RVSPY is not clear yet, but it roughly aims for the red bulge to to left top, referred to as hot Jupiters. One can also see that all the planets, marked with green letters, in our own solar system are below or at the edge of detectability.

1.2 Planet and Star Formation

Planet formation goes hand in hand with star formation,see Fig. 1.4. Thus in Sect. 1.2.1 the star forming mechanism is explained, before Sect. 1.2.2 explains how planets are believed to end up around those stars.

1.2.1 Star Formation

Many parsec large interstellar gas and dust clouds are subject to two predominant forces: on the one hand the attractive gravitational force

$$F_{\mathrm{G}} = -\frac{G\rho(r)M_{\mathrm{enc}}(r)}{r^2}$$

and on the other hand the countering pressure gradient

$$F_{\mathrm{P}} = \frac{\mathrm{d}p}{\mathrm{d}r},$$

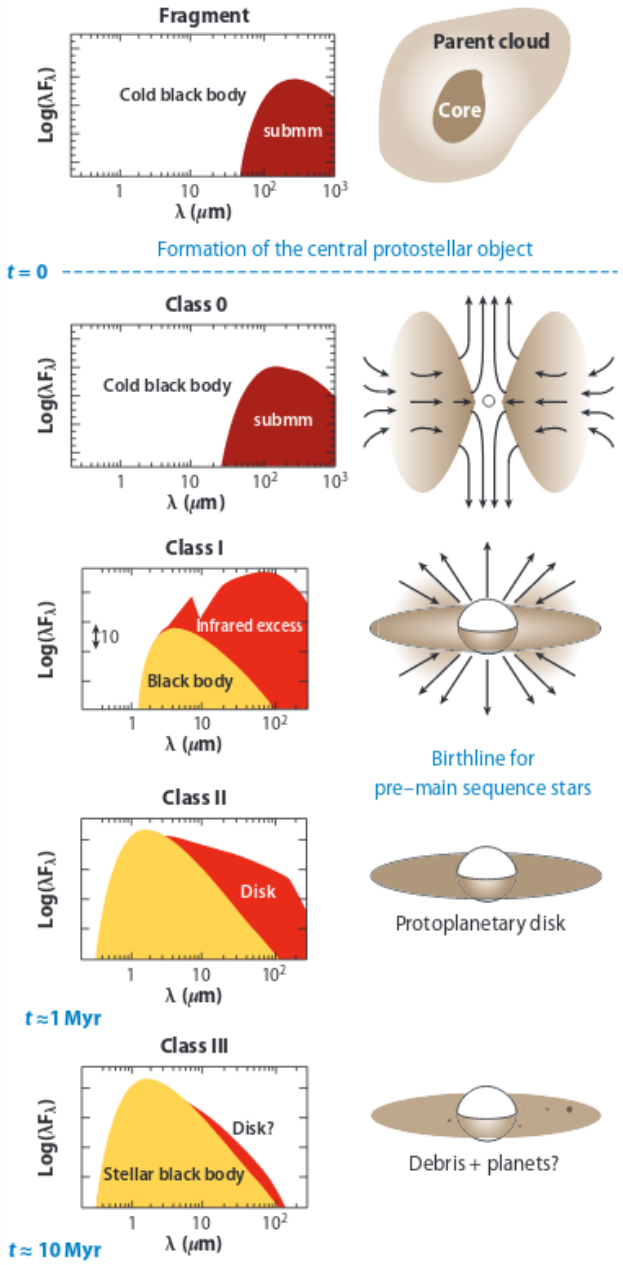

Figure 1.4: Schematic overview of planet and star formation. The formation and the different stages are explained in Sect. 1.2.1. λ denotes the wavelength and F_λ is the spectral flux density in arbitrary units. Credit: Thesis by Laura María Pérez Muñoz[8]

where G is the gravitational constant, p is the pressure, $\rho(r)$ is the gas density and M_{enc} is the enclosed mass. If the gravitational force is larger than the pressure gradient, $F_G > F_P$, the cloud starts to contract. The so-called Jeans instability. At least at the beginning, the clouds are optically thin and diffuse, thus we can neglect radiation and other forms of pressure and p reduces to the gas pressure. Due to homogeneity, turbulence and magnetic fields, the clouds typically do not contract to form one core, but break into multiple fragments. Each of these fragments then becomes more and

more dense and – due to the released potential energy – hotter. The innermost region eventually becomes dense enough to be optically thick. This dense core is then called a protostar of class 0, following the Lada sequence (Lada & Wilking, 1984).

At the same time, the conservation of angular momentum causes the surrounding material to form a disc. The orientation of that disk is perpendicular to the rotational axis of the star[9]. The further contraction and accretion onto the star is then weakened, since the conservation of angular momentum will lead to an ever bigger centrifugal force, ultimately balancing the gravitational force within the disk. Once a disk has formed, this object is referred to as a class I object. Due to e.g. shearing forces, angular momentum is continuously transported outwards, so that the contraction and accretion process is never fully halted.

The star continues to contract and increase its luminosity. Due to the high luminosity of the central star, its radiation pressure becomes high enough to blow out any particles smaller than a blow-out size D_{bl}, typically a few micron. The blow-out size is described via

$$D_{\mathrm{bl}} = 0.8 \left(\frac{L_*}{M_*}\right) \left(\frac{\rho}{2700} \cdot \frac{\mathrm{m}^3}{\mathrm{kg}}\right)^{-1} \mu\mathrm{m}\,, \tag{1.1}$$

where L_* and M_* are the stellar luminositiy and mass in solar units, and ρ is the particles density (Wyatt, 2008)[10]. Once all material below the blow-out size apart from within the disk is removed, we refer to the star as class II object. Alternatively high mass stars are called Herbig Ae/Be stars and lower mass stars are referred to (classical) T Tauri stars and the disk is referred to as ProtoPlanetary Disk (PPD). The star is now has an age of about 1 Myr, and for the next about 10 Myr, it continues to contract along the Hayashi-rack and to remove gas and small particles from the disk (Ercolano & Pascucci, 2017). The contraction is eventually stopped by radiation pressure from the starting nuclear fusion in the stellar core. Once the disk is cleared of small particles, one is left with debris and, as we now know, often planets (Cassan et al., 2012).

The stage of the disk can usually be determined by its Spectral Energy Distribution (SED), schematically shown in the left part of Fig. 1.4. Smooth transitions between the different stages and variations of the precise distribution of the SED sometimes make it hard to classify the stage of the (proto)star, especially between class II and III. Herbig Ae/Be stars often show a dip in the Mid Infrared (MIR) to Far Infrared (FIR) spectrum, which classifies them as group I (Waelkens et al., 1994), in opposite to group II, when this part of the spectrum can be described by a powerlaw (Meeus et al., 2001). First it was believed that group I disks posses a gap causing this dip. However, this is now put into question and maybe self-shadowing in flat disks vs. not-shadowed flared disks might play a role here (Maaskant, K. M. et al.,

[9] The same phenomenon of a disk forming due to angular momentum conservation is also seen in rings around planets (e.g. Saturn), Spiral galaxies or accreting (active) black holes.

[10] The stars high temperature is due to the released potential energy, the nuclear fusion setting in later will prevent the star from further heating.

2013; Menu et al., 2015). E.g. HD 101412, a young transition disk presented in Sect. 3.1, shows those dips. Still we were not able to image it, even though equilibrium temperature, Black Body (BB) estimates would have suggested it to be large enough. This is different for Class III or Debris Disk (DD) stars. In Launhardt et al. (in prep.) we can show that our estimated disk sizes from BB fits agree very well with the imaged sizes. This is particularly important for NaCo Imaging Survey for Planets around Young stars (NaCo-ISPY), since part of the target selection is based on these disk size estimates.

The mass distribution of the stars formed in this process is known as Initial Mass Function (IMF) $\xi(m)$, where m is the mass of the star. It was first described by Salpeter (1955) to be

$$\xi(m)\Delta m = \left(\frac{m}{M_\odot}\right)^{-3.5} \left(\frac{\Delta m}{M_\odot}\right) , \tag{1.2}$$

where Δm is the, infinitesimally small mass range probed and $M_\odot$ denotes one solar mass. It was later refined e.g. by Miller & Scalo (1979) and Chabrier (2003), where the main changes apply to the low mass stars .

1.2.2 Planet Formation and Planet Disk Interaction

Planet formation The previous Sect. briefly described how stars form and how a disk comes up naturally in that process and that disks are the birth place of planets. Unfortunately, a large range of the particles' sizes cannot be probed in these disks directly. E.g. scattered light images from SPHERE probe only micron sized particles (Avenhaus et al., 2018), and the new Atacama Large Millimiter Array (ALMA) observes in the mm wavelength range and is sensitive only to similarly sized particles (Andrews et al., 2018, see Fig.1.5 and). We are blind for anything in between and the next observable step are planets with thousands of kilometers in diameter. Those can be probed using the techniques presented in the later part of this Chapt. This lack of observations from bodies of millimeter sizes to thousands of kilometer sized protoplanets is one of the main reasons why the precise way of planet formation is still not understood. This subsection is intended to give an overview of the current status. Especially with a focus on the parts important to understand the selection criteria of the NaCo-ISPY survey and other surveys described in Sect. 1.6. For a deeper understanding of the formation process see e.g. the review paper by Mordasini et al. (2010).

We cannot observe the planet's formation directly, but simulate it with computers. When trying to simulate the growth of particles due to coagulation, many growth barriers are hit, preventing the planetesimals[11] to grow any further. These barriers are either related to growth limits of the dust grains, such as fragmentation, bouncing and repellent electromagnetic forces (e.g. Johansen et al., 2014; Bitsch et al., 2015) or due to radial drifts, where the planetesimals drift much faster towards the

[11] Planetesimal refers to a dust or rocky object we cannot detect. It can have a size between a few meters and hundreds of kilometers.

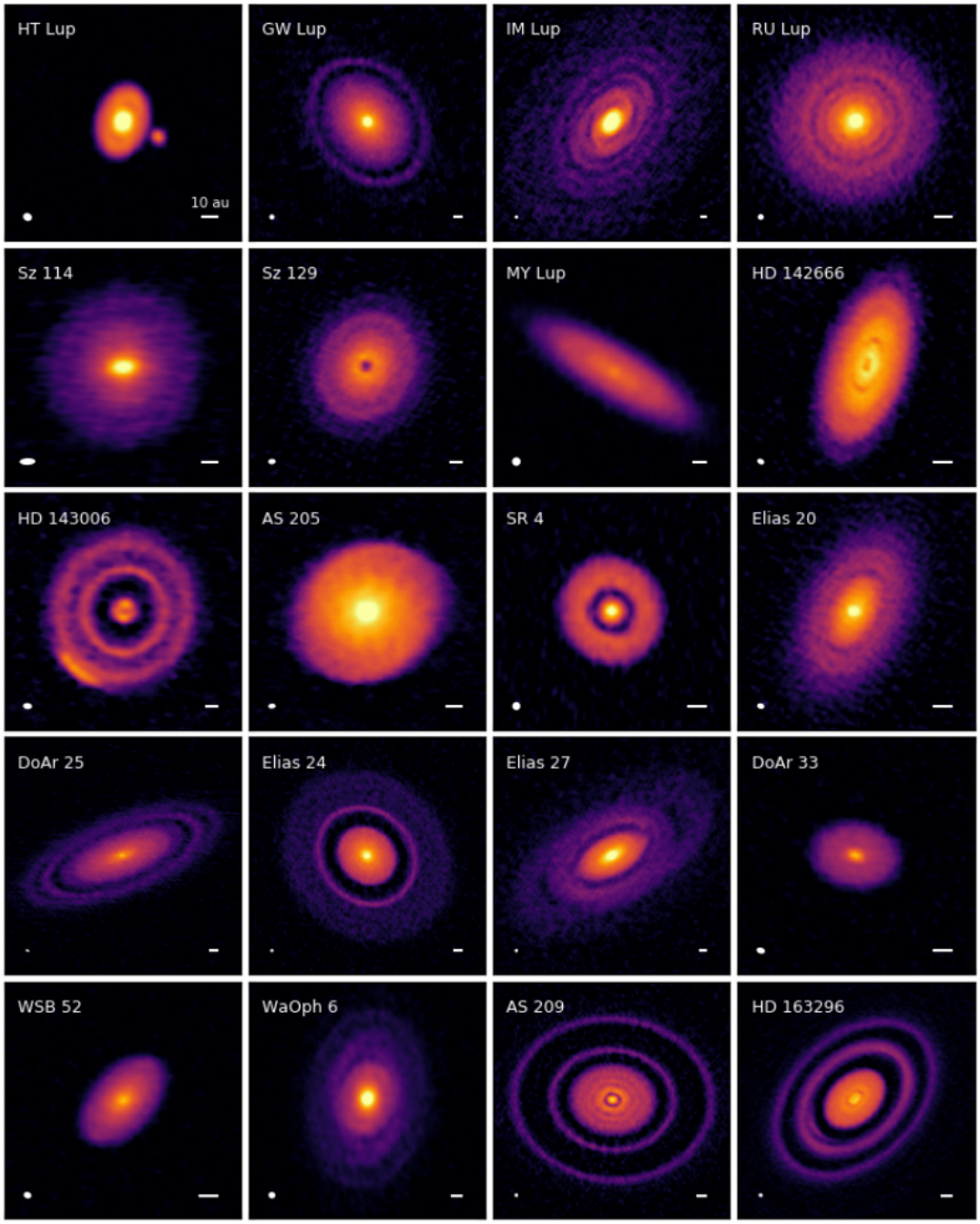

Figure 1.5: Disks taken with ALMA in the course of the DSharp survey. They are taken at a wavelength of 1.25 mm (240 GHz) showing the variety of disks including many unexplained features as e.g. the bright blob in the lower left of HD 143006. The beamsize (white ellipse) and 10 AU (white bar) are shown in the lower parts of each panel. All images are shown with an asinh stretch to reduce the dynamic stretch.
Credit: Andrews et al. (2018)

star than they grow (e.g. Klahr, 2008). This often stops simulated growth at roughly meter sized bodies at the so called meter barrier (Mordasini et al., 2010, and references therein). Many mechanisms have been proposed to overcome this barrier, one of the first was the proposition by Goldreich & Ward (1973) to have them stick by self

gravity. Therefore the pebbles would need to assemble in a thin layer in the PPD, which seems not possible due to shear forces between the particles moving at keplerian speeds and the surrounding gas moving slightly slower due to the gas pressure or other mechanisms. But the idea of creating over densities where planet embryos can form fast enough remains, e.g. in vortices (Raettig et al., 2015) or streaming instabilities (Johansen & Youdin, 2007) and pebble accretion (Bitsch et al., 2015, Fig. 1.5). The dust trapping mechanism with the aforementioned mentioned pressure bumps is analyzed in Dullemond et al. (2018).

With these mechanisms we could form rocky planets. But to form the gas giants observed in DI surveys or as hot Jupiters in RV surveys, two theories are currently discussed:

The first one, **core accretion**, uses a planetesimal which "collects" the gas which is roughly within the hill sphere. One of the issues here is, that the lifetime of the protoplanetary disk seems shorter than the formation time of the protoplanetary disk itself (Pollack et al., 1996; Levison et al., 2010). Proposed solutions to this problem are a drastic increase of solids as described in the formation of rocky planets, or accounting for accretion of small pebbles (Ormel & Klahr, 2010; Morbidelli & Nesvorny, 2012). This can shorten the formation of a core of $\sim 10 M_{\text{earth}}$ at ~ 5 AU to 1 Myr (Bitsch et al., 2015). This is important because the gas accretion cannot have a high rate before the core is formed, because a) The escape velocity of the body needs to be sufficiently high and thus the body sufficiently massive b) Heating of the atmosphere by the impacting particles during accretion hinders the cooling and contraction of the atmosphere below the high escape velocity (Bitsch et al., 2015).

The second theory of GP formation is via **disk fragmentation** (Stamatellos & Whitworth, 2008). The process is similar to the disk fragmentation into multiple stars, but this time in the gravitational neighborhood of a star, such that the resulting body is gravitationally bound and rotation plays a more important rule. Due to the similarity of these methods, the disk fragmentation is believed not only produces gas giants, but also Brown Dwarfs (BDs) or Low Mass Stellar Objects (LMSOs). Since the process takes place in a rotating disk instead of a quasistatic sphere, the jeans criterium from Eq. 1.2 gets replaced by the Toomre criterion, where the dimensionless Toomre Q has to be smaller than 1 for the disk to collapse. The Toomre Q is defined by:

$$Q := \frac{c_s \kappa}{\pi G \Sigma}. \tag{1.3}$$

Here c_s is the speed of sound (accounting for pressure and temperature), κ is the epicyclic frequency G is the gravitational constant and Σ is the surface density. Note that the shear forces in the differentially rotating disk act as a stabilizing parameter making it harder to collapse. Thus a lower limit for planets forming this way is assumed to be around $\sim 1 - 5 \text{M}_{\text{Jup}}$ (Low & Lynden-Bell, 1976; Stamatellos, 2013). Observations indeed seem to find two relatively distinct populations, at least for close in planets, see Fig. 1.3. This unpopulated () for masses between $\sim 0.1 - 1 \text{M}_{\text{Jup}}$ could be enclosed by core collapse planets on the high mass end, and core

accretion planets on the low mass end. However, nothing is known for sure yet, but progress on the observational side is made, e.g. just recently the first planet inside the transition disk of PDS 70 was found (Keppler et al., 2018).

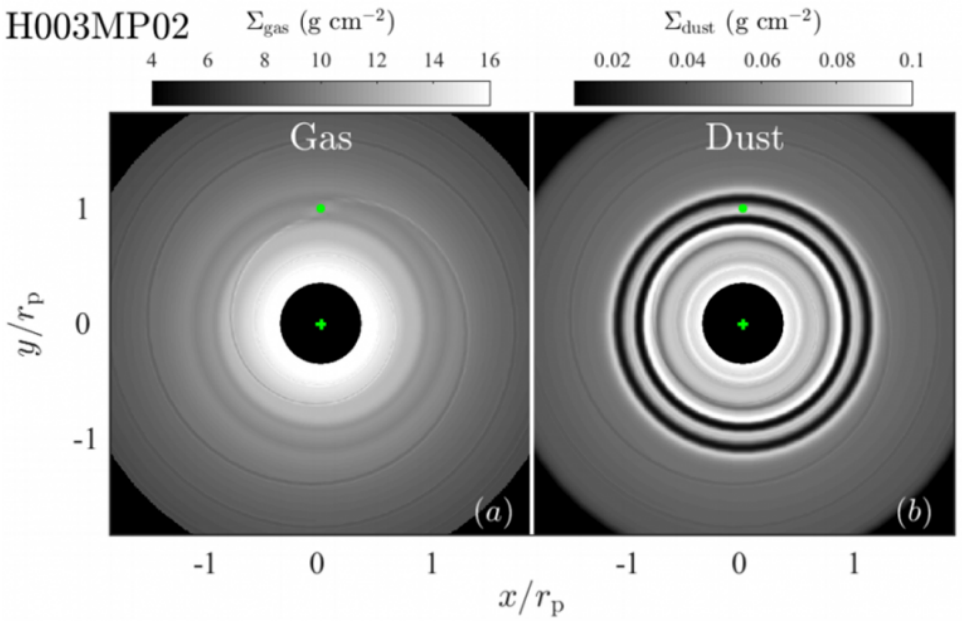

Figure 1.6: A snapshow of a 0.26 Myr disk showing how the dust may show multiple gaps, whereas in the gas hardly any gap is visible. The green plus marks the star and the green dot the planet's location. Credit: Dong et al. (2018).

Planet disk interaction As mentioned in the previous section, if gas in the disk is still present, it can assert a force on the planets and particularly make them drift inwards within in few million years only. But how does the disk's appearance change with a planet present? This is the aim of this section. We need to differentiate if gas is still present as in ProtoPlanetary Disks (PPDs) or already gone as in Debris Disks (DDs).

First **PPDs** are considered. Looking at the ALMA pictures in Fig. 1.5, we find many rings and spiral structures. Asymmetries as in HD 143006 are still of unknown origin and thus not part of this overview. But already looking at those rings makes clear that the assumption of a simple powerlaw of the disk's Temperature, aspect ratio H/r and especially surface density, as typically assumed in Mimimum Mass Solar Nebula (MMSN) models (Weidenschilling, 1977; Hayashi, 1981), cannot be hold. Thus two questions arise: a) How do these structures affect planet formation? b) Where do they come from? Answering the first question in full detail is beyond the scope of this work. But it can be noted that those gaps can slow, stop or reverse planet migration (Dullemond et al., 2018). This is especially true for small particles, which tend to assemble at the outer edges of pressure bumps, and thus simplify planet formation due to the enhanced particle densities (e.g. Bitsch

et al., 2015; Teague et al., 2018; Dullemond et al., 2018). Answering the second question about the origin of those gaps is still under discussion. Different mechanisms have been proposed: Secular gravitational instability (Takahashi & Inutsuka, 2014), self-induced dust pile-ups (Gonzalez et al., 2015), radially variable magnetic winds (Suriano et al., 2017), dust evolution at snowlines (Zhang et al., 2015) and, of course, planet formation (e.g. Dong et al., 2015). But recently Dong et al. (2018) have shown in simulations that even if planet formation was the only explanation, there is no need for one planet per gap: They show that a 0.2 M_{Jup} planet can open up to at least 5 gaps, all detectable by e.g. ALMA. But they show that also the opposite is possible: Multiple planets can open only a single, but therefore larger, gap. To make things even more complicated, they shows that those gaps might sometimes be visible in mm images, whereas DI imaging surveys probe too small particle sizes and thus do not find them, see Fig. 1.6. Those smallest particles probed by the DI surveys have not been removed efficiently from the gaps due to dust filtration effects, ultimately related to the gas coupling (Dong et al., 2018). This phenomenon is known as missing cavity problem (Dong et al., 2012).

Despite those complications, Teague et al. (2018) and Pinte et al. (2018) independently predict at least one Jupiter-mass planet in the famous PPD of HD 193296 purely based on disk dynamics. The trick they use is to use density gradients instead of absolute densities, which avoids many problems like the unknown gas to dust ratio or other unknown abundance ratios. I would like to note though, that Pinte et al. (2018) predict one two Jupiter-mass planet at $\approx$ 260 AU and Teague et al. (2018) two one Jupiter mass (M_{Jup}) planets at 83 AU and 137 AU, respectively. And despite large efforts, e.g. by NaCo-ISPY or SPHERE-SHINE, none of the planets has been imaged by the surveys. And even though the DI surveys mentioned cannot fully rule out the presence of those predicted planets, they at least can exclude significant parts of the possible parameter space. This example shows that much hast still to be understood.

For **Debris Disks (DDs)**, where the dust and smallest particles have been cleared, we have a different situation: Due to the missing small particles with a large surface to volume ratio, the disk is optically thin and comparably dim at almost all wavelengths. However, even for those disk we do find significant InfraRed (IR) excess not explicable by the debris. E.g. Chen et al. (2014) and van der Marel et al. (2016) have created a collection of such disks, identifying them by SPITZER, 2Mass and other all sky surveys' data. The explanation for this IR excess is that the dust gets replenished by collisions from the larger bodies (e.g. Dominik & Decin, 2003; Pawellek & Krivov, 2015). If bodies with non vanishing eccentricities e are present, the bodies collide due to secular perturbations that cause orbits to cross, that were not crossing initially. Those then start a cascade to ever smaller particles down to the blow-out size given in Eq. (1.1), where they then get removed from the system. Due to the higher velocities closer to the star, this self stirring process starts at the stellar position and is then moving outwards.

But this collisional cascade can be speeded up significantly, if large bodies are present in the disk. Not saying whether the body needs to be inside or outside the disk to stir, Mustill et al. (2018) show that the crossing timescale $t_{\rm cross}$ starting those cascades depends like

$$t_{\rm cross} \propto a_{\rm disk}^{9/2} / (m_{\rm pl} e_{\rm pl} a_{\rm pl}^{3}) \tag{1.4}$$

on the planetary mass $m_{\rm pl}$, eccentricity $e_{\rm pl}$ and semi-major axis$a_{\rm pl}^3$ as well as the semi-major axis $a_{\rm disk}$ of the disk. Thus, if the age and the SED of a DD system is known, via BB fitting one can determine the sizes and luminosities of present belts. And if those are too large for self stirring, the presence of a massive, potentially eccentric companion is likely. Thus the NaCo-ISPY survey, presented in Sect. 1.6.1, analyzes the SED of DD stars and selects those with oversized belts as primary targets.

Finally, similar to in PPDs, there is of course also feedback from the disk on the planet and from planets on planets. One of those is migration of the planet. Various migration mechanisms due to the disk have been proposed, such as Type I migration (Lindblad torques, inward migration Papaloizou et al., 2007), Type II migration (gap opening migration, inward migration Ward, 1997) and Type III migration (partial gap opening, in and outward migration Masset & Papaloizou, 2003). Since this might change the system's architecture completely and thus lead to wrong conclusions about its formation, it is important to look for young systems, ideally while planet formation is still ongoing. Since this thesis focuses on surveys specifically targeting those young systems, I leave the interested reader with the very good review about planet migration from Chambers (2009).

1.3 Direct Imaging of Exoplanets

1.3.1 Introduction

In contrast to other exoplanet detection methods, Direct Imaging (DI) belongs to the direct detection methods, since the planet is imaged directly. This holds the huge advantage that, e.g. the planetary spectrum can be measured directly without having to worry too much about stellar contamination, one of the major limitations if one tries to determine planetary atmospheric features in e.g. transit spectroscopy[12]. For example, from the extracted spectrum of 51 Eri b, see Fig. 1.7, Samland, M. et al. (2017) were able to determine planetary parameters, such as effective temperature $T_{\rm eff}$, surface gravity $\log g$, metallicity Fe/H, planetary radius R and even the cloud sedimentation value f, since cloud free models could not explain the spectrum shown in Fig. 1.7. With a sufficient baseline also the orbital parameters can be

[12]Despite large efforts e.g. in Espinoza et al. (2019) for WASP–19 b, there was no ROBUST detection of atmospheric features in exoplanet atmospheres using transit spectroscopy yet. Assuming those are present, the main reason for the non-detection is the dominant stellar variability dominating any subtle planetary signal. See Rackham et al. (2019)'s white paper for a discussion about how future instruments need to be designed to support the JWST in finding those signals.

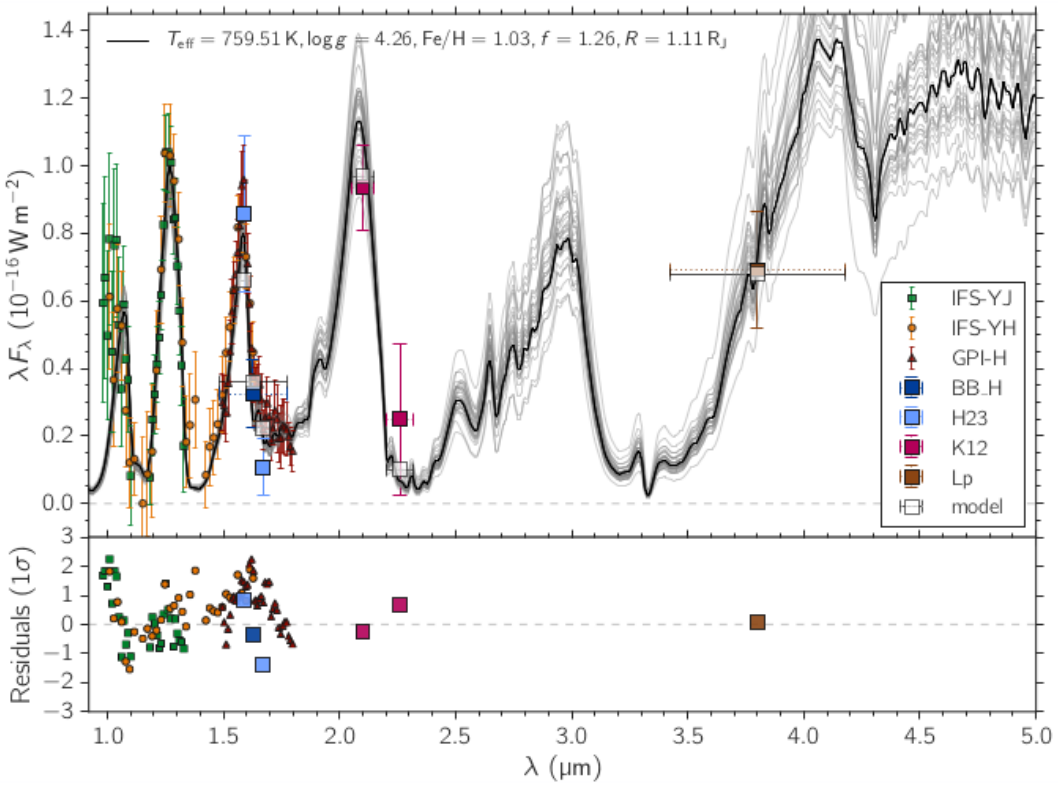

Figure 1.7: Spectrum of 51 Eri b. The Colored symbols mark data obtained with SPHERE, GPI and NIRC2 (L' data point). The black line shows the best model using the petitCODE (Mollière et al., 2015), the grey lines 32 randomly drawn samples from the posterior probability distribution to show the spread of plausible models. The parameters used for the best fit are given at the top of the plot. The horizontal error bars reflect the filter width rather than an error. The residuals are given in multiples of 1-σ uncertainties.
Credit: Samland, M. et al. (2017)

determined unambiguously[13]. And if one is lucky (or selected the targets wisely), even a disk can be imaged (e.g. Milli et al., 2017), possibly even during the planets' formation (e.g. Keppler et al., 2018). The main drawback is that it is extremely difficult and time intensive to find new planets, since the detection space is limited to young ($\lesssim$ 100 Myr), far out ($\gtrsim$ 10 AU) massive ($\gtrsim$ 1 $M_{\rm Jup}$) planets, see Fig. 1.3. Thus typically very large telescopes ($\gtrsim$ 8 m) are needed, supported by (extreme) Adaptive Optics (AO) consisting of a wavefront sensor and a deformable mirror that corrects for the atmospheric turbulence in real time (at a frequency of $\sim$ 1000 Hz, see Table 1.1). E.g. in the case of SPHERE's SAXO AO system, 41 $\times$ 41 41 actuator Deformable Mirror (DM) is used to correct for the atmospheric turbulence with a frequency of 1.38 kHz. (Beuzit et al., 2019). Additionally coronagraphs are being used to suppress the stellar light. Those technical developments as well as sophisticated post processing algorithms are described in the following section.

[13]Do not miss the amazing video of four GPs orbiting HR 8799: https://www.eso.org/public/videos/eso1905b

1.3.2 Observational Challenges

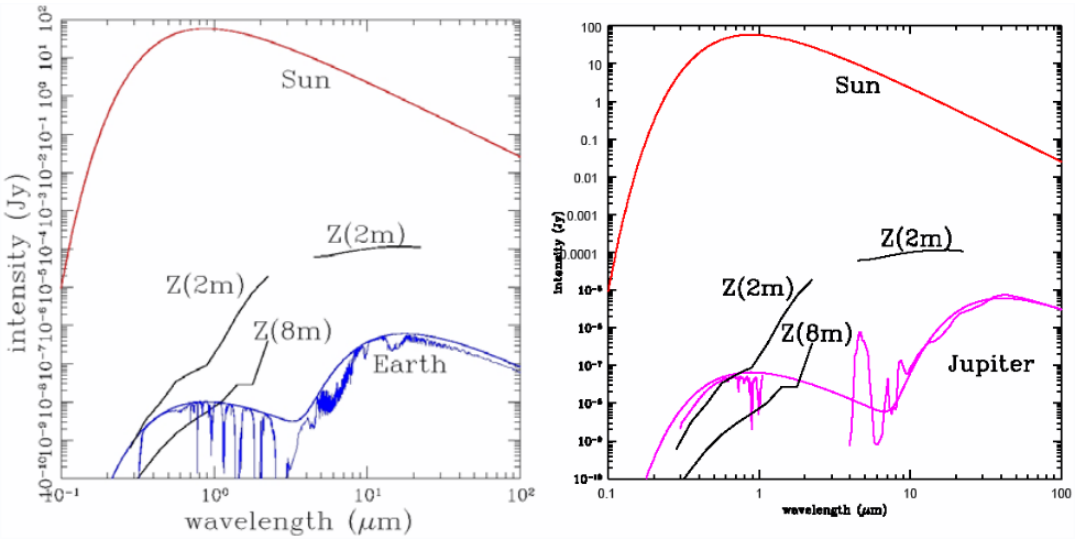

Figure 1.8: The Contrast of the Sun, approximated as a BB, compared to Earth and Jupiter. Earth' and Jupiter's SEDs are composed of reflected sunlight peaking in the optical and heat radiation peaking in the Mid Infrared. The contrast of Earth is about 10^{-10} in the visual and about 10^{-7} at $\sim 10\,\mu$m, why most imaging surveys operate in the Near InfraRed.
Credit: Kasting et al. (2009).

There are two major challenges when trying to image an exoplanet: First the enormous contrast of at least 10^6 for Jupiter for Jupiter, see Fig.1.8. And second, the tiny projected separations of e.g. a phase-dependent maximum of $0.1''$ for Earth seen from 10 pc . To minimize the contrast required, DI surveys typically operate in the Near InfraRed (NIR) (Table 1.2) and focus on young systems ($\lesssim$ few 10 Myr), where the planet is still hot from the formation process (e.g. Mordasini et al., 2017). To maximize the projected separation, targets are selected by their distance ($\lesssim$ few 100 pc). Since even the closest star forming region, ρ Oph, is at $\sim$ 160 pc distance (Loinard et al., 2008), often a trade off between age and proximity has to be made.

The following two sections provide an overview of the current status on how to tackle these challenges: The first presents the Adaptive Optics (AO) technique enabling observations at the diffraction limit of the telescope and the second presents coronagraphs that help achieving the required contrasts at those small separations. But even though they are split here, of course both require one another in order to achieve maximum performance. For example, a coronagraph unfolds its maximum capabilities only in the presence of an AO system "focusing" the stellar light coherently on the coronagraph.

Atmospheric Turbulence and Adaptive Optics

Seeing Due to temperature in the atmosphere, the atmosphere has an inhomogeneous refractive index. Thus an incoming coherent light-wave arrives at the ground

with phase shifts[14]. The Power Spectral Density function (PSD) of those distortions contains all sizes, but most relevant for current telescopes can be modeled with a fall off of $\sim 11/3$ and cut offs from 0.4 cm to 20 m (Traub & Oppenheimer, 2010). To characterize the effects of those disturbances in a simple way, the Fried parameters r_0 defines the length under which a wavefront is shifted by 1 rad ($\approx 57°$) at 500 nm (Fried, 1966). A telescope whose aperture D is much larger than r_0, will then be limited by the atmospheric turbulence rather than diffraction. The Full Width Half Maximum (FWHM) of the resolution argument is defined by $s := \frac{\lambda}{r_0}$ and called seeing[15]. It enlarges the size of the Point Spread Function (PSF) from its theoretical diffraction limit $\frac{\lambda}{D}$. The seeing has a wavelength dependence of $r_0 \propto \lambda^{6/5}$. E.g. on Paranal, home of the VLT and one of the best sites in the world, the median seeing is 0.66″[16], compared to a diffraction limit of $\frac{1\,\mu m}{8.2\,m} = 0.025''$ for an 8.2 m telescope observing at 1 µm.

Coherence Time Another important parameter when characterizing turbulence is the coherence time τ_0. In the frozen atmosphere approximations where the distortions are purely carried by the wind, it is defined as $\tau_0 := 0.314\frac{r_0}{v}$, where v is the wind speed perpendicular to the line of sight[17] (Roddier, 1981). This parameter is especially important for lucky imaging and modern AO corrected surveys, since it tells you how fast you need to expose or correct, respectively. Typical values of wind velocity at Paranal are 3-10 ms.

Adaptive Optics Besides the larger collecting area, one of the main reasons to build bigger telescopes is a higher spatial resolution. Being limited by the seeing is very thus very unsatisfying. This is where the Adaptive Optics (AO) system is used[18].

The AO system analyzes the incoming wavefront by using a Wavefront Sensor (WFS) and sends the results of the analysis to a DM which corrects for it. This is continuously done several hundred to thousand times per second, ideally significantly faster than the coherence time. The earliest publication suggesting the concept of an AO system is Babcock (1953), and the first on-sky system tested was COME-ON in 1989 at the 1.52m telescope of the Observatoire de Haute Provence (Rousset et al., 1990).

As WFS mainly three designs are used:

1. The Shack-Hartmann WFS (Shack & Platt, 1971) is the most widespread one and uses a set of lenslets to split up the light into many sub pupils. These are then imaged onto a camera. The position of each lenslet's image is proportional

[14] One of the reasons to observe in space is the absence of these aberrations in space.

[15] See Tokovinin & Kornilov (2007) and references therein for more thorough descriptions of the seeing and practical considerations how to measure it.

[16] `https://www.eso.org/sci/facilities/paranal/astroclimate/site.html`

[17] Since the wind speed is in general different at different altitudes, a mean weighted by the turbulence profile is used (Poyneer et al., 2009).

[18] Even though the tip/tilt correction can be seen as the first order AO correction, due to the large correction amplitudes it is made by an separate system and thus ignored here.

to the slope if the respective incident wavefront. It is used for example in SPHERE, NaCo and GPI.

2. The pyramid WFS (Ragazzoni & Farinato, 1999) is a pyramid prism. The light gets focused at its top, diffracting the light in four areas onto an underlying camera. By comparing the light intensity distribution in those four areas, the slope of the incident light can be derived and corrected for. It is used for example at the LBT and planned for many upcoming instruments.

3. The curvature WFS (Roddier et al., 1988) measures the curvature and not the slope of the wavefront. This is done by sensing the luminosity before and after the focal point of the imaged pupil. It is used at the Subaru telescope.

The main limitations of correction in an AO system are photon noise, chromaticity, aliasing, time delay, scintillation and non-common path errors. Details of those errors and potential improvements to the AO correction are e.g. explained in Sect. 4.6 of Traub & Oppenheimer (2010).

The imperfections resulting from these limitations then result in speckles. Due to e.g. flexures and temperature changes, they are neither perfectly static nor random noise, but have lifetimes of a up to multiple minutes (Hinkley et al., 2007; Milli et al., 2016). This means that they do not average with time like $\sqrt{t}$, as gaussian noise does. This makes sophisticated post processing algorithms extremely important.

In AO systems the uncorrected wavefront from the atmosphere can be represented by orthogonal basis sets, called modes. Ideally, an AO system would correct all of these, however since the number of the sensors and actuators on the DM is finite, the system cannot correct for spatial frequencies above the inter-actuator pitch. This pitch is the cutoff frequency equal to $N_{\mathrm{act}}/2$ in units of λ/D, where N_{act} is the number of actuators. Below this cutoff frequency is the corrected zone and above this is the seeing-limited zone. The spatial area those modes cover is sometimes referred to as dark hole, referring to an area where ideally the correction would be perfect and all speckles would be removed.

The correction quality can then be quantified using different metrics. One can to look at the residual phase left after the correction, ϕ_{res}. One can then define the mean variance $\sigma^2_{\phi_{\mathrm{res}}}$, which gives the energy present in the residual phase, averaged of the exposure time T. It is defined as

$$\sigma^2_{\phi_{\mathrm{res}}} = \frac{1}{T}\int_0^T \left[\frac{1}{D}\oint (\phi_{\mathrm{res}}(\vec{r},t))^2 \mathrm{d}\vec{r} - \left(\frac{1}{D}\oint (\phi_{\mathrm{res}}(\vec{r},t)\,\mathrm{d}\vec{r}\right)^2\right]\mathrm{d}t\,, \tag{1.5}$$

where D is the considered pupil size; see Sect. 1.2.1.3 in Cantalloube (2016).

Alternatively one can measure the resulting image quality. The standard metric here is the Strehl ratio, a number between 0 and 1. It is defined as the peak ratio between the obtained image and the theoretically ideal image only limited by diffraction. A Strehl of 1 would refer to a perfect system, e.g. an Airy function was

returned[19]. NaCo typically achieves a Strehl of 40-50% and SPHERE a Strehl of 80-90% in the H-band (see Table 1.1). Note that it is easier to obtain a higher Strehl at longer wavelengths.

Coronagraphy

Introduction Now with the AO focusing most of the stellar light in a stable, almost diffraction limited PSF, one has achieved a very high spatial resolution. However, in systems with a bright star and a faint planet, the achievable contrast is still very poor. This is where coronagraphs come in. But in order to understand how they work, one needs to know a bit more about the telescopes optics. The red, dashed arrows in Fig. 1.9 sketch the light path through a modern telescope (the E-ELT in this case), where the "lenses" are realized by mirrors: Plane (1) denotes the entrance pupil, plane (2) is the first image plane, plane (3) the reimaged pupil and plane (4) the reimaged image plane where the detector is located. A simple telescope only consists of the first two planes and one could calculate the resulting PSF $h(x, y)$ created by the aperture $\mathcal{P}$ of an incoming wavefront of phase Φ as

$$h(x, y) = \left| \mathcal{FT}^{-1}(\mathcal{P}(u, v) \cdot \mathrm{e}^{i\Phi(x,v)}) \right|^2 (x, y). \tag{1.6}$$

Here (x, y) and (u, v) are the coordinates in the focal plane and in the pupil plane, respectively. Further $\mathcal{FT}$ denotes the fourier transform and i is the imaginary unit. In the case of multiple planes the core of Eq. (1.6) simply needs to be evaluated multiple times then, see e.g. Cantalloube (2016). As seen in Fig. 1.9a, these multiple planes are needed to accomodate the different elements of the coronagraph.

Characterization Coronagraphs can be rated by five attributes, where the importance of each depends on the application. Since not all of which can be fulfilled simultaneously, often different designs of coronagraphs are present in an instrument:

1. *Throughput*: The relative flux from an off-axis source that is preserved.
2. *Inner Working Angle (IWA)*: The closest separation to the star at which the throughput is at least 50%.
3. *Contrast*: The flux ratio of the unobscured stellar PSF peak to the residuals at the considered position.
4. *Spectral Bandwidth*: Wavelength range for which the coronagraph works as intended.
5. *Sensitivity*: Robustness of the coronagraph to aberrations such as imperfect stellar centering (tip-tilt errors).

[19]The Strehl is a very useful number determining the image quality of imaging observations . In spectroscopy often encircled energy (e.g. energy into a fiber) is of primary interest.

Dependent on the plane they operate in, one can differentiate between two kinds of coronagraphs: Focal Plane Mask (FPM) coronagraphs operate in the focal plane(s), and pupil masks, operate in the pupil plane(s). Independent of where they are placed, they can either alter the light wave's amplitude or phase, dependent on the technology used. One can now decide to use a single such element as e.g. the pupil shaped apodizer of HARMONI, or combine multiple elements as for the Ring Apodized Vector Vortex Coronagraph (RA-VVC), both presented in the next section. For an introduction of basic the principles of coronagraphs, e.g. why apodizing the pupil can enhance your contrast, and also on their interplay with AO systems, I recommend the recent summary of Martinache (2019).

Examples In this paragraph I will describe some types of coronagraphs, paying particalar attention to the classical Lyot coronagraph and the Annular Groove Phase Mask (AGPM), the latter one is used by NaCo-ISPY. Guyon et al. (2006) gives a review on many of the coronagraphs currently in existence, including the two mentioned ones. Thus I will present four recent coronagraphs as they are currently discussed for use in the METIS instrument (Brandl et al., 2018) built for the E-ELT (de Zeeuw et al., 2014). Very similar ones are planned for MICADO (Baudoz et al., 2014), an instrument also currently build for the E-ELT.

The classical Lyot coronagraph was developed and used by Bernard Lyot to observe our Sun's corona Lyot (1939). This is also why are called coronagraphs, even though they are not intended to observe stellar coronas. The principle is sketched in Fig. 1.9a and composed of a simple obscuration (focal plane mask) is put at the first image plane (2) in order to suppress the stellar light. But at the sharp edges of the mask, light gets diffracted. That is why in the second pupil plane (3) a Lyot stop is is inserted, blocking that out scattered light. In the design of the METIS, additional covers to block light diffracted off the six spiders and from the M2 are added. That this coronagraph is still used in future instruments, shows how good the design is. Its advantage is that it preserves the full Field of View (FoV) and has a small Inner Working Angle (IWA). The main disadvantage is that Lyot stop effectively makes the pupil smaller, leading to a reduced spatial resolution and overall throughput. It is intended for extended and/or very bright targets.

In contrast to the amplitude modulating Lyot FPM, the **AGPM** coronagraph (Mawet et al., 2005; Absil et al., 2013) is a phase modulating FPM and part of the vortex coronagraph family. Half of the light of an on-axis source is shifted by half a phase so it is nulled at the image center. But of course energy is conserved, and the light is scatter far out, typically outside the detector. A Lyot stop is added blocking the spiders and the light directed outside. As can be seen in Fig. 1.9b, for METIS additionally a ring like apodizer is used, to smooth the outer edges of the primary mirror's aperture. Thus it is referred to as **Ring Apodized Vector Vortex Coronagraph (RA-VVC)**. Its advantage is a preservation of the FoV and a small IWA. Its disadvantage is its sensitivity towards jitter and its strong chromatic dependence.

The **grating vector Apodizing Phase Plate (gvAPP)** is an evolution of the APP: By putting a glass plate with small sinusoidal ripples in the telescope pupil plane, the APP moves energy from the central Airy core into speckles on either side of the Airy core. Due to the phase shift, small parts of the diffraction halo cancel. As more

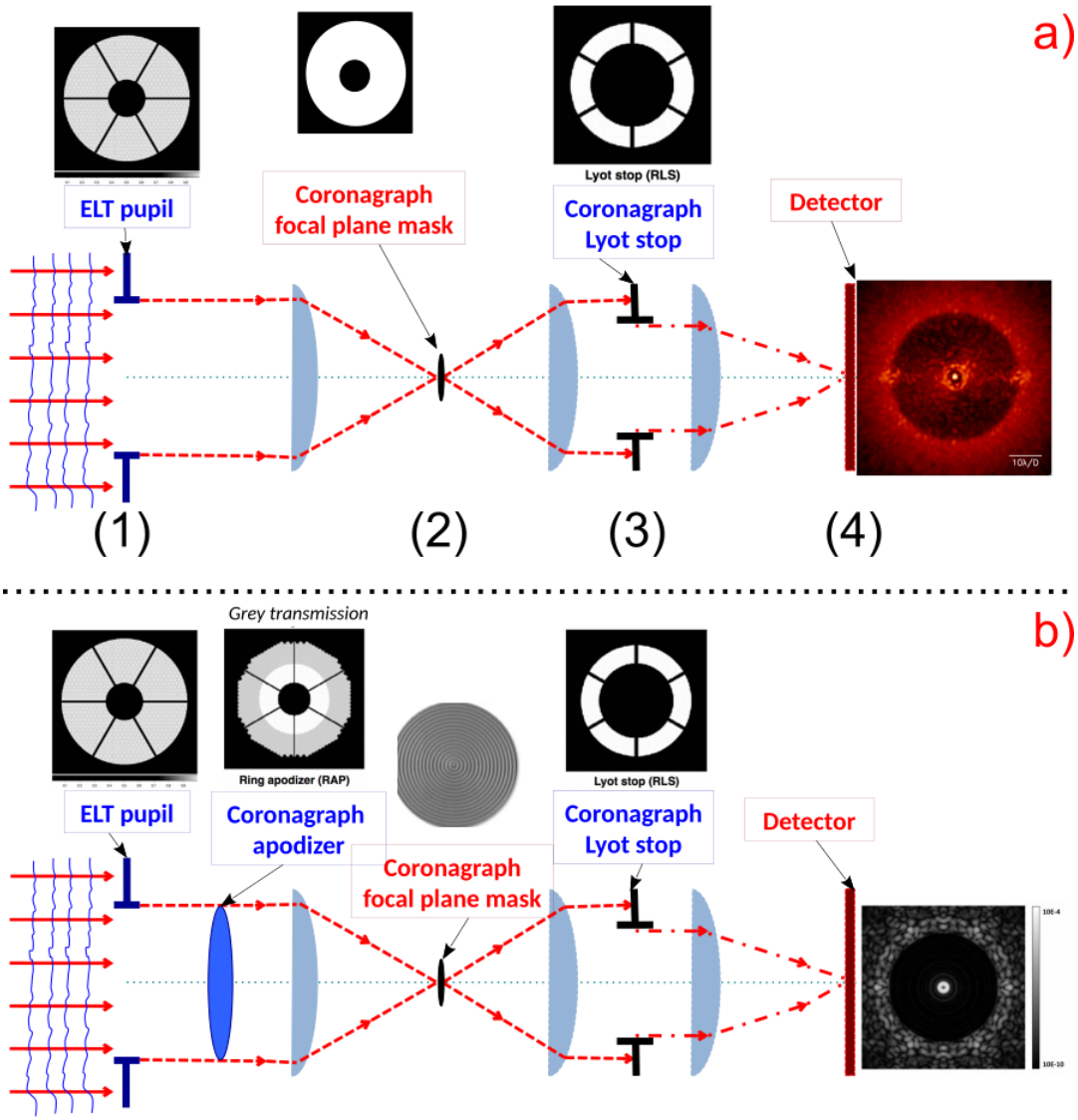

Figure 1.9: Examples of first light coronagraphs for the E-ELT as they are planned in their current design review. Panels a) - c) show coronagraphs for METIS, whereas Panel d) shows the pupil shaped apodizers for HARMONI. The schematics mark the path of an incoming lightwave across the telescope and instrument. (1) marks the first pupil plane, (2) the first image plane, (3) the second pupil plane and (4) the second, reimaged image plane where the detector is located. The small images at the top of each panel are schematics or images of the elements and the arrows mark where they are located. To the right of the detector simulated PSFs are shown. More details on the individual coronagraphs are given in the text.
Credit: Cantalloube et al. (ESO messenger, June 2019) for the schematics. The embedded images come from the various references provided in the text.

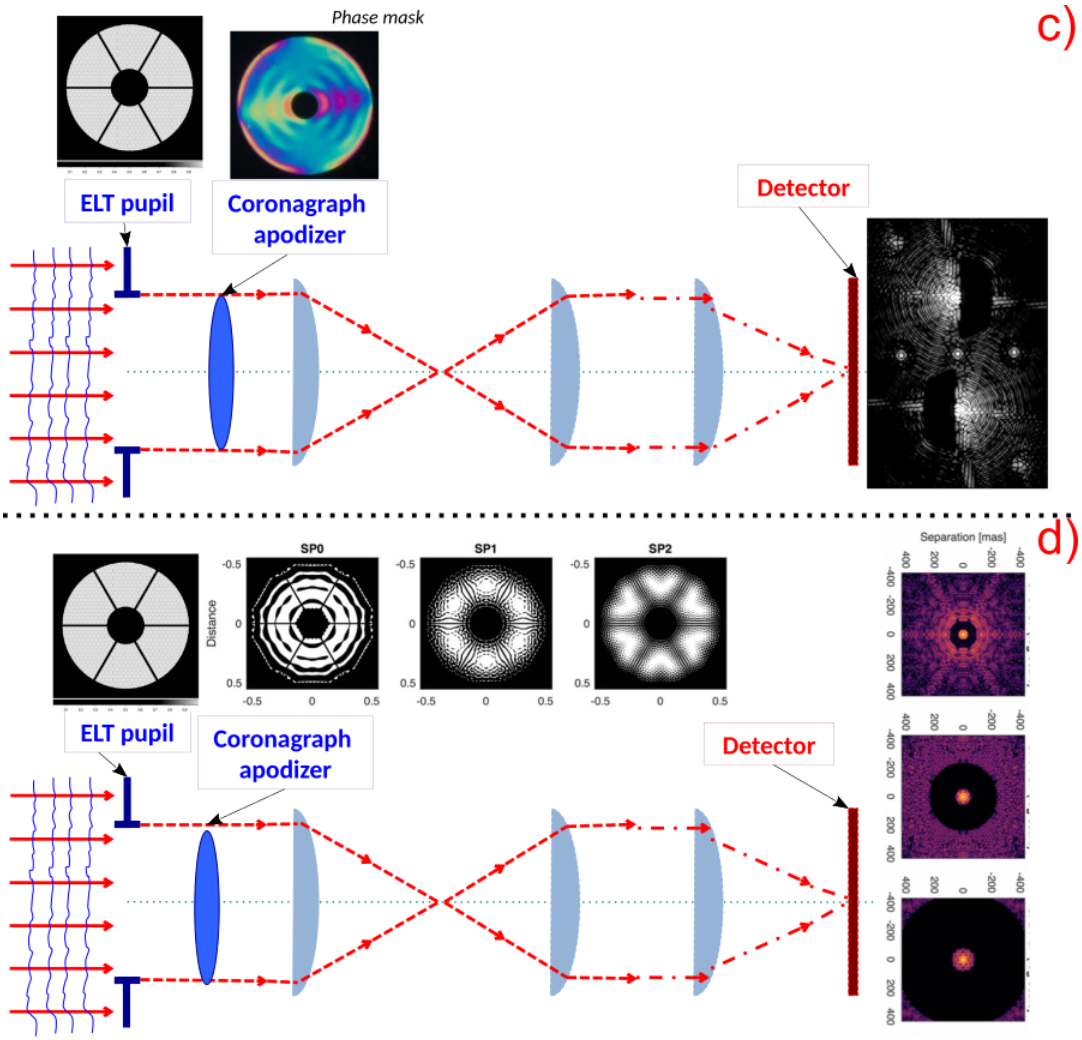

Figure 1.9: Continued.

and more of those ripples are added, one can remove all Airy rings on one side, down to a IWA of $\sim 2\lambda/D$ (e.g. Snik et al., 2012; Otten et al., 2014). However, since only one side is nulled, two observations are necessary. Another disadvantage is its strong chromaticity. To overcome the first issue, the grating vector Apodizing Phase Plate (gvAPP) uses a multiple layers of liquid crystal polymers instead of one glass plate. This allows a grating to be placed on the gvAPP to split the light in three PSF cores: One unocculted at the center containing only a few percent of the flux, and two in opposite directions with each one opposite side nulled, see Fig. 1.9c. Thus only one observation is needed to probe both sides. And, in the case of unpolarized light and sufficiently separated PSF cores, at the cost of only $\sim$ 50% flux loss on both sides – which is not a major problem in contrast limited observations. Its strength is the use of the full aperture, the full FoV and, because it is in the pupil plane, robustness towards tip-tilt vibrations and tip-tilt errors.

Since METIS will not have a pure pupil shaped coronagraph, I want to present the **Pupil Shaped Apodizer** that will be installed at HARMONI (Rodrigues et al., 2018), an Integral Field Spectrograph (IFS) of the E-ELT. Three apodizers are planned

in the preliminary design review, all printed with the microdot technology that allows to create quasi-transparent stages, see Fig. 1.9d and Carlotti et al. (2018). As masks in the pupil plane, they reduce the throughput down to about 35%, which is their major disadvantage, but can therefore enhance the contrast in an area around the central core. Here, as always for pupil masks, it is a trade off between the size (e.g. FWHM) of the central core and the higher order airy rings. So the first (left in Fig. 1.9d) coronagraph (SP0) has the smallest IWA and produces a post processed contrast of 10^{-5} at 3 λ/D (top PSF in of Fig. 1.9d). In contrast the last one (SP2, right in the Fig. and bottom PSF) has the largest IWA, but also the largest radius of speckle suppression, planned to achieve a contrast of 10^{-6} at 5 λ/D (Carlotti et al., 2018). Since they are shaped pupils, they are achromatic allowing their use in both, *H*- and *K*-bands and are insensitive towards tip-tilt vibrations and alignment errors.

Finally NaCo-ISPY mostly uses the AGPM coronagraph (Mawet et al., 2005; Absil et al., 2013) to suppress the stellar light. Additionally, NaCo-ISPY uses the Apo_165 Lyot stop to suppress the spiders and the secondary mirror's thermal emission (Kaufer, 2018, Fig. 5-7), but at the cost of losing about 60% of the throughput (Mawet, 2013). According to (Mawet et al., 2005) the simulated, theoretical transmission curve is

$$1 - \exp^{-(\alpha)^{1.5}/0.866} \quad , \tag{1.7}$$

where α is the angular separation of a source from the coronagraph's center. However, NaCo-ISPY performed a thorough on-sky throughput analysis which suggests a significantly worse throughput than the theoretical transmission curve predicts. The results will be presented in the future.

Because of this worse throughput and the still unknown movement of the AGPM with respect to the detector on minute timescales (see Fig. 2.1d), the AGPM is only used for stars brighter than $L' = 6.5$ mag. For fainter stars the centering is too difficult and thus takes too long, as the Detector Integration Time (DIT) needs to be increased to see the stellar PSF. And since the centering had to be redone every ~ 8 minutes because of the moving AGPM, it is not used for the dim stars.

1.3.3 Data Analysis Methods

In order to overcome the huge contrasts ($\gtrsim 10^5$, see Fig. 1.8) at very small angular separations ($\lesssim 1''$), high performance instruments and sophisticated observing and data analysis methods have been developed. And while for disk images and space observations the Reference Differential Imaging (RDI) technique dominates, where reference PSFs are used rather than a single observing block, I focus here only on the detection of point sources such as planets. For examples of RDI based techniques and capabilities, I refer to the following examples for RDI with Hubble (Lafrenière et al., 2009), RDI with GPI (Gerard & Marois, 2016) or RDI with NIRC2 (Ruane et al., 2019). As you can see, there are also references for ground based instruments (GPI and KECK), and also the NaCo-ISPY consortium (Sect. 1.6.1) is setting an RDI based

pipeline at the moment. This is possible thanks to the modern AO instruments, where the PSF becomes stable enough, even over years, to allow for this technique.

Besides RDI, there are two major data reduction strategies to suppress the stellar light in High Contrast Imaging (HCI): Spectral Differential Imaging (Sparks & Ford, 2002) and Angular Differential Imaging (Marois et al., 2006). Both of them make use that the planet "moves", while the stellar PSF remains static: Spectral Differential Imaging (SDI) uses the fact that diffracted stellar light (including speckles) "moves" radially outwards, proportional to the increasing wavelength. In contrast, a physical source remains at its projected separation independent of wavelength. This different behavior can then be used to disentangle the planet from speckles. The same idea is behind the Angular Differential Imaging (ADI): The telescope's de-rotator is switched off (pupil tracking) and, if centered on the star, anything (such as a planet) seems to rotate around the star with the Parallactic Angle (PA) changing. However, the PSF remains static. Note: For SDI one can also abuse different spectral features in the star and the planet, but this goes beyond the scope of this work, also since NaCo-ISPY observes at one wavelength only. Thus I will only talk about ADI in the rest of the section, basically the same procedures can be applied to SDI data, as explained before.

PCA is a fast and powerful technique with only one free parameter (e.g. in opposite to LOCI and its various derivatives (Lafrenière et al., 2007; Wahhaj et al., 2015)). In general Principal Components Analysis (PCA) (or Karhunen-Loève transformation, singular value decomposition), any data gets projected onto a lower dimensional space, minimizing the remaining scatter in a least-squares sense (e.g. Wold et al., 1987). Applied to HCI, one image gets approximated by an combination of all the other images, serving as reference frames. The dimension to be chosen represents the complexity of this approximation (or projection), and the higher it is, the more details will be removed. Since the planet has moved and thus is at a different location in the reference frames (if too slowly, a protection angle can be inserted), all similar parts between the images will be removed. Ideally this removes the (quasi) static stellar PSF, but keeps the moving planet. Later the frames are derotated and co-added. This method is perfect in a least square sense, when approximating one image by a lower dimensional representation of other images. However, it does not take into account that we the know precise motion of any possible point source between the images. A weakness tackled by the following example.

ANDROMEDA Cantalloube et al. (2015) introduces the ANgular Differential OptiMal Exoplanet Detection Algorithm (ANDROMEDA), a maximum likelihood approach to ADI data. In contrast to most other ADI techniques, ANDROMEDA uses the information of the motion of a possible point source in the image. It does this by subtracting two frames and then searches those for any planet signature: a positive

and a negative PSF of the planet, separated by the differential PA between those observations. All combinations of images are then correlated with the corresponding planet signature at the corresponding radial distance. Adding those flux maps and comparing them to the underlying noise, allows to create a Signal to Noise Ratio (SNR) map which gives you the likelihood of a source being at any position. An additional flux map holds the information about the flux at that position.

TRAP The Temporal Reference for the Analysis of Planets (TRAP) (working title) is a very recent recent approach to increase the sensitivity, especially close to the IWA. The main goal of the TRAP is to overcome the issue of the previously mentioned methods, that images close in time cannot be combined efficiently to enhance the companions signal, due to a minimum needed field rotation. This is especially true at small angular separations. But Milli et al. (2016) showed that there are at least two temporal regimes of speckle decorrelation: One having correlation times of a few seconds, and one slowly decaying over minutes to hours. Thus the images closest in time show strong correlations one could make use of. Therefore Samland et al. (in prep.) propose to create a data-driven model of the temporal systematics using reference pixels. Simultaneously a model of the planet "transiting" over the detector is fitted, probing a grid of planetary positions. This is then used to create a 2D detection map, similar to the one of ANDROMEDA. They can show that this approach gains up to a factor of six in contrast compared to ANDROMEDA. The gain is highest at small angular separations ($\lesssim 3\,\lambda/D$) and with short integration times ($\lesssim 10$ s) .

1.3.4 Instruments: NaCo, GPI and SPHERE

This Sect. is dedicated to compare the three HCI instruments NaCo, Gemini Planet Imager (GPI) and SPHERE.

All the instruments operate in the NIR, where GPI and Spectro-Polarimetric High-contrast Exoplanet REsearch (SPHERE) can observe from Y- to K-bands, and NaCo from J to M', where shorter narrow band filters down to 1.04 µm are available (Kaufer, 2018). They all have AO systems, relying on Shack-Hartmann WFSs, as well as coronagraphs installed. But the performance of those differs and is explained in more detail for each instrument in the next paragraphs. Also key aspects are summarized in Table 1.1.

NaCo

Naos Conica (NaCo) was the first AO instrument installed at the VLT in 2001 and is currently VLT's only imager capable of correcting in the IR. It is a multipurpose instrument, and after its decommissioning end of 2019, one will need to wait for ERIS (Kenworthy et al., 2018) to fill this gap[21]. NaCo offers a wide range of modes,

[21] Especially for observations of the galactic center, where IR-AO is needed this is crucial

Instrument	NaCo	SPHERE	GPI
Filter Range	$J - M'$ [a]	$Y - K$ [e]	$Y - K$ [d]
WFS		– Shack-Hartmann – [a e g]	
Lenslets Array	14×14 [a]	40×40 [f]	44×44 [g]
λ WFS [µm]	$0.8 - 2.5$ [a] $0.45 - 1.0$	$0.55 - 0.9$ [e]	I-band [h] H-band
Number of Actuators	185 [b]	1681 (41×41) [e]	1493 [g]
AO range [mag] Opt. – Min.	$12 - 16.7$ (Vis) $9 - 12$ (IR)	$10 - 15$ [e]	$7 - 9$ [h] (both Filters)
AO frequency [Hz]	440 [d]	1380 [e]	1500 [h]
Strehl H-band	47 [a]	90 [e]	95 [h]
Coronagraphs	2 4QPMs (H, K) [a] AGPM (L')	classical Lyot [f] APLC 4QPM	4 APLC [h] ($Y, J, H, K1 + K2'$)
IFU Resolution	...	50 ($Y - J$) [f] 30 ($Y - H$) 350 (LSS)	30 (Y) [h] 80 (K)

Table 1.1: Comparison of key aspects of NaCo, GPI and SPHERE. NaCo operates at longer wavelengths, but therefore has "only" an AO system, compared to the extreme AO systems of GPI and SPHERE. GPI and SPHERE are similar but not equal instruments. The main differences are given in the text. Th IFU Resolution refers to the spectral resolution.
References: [a] Kaufer (2018); [b] Rousset et al. (2003) ; [c] Lenzen et al. (2003); [d] Brandner et al. (2002); [e] Beuzit et al. (2019); [f] Kaufer (2019); [g] Macintosh et al. (2014); [h] GPI Online Manual[20]

including spectroscopy, polarimetry and coronagraphy. It played a key role, e.g. in imaging the first exoplanet 2m 1207 b (Chauvin et al., 2004, Fig. 1.1), or imaging the orbit of stars around the Milky Way center (e.g. Gravity Collaboration et al., 2018). However, I am focussing on the imaging part here. Further modes, such as spectroscopy, are not offered anymore. Almost a year ago, also the Visible (VIS) WFS broke[22], so the AO can only correct in the IR, see Sect. 1.6.1.

The key parameters for HCI of NaCo can be found in Table 1.1. One can see

[22] https://www.eso.org/sci/facilities/paranal/instruments/naco/news.html

that the AO system, NAsmyth Adaptive Optics System (NAOS), is inferior to the newer GPI and SPHERE instruments. The reason it can still compete with those instruments is the longer wavelength accessible, drastically reducing the required contrast for planetary detection, compare Sect. 1.3.1. Originally COudé Near Infrared CAmera (CONICA) posessed an Aladding 2 array detector. But From 2004 to 2013 it was changed to an Aladdin 3 1024×1024 px InSb array detector (Lenzen et al., 2003). However, since December 2014, and thus before the beginning of NaCo-ISPY, the detector was replaced by the old 1024×1024 Aladdin 2 detector from the ISAAC (Hummel et al., 2002) instrument (Kaufer, 2018). Its pixelscale is about 27.19 mas/px (see Sect. 2 for more details) and its sensitive to wavelengths from $0.8 - 5.5\,\mu$m (Kaufer, 2018). Additionally a 1024×1024 Rockwell Hawaii camera is present for observations between $0.8 - 2.5\,\mu$m with a finer spatial resolution of about 13.2 mas/px (Kaufer, 2018).

SPHERE

The 2015 commissioned SPHERE instrument is dedicated to find and characterize exoplanets via DI. Therefore SPHERE is equipped with three main systems: The InfraRed Dual-band Imager and Spectrograph (IRDIS) (Dohlen et al., 2008), the Integral Field Spectrograph (IFS) (Claudi et al., 2008) and the polarimeter ZIMPOL (Schmid et al., 2018). Those are supported by the SAXO extreme AO system (Fusco et al., 2006). Its key parameters are given in Table 1.1. The performance of the interplay of those systems has been shown in various publications, e.g. the highest quality spectra of HR 8799 d and e (Zurlo & Bonnefoy, 2015) – maybe with the exception of the recently acquired R 500 GRAVITY spectrum of HR 8799 e (Lacour et al., 2019). SAXO also showed its unprecedented performance, by suffering from low wind effects at the telescope dome – an unconsidered phenomenon before, since it usually is dominated by the much stronger atmospheric turbulences (Milli et al., 2018). But so far SPHERE's highlight is certainly the discovery of the exoplanet HIP 65426 b (Chauvin et al., 2017) and the exoplanet PDS 70 b inside a disk (Keppler et al., 2018; Müller, A. et al., 2018).

ZIMPOL is the polarimeter of SPHERE allowing for the characterization of disks in the V-, R- and I-band and with an angular resolution down to 22 mas (Fusco et al., 2006). It is built for the detection and characterization of disks, which emit polarized light.

IRDIS can be used in four imaging modes: Dual-band imaging (Vigan et al., 2010), Longs Slit Spectroscopy (LSS) (Vigan et al., 2008) and dual-polarization imaging (Langlois et al., 2010) and a classical imaging mode. The two respective filters of the Dual-band imaging mode have been chosen such, that one of the filters should hit an absorption line of the potential exoplanet, nulling the signal there and allowing for very efficient differential imaging. The LSS has a spectral resolution R of either 50 in

narrow band mode, or 350 in BB mode[23]. The 2048 × 1024 Hawaii II detector offers a 11″ × 11″ FoV, with a 12.25 mas/px Nyquist sampling at 0.95 µm. Furthermore it can observe simultaneously with IFS in the so called IRDIFS and IRDIFS_ext modes.

IFS offers two modes: The high resolution mode with as spectral resolution $R \sim 50$ and a wavelength coverage from $0.95 - 1.35\,\mu m$, and the low resolution mode with $R \sim 30$ a wider wavelength coverage from $0.95 - 1.65\,\mu m$ (Claudi et al., 2008). In the high resolution mode it can be combined with IRDIS observing the H-band (IRDIFS mode), and in the low resolution mode with IRDIS observing in the K-band (IRDIFS_ext mode). This simultaneous observation at all wavelengths is the major difference and advantage over GPI.

GPI

The GPI instrument (Macintosh et al., 2014) is currently located at the Gemini South observatory one Cerro Pachon, Chile, close to the VLT. Gemini north is a twin telescope on Mauna Kea, Hawaii, GPI will to be moved to this site in the next few years to explore the northern hemisphere (Rantakyrö et al., 2018). GPI can observe in the Y, J, H, $K1$ and $K2$[24]-bands. It observes either in coronagraphic mode using an Apodized Pupil Lyot Coronagraph (APLC) or no coronagraph. With this setup, one chooses between spectroscopic observations (Larkin et al., 2014), where the spectral resolution reaches from $R \sim 35$ in the Y-band to $R \sim 80$ in the K-band, or polarimetric observations (Perrin et al., 2015).

Thus having a comparably simple setup, GPI's strength lies in its extreme AO system (Poyneer et al., 2014) Table 1.1 shows its very similar performance compared to SPHERE. A robust study between the two instruments quantifying their on sky performance is still missing, but the results seem comparable.

The highlight of GPI is certainly the discovery of the exoplanet 51 Eridani b (Macintosh et al., 2015, see also Fig. 1.7 for a spectrum) in the course of the GPI Exoplanet Search (GPIES). A summary of the first 300 stars observed with GPIES is given by Nielsen et al. (2019).

1.4 Detection of Exoplanets using the Radial Velocity Method

Radial Velocity (RV) is an indirect method to identify exoplanets. The NASA exoplanet archive[2] lists 707 confirmed planet discoveries, making it the second most successful technique after the transit method (as of January 2019). The basic idea is based on the Doppler shift of the stellar light, when the star and its companion orbit around their common center of mass and thereby move radially with respect to the

[23] Here GPI has no comparable mode.

[24] According to GPI's website, $K2$ suffers from throughput issues since its commissioning and has no guaranteed performance.

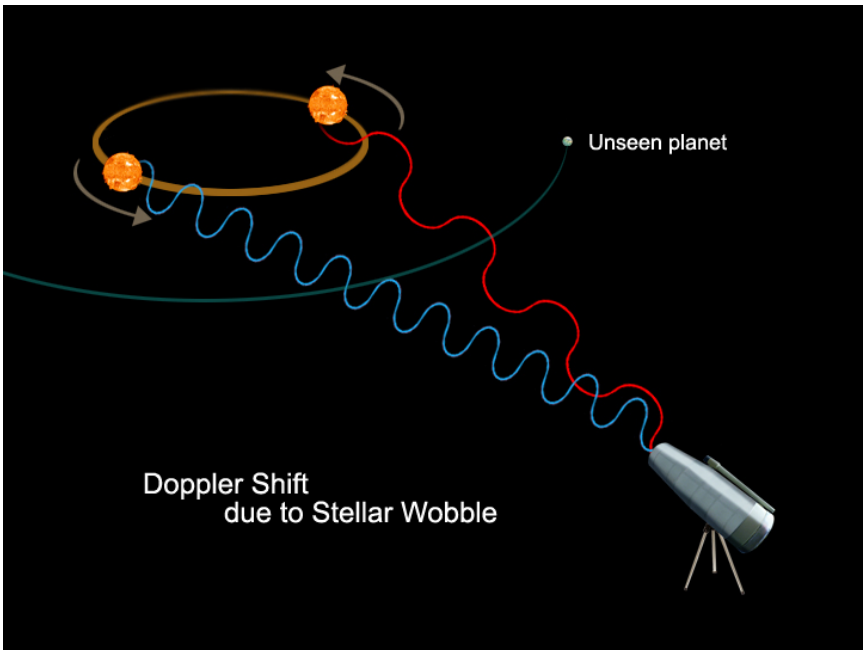

Figure 1.10: Schematic of the idea of the RV method: The planet pulls on the star, making it move in an ellipse. The radial motion of this movement can be detected using the optical Doppler shift.
Credit: NASA/JPL

observer, see Fig. 1.10. The Doppler shift is given by (Einstein, 1905)

$$\lambda = \lambda_0 \cdot \frac{1 + \frac{1}{c} \cdot \vec{k} \cdot \vec{v}}{\sqrt{1 - \frac{\vec{v}^2}{c^2}}} \quad , \tag{1.8}$$

where λ is the wavelength of a photon received by the observer, λ_0 is the emitted wavelength of this photon, c is the speed of light, $\vec{k}$ is the unit vector pointing from the observer to the source and $\vec{v}$ is the velocity vector of the star during the emission of the photon with respect to the observer. If a planet of mass m_{Pl} orbits this star with mass M_* on an orbit with semi-major axis a, eccentricity e, period P and inclination i, Kepler's laws give the semi-amplitude K of the Doppler shift as

$$K = \sqrt{\frac{G}{(1-e^2}} m_{\mathrm{pl}} \sin i (m_{\mathrm{pl}} + M_*)^{-1/2} a^{-1/2} \, . \tag{1.9}$$

Or one can express this in more practical units, this reads

$$K = \frac{28.433 \frac{\mathrm{m}}{\mathrm{s}}}{\sqrt{1-e^2}} \frac{m_{\mathrm{pl}} \sin i}{\mathrm{M_{Jup}}} \left(\frac{m_{\mathrm{pl}} + M_*}{\mathrm{M}_\odot} \right)^{-1/2} \left(\frac{a}{\mathrm{AU}} \right)^{-1/2} , \tag{1.10}$$

or, equivalently when using Kepler's third law

$$K = \frac{28.433 \frac{\mathrm{m}}{\mathrm{s}}}{\sqrt{1-e^2}} \frac{m_{\mathrm{pl}} \sin i}{\mathrm{M_{Jup}}} \left(\frac{m_{\mathrm{pl}} + M_*}{\mathrm{M}_\odot} \right)^{-1/2} \left(\frac{P}{\mathrm{yr}} \right)^{-1/3} . \tag{1.11}$$

Note that the planet's mass and the inclination of the system are degenerate and therefore cannot be determined via the RV method. This is why the mass of a planet determined by the RV method is typically given as a lower limit, which then has to be multiplied with the sinus of the inclination i, once this has been determined otherwise. If determined, most often this is done when the planet is also transiting its host star, the inclination is then extremely close 90°, and the true mass is basically equivalent the previous minimum mass. Alternatively, if you wished to break the degeneracy in inclination, one could assume the planet to be coplanar to some disk where the inclination has been determined else how. However, since the obliquities of at least hot Jupiters around high mass stars are pretty random (Albrecht et al., 2012), this assumption is questionable. And even if not, systems with known disk inclinations are rather rare.

1.4.1 Data Analysis Methods

In order to achieve the required precision for exoplanet detection, spectral features, such as absorption lines, are required for the Doppler shift measurements. For hot stars ($T_{\rm eff} \gtrsim 10,000$ K), all chemical elements are at least partly ionized and therefore there are hardly any possible electron transitions to cause these absorption lines in the optical or NIR. But those are the only wavelengths where the star is bright enough and accessible from the ground. If however the star is too cold ($T_{\rm eff} \lesssim 3500$ K), the lines become so densely packed due molecular bands, that it gets harder and harder to identify individual lines and thus precisely determine the RV of the star (e.g. Lovis & Fischer, 2010; Figueira et al., 2016). This is why most RV surveys focus on the intermediate stars of Spectral Type (SpT) FGK. Besides the number of lines, also the relative depth of the lines is important to determine the achievable precision $\sigma_{\rm RV}$. And for a given, sufficiently equipped instrument, it scales like

$$\sigma_{\rm RV} \propto \frac{\sqrt{\rm FWHM} \cdot \sqrt{\rm N_{lines}}}{\rm C \cdot SNR}\,. \tag{1.12}$$

Here FWHM is the full width at half maximum of the lines, $\rm N_{lines}$ is the number of lines, C is the depth of the line compared to the continuum level and SNR is the signal-to-noise ration in the continuum (see Lovis & Fischer, 2010).

In order to determine the RV now, in the classical approach one creates a binary mask (or multiples for different SpTs), which is then correlated with the measured spectrum of the star. Spectral regions with strong telluric features are simply ignored. The Data Reduction Software (DRS) for HARPS can achieve a precision of about 1 m/s with this method (Mayor et al., 2003), sufficiently precise to discover Jupiter in our own solar system if seen from a distant world edge on. But there are other strategies. E.g. the Calar Alto high-Resolution search for M dwarfs with Exoearths with Near-infrared and optical Échelle Spectrographs (CARMENES) survey (Reiners et al., 2018) observes mainly cool M dwarfs, where the above mentioned

problem of overlapping lines occurs. Similar, if one wanted to detect an Earth analog orbiting a Sun like star, another factor of about 10 to the currently available precision is required. But at this precision you will start being limited by stellar noise, see Chapter 5. Thus methods have been developed to disentangle RV induced by companions and RV signals induced by stellar activity. Those so called activity indicator are then analyzed together with the RV signal to look for correlations. An often used approach is to analyze the absorption strength in individual lines, which are known to often show correlations with stellar activity. Another approach is to measure the asymmetry of the absorption lines, e.g. using the Bisector Span (BIS)[25] (Voigt, 1956; Hatzes, 1996). Since a companion would not deform the absorption lines, a correlation between the BIS and the RV is seen as a strong indicator for stellar activity. Günther et al. (2018) showed that this correlation could also be caused by a background eclipsing binary, why one should not discard those candidates too quickly. These methods are not capable of identifying all stellar activities[26] neither can they correct for it. Alternative methods have been proposed to circumvent these limitations. Here I present three promising ones that were developed in the recent years.

SERVAL The SpEctrum Radial Velocity AnaLyser (SERVAL[27], Zechmeister et al., 2018) was mainly developed for the CARMENES survey and comes with two main advantages over the standard approach of using binary masks: First it can also handle dense spectral regions where lines are overlapping and no continuum can be identified. And second it uses the advantage of the broad spectral range of CARMENES from about 520–1710 nm (Quirrenbach et al., 2014) to determine the chromatic index: a dependence of the RV signal on the wavelength. Further it has precision close to the benchmark HARPS DRS when applied on HARPS data. This is why it has been chosen as the reduction pipeline for Chapter 5.

SERVAL does not rely on binary masks, but creates its own template for each star. This is done by co-adding the spectra of the individual exposures, after shifting them to account for the Doppler shifts.Wavelength regions with known strong telluric features are simply ignored. The co-added spectrum serves as a template which is correlated against each individual measurement to determine the differential RVs. This approach makes sure that the RV can be determined also in regions with dense stellar lines and without any a-priori knowledge of the stellar spectrum.

The chromatic index is determined on an order basis: Since the above procedure is done on a per order base, it returns as many RV measurements as the spectrograph

[25] The bisectors of the Cross Correlation Function (CCF) of the mask with the spectrum are measured. CERES, the pipeline used in large parts of this thesis, for example defines the BIS then as $\bar{B}_{0.1-0.4} - \bar{B}_{0.6-0.85}$, where $\bar{B}_{a1-a2}$ gives the mean of the bisector values from relative absorption depth $a1$ to $a2$ (Brahm et al., 2017).

[26] Despite analysing the above mentioned activity indicators, e.g. the discovery of a planet around TW Hya (Setiawan et al., 2007), the discovery had been put to question by Huélamo et al. (2008) and remains unsolved to date.

[27] www.github.com/mzechmeister/serval

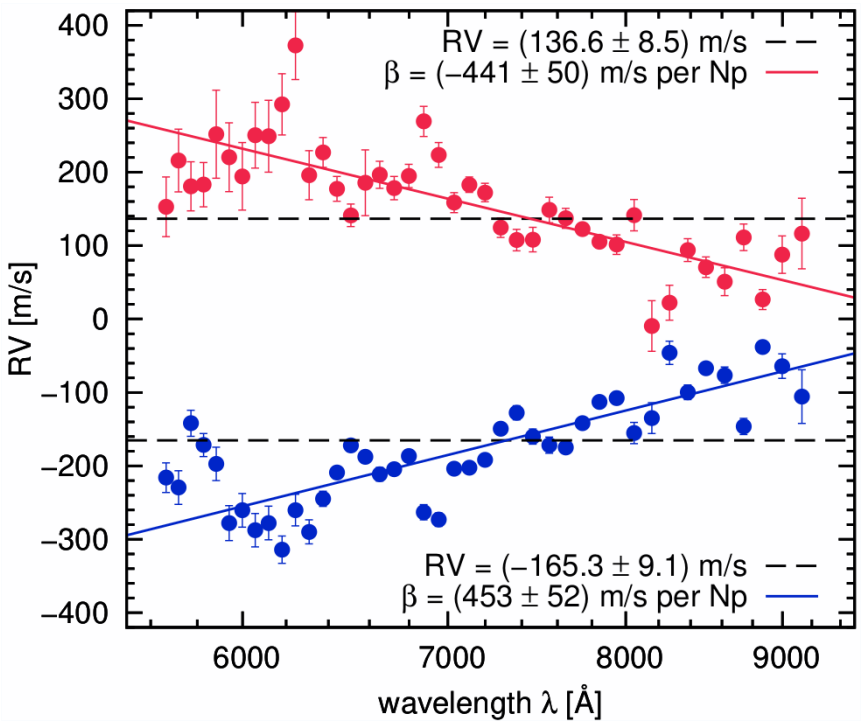

Figure 1.11: RVs measured in 42 orders of two CARMENES observations of YZ CMi using only the VISual channel demonstrating the power of the chromatic index (solid blue and red lines). The dashed black lines show the simple weighted average of the data.
Credit: Zechmeister et al. (2018)

has orders (assuming a sufficient data quality, otherwise single orders might have to be removed). Many activity related stellar features (such as star spots) affect different wavelengths (or probed temperatures) differently. E.g. for star spots, this can be easily understood, since the contrast at short wavelengths (high temperatures) is higher than at longer wavelengths (lower temperatures). Since a planet would affect all wavelengths the same, a wavelength dependence of the RV shift can be used as an activity indicator. To first order, a straight line in log space, $\mathrm{RV}(\lambda) = \alpha + \beta \ln \lambda$, can then be fitted, where α and β are the free parameters and β represents the chromatic index. An example where a clear activity sign is seen, is shown in Fig. 1.11. Of course this chromatic index is not limited to the SERVAL approach, but can (and is) also be used on data using binary masks. The data only needs to be analyzed on a per order base. However, it works best on data with a broad spectral range, where CARMENES is certainly predestined with its VISual and IR channels. (Zechmeister et al., 2018)

Measuring RV on Individual lines As aforementioned, detecting an exoearth requires a precision of at least 10 m/s. In this regime, stellar activity is the main limitation for RV observations. Dumusque (2018) quantifies the idea of measuring the RV not on all lines simultaneously, but rather to measure the RV signal on individual lines. Of course, the measurement on each individual line is, to first order, a factor

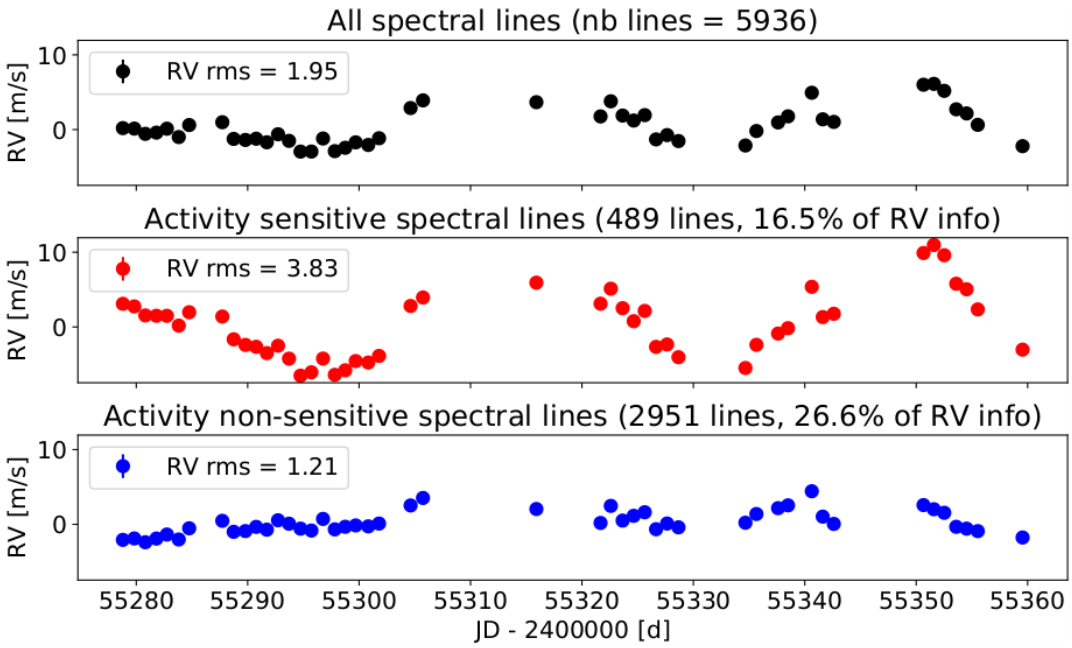

Figure 1.12: Comparison of 2010 RVs of α Cen B as derived when using all the spectral lines (black), "active lines" (red) and "inactive lines" (blue). The title gives the number of lines used in each group, as well as their overall influence on the total RV. One can see that the "inactive lines" decrease the activity signal by a factor of 1.6, whereas the "active lines" increase it by a factor of 2.
Credit: (Dumusque, 2018)

of $\sqrt{N_{\text{lines}}}$ worse than for all N_{lines} lines measured simultaneously, see Eq. 1.12). But since one has N_{lines} measurements, this evens out. The advantage is, that one can categorize the individual lines. E.g. the Ca II H and K lines at 3933 Å and 3968 Å are used as activity indicators in the R_{HK} index. Thus those lines are prone to increase the measured jitter and are better ignored. But since it is not known which lines contribute more to the unwanted stellar RV scatter in general, Dumusque (2018) came up with an algorithm which automatically quantified the lines, based on their RV scatter in multiple observations of the same star. He then showed, that in the case of α Cen B, the RV signal of the "active lines" has a 2 times higher standard deviation, compared to if all lines are used. If, on the contrary, he used only the "inactive lines", he could suppress the RV scatter by a factor of 1.6. This result is shown here in Fig. 1.12. Currently the main problem with this method being the large number of RV measurements ($\gtrsim$ 1000) with a high SNR ($\gtrsim$ 100) are required to significantly outperform the HARPS DRS.

WOBBLE Bedell et al. (2019) developed the open source program WOBBLE[28] mainly to tackle the issue of telluric lines. As mentioned before, telluric regions are often simply ignored, which directly leads to two problems: First we lose significant information still present in those regions (Bottom et al., 2013). This is particularly true

[28] https://github.com/megbedell/wobble

when observing in the NIR, where many more telluric features are present. Second, not all telluric features are removed. Thus, even if all strong telluric active regions could be identified and masked, microtellurics can still affect the achievable RV at the sub 1 m/s level (Cunha et al., 2014). This issue has been tackled by others before, e.g. by creating telluric models (Gordon et al., 2017), but the calibrations of those models require additional observing time.

The approach of Bedell et al. (2019) is to model the telluric features simultaneously with the stellar spectrum, without the requirement extra observations. This idea is not completely new, but has been done e.g. by Simon & Sturm (1994) or Czekala et al. (2017). However, both assume the telluric spectrum to be static and only changing with the doppler shift by earths motion. Bedell et al. (2019) now extend this, that only the stellar spectrum is assumed static, whereas the telluric spectrum may change between different observations. They can show that WOBBLE gives similar results as the benchmark HARPS DRS, given enough observations ($\gtrsim 50$) are are present to disentangle the stellar from the telluric absorption features. Thus with further improvements, this approach might turn out very useful, especially for IR surveys.

1.5 Other Methods to Detect Exoplanets

Besides the DI and RV method, there are various other methods, where I briefly want to explain the most important ones in this chapter. Other successful techniques not part of this overview include timing variations, e.g. of pulsars, eclipsing/transiting systems or other regular events: The the earlier mentioned first exoplanet PSR 1257+12 b was detected using tiny variations in the pulsar's time-of-arrival signal, because, similar to the RV method, the planet pulls the neutron star further and closer towards us, altering the travel time of the light signal. A deeper analysis of these timing variations are beyond the scope of this thesis and thus not discussed here. I refer to Schwarz et al. (2016) using timing variations of eclipsing binaries, Agol & Fabrycky (2018) for transiting planets' timing variations and Kramer (2018) for the pulsar timing method. For the chances of finding exoplanets using gravitational waves with the (e)LISA space interferometer, I refer to the discussion between Cunha et al. (2018) and Wong et al. (2019), where the first group has a rather optimistic view, which the second does not share.

The techniques explained in more detail are the microlensing technique, introduced in Sect. 1.5.1, the astrometric detection introduced in Sect. 1.5.2 and the transit method introduced in Sect. 1.5.3.

1.5.1 Microlensing

Microlensing uses the consequence of Einstein's general theory of relativity, that masses bends space-time itself, and thus also a light ray gets deflected in the presence of a mass. It can be shown that a Foreground (FG) mass (e.g. a star) can act in a

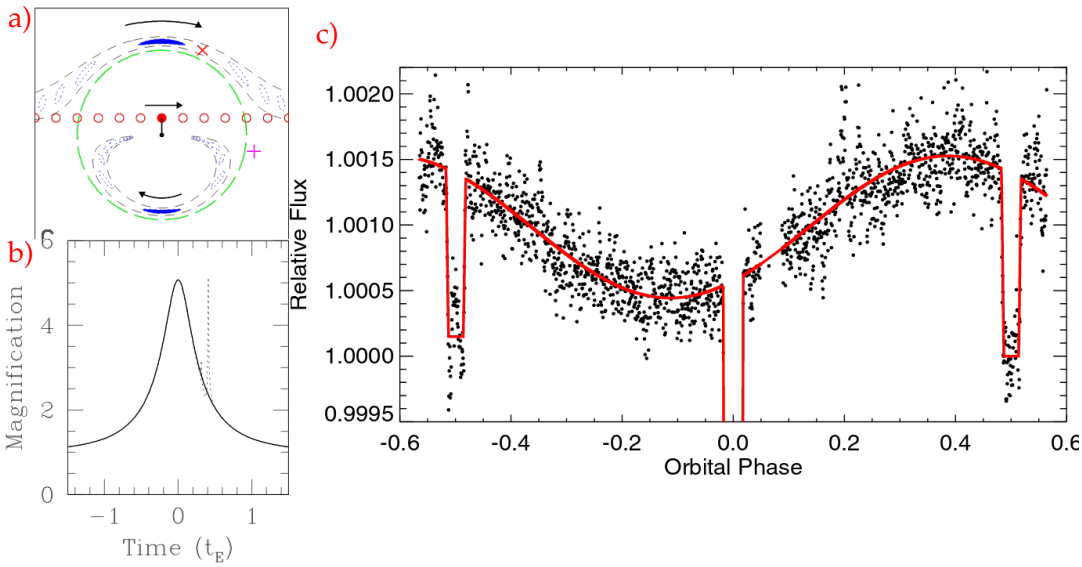

Figure 1.13: a): Schematic of the microlensing event. The red background star passes behind the foreground star (small black dot). Green area is the Einstein ring, the dotted blue areas marks the images if not fully aligned. Panel b) shows the respective lightcurve. If a planet is present, the light curve will get disturbed (dashed line). Panel c) shows the phase-folded lightcurve of HD 209458. The red line denotes the fitted model, where the primaray (phase 0) and secondary eclipse (phase 0.5) is visible. The planet also adds significant flux to the system, inducing the sine wave.. Its hottest point is shefted eastwards with respect to the star, why the maximum is not aligned with the secondary eclipse.
Credit: Microlensing: Gaudi (2010), Transit: Zellem et al. (2014)

similar way as a lens on the light coming from a Background (BG) source. Assuming both sources are point like and perfectly aligned, the BG image of the BG source gets projected into a so called Einstein ring, where radius θ_E of this ring is given by

$$\theta_E = \frac{2.2\,\mathrm{AU}}{D_l}\left(\frac{M}{0.3\,\mathrm{M}_\odot}\right)^{1/2}\left(\frac{D_s}{8\,\mathrm{kpc}}\right)^{1/2}\left(\frac{x(x-x)}{0.25}\right)^{1/2}, \tag{1.13}$$

where M is the lenses mass, D_l is the distance from the observer to the lens, D_s is the distance from the observer to the BG source and $x := D_l/D_s$ is the normalized lens distance. If the sources do not align perfectly, instead two images of the BG source are shown, one inside and one outside the Einstein radius, see Fig. 1.13a. In the context of exoplanets, where the FG and BG sources are stars, this is usually not resolvable. However, it leads to a magnification of the BG star. This amplification is shown schematically in Fig. 1.13b. If now a planet orbits around the star in the lens plane, it acts as a separate lens with its own Einstein radius. This than leads to a distortion of the profile of the magnification of the BG star and shown as dashed line in the magnification curve. Since the magnification is proportional to the square root of the mass of the lens (similar to the Einstein radius), the effect is usually much smaller than in the panel shown, and also it favors massive planets. In principle one could detect any amount of objects in a systems. E.g. Gould et al. (2014) present a

system, where a planet is found orbiting a binary system in a S-type configuration.

A major weakness of the microlensing technique is that events are extremely rare and unrepeatable. Thus most surveys focus close to the galactic center to increase the chances of an alignment. However, Klüter et al. (2018) proposed to use the precise Gaia measurements to predict such microlensing events and follow them up with VLTI's GRAVITY instrument (Gravity Collaboration et al., 2017). For further information about microlensing I refer to Gaudi (2010).

1.5.2 Astrometric Detection of Exoplanets

Astrometric detection of exoplanets is similar to the RV method in that sens, that both observe the orbit of the host star around the common center of mass. The difference is that RV measures the one dimensional radial motion, whereas astrometry measures the tangential, two dimensional motion. With those two dimensions, the orbit of the star, and therewith the planet, can then then be determined without any ambiguity. The orbit on the sky can be described using Kepler's Laws and simple geometry. With the approximation of that the planet's mass is much smaller than the stellar mass, $m_{\mathrm{pl}} \ll M_*$, the astrometric signal θ_{A} is given as

$$\theta_{\mathrm{A}} = 3\,\mu\mathrm{as}\,\frac{m_{\mathrm{pl}}}{\mathrm{M}_\oplus}\left(\frac{M_*}{\mathrm{M}_\odot}\right)^{-2/3}\left(\frac{P}{\mathrm{yr}}\right)^{2/3}\left(\frac{d}{\mathrm{pc}}\right)^{-1}, \tag{1.14}$$

for a planet on a circular orbit with Period P, and a distance from the observer to the system d. Differently than expected, astrometry has not played a big role in the detection of exoplanets, see e.g. Fig. 1.2 which lists the detections per year of each detection type. However, with the astrometric GAIA satellite observing at this very moment, this should change with its future data realeases. Sahlmann et al. (2015) assume that GAIA will identify up to 500 exoplanets only in binary systems. For further reading about astrometric detection and characterization of exoplanets, I refer to (Quirrenbach et al., 2014).

1.5.3 Exoplanetary Transit Detections

In terms of detected extrasolar planets, the most successful technique to date is the transit technique, in particular because of the Kepler space telescope (Borucki et al., 2010). But also the recently started TESS mission (Ricker et al., 2014) should lead to many new discoveries.

The transit method is an indirect method. Similar to the gravitational lensing it measures the changes of the flux of a star. But here the flux of a star does change when its planet transits between us and its host star. Since the radius of the star is usually known, one can then determine the radius of the planet via the depth of the obscuration, eventually correcting for limb-darkening. Via the Rossiter-McLaughlin effect (Rossiter, 1924; McLaughlin, 1924) one can than further predict the obliquity (stellar alignment) of the planet's orbit with respect to the stellar rotation axis. A still

unexplained result of this is, that hotter stars tend to have less aligned orbits than colder stars (Albrecht et al., 2012).

Further one could, in principle, derive properties about the planet's atmosphere, measuring the observed radius at different wavelengths. When the planet transits in front of the star (primary eclipse), or a reflected spectrum if the planet disappears behind the star (secondary eclipse). With this method Wakeford et al. (2017) could detect water absorption bands in HAT–P–26 b's transmission spectrum. Figure 1.13c shows the phase-folded light curve of HD 209458, where both transits are clearly visible. One can also see that the hottest point of the planet is not facing the star directly, but shifted eastwards. I refer to Winn (2010) for further information about the transit technique.

1.6 Direct Imaging Surveys

1.6.1 NaCo Imaging Survey for Planets around Young stars

This Sect. is dedicated to describe the ongoing NaCo-ISPY survey, where I primarily work on. Section 1.6.1 presents the survey and lists key numbers. Section 1.6.1 explains how the targets were selected and prioritized and why this selection makes NaCo-ISPY unique. The standard observational setup used during the NaCo-ISPY setup is explained in Sect. 1.6.1. Finally Sect. 1.6.1 lists the current results and highlights of the survey. Further results where I am leading scientist are listed in Chapt. 3.

Introduction

The NaCo Imaging Survey for Planets around Young stars (NaCo-ISPY)[29] is a 120 nights Guaranteed Time Observations (GTO) survey aimed at detection exoplanets using the DI technique. As the name says, NaCo-ISPY uses the NaCo instrument (Clenet et al., 2004) at the VLT operated by ESO. NaCo was commissioned in 2002 and with its IR WFS and AO it is perfectly suited for any DI NIR survey as NaCo-ISPY. NaCo-ISPY started its first observations in December 2015 and will probably take last data in August 2019, which will also shortly before the decommissioning of NaCo. Since the planet-star contrast is favorable compared to shorter wavelengths other DI surveys like SPHERE–SHINE (Chauvin et al., 2017) or GPIES (Patience et al., 2015) use, NaCo-ISPY observes in the L'-band ($3.8 \pm 0.4\mu$m). A comparison of the NaCo instrument with GPI and SPHERE is presented in Sect. 1.3.4.

In order to maximize the achievable contrast and minimize the IWA, NaCo-ISPY uses the AGPM coronagraph for all stars brighter than $L' \lesssim 6.5$ mag, where the precise limit can vary slightly with weather conditions. The AGPM is a vector vortex coronagraph with an IWA of $0.09''$, which is the diffraction limit of the VLT in the

[29] http://www.mpia.de/NACO_ESPRI_GTO

L'-band. A more detailed description of the AGPM can be found in Mawet (2013), Absil et al. (2013) and Sect. 1.3.2.

Table 1.2 lists a selection of the largest DI surveys of the past and present. It seems like the NaCo-ISPY survey is just in a row with many other L' surveys. However, a unique feature of NaCo-ISPY is its target selection (with the exception of NaCo-ISPY's northern extension LIStEN), which is described in the following Sect. But also NaCo-ISPY spends much more time ($\sim$ 3 hrs) on a target, so that in addition with its AGPM coronagraph, it goes much deeper than the previous L' DI surveys, maybe with the exception of LEECH. But of course there are similarities and overlaps in the targets with other surveys. Thus a collaboration with SPHERE–SHINE has been set up, out of which e.g. the papers of PDS 70 b (Keppler et al., 2018) and HIP 65426 b (Cheetham et al., 2019) arose.

Target Selection

The targets of NaCo-ISPY are split in two groups: the Debris disk hosting stars (DEBs) and the PPD group. As the names indicate, the DEB group contains more mature DD stars, whereas the PPD group contains the very young stars. The precise differences between those stellar groups are explained in Sect. 1.2. Since proximity is a key property for DI surveys and close star forming regions are rare, most PPDs stars closer than a few 100 pc without available, good HCI data and visible with NaCo were selected and given high priority. As for the DEB sample, known binaries with projected separations $\lesssim 1''$ were excluded. This is because a large, scientifically interesting area is blocked by the companion, turn the coronagraph mainly useless, and also close binaries can easily can confuse AO. To exclude the binaries, we searched the literature and catalogs, including the the Washington Double Star catalog (Mason et al., 2001, WDS;) and Spectroscopic Binary Catalog 9th edition (sb9; Pourbaix, D. et al., 2004), on an individual basis.

For the DEB targets, the selection was more complex and also makes the NaCo-ISPY survey unique among the various other DI surveys listed in Table 1.2. Besides being young ($\lesssim$ 200 Myr), close ($\lesssim$ 150 pc) and visible from NaCo's position at Paranal ($-70\,\mathrm{deg} \lesssim \mathrm{DEC} \lesssim +15\,\mathrm{deg}$), the SED plays an imortant role for the selection: As explained in Sect. 1.2.2, certain sizes of DD belts cannot be explained by self-stirring processes. But one of the most likely explanations is a massive companion inside or outside of the disk. Thus, even though there are no images of the disks available, using the fits to the SEDs provided by Chen et al. (2014), and corrected using Pawellek & Krivov (2015), and van der Marel et al. (2016), NaCo-ISPY selected the targets where an internal or external stirring companion is likely according to Mustill et al. (2018). Of course there is still a large uncertainty left, if there really is a detectable companion, but chances thought to be increased significantly Launhardt et al. (in prep.). In this paper it will also be shown, that at least the SED fitting to determine the disk sizes works reliably, by comparing the predictions for disk sizes with their actual images. A thorough analysis of the occurrence rate of GPs around

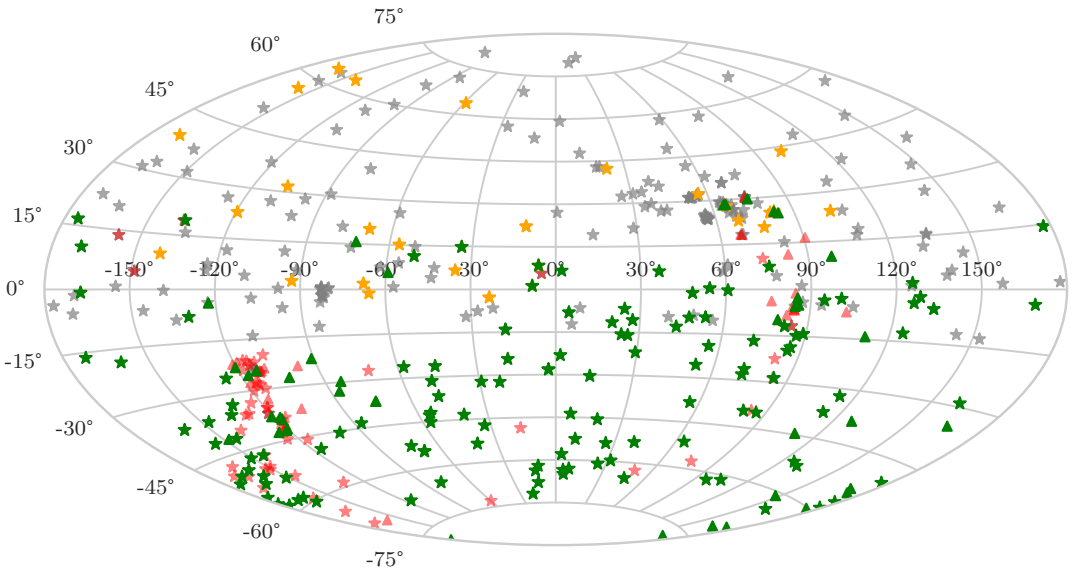

Figure 1.14: Sky distribution of the NaCo-ISPY and LIStEN targets showing how they complement each other covering the whole sky. The green and red symbols mark the respective observed and not yet observed NaCo-ISPY targets. The yellow and grey symbols mark the respective observed and not yet observed LIStEN targets. Star symbols represent stars with DDs, whereas triangles mark stars with PPDs.

DD stars will be done after the observations are finished. Finally the 311 DEB candidates were prioritized based on whether a 22 M_{Jup}planet would be visible at 20 AU, assuming our average achievable contrast. To tell this, the distances from Hipparcos (van Leeuwen, 2010) and later GAIA DR2 (Gaia Collaboration et al., 2018) were used. To compute the brightneess of the imaginary companion, we used the BT-settl models (Baraffe et al., 2015) and ages we found in various literature.

The complete target list and properties of the stars observed in the first 4 semesters, as well as the obtained contrast curves will be presented in Launhardt et al. (in prep.). Four examples can be found at the end of this Sect., as well as five more in Chapt. 3.

Standard Setup

Most NaCo-ISPY observations are done with similar setups, where small changes, e.g. on the DIT are made on site to account for the respective weather conditions. But except for follow-up observations and characterizations, all observations are performed using NaCo's L'-band filter ($3.5 - 4.1$ µm[30]).

As mentioned, for bright stars ($L' \lesssim 6.5$ mag) the AGPM coronagraph, where we do not gain for fainter stars. This is because the use of a coronagraph comes with significant overheads during the observations (see below), also the precise centering become very difficult for fainter targets r stars brighter than $L' = 6.5$ mag.

[30]The precise filter curve can be found here: http://www.eso.org/sci/facilities/paranal/instruments/naco/inst/filters.html

Since the sky is very bright in the L'-band ($\sim$ 3.9 mag[1]), sky frames have to be taken regularly to measure the background level. When not using the AGPM, this is done by dithering the three working quadrants of the detector (in the bottom left quadrant three eights of the columns are broken in a repeated pattern. Even though internal research indicates that this does not seem to influence the achievable contrast, it is not used as stellar center; Launhardt et al., in prep). This observing strategy reduces each length of the FoV by at least a factor of two in the reduction process, but still leaving a large FoV of $\sim 10''$. In the coronagraphic observations the stars needs to kept precisely ($\lesssim$ 0.2 px $\hat{=}$5 mas; see Sect. 1.3.2) centered behind the coronagraph. Thus the sky needs to be measured by moving to an empty sky position. Since for unknown reasons the AGPM moves significantly ($\sim$ 2 px, precise research is ongoing) and the sky frames are also needed to subtract the signifcant thermal emission of the non-cooled AGPM, this is done every $\sim$ 9–13 minutes, where the frequency increased in the later observations. Since the sky sequence and the recentering process take about 1 min, this leads to a loss in on-source time of about 10%.

One of the unique features of NaCo is it's capability to operate the AO by measuring the flux in the NIR, allowing for better corrections (see Sect. 1.3.4). Due to saturation of the WFS camera, this can only be done for stars fainter than $K = 4$ mag, where else the VIS-WFS needs to be used, correcting at $0.45 - -0.95\,\mu$m instead of $1.9 - 2.55\,\mu$m for the IR-WFS (Kaufer, 2018). Note that the VIS-WFS broke in July 2018, forcing the use of the VIS dichroic combined with the IR-WFS – a setup usually not allowed and therefore not tested. The results look promising though, but no thorough analysis of the effects has been performed yet.

Because of the bright sky in L', the DIT is set to 0.35 s when using the AGPM and 0.2 s when not using the AGPM to not penetrate the non-linear regime of the detector beyond the VLT's diffraction limit of $0.09''$ in L' around the unobscured star.

Finally during each run at least one astrometric calibrator field, either 47 Tuc or Trapezium, is observed. There is no significant change of the instruments astrometric properties observed, but they are stable with a platescale of $\sim$ 27.2 mas/px and a true north of $\sim 0.55°$, see Chapt. 2.

Results

Since the NaCo-ISPY survey is still ongoing, no final results can be presented yet. In Chapt. 3 I list systems of NaCo-ISPY I was and am working on. Current highlights of the NaCo-ISPY survey are I am not the primary author of are:

- PDS 70 b (Keppler et al., 2018): A combined discovery with SPHERE–SHINE of the 5-14 M_{Jup}planet inside the transition disk of PDS 70 b, see Fig. 1.15. The large uncertainty of the mass is due to modeling uncertainty, and in particular whether to use the "hot start" or the "cold start" models of planet formation (e.g. Mordasini et al., 2017)

- HIP 65426 b (Cheetham et al., 2019): HIP 65426 b is an exoplanet recently discovered in the course of SPHERE–SHINE (Chauvin et al., 2017). With the NaCo-ISPY data taken in the L'- and M'-bands as well as a new SPHERE $Y-H$ spectrum, the planetary mass, temperature, radius and surface gravity can be narrowed down. With this data the best mass estimate is now $8 \pm 1\,M_{Jup}$, compared to the $9 \pm 3\,M_{Jup}$ published before (Chauvin et al., 2017). Additionally first estimates on the orbital motion could be made.

- R CrA (Cugno et al., 2019): R CrA is a member of the 1-3 Myr young (Meyer & Wilking, 2009), intensively studied Corona Australis (CrA) star forming region, in particular part of the deeply embedded Coronet region. In particular Takami et al. (2003); Forbrich et al. (2006) and Kraus et al. (2009) predicted the presence of a companion to Coronet's main star R CrA. However they were not able to find it. Here NaCo-ISPY presents the detection of probably this companion detected in two epochs, and determined a mass of $0.1-0.6\,M_{\odot}$. The large mass uncertainty results from the unknown age as well as the very uncertain L' magnitude of R CrA. Note that almost simultaneously an independent discovery by SPHERE–SHINE has been published (Mesa et al., 2019) confirming the discovered companion in three epochs and different wavelengths.

- HD 193571 B (Musso Barcucci et al., accepted): HD 193571 is a DD hosting A0 star, where we could determine an age of $\sim 60-170$ Myr. Around this star, NaCo-ISPY discovered an approximately $0.31-0.39\,M_{\odot}$ companion which is still with the DD. The interesting part is that only two binary systems with the companion in the disk and the disk imaged are known: HR 2562 (Konopacky et al., 2016) and HD 206893 (Milli et al., 2017). Unfortunately attempts to image the disk with SPHERE been unsuccessful, but still SED fitting provided good constraints.

- Further highlights include almost 20 disks and numerous Companion Candidates (CCs) which still have to be analyzed but a first peak will be presented in Launhardt et al. (2019). One of the most promising CCs is HD 101412, which is presented in Sect. 3.1.

1.6.2 LBTI Exozodi Exoplanets Common Hunt

LBTI Exozodi Exoplanet Common Hunt (LEECH) is a DI survey in the northern hemisphere using the Large Binocular Telescope (LBT) with its 2×8.4 m mirrors atop Mount Graham, Arizona (Hill, 2010). The survey started in Spring 2013 and observed 98 stars during its ~130 nights campaign, which made it the biggest Direct Imaging (DI) survey until its end in 2017 (Skemer et al., 2014, see also Table 1.2).

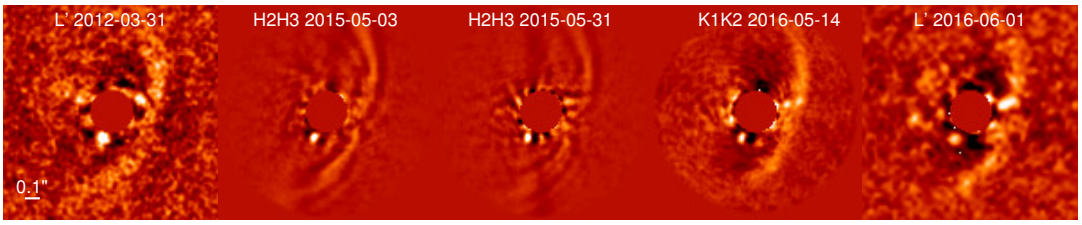

Figure 1.15: Reduced images of the planet discovered around PDS 70 b using PCA and gaussian smoothing with a kernel of 0.5×FWHM. The planet is at the south-west of the masked star at the center of each frame. The disk is also clearly seen in all images. The instrument are (from left to right): NICI, IRDIS, IRDIS, IRDIS and NaCo. The filters and dates of the images are given as labels.
Credit: Keppler et al. (2018)

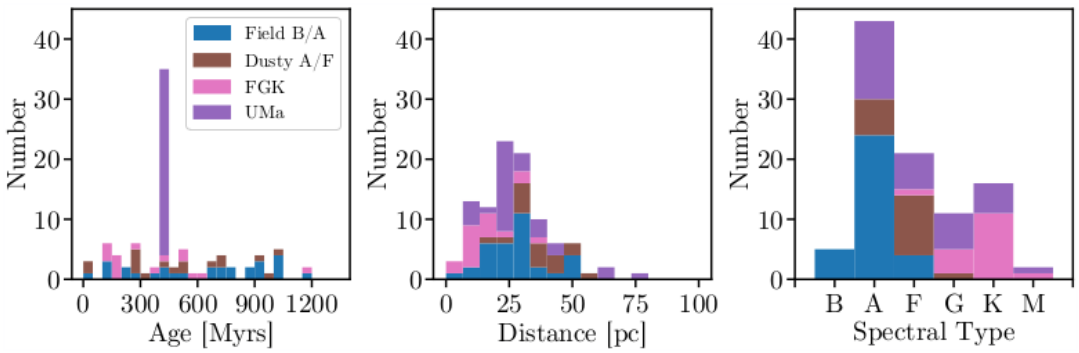

Figure 1.16: Key histograms of the 98 targets observed by LEECH. The peak in age is due to the Ursa Major subsample.
Credit: Stone et al. (2018)

Target Selection

LBTI Exozodi Exoplanet Common Hunt (LEECH) observes in the L'-band, optimizing the required contrast between a potential GPs and the host star. The main selection criterion was the proximity, maximizing the physical separation that can be probed, see Fig. 1.16. The age was a slightly less emphasized, but stars should at least be younger than about 1 Gyr.

In total four sublists were used: 17 stars were observed from the FGK sublist, compiled from Mamajek & Hillenbrand (2008) and Heinze et al. (2010). Further 31 targets from the Ursa Major moving group (King et al., 2003), 17 stars DD hosting stars from Gáspár et al. (2013) and 33 young ($\lesssim$ 1 Gyr) B- and A-type field were observed. The discovery probability was also tried to be maximized by using planet-frequency estimates from Crepp & Johnson (e.g. 2011). Since the age is needed in order to estimate it to a planetary luminosity, Bayesian isochrone fitting to the Hipparcos parallaxes and magnitudes of close stars was done. Therefore the PARSEC-COLIBRI isochrones from Marigo et al. (2017) were used the ages of 35 field stars without previously known ages was estimated. The results and comparison to other work is given in Stone et al. (2018). In order to ensure sufficient field rotation during the meridian passage, no stars with DEC $< -20°$ were scheduled.

Observations

Even though the AGPM vortex coronagraph was installed and tested at the LBT in 2014 (Defrère et al., 2014), it was not used throughout the survey (Stone et al., 2018). The main reason therefore is that the AGPM was never fully commissioned and offered in service mode. This is supposed to change in the future. Therefore all observations are performed in an unobscured, "saturated" mode, where eventually one of L/M-band InfraRed Camera (LMIRcam)'s neutral density filters was used to avoid excessive saturation of the detector.

Originally it was planned that LMIRcam can interfere the two beams coming from LBT Interferometer (LBTI)'s two mirrors coherently, acting like a 23 m mirror on one baseline. That is why its pixelscale with $\sim 10.7\,\mathrm{mas/px}$ is only half of Nyquist sampling of one mirror (Wilson et al., 2008). But instead, the two beams are sent incoherently to two different parts of the detector, thus having a relatively small FoV of $11'' \times 11''$. In LEECH the two beams are sent to two different locations of the detector, with a separation of $3''$ to the detector edge and $5''$ between the images. It is nodded every 150 frames $\times 0.3\,\mathrm{s} = 45\,s$ between the four available positions are then, so the BG measurements are part of the science images. For very close targets like Altair or Vega, only one beam was used to benefit from the full FoV.

Data Reduction

If both mirrors were used, two mainly independent datasets were obtained, since there are two independent AO systems for each mirror, as well as two almost independent light paths (Bailey et al., 2014). In the reduction process those images will be kept in four separate image cubes. This reduction process has the following steps:

First Bad Pixel Correction (BPC) using the nearest 8 good pixels and a Bad Pixel Map (BPM) is applied. Then the offset in all 64×1024 px channels is removed by subtracting the median of those channels. The image distortion is performed according to Maire et al. (2015b). Due to the high oversampling, 2×2 px median binning is possible due to the high oversampling, removing any remaining bad pixel. Then the reduction pipeline divides the detector in left and right (for up and down nodding, else it is split in up and down), so that each half only contains data from one side. Then the star's position (up or down) is identified using the median of the 1 % of the brightest pixels. Sequences of up and down images are registered. For each frame, the mean of the medians of the neighboring sequences is subtracted. This removes the background and introduces a negative PSF at the "empty" stellar position. If there are gaps in the observing sequence or it is the first or last sequence, only the median of the one adjacent observation is used for this subtraction, since conditions might have changed during that observational gap. Finally each star is cut out with a $3''$ FoV. All images of each of the four nod positions are co-aligned using an iterative sub-pixel cross-correlation, first to an arbitrary frame and then to the median frame. Finally, images with the lowest correlation in each set are thrown

away. The fraction of the frames to discard has to be set manually, dependent on the conditions, but is 30% by default.

Each of final image cubes can then by passed to any of the routines described in Sect. 1.3.3. The standard algorithm for LEECH was a PCA like approach, described in more detail in Stone et al. (2018). The four resulting images are combined in a weighted mean, where the weights are calculated by the SNR of a fake-injected planet in each cube.

Besides removing bugs and speeding up the LEECH-pipeline, I added a functionality to the pipeline, where one could recover the total FoV of LMIRcam, by setting the keyword `full_frame = True`. With this keyword, all processes are the same as described above, but additionally an uncropped version of each image is stored. At the end, the registered shifts and frame selection are also applied to the full frame images. All frames were then collected in one aligned image cube, where each frame is now about 2000×2000 px in size, with NaNs outside of the original detector range. There were positive and negative images from the observation as well as the background subtraction. But since they are static, in principal they should be removed in the ADI process. The adaptation of the Phishi pipeline, developed by Matthias Samland during his master work (Samland, 2015), to be capable of handling those frames has not been done yet. The idea is to do a PCA reduction in the inner region where all frames have valid data and classical Angular Differential Imaging (cADI) in the outer regions. The motivation is to increase the FoV, since there might also be planets at greater angular distances, now removed in the cropping process. E.g. the famous planet Fomalhaut b was detected at an angular separation of $12.7''$ (Kalas et al., 2008), and since the survey focuses on nearby stars, chances are good to find a new companion.

Results

Unfortunately LEECH follows many other DI surveys in that sence, that did not discover a new planet. However, with the non-detection LEECH can but tighter constraints on the occurrence rate of GPs around FGK stars. The precise limits depends on the assumptions of the planetary formation scenario, hot start vs. cold start. Using the more conservative assumptions of the cold start scenario to be true, it can be concluded that $\lesssim 90\%$ of FGK stars can host a $7 - 10 M_{\mathrm{Jup}}$ planet from 5 to 50 AU (Stone et al., 2016).

Further the coldest imaged explanet GJ 504 b could be further characterized, using three different narrow L-band filters. Its temperature is now very well constrained constrained to be $T_{\mathrm{eff}} = 544 \pm 10$ K, whereas his mass of $3 - 30$ M_{Jup} remains unconstrained, due to its unknown age (Skemer et al., 2016).

Also the orbital constraints of the four planets around HR 8799 could be updated further (Maire et al., 2015a), now also helping the most recent analysis of the system adding GPI data (Wang et al., 2018).

One more highlight is the resolved image in the H-, K_s- and L'-bands of the known spectroscopic and astrometric binary NO UMa with an orbital separation of only less than 0.09″ (Schlieder et al., 2016).

Finally LEECH could classify three objects around HIP 93747, HIP 92161 and HIP 62512 as BG objects via common proper motion analysis. One new CC in the δ *Cyg* (HIP 97165) system, probably of stellar mass, has still to be confirmed or rejected (Stone et al., 2018).

1.6.3 L-band Imaging Survey to find Exoplanets in the North

Introduction and Target Selection

L-band Imaging Survey to find Exoplanets in the North (LIStEN) can be seen as the northern extension of the DEB sample of the NaCo-ISPY survey presented in Sect. 1.6.1: It also observes in the L'-band and focuses on stars with prominent DDs. However, due to its location in the north, the LBT (Hinz et al., 2016) atop Mount Graham in Arizona, USA is used instead of NaCo at the VLT. And during the first semesters, the target selection was identical to the DEB stars showing over sized disks. Only the stars presented in Chen et al. (2014) were complemented targets from van der Marel et al. (2016). But from semester 2018B, instead of relying only on the BB fits to the SEDs, stars are prioritized where actual images of the disks are available. To identify those, two online catalogs are used: The "Catalog of Circumstellar Disks"[31] containing 93 DDs, and the "Catalog of Resolved Debris Disks"[32], containing 146 resolved disks. But also a few other known disks not part of those catalogs were added.

Then the same selection criteria were applied to all targets: First they need to be observable from LBT's position, requiring $\texttt{DEC} > -10°$. All targets with existing HCI data in the IR are removed, as well as duplications with NaCo-ISPY avoided. Additionally a distance cut at 250 pc using Hipparcos (van Leeuwen, 2010) and later GAIA (Gaia Collaboration et al., 2016, 2018) was applied. In order for the AO to work properly, a brightness cut of $R \leq 15$ mag, was applied. Since close ($\sim 1''$), similarly bright (Δmag < 1 mag) companions are known to confuse LBT's AO system, known binary stars with these properties listed in the WDS (Mason et al., 2001) or elsewhere in the literature were removed. We were left with 30 targets with resolved disks and 200 targets without resolved disk images and which are suitable for observations with LBTI's LMIRcam (Wilson et al., 2008). The sky distribution is shown in Fig. 1.14 (yellow and grey stars), where one can see LIStEN complementing NaCo-ISPY in the north. I refer to Musso Barcucci et al. (in prep.) for the individual target's properties.

[31] https://www.circumstellardisks.org

[32] https://www.astro.uni-jena.de/index.php/theory/catalog-of-resolved-debris-disks.html

Observations

Each target is observed using the L'-filter for at least two hours around the meridian passage to obtain sufficient field rotation to perform ADI. Since the AGPM is still being revised and not offered as a regular setup, the observations are done without a coronagraph. This usually saturates the star, so that flux calibration frames bracket each observations, where the DIT and the use of a neutral density filter are chosen such that the peak flux remains in the linear regime of the detector. And as described in the previous section, one of the advantages of LMIRcam is that the two mirrors with their independent AO systems can be used to create two mostly independent images of the star.

The survey was planned to start observations in semester 2017A, but due to bad weather, all of the scheduled 14 hours were lost. Thus the first observations started in semester 2017B, where 9 targets could be observed. Unfortunately there were problems with the simultaneous observations so that only one mirror could be used at a time. Since then, 116 hours of observing time were scheduled, out of which 35 hours ($\sim$ 30%) were lost due to bad weather, but the instrument was working properly.

Results

So far (April 2019), 28 stars have been observed in the course of the LIStEN project, out of which 11 are from the sample of resolved disks. Early analysis using a combination of the LEECH data reduction pipeline described in Sect. 1.6.2 and Pynpoint[33] (Amara & Quanz, 2012; Stolker et al., 2019) data is not conclusive yet and will be made publicly available in Musso Barcucci et al. (in prep.).

[33] https://pynpoint.readthedocs.io

Survey Acronym [a]	Instrument, Telescope	Ref.	Observed targets	Status	Band
...	NaCo, VLT	Kasper et al. (2007)	22	Compl.	L'
...	Clio, MMT	Heinze et al. (2010)	54	Compl.	L'
NICI-PFC	NICI, Gemin	Liu et al. (2010)	250	Compl.	H
IDPS	NIRI+NaCo, Gemini+VLT	Vigan, A. et al. (2012)	42	Compl.	$H + Ks$
...	NaCo, VLT	Rameau, J. et al. (2013)	59	Compl.	L'
...	NaCo, VLT	Meshkat et al. (2015)	13	Compl.	L'
NaCo-LP	NaCo, VLT	Desidera et al. (2015)	86	Compl.	L'
MASSIVE	NaCo, VLT	Lannier et al. (2016)	58	Compl.	L'
SEEDS	HiCIAO, SUBARU	Tamura (2016)	~ 500 [c]	Compl.	H
LEECH	LMIRcam, LBTI	Stone et al. (2018)	98	Compl.	L'
NaCo-ISPY	NaCo, VLT	Launhardt et al. (in prep.)	~ 210	Ong.	L'
LIStEN [b]	LMIRcam, LBTI	Musso Barcucci et al. (in prep.)	$\sim$50	Ong.	L'
GPIES	GPI, Gemini South	Patience et al. (2015)	$\sim$600	Ong.	$J - K$
SPHERE–SHINE	SPHERE, VLT	Chauvin et al. (2017)	$\sim$500	Ong.	$J - K$

Table 1.2: Overview of larger Direct Imaging (DI) surveys without the intention to be exhaustive. The band denotes the default band used for observations, where often other bands are also used for individual targets. Additionally GPI and SPHERE have spectrographic capabilities by default.

Notes. [a]Where available. [b]LIStEN is the extension of NaCo-ISPY to the northern hemisphere by making use of the LBTI. [c]Contains duplicate observations.

Chapter 2

Astrometric Calibration

2.1 Introduction

Observational data can only be as good as its calibration. When using DI, there are two important values: The flux, e.g. to characterize a detection or create detection limits, and the position of any object detected. In DI mostly the relative positioning of any two objects, such as the central star and any companion, is of interest. And since observations of different instruments are typically compared, we require high accuracy and not only high precision. This astrometric calibration tackles the second requirement of accurate determination of relative positions. Applications where the absolute astrometric calibration is crucial to characterize objects, are given in Chapt. 3, and in particular in Sect. 3.5, where with archival data a CC to HD 97048 was identified as a BG source. Another application where a good astrometric calibration is important, is to determine orbital motion of systems.

Therefore I developed a fully automatized pipeline, determining the true north and platescale of the L27 detector with and without the us of the AGPM coronagraph. This setup corresponds to the standard observational setup of NaCo-ISPY. Section 2.2 describes the astrometric fields and observations used for the calibration.

The methods, Sect. 2.3, then describe how the pipeline works to identify the sources and calculate the platescale. Limits of the automatization are also presented. The results of the calibration are presented and compared to the official values provided in the handbook as well as to the independently derived values of ISPY's primary calibration pipeline in Sect. 2.4.

2.2 Observations

In order to make the astrometric calibration of the true north and the platescale possible, we need to observe any previously well calibrated system consisting of at least two sources on the sky. Since the geometry of the telescope and/or the instrument may change over time, we try to execute at least one observation per run as part of the NaCo-ISPY survey. The Trapezium cluster, the 47 Tuc cluster and 70 Oph, a well studied binary system with $5 - 6''$ separation, were discussed as possible targets. The coordinates of these systems are given in Table 2.1.

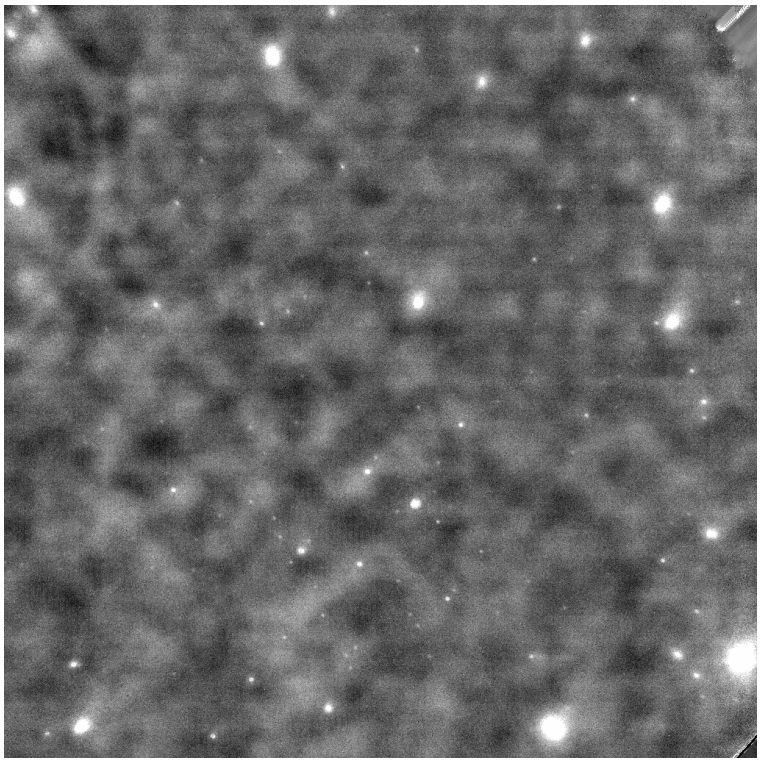

(a) Observation from 2016-07-31 09:43:02 without the AGPM. An example of good data quality.

Figure 2.1: Two good and three bad examples of calibration images returned from the NaCo-ISPY reduction pipeline managed by André Müller. All images show the 47 Tuc field.

Since the statistics improve with more identified sources in the field, NaCo-ISPY decided to use only Trapezium and 47 Tuc, two dense stellar clusters, as reference objects.

The observations consist of two observing blocks: One with and one without the AGPM. Even though the exposure time is only 3:20 min, each observing block requires about 18 minutes in total. This is because often the AO takes multiple attempts to work, because of the many sources in the field. One observing block consists of sequences of 5×100 frames with a DIT of 0.2 s for each frame. Then dither pattern an offset of $20''$ towards north and $20''$ towards the east is done, where it

Field	RA J2000	DEC J2000	# Measurements
Trapezium	$05^{h}35^{m}15^{s}.84$	$-05°23'22''.6$	54
47 Tuc	$00^{h}23^{m}58^{s}.12$	$-72°05'30''.19$	210
70 Oph	$18^{h}05^{m}27^{s}.4$	$+02°29'57''$	0

Table 2.1: Coordinates and number of measurements that lead to a result for the astrometric calibrators.

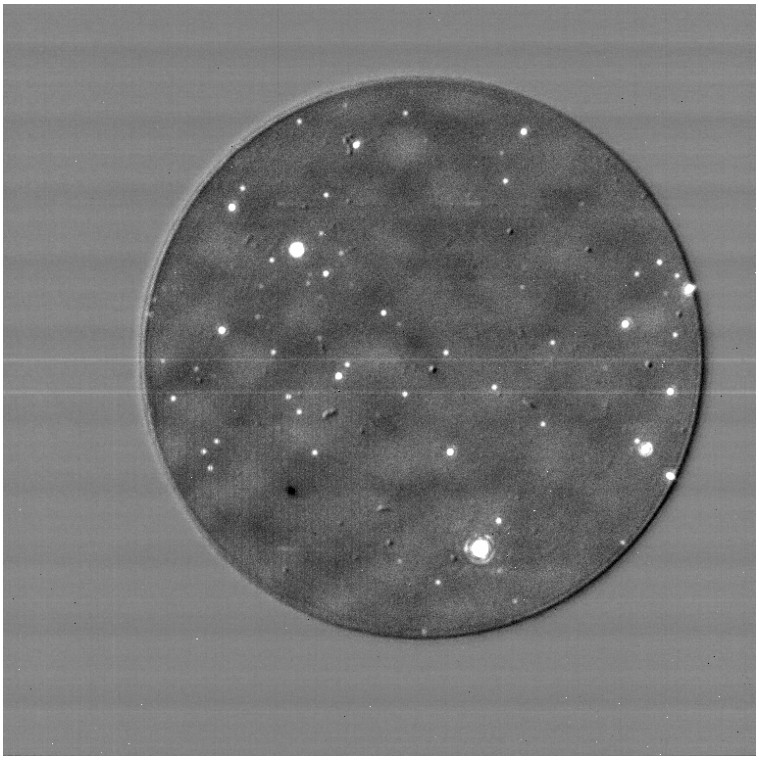

(b) Observation from 2016-07-31 09:43:02 with the AGPM. An example for good data quality, even though still some traces of the AGPM can be found.

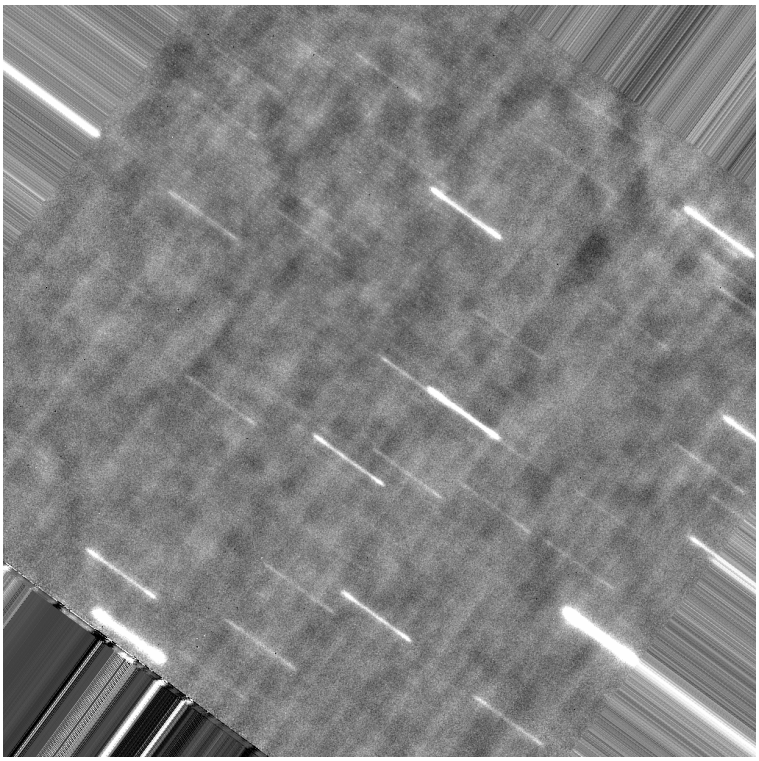

(c) Observation of 47 Tuc from 2016-11-09 00:05:17. For unknown reasons, the guiding was not working properly during this sequence and so it was removed.

Figure 2.1: Continued.

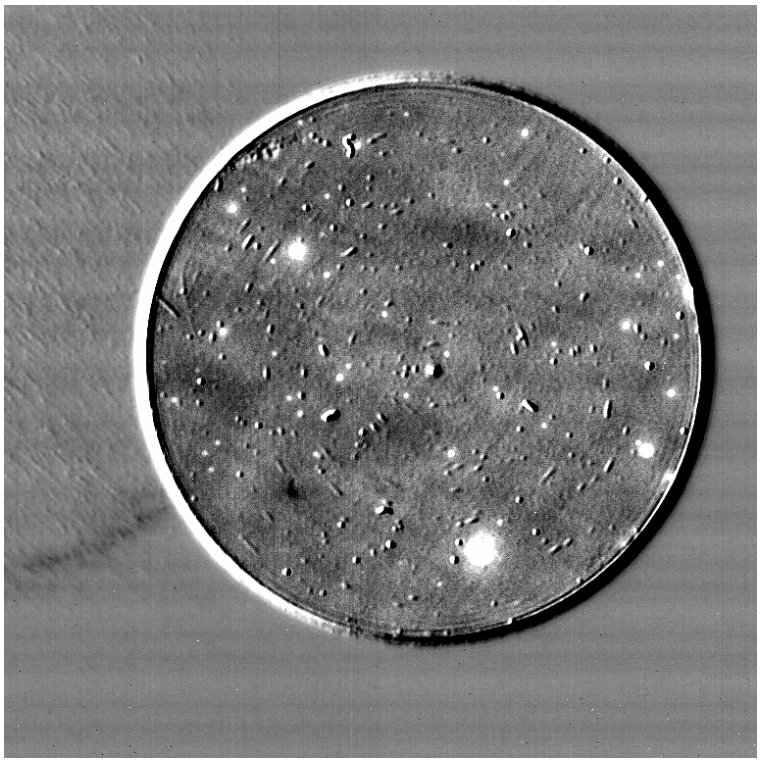

(d) Observation from 2017-11-01 00:21:43 using the AGPM. The bright and dark spots on the image is dust on the warm AGPM. For some still unknown reason, the AGPM moves significantly even during a few minutes, why the sky subtraction leads to these artifacts. The algorithm is not capable of telling the difference between those artifacts and stars. Consequently this image was also removed.

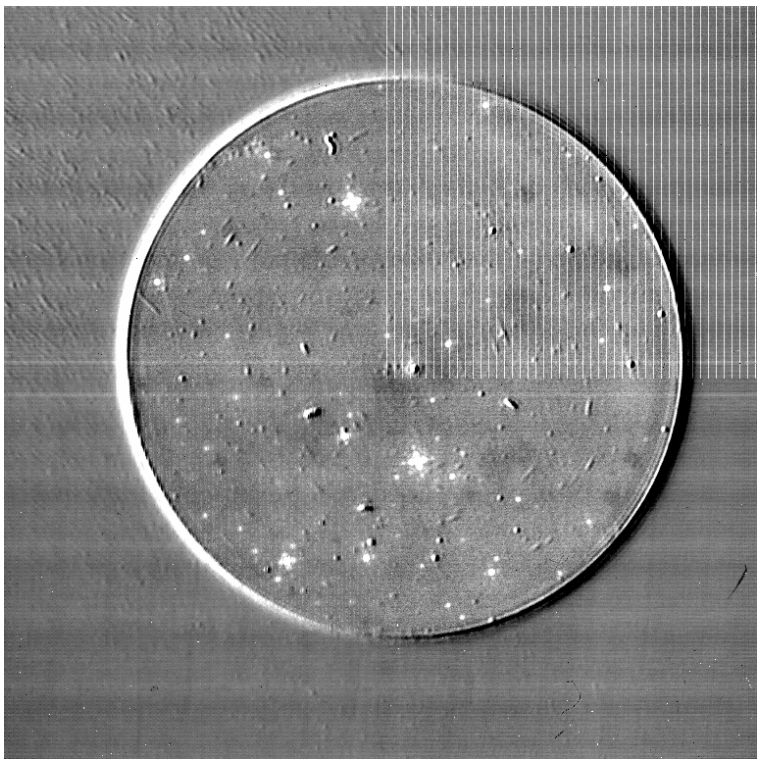

(e) Observation from 2018-11-27 01:13:14 using the AGPM. In addition to the moving AGPM (Fig. 2.1d), stripes on the top right quadrant appear, returning this picture also unusable for my algorithm. In principle these stripes are corrected in the run of the NaCo-ISPY survey routinely, but since they blink on and off in the top right, sometimes the algorithms miss them and in this case, the moving AGPM renders the data unusable anyway, thus no further reduction was performed.

is jittered. The jitter process consists of six positions in a 15″ wide box, where at each position 100 frames with 0.2 s DIT are taken. The sky frames can then later be median combined, removing all stellar objects.

As positions of the catalog we use the catalog of Close et al. (2012) for Trapezium and a catalog provided by Andrea Bellini (priv. comm. with André Müller). We are kindly asked not to share the catalog outside the NaCo-ISPY consortium. Thus this catalog is not part of the above mentioned github repository and one will need to find another catalog in order to use this field. A suggestion would be to use McLaughlin et al. (2006), which therefore is also included in the github repository.

2.3 Method

For many purposes, `astrometry.net` is the tool of choice that returns the precise position on the sky, as well as the orientation (true north) and the platescale of any uploaded image or *.fits*-file. It also allows to feed it with your own star catalogs. However, after a many discussions with the *astrometry.net* developers, it was clear that it cannot handle observations with FoVs as small as ours ($\sim$ 20″) due to not easy to overcome rounding errors in the software. Thus we needed to develop our own software. This Sect. will describe how the routine I developed works. For the pre-reduction of the images, e.g. flatfielding, bad pixel correction and background subtraction, we use the standard NaCo-ISPY routines used for the science images, which are described in Launhardt et al. (in prep.).

2.3.1 Rough Sky Position

First one needs to find the rough position of the observation to decide which input catalog to use. This is done by scanning the `OBJECT` keyword for a known calibrator (e.g. Trapezium or 47 Tuc). If this keyword was not set, the telescope pointing coordinates are used, and which are stored in the header automatically under the header keywords `CRVAL1` and `CRVAL2`.

After this, the sources are extracted from the image using Source Extractor (SExtractor) (Bertin & Arnouts, 1996). SExtractor offers a variety of parameters to identify the right sources, since it is also capable of identifying extended objects like galaxies. The parameters go from simple arguments like the minimum size of an object, the minimum brightness above the noise level, image smoothing kernels and parameters, to values which determine the minimum flux contrast from which a source will be split into two sources or kept as one source. Even though SExtractor is more than 20 years old, a complete manual is still missing. Fortunately a detailed, but still unofficial, review about SExtractor was written by B. Holwerda[1]. Experience has shown, that one needs significantly different values for observations with and without the AGPM coronagraph (Mawet, 2013). Looking at the images presented in

[1] `http://mensa.ast.uct.ac.za/~holwerda/Site/Source_Extractor.html`

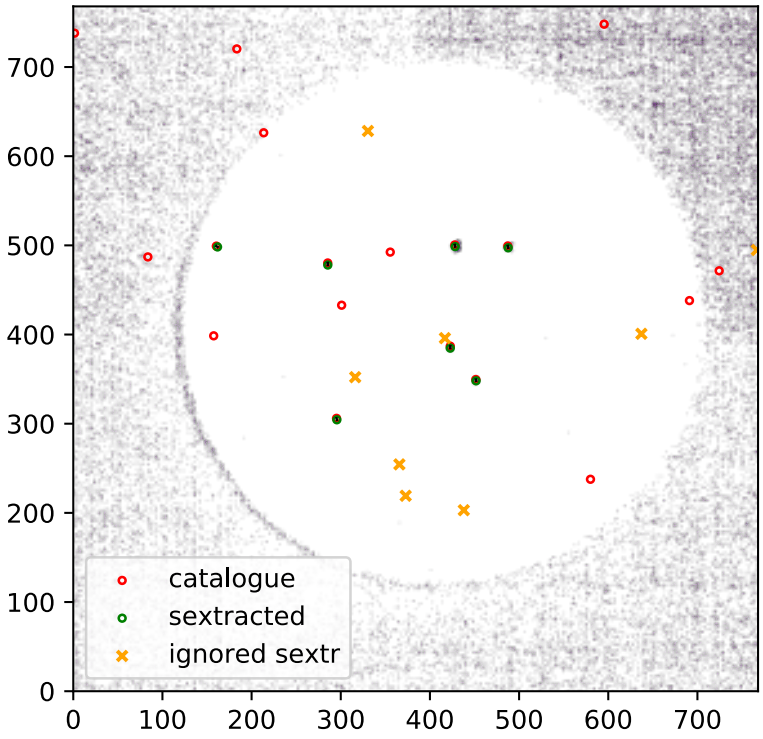

Figure 2.2: Example plot of the extracted stellar sources at the example of the AGPM data from 2019-01-19T03:40:51.375. As can be seen sources are extracted from the image that are not listed in the catalog (false positives), as well as sources from the catalog are missed (false negatives), indicating that the sensitivity of Source Extractor (SExtractor) is not completely off.

Fig. 2.1, this is not surprising: A large fraction of the image is blocked by the AGPM, but SExtractor will still use it to make assumptions on the underlying noise. Additionally we provide different configuration files for 47 Tuc and Trapezium, making a total of four parameter files for SExtractor to further optimize for detection of the sources of the different fields.

2.3.2 Fine Overall Positioning

SExtractor is able to extract many parameters, but returns only those selected in `sex.params`. The ones used here are the pixel positions (`X_IMAGE`, `Y_IMAGE`), the not-absolute calibrated magnitudes (`MAG_AUTO`) and the FWHM of the identified sources (`FWHM_SKY`), as well as the binary image file, which is 1 where an object was identified and 0 where not. `FWHM_SKY` serves to reject non-stellar sources (e.g. dust on the AGPM or reduction artifacts) and is filtered to be between 0.08″ and 0.25″. Since the position was roughly identified earlier, one can now create an artificial map of all the sources from the input catalog which are within a radius of 30″ of thearlier positon. This value is picked to ensure that all targets of the $28 \times 28''$ total FoV (not radius) of NaCo's L27 cam will be part of the now reduced catalog.Additionally all stars fainter than 14 mag were removed from the input catalog, to avoid wrong identifications later in the process. And during the only a few minutes observations we do not get

deeper than $L' \approx 12$ mag. Then an artificial map of those sources, where each source is represented by a gaussian with $\sigma = 10$ px (≈ 27 mas) and scaled by $10^{\text{mag}_x/25}$, where mag_x is the magnitude of the star in the filter of the catalog provided. This scaling factor downweights the provided magnitudes drastically, but still attributes them a little weight. It is chosen completely arbitrary, but prevents the algorithm from just aligning the brightest source from the catalog with a source from the image. For the catalogs mentioned, the provided flux measurements were taken in the K-band filter. Afterwards this artificial sky image is cross correlated to the binary image returned by SExtractor and we end up with a relatively precise position of all sources in the calibration image relative to the source catalog. In this process the rough initial pixelscale and orientation are needed, otherwise the cross correlation will not work. These values have to be given or are attempted to be extracted from the header. For NaCo's L27 detector, a pixelscale of $27.19''$ and a true north of $0.6°$ are used.

2.3.3 Source Matching and Refined Positions

After the position of the image is known up to a few pixels, one needs to match each source found in the image to a corresponding source in the catalog, see Fig. 2.2. One major issue is that sometimes NAOS creates some mickey mouse pattern, which SExtractor identifies individual sources. Figure 2.1e shows such an example of a sub-optimal diffraction pattern. Since they share roughly the same FWHM as real sources, they were not captured by the earlier filter. To overcome this issue and to also remove other falsely identified sources, the following approach has proven successful: First all found sources are sorted by brightness. It is then started with the brightest source which is identified to the brightest source in the catalog within a search radius of 8 px ($\approx 0.2''$). In decreasing order, each source found in the image is matched to the closest source in the catalog. If multiple sources are found within the search radius, they are combined in such a way, that the summed discrepancies between all sources in the catalog and the image are minimized. Identified sources which do not have any corresponding entry nearby are considered false positives (e.g. airy rings or dust on the AGPM, compare Fig. 2.1d) and ignored in the further process. Since the diffraction patterns are dimmer than the primary source, they will not be assigned a source in the catalog and thus are ignored in the later process.

To match the precise positions of the image sources, a master PSF from all the sources identified before is created. This master PSF is then correlated to each source, to refine the positions of all the stars found before. In more detail, this is done by taking the brightest star from the image and all correlating and aligning all the other stars to it. Then the median of all stars is taken and again all stars are correlated and shifted, but this time to the median. Next all stars are upscaled to share the same maximum pixel value. Then the stars are subtracted from the median and sorted by the sum of the squared residuals. The best 40% of the star images are kept. The median of those remaining images is then used as the master PSF. Since stars too close to the border are often distorted (e.g. far from the AO correction) or

	With AGPM		Without AGPM	
	Median	Single	Median	Single
Frames	1	73	1	127
Valid Frames	1	67	1	113
Valid Connections	10	270	78	2433
<Connections/image>	10	270	78	21
Platescale	27.193	27.211	27.169	27.167
True North	0.633	0.630	0.611	0.638
σ–Platescale	**0.0977**	0.0988	**0.0538**	0.0772
σ–True North	0.155	**0.135**	**0.1038**	0.1147

Table 2.2: Comparison of the astrometric calibration if only the median image is analyzed or also the single images are analyzed. Valid frames and connections are the measurements of the platescale and true north, which were not discarded due to too many bad measurements.

prone to image reduction artifacts, stars closer than 20 px ($\approx 0.5''$) are not used for the master PSF generation. Since only relative positions of the sources are needed, precise centering of the master PSF is not needed and thus not performed.

2.3.4 Repeating the Process on Individual Images

One could now repeat the process mentioned above on each of the typically $\sim$ 500 individual frames created during one astrometric calibration observation, but using the identified stars as proxys to simplify identifications. Thus I compared the results of the different approaches. As one can see in Table 2.2, single images mostly increases the overall scatter of the measured distances. We thus decided in NaCo-ISPY to only run the astrometric calibration on the median image.

2.3.5 Calculating the Platescale and True North

For each possible combination between two stars, you get a measurement of the true north and the platescale, see Fig. 2.3. For N stars identified, this corresponds to

$$M := \frac{N(N-1)}{2} \tag{2.1}$$

measurements. To create the final values, the measured values are 5-σ clipped iteratively. Then the weighted average of the measurements is taken. The weights are given by the inverse of the squared sum of the positional fitting error and the catalog precision. The weighted standard deviation of the values, divided by the square root of the number of stars N is used as the confidence interval of the result. As confidence interval of the result, the weighted standard deviation of the values divided

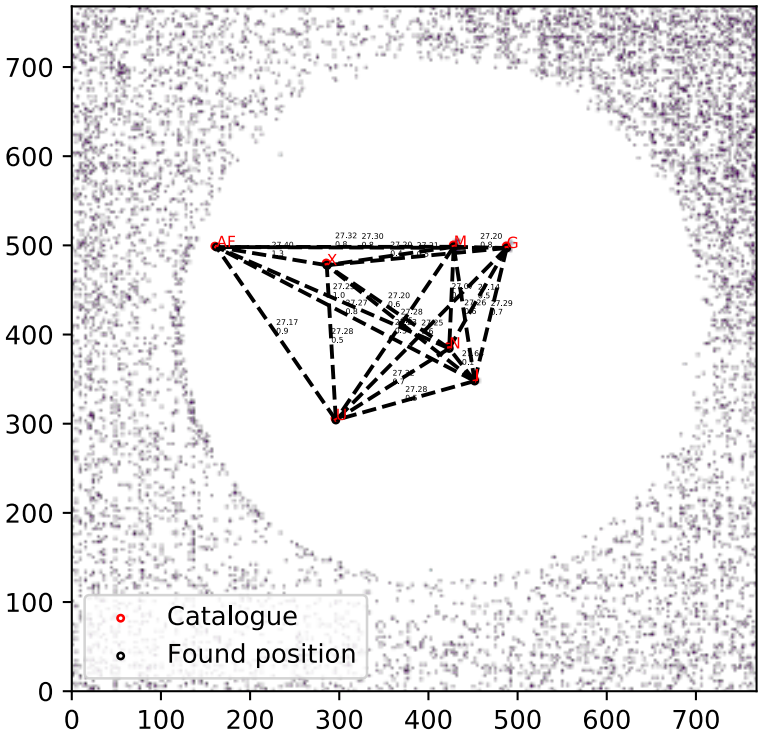

Figure 2.3: Example plot of all the different combinations possible using the AGPM data from 2019-01-19T03:40:51.375. The background image is in log-scale, so only the AGPM's outer region and the stars are visible, but the latter are mainly covered by the circles marking their positions. The red letters mark the names given in the stellar input catalog and the numbers at the lines give the platescale (upper) and true north for each measurement.

by the square root of number of stars N is used. I do not divide by the square root of the number of stars N and not the number of measurements M, because only the first are independent measurements.

Experiments of disqualifying stars completely, if e.g. 70% of its measurements are removed during the 5-σ clipping process, did not result in any improvements of the results. The reason is that there does not seem to be stars with significantly more bad measurements, i.e. one star being very off. This means one either removes all stars or no star, dependent on the percentage chosen above.

2.4 Results

Of the 276 calibration measurements, 263 values could be obtained: 120 with the AGPM coronagraph and 143 without it. For the other 13 observations, not at least three stars could be identified and matched to the catalog, or they were removed manually, as they contained bad data as shown in Fig. 2.1. Those observations were accounted as bad, where Fig. 2.1 gives examples of such bad images. The median numbers of stars identified are 14 with and 35 without the coronagraph. The results of the individual measurements are given in Table A.1 and are visualized in Fig. 2.4.

The mean results, weighted by the inverse of the squared error, yields a platescale of (27.214 ± 0.039) mas/px and a true north of $(1.00 \pm 0.27)^\circ$ when using the AGPM; and a platescale of (27.173 ± 0.0015) mas/px and a true north of $(0.69 \pm 0.29)^\circ$ without the AGPM. The values with and without the coronagraph agree within uncertainties. The larger errors when using the AGPM are expected because of the smaller FoV and thus reduced number of stars, as well as the reduced image quality due to the movement of the AGPM, see Figs. 2.1d and 2.1e.

2.5 Discussion

No significant difference in the values with and without the AGPM could be found. Also the platescale is in good agreement with the official value given in NaCo's official handbook (Table 5-3, Kaufer, 2018). The true north should ideally be zero, but here a significant offset towards the east of $\lesssim 1^\circ$ is found (meaning an image where north is supposedly up and east is supposedly left has to be rotated clockwise to obtain the correct orientation). Between observations with and without the AGPM no significant offset is found, see Fig. 2.4.

The values presented here are not the values used for the NaCo-ISPY survey, but are intended as an automatized consistency check of the values obtained by André Müller who maintains NaCo-ISPY's primary astrometric calibration pipeline. He developed a different, completely independent pipeline written in IDL to derive the astrometric values. He obtains respective values of the platescale of 27.208 ± 0.088 mas/px and 27.193 ± 0.059 with and without the AGPM, which are in agreement with the findings of this work. The measured true north is 0.572 ± 0.178 and 0.568 ± 0.115 with and without the AGPM, respectively. These measurements agree very well, which is not surprising given they are based on the same data. The only exception is the measurement of the true north with the AGPM, but also here the uncertainties overlap. This difference could be caused by a more rigorous rejection of artifacts of the AGPM by André (see Figs. 2.1d and 2.1e). The selection used here is not ideal, because it is only based on one FWHM value, e.g. not accounting for asymmetries of the source, whereas the default NaCo-ISPY pipeline also accounts for asymmetries.

This more rigorous rejection of sources would also be the main improvement that can be done to the results. A further possible improvement could also be, to be independent of the initial guess values. This could be done by not only crossmatching the shift of the image, but also its orientation and pixelscale. Currently a risk is, that one needs to insert the values one expects and then blindly trusts the algorithm when they are returned. Here this was avoided by checking manually on example images, that the the correct stars from the catalog are matched to the image, and by having a second, independent routine analyzing the images. Further improvements point towards a better PSF template generation for finer positional fitting. Fig. 2.1c shows that stars are elongated in radial direction from the correction center of the

AO. In the case of not too strong spider or bad AO features (as in Fig. 2.1e), the PSFs could then be rotated to find a precise center. However, one has to be careful in identifying the true stellar position in that case, which is not needed in the present pipeline.

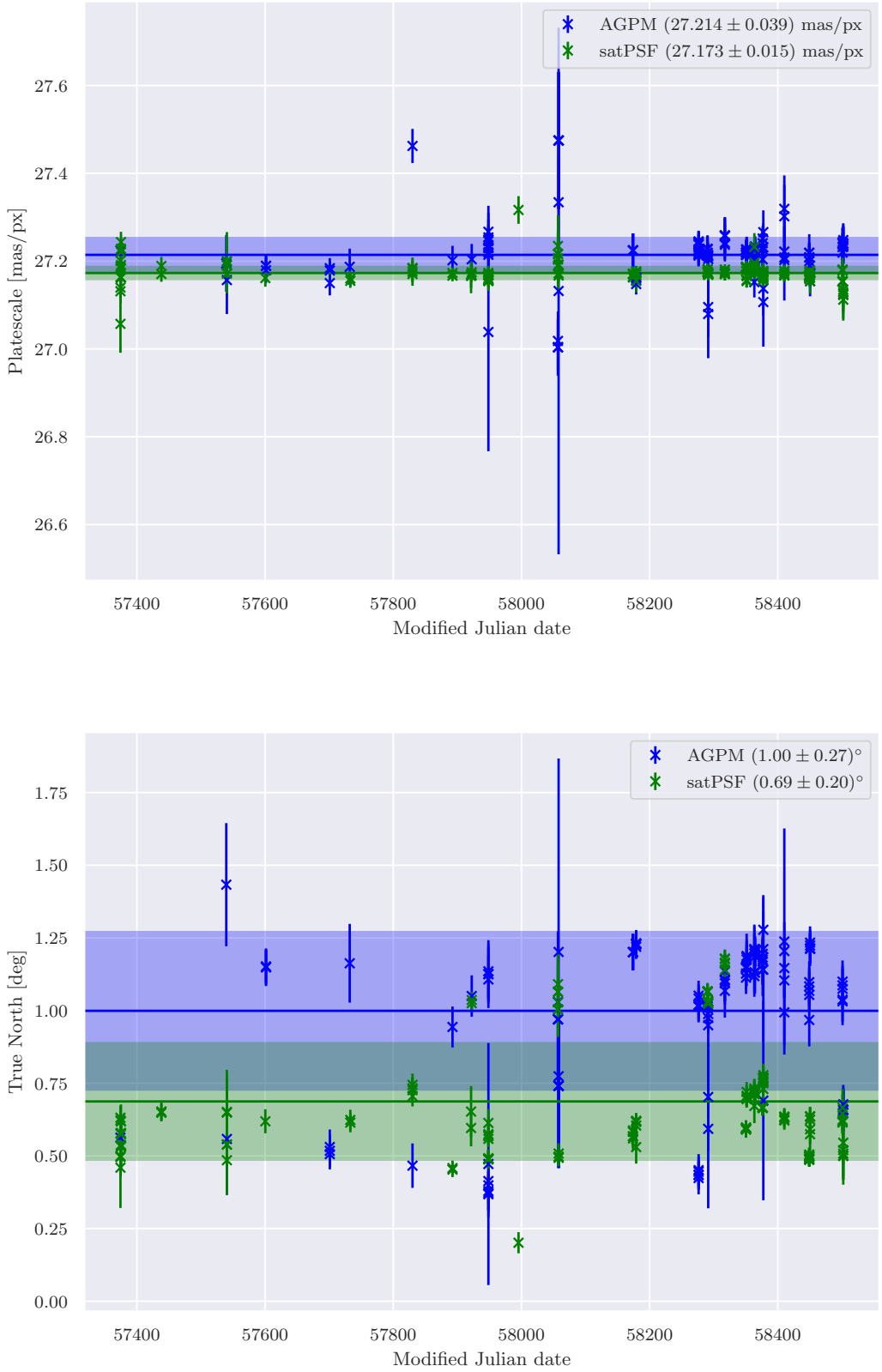

Figure 2.4: Platescale (top) and true north (bottom) of all calibration observations performed with NaCo-ISPY, where more than two stars could be identified. The horizontal lines mark the weighted mean for observations with (blue) and without (green) the AGPM and the shaded region indicate the weighted uncertainties.

Chapter 3

Individual Systems of the NaCo-ISPY Survey

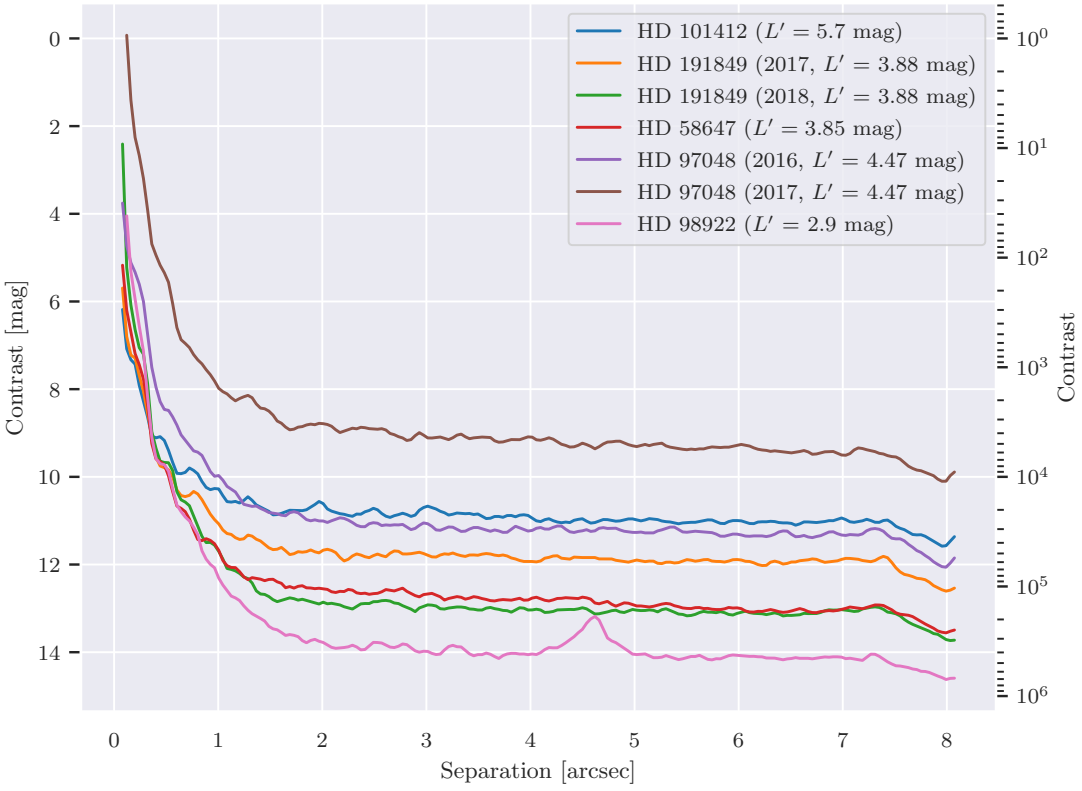

Figure 3.1: 5-σ stellar contrast curves for the five systems presented in this chapter. To obtain the total limiting magnitude, the stellar magnitude needs to be added to the stellar contrast, why they are given in brackets. Note that HD 97048 and HD 191849 have been observed twice, but the observation from 2017 suffered strongly from bad conditions in both cases and therefore have a worse contrast.

Here I discuss systems observed in the course of the NaCo-ISPY survey, where we identified sources in our data – or as in the case of HD 191847, at least thought we did. Due to the longer wavelength of the used L' band, the NaCo-ISPY survey identifies much less BG sources compared to surveys operating at shorter wavelengths. One reason is the higher sky background which limits the sensitivity of the survey.

E.g. ESO[1] gives the *L* sky brightness as 3.9 mag, compared to 13.0 mag for the *Ks* band. Thus, after integrating about 3 hrs, we reach a sensitivity of $\sim$ 16.5 mag BG limited regime outside $\sim$ 2″, compare Fig. 3.1 where the stellar contrasts are plotted for the five systems presented in the following sections. The second reason is the lower luminosity of stars at these wavelengths, which typically peak in the optical or near infrared. Note that this lower brightness is of course the reason for contrast limited DI surveys to operate at those longer wavelengths, since the cooler planets peak at those longer wavelengths.

But still, as of January 2019, we identified 148 CCs in 88 different data sets. These CCs then need to be analyzed and decided whether those are BG sources (stars, galaxies, ...) or real companions (stellar or substellar).

I took responsibility for the following 23 stars. The label classifies the star in terms of what I could conclude from the analysis: If the star either does not show any companion (e.g. only speckles/reduction artifacts, OS), is inconclusive (IC), has an imaged disk (DISK) or could be classified as a background source (BG).

- HD 1466 (OS)
- HD 1581 (OS)
- HD 36112 (BG)
- HD 7570 (OS)
- HD 11171 (OS)
- **HD 58647 (IC)**
- HD 92945 (OS)
- **HD 97048 (BG)**
- **HD 98922 (BG)**
- HD 100453 (BG)
- HD 100546 (DISK, IC[2])
- **HD 101412 (IC)**
- HD 102458 (OS)
- HD 104231 (IC)
- HD 138813 (OS)
- HD 163296 (DISK, IC)
- **HD 191849 (OS)**
- HD 199260 (OS)
- HD 218511 (DISK)
- HIP 35488 (BG)
- MML28 (BG)
- V 4046 Sgr (BG)

In the following, I am going to present the five examples marked in bold in the above listing in more detail.

3.1 Two Companions around HD 101412?

3.1.1 Introduction

With HD 101412 we could have identified a system, that might hold further clues to planet formation: HD 101412 is a 2 Myr-old B9/A0 Herbig star (Wade et al., 2005) at 412 pc (Gaia Collaboration et al., 2018) with a well-known mid- to far-infrared excess (The et al. 1994, also see Fig. 3.2), within 0.6″ of which we have discovered two probable substellar companions (Fig. 1). The projected physical separations of

[1] https://www.eso.org/gen-fac/pubs/astclim/paranal/skybackground

[2] A CC thought to be a planet (Quanz et al., 2015), but now thought to be a disk feature e.g. Rameau et al. (2017). We detect the disk but cannot contribute significantly to this discussion.

Property	Value	Reference
Identifiers	HD 101412, TYC 8972–1154–1	
	2MASS J11394445–6010278, CD–59 3865	
SpT	B 9/A 0 V	Houk & Cowley (1975)
Distance	411 ± 5 pc	Gaia Collaboration et al. (2018)
Age	2 ± 1 Myr	Wade et al. (2005)
RA (ICRS)	11:39:44.456	Gaia Collaboration et al. (2018)
DEC (ICRS)	−60:10:27.718	Gaia Collaboration et al. (2018)
pmRA*cos(DEC)	-3.765 ± 0.043 mas/yr	Gaia Collaboration et al. (2018)
pmDEC	-4.138 ± 0.045 mas/yr	Gaia Collaboration et al. (2018)
l (GAL, J2000)	294.124 263°	
b (GAL, J2000)	+1.465 592 0°	
Luminosity	$26.8 \pm 0.5\,L_\odot$	Gaia Collaboration et al. (2018)
Effective Temp.	7840 ± 140 K	Gaia Collaboration et al. (2018)
L' luminosity	5.7 ± 0.1 mag	WISE interpolated (Cutri et al., 2013)
I SPY priority	1	Reason: PPD
I SPY Group	PPD	

Table 3.1: Basic properties of HD 101412.

the 0.19″ and 0.53″ companion candidates are 78 AU and 222 AU, respectively, and their estimated masses from the discovery L'-band photometry and BT-Settl models (Allard et al. 2012) are ∼150 and ∼60 times Jupiter's.

In order to characterize this very interesting system further, I thus applied for SPHERE (Beuzit et al., 2008) spectroscopic data in 2018 to complement the GPI spectroscopic data. My proposal was accepted and ranked B, but unfortunately could not be observed due to an oversubscription of the SPHERE instrument in the first half of the demanded Period 101. As compensation for this loss I then received spectroscopic data for HD 191849, which results are described in section 3.2. Follow up applications for GPI spectroscopic data in Y- and J-band were then executed on February 26th and February 27th, 2019. The results of these observations will not be part of this thesis, but are planned to be made public by me in the second half of 2019.

The following section explains why it is not feasible to follow this target up with NaCo. Section 3.1.3 describes the observations we have from NaCo and GPI. It also describes what we can know about the CCs from the NaCo L'-band photometry, and what we expect from the GPI spectroscopy. Sect. 3.1.4 then describes how I estimated the chances of the two sources to be background objects. This was important to decide whether it is worth applying for different instruments, such as SPHERE

and GPI. Section 3.1.5 then concludes on the findings.

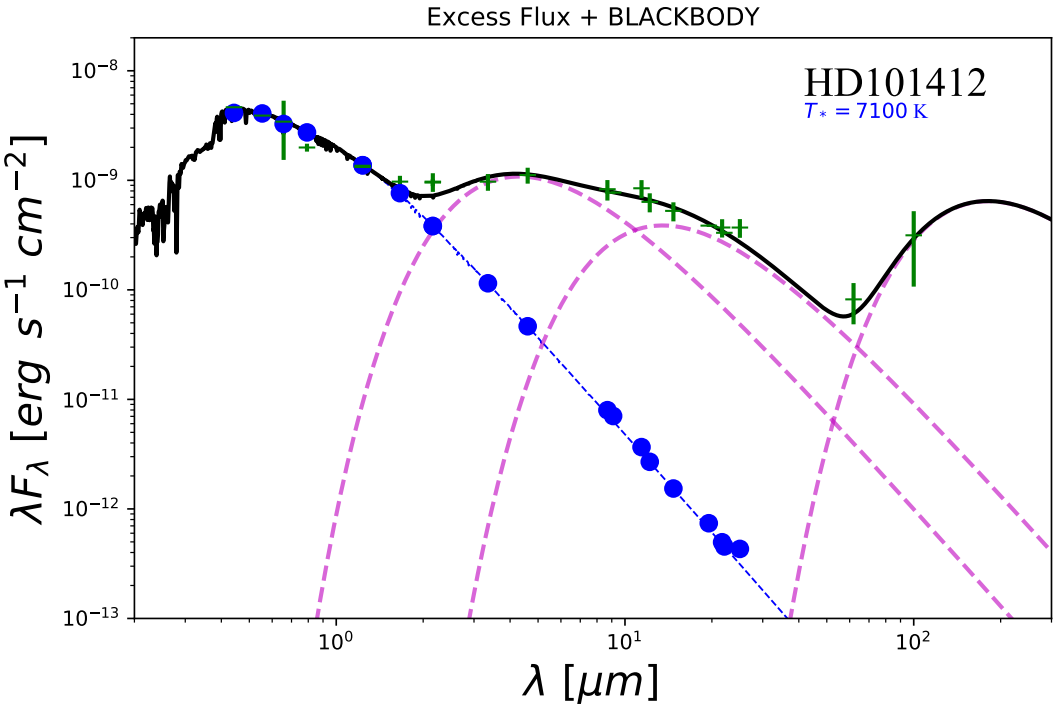

Figure 3.2: SED fit using the TWINKLE code[3] from Rahul Patel. TWINKLE uses the NextGen stellar models (Hauschildt et al., 1999) to fit the SED. The green points mark the measurements from different instruments, where the errorbars denote the 3-σ confidence intervals. The black line denotes the total SED of the fit, composed of the stellar (dashed blue) and three BBs (dashed pink) emissions. The inner belt looks like an optically thick disk, which we approximated as two BBs ($T_{\rm eff}$ = 891 K and $T_{\rm eff}$ = 283 K). The second disk is approximated by a 21 K outer disk and evidenced by the 60 µm and 100 µm IRAS data points. The IRAS 100 µm map does not show significant interstellar cirrus at the location of HD 101412, so we assume that the 100 µm is associated with the star.

3.1.2 Follow up with NaCo

Usually within NaCo-ISPY we try to follow up candidates within our GTO program, e.g. only using the NaCo instrument. The main method is common proper motion analysis, as e.g. shown in Sect. 3.5. However, as shown in Table 3.1 the Proper Motion (PM) of *HD* 101412 is only about 5.6 mas/yr. Since especially in the close in regions, we need about a pixel of motion for NaCo, where a pixel is $\sim$ 27 mas. Thus we needed to wait at least for 5 years before seeing differential motion (compare e.g. Fig. 3.21). But NaCo will be decomissioned spring 2020, and since for other instruments systematics add, astrometric follow up is not an option in the near future.

I thus looked into photometric determination. Assuming we would invest the time to follow up HD 101412 in the Y, J, H, K, and M' bands (remember, it is about 3 hrs VLT time per observation), we would want to be sure that we can exclude the

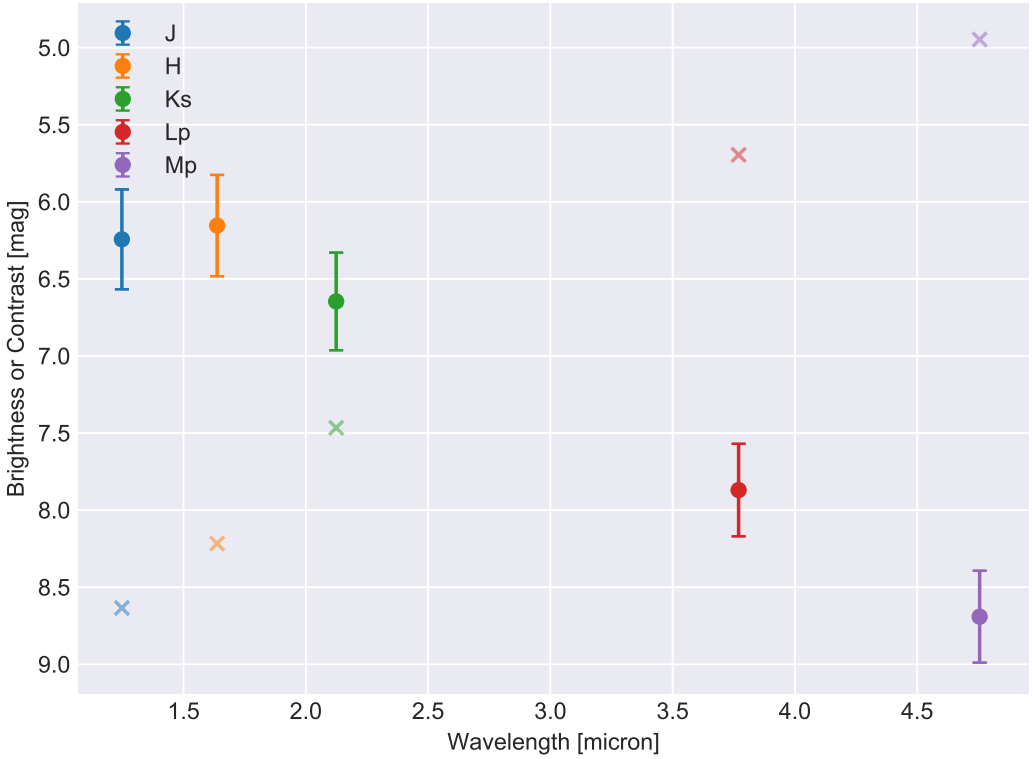

Figure 3.3: Solid points with error bars: Predicted contrast at different Wavelengths if HD 101412 assuming HD 101412 b was a 70 M_{Jup}BD at 2 Myr using the BT-settl models (Allard, 2014). The light crosses denote the brightness of HD 101412 in Vega magnitudes. Due to the huge IR excess of HD 101412, the contrast is most favorable in the *H*-band, whereas usually it is most favorable at the longer wavelengths.

CC are BG giants. However, even with all of those filters, it would still be unclear if it are background K-giants or BDs/Low Mass Stellar Objects (LMSOs):

Taking the newest BT-Settl models (Baraffe et al., 2015) and assuming they are at the same distance (412 pc, e.g. are bound), share the same age as the host (2 Myr) and according the the NaCo-ISPY L'-band observations, I computed the colors for all of those bands' combinations. As errors, I assumed the 0.2 mag error we determined in the L' using the fake injection technique, a standard technique in HCI. As comparison for the K-giants I used the values listed in Cox (2000, Table 7.7) for K0, K2.5 and K5 III giants. Given we already have the L' magnitude, the most indicative bands would be the J- and the M'-bands, since the colors of K giants and the BT-settl model then differ most. But as you can see in Fig. 3.4, even with the model being correct, the K giants photometry would still be the same within 1.5-σ.

Since we can neither confirm nor reject that the CCs are bound using NaCo photometry or common PM analysis, another method had to be found. Those are:

1. Imaging the circumstellar and potential circumplanetary disks and show dynamics as proof of their interaction

2. Spectroscopic characterization.

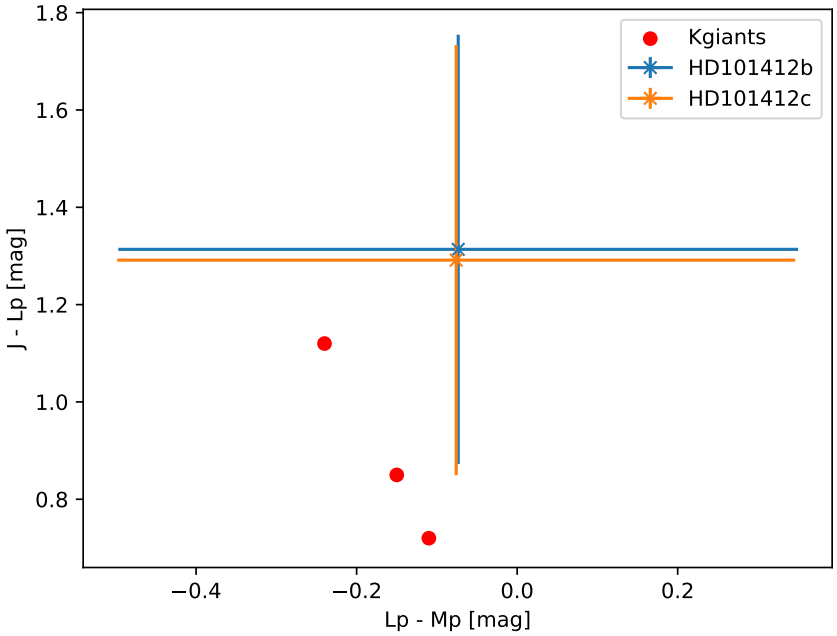

Figure 3.4: Expected color-color diagram of the two inner companions of HD 101412 according to the prediction of the BT-settl models (blue and orange) based on the NaCo-ISPY L' photometric measurement, assuming they share the same age and distance (e.g. they are bound). The errors assume a measurement precision of 0.2 mag per band, which is what we received for the inner Companion Candidate (CC). The red dots compare those colors to typical colors of a K0, K2.5 and K5 III giant (from left to right). You can see that even with those three bands it is not possible to rule out that the CCs are background sources.

For the imaging of the disks we applied and took H-band polarimetric data with GPI. The results are shown in Sect. 3.1.3, however, no sign of any of the disks was found. For the spectroscopic determination we received Y and J band spectra end of February 2019 also using GPI. But a said before an analysis of this data cannot be done before the submission of this thesis and will thus be made in a publication planned to follow this year. I therefore show the analysis of what we expect from the spectra with GPI. I therefore compare two BT-settle BD spectral models, four real BD spectra and a K0 spectrum. I then bin them according to the GPI resolution. The results are shown in Fig. 3.5. One can see that it is easily possible not only to tell the difference between a background K0 giant and a LMSO, but also to determine the SpT of the CCs.

3.1.3 Observations

To best characterize the system, we have applied and received polarimetric and spectroscopic data with NaCo and GPI. Table 3.2 summarizes the observations, which

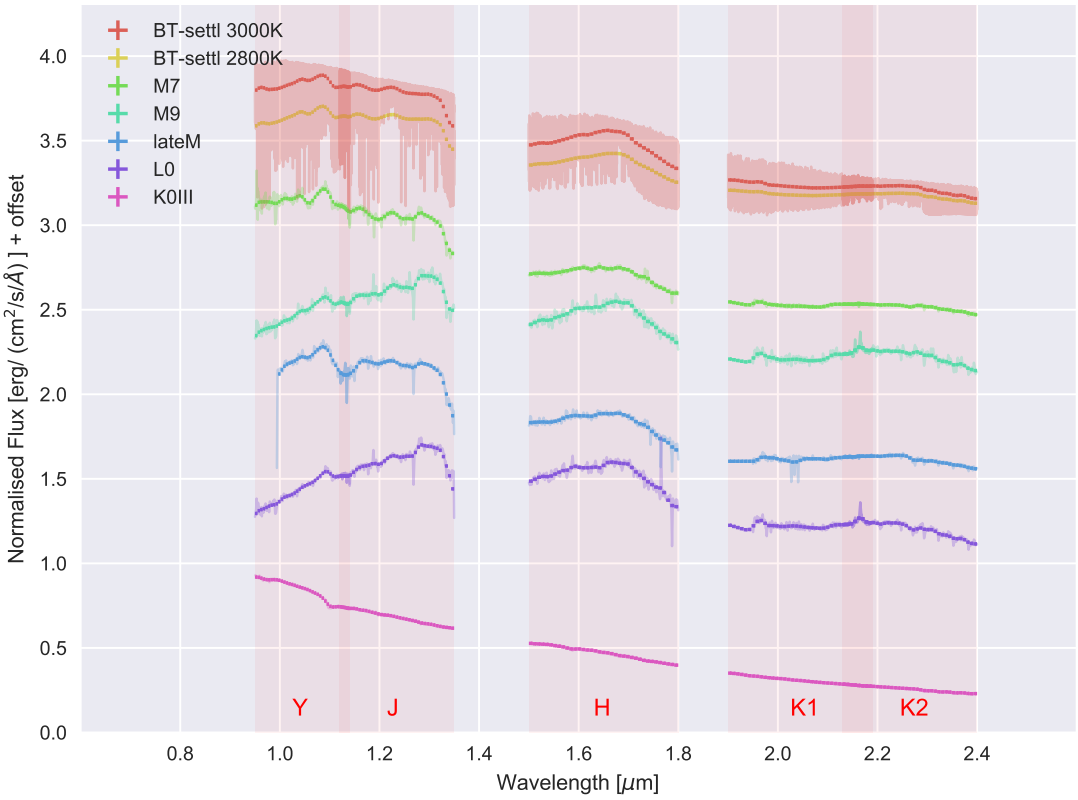

Figure 3.5: Example 2800 K and 3000 K theoretical M dwarf photospheres, spectra of young M7−L0 brown dwarfs (gracefully received from Elena Manjavacas in priv. comm.), and a K0 III model spectrum (Kurucz models from Castelli et al., 1997) that show the range of spectroscopic appearances that we could expect for the candidate companions to HD 101412. The *Y*- and *J*-band GPI spectra will be most diagnostic of spectral type, hence we only requested GPI spectroscopy in these bands. The light background curves show the highest available spectral resolution while the small bars show them binned to GPI's resolution. It can be seen that the photometric colors of a K0 giant are not very different from a $\sim$ 3000 K Brown Dwarf (BD). That is what makes it impossible to distinguish them using NaCo only, see Sect. 3.1.2. But since many spectral features are present in BDs, it should be relatively easy with spectroscopic data.

are described in more detail in the following paragraphs. Note that GPI does a sufficiently large FoV to image the two additional CCs further out, see Fig. 3.6. Since we look close to the galactic plane (1° above), chances are very high those are BG sources, compare Sect. 3.1.4. Thus we do not plan to spend any time on characterizing those.

NaCo-ISPY Observations

We observed HD 101412 during the curse of the NaCo-ISPY survey on March 17, 2017 in L' using the survey's standard setup when using the AGPM coronagraph. The conditions were good with seeing of $\sim$0.7″ and a coherence time of $\sim$ 6 ms.

Date [yyyy-mm-dd]	Inst.	Band	Mode	Time spent [hh:mm]	Comment
2017-03-17	NaCo	L'	Photometry	3:49	Discovery observation
2018-03-12	GPI	H	Polarimetry	1:20	Bad data, not used
2018-03-15	GPI	H	Polarimetry	0:55	Combined with 18-03
2018-03-18	GPI	H	Polarimetry	0:50	Combined with 15-03
2019-02-25	GPI	Y	Spectroscopy	2:55	To be analyzed
2019-02-26	GPI	J	Spectroscopy	3:02	To be analyzed

Table 3.2: Performed high contrast observations for HD 101412. The spectroscopic data was only taken in 2019 because the applied and accepted spectroscopic data with SPHERE unfortunately was not taken in 2018.

Only the humidity of 52% was higher than usual, but still we could reach a 5 σ background limit of 16.7 mag during the 3:49 h we spent on this target (UT 2:39 – 6:28 including preset). The DIT was set to 0.15 s for the unsaturated PSF frames needed for absolute calibration and 0.3 s for the science frames. During this time we achieved a field rotation of 73°. For more informationson the NaCo-ISPY observations for coronagraphic data see Sect. 1.6.1 or Lauhardt et al. (in prep.).

GPI observations

Motivated by the SED of HD 101412 shown in Fig. 3.2, we aimed for GPI poarimetric observations[4].

The polarimetric H-band follow up observations with GPI were taken in three nights of March 2018: March 12th, 15th and 18th, taken under the proposal ID GS-2018A-FT-101. We used the recommended setup for H-band coronagraphic observations (*H-coron*), where the coronagraph blocks light within a radius of 123 mas around the star. HD 101412 as an $I \approx 9.0$ mag, so that the GPI's AO operates just at the lower brightness limit[5] (Poyneer et al., 2014). But according to the night log and the results, this did not cause any problems. For the polarization angle the first two nights the polarization angle changed from 0.0° to 22.5°, 45.0° and 67.5° after a quarter of the total observing time, so that the angle was changed 3 times in total. In the last night, without our request, this was changed such that the polarization angle was changed after each frame, e.g. every 60 s. This mode is a bit more robust

[3] https://github.com/astropatel/twinkle

[4] If the disks were simple BBs with the equilibrium temperature at there respective distance, we probably should have found a disk. But it is known that PPDs are much more complicated than simple BB fits. This is probably why we could not image the disk.

[5] See also the GPI website at https://www.gemini.edu/sciops/instruments/gpi/instrument-performance/limiting-magnitudes

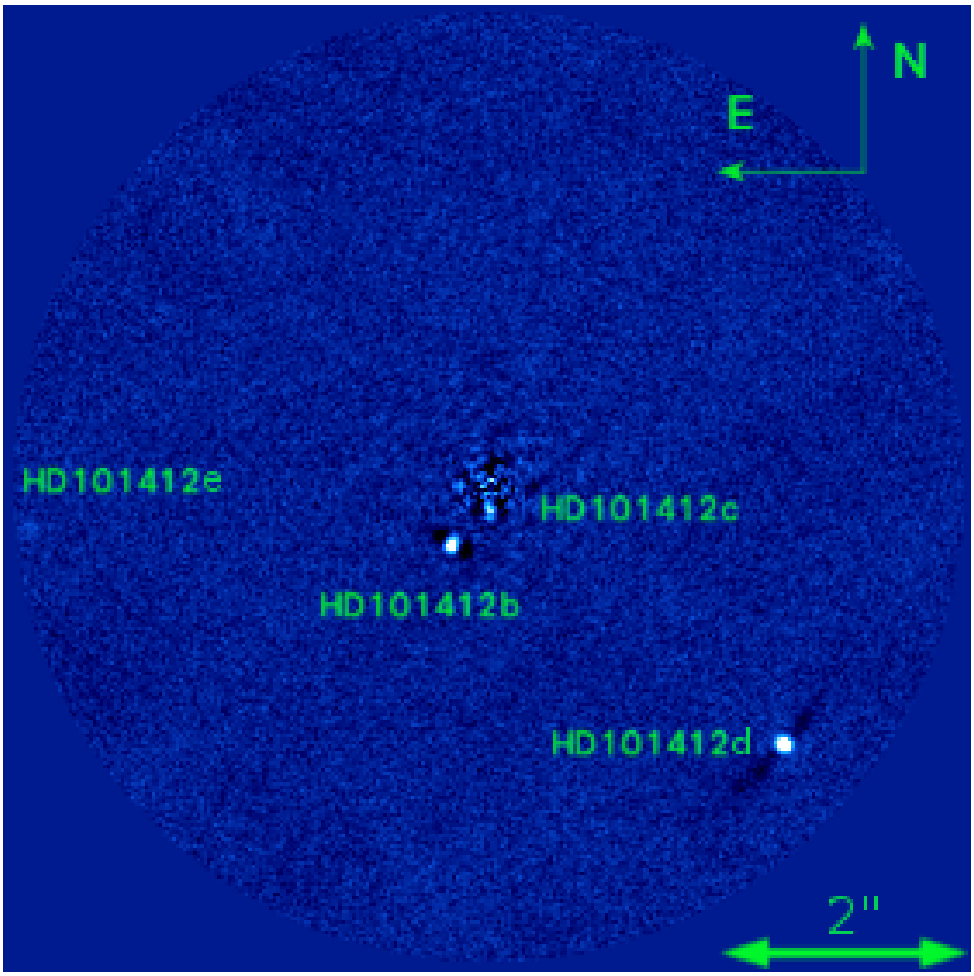

Figure 3.6: The detection image of taken during the NaCo-ISPY survey in L'-band. The inner two companions, labeled 'b' and 'c', are the prime targets of interest. The outer companions, labeled 'd' and 'e', are outside the FoV of GPI. And since the target is only 1 degree above the galactic plane and at over 400 pc, chances are extremely high that those are BG sources (compare Fig. 3.11) so we do not consider them any further. A zoom in on the inner region is shown in Fig. 3.8.

if e.g. the weather changes over time. However, we did not experience any effect of this on the observations' quality.

The first night there were issues with the centering of the star behind the coronagraph, see Fig. 3.7. The centering was so bad, that we do not use the data at all, but only combine the other two observation sequences. Despite the bad centering, one can still see the inner companions in any single 60 s exposure, demonstrating the exquisite performance of GPI's extreme AO system. Even though we could have asked for compensation of this lost night, we did not, since the data from the following two nights was of very high quality and did not show the slightest hint of any disk. And chances that one more night will change that are too little to scientifically justify another observation.

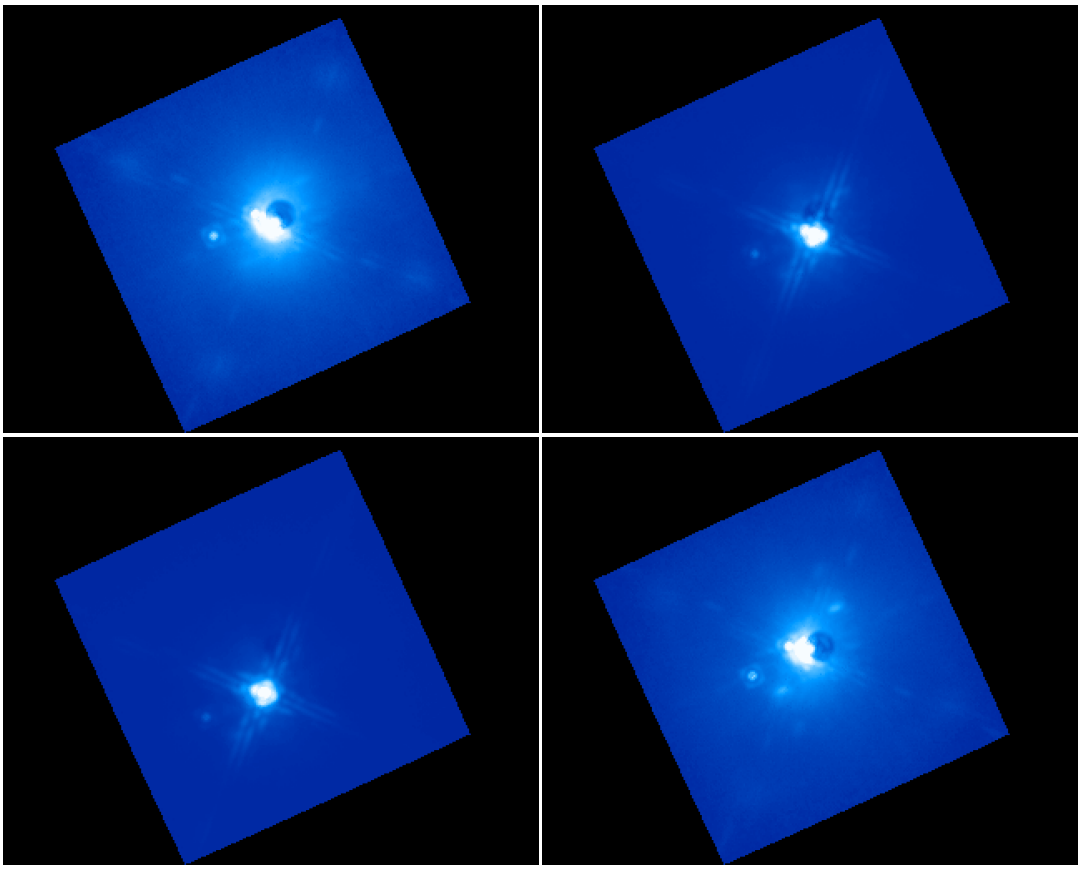

Figure 3.7: Four images of the GPI polarimetric H-band data from March 12, 2018 showing the centering problems. Usually the bright star should aways be behind the coronagraph (black spot roughly at the center of each frame). This is why the data set could not be used, in particular was not combined with the other data sets from the following days. Still HD 101412 b and c can be seen in any of the frames. The DIT was set to 60 s.

Spectroscopic GPI Observations Spectroscopic Y- and J- band observations with GPI were taken in 2019 on February 25 and 26, respectively. Again HD 101412's I magnitude of 9.0 is just at the faint limit of GPI's extreme AO system, but was working fine according to the night logs. We used the standard setup for the IFS in each band as well as the corresponding coronagraphs: The *Y-coron* with its 156 mas diameter and the *Y-coron* with its 184 mas diameter for the Y- and J-band observations, respectively. The spectral resolution for the Y-band is R =34-36 and R =35-39 for the J-band. Both bands have an underlying Nyquist sampling for each Spectral Pixel (Spaxel). The observations were executed in pupil stabilized mode.

We integrated on the target for about 3 h (5:05–8:00 UT) on the night of the 25th for the Y-band and also about 3 h (4:19–7:22 UT) on the night of the 26th for the J-band. We achieved field rotations of about 40° in both nights.

Since the data was only taken recently, this data will not be analyzed within this work. However, Fig. 3.5 shows example spectra of what we expect to see with these data sets.

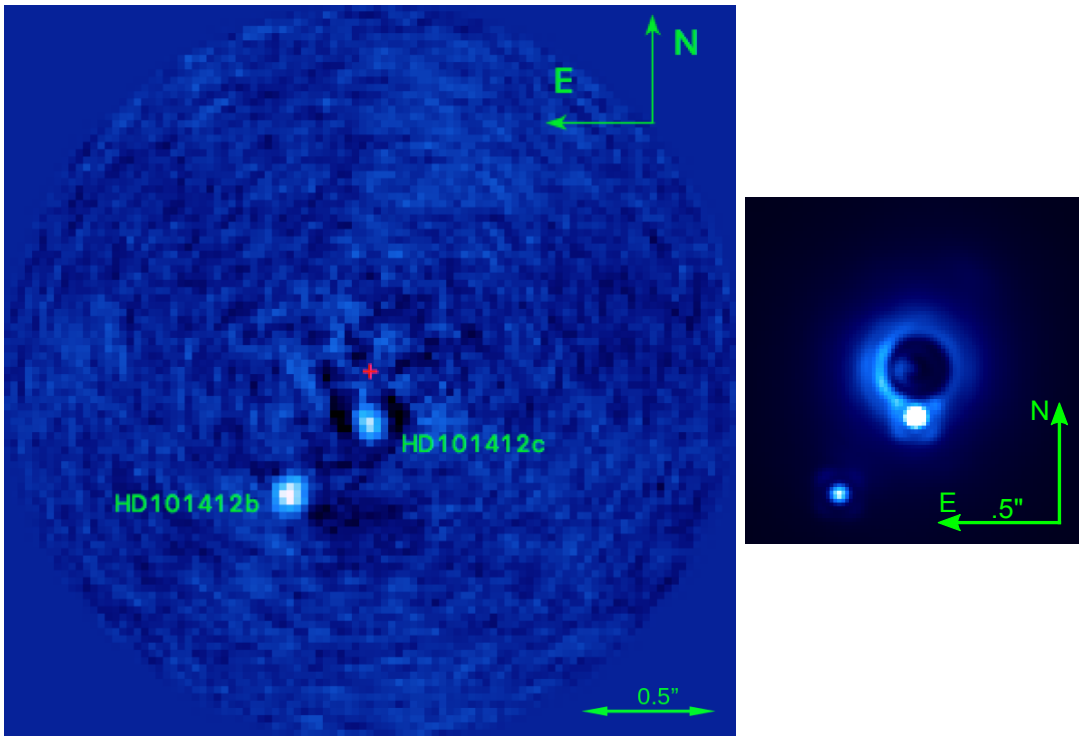

Figure 3.8: Images of the two companion candidates around HD 101412. (a) Discovery L'-band image from a combined 3 h sequence from the NaCo-ISPY survey, taken on March 17, 2017. Candidate 'c' is 0.19″ from the star and 'b' is at 0.56″. (b) Stokes I (intensity) H-band image from a 3 h sequence with GPI in polarimetry mode from combined imaging on March 16 and 19 2018. The two images are on the same angular scale. The companions did not show any relative motion over the year between the two observations. The smaller apparent brightness of the closer-in companion in the NaCo image (a) is on account of ADI post-processing, which was not required for the GPI differential polarimetry image (b). However, the present GPI IFS request requires ADI, and so a minimum of 3 h per band to achieve adequate field rotation for ADI to reveal the inner companion.

3.1.4 Background Statistics

In order to estimate the chances that those four sources are BG sources, I tried to estimate the background source density in this area. Since we have observations as deep as $L' \approx 16.5$, see Fig. 3.11, I need a near to mid infrared survey which covers sources at least to that brightness limit. HD 101412 is close to the galactic plane ($b = +1.46°$). That means I could use the VVV survey for this source density estimation [6]. VVV (Minniti et al., 2010) is a survey deeply ($Ks \lesssim 18$ mag) imaging the galactic center and galactic plane mainly, but not only, in the Ks-band using the VISTA telescope (Emerson et al., 2006; Dalton et al., 2006). Unfortunately, the newest and most complete VVV data release 4[7] only images the galactic plane for galactic

[6] The GAIA DR2 was not released yet back in 2017, making it impossible to use it, and also GAIA is often *crowd limited*, and operates in a completely different wavelength range (optical instead of NIR), compare Fig. 3.10.

[7] http://www.eso.org/rm/api/v1/public/releaseDescriptions/80

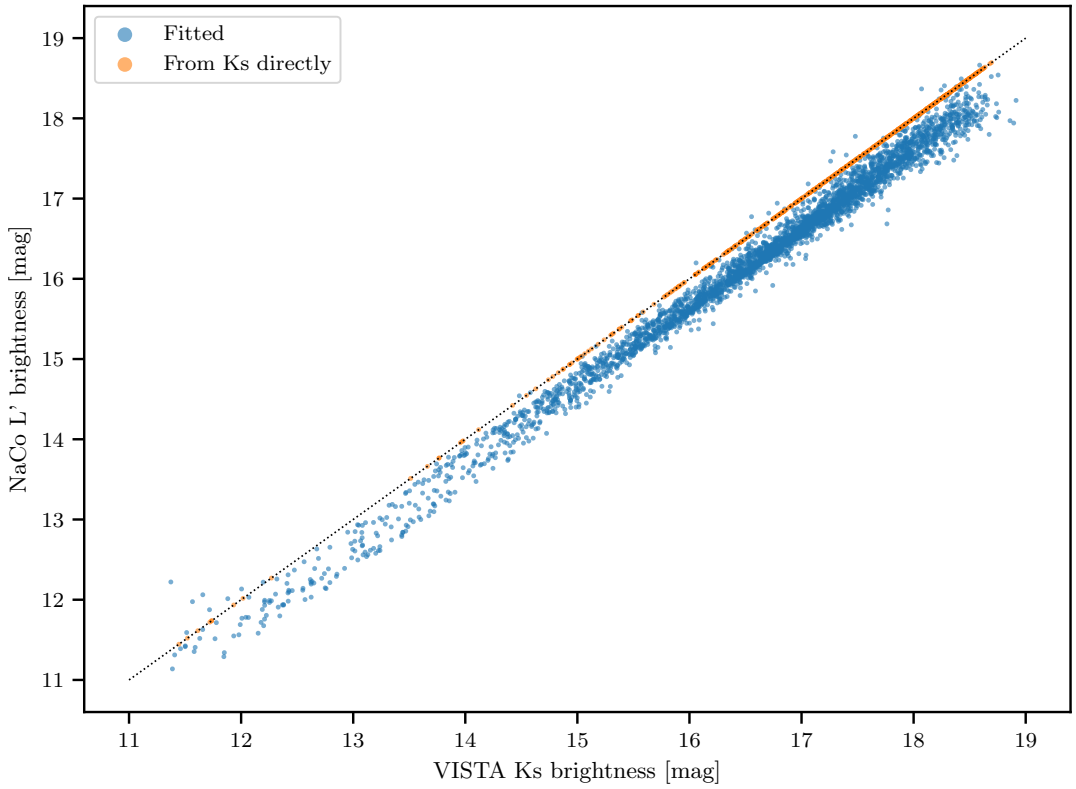

Figure 3.9: The change of the brightnesses found in the reference field when trying to estimate the stellar density around HD 101412. The orange points (1141 in total) did not have measurements in all three VISTA bands, thus the *Ks* magnitude was used as proxy for the L' magnitude. For the blue points (3301 in total), measurements of all three bands were available so I could fit extinction and a stellar model and extract the L' magnitudes. Their mean color of is $Ks - L' = 0.35$, roughly corresponding to *M*3 stars.

longitudes l with $l \geq 295$ or $l \leq 10$. But since HD 101412 has $l = 294.124°$, it is barely outside the range of VVV.

To overcome this issue, I used the Two Micron All-Sky Survey (2MASS) (Skrutskie et al., 2006) as a proxy to find a similar field in the nearby region. To find this similar field, I used a regular grid of 400 points which have their FoV of 180″ within the square enclosed by the galactic coordinates $l, b = 297.0°, -2.0°$ and $l, b = 295.0°, +2.0°$ (J2000), i.e. are closest to HD 101412 and covered by VVV. For each of those centers I compared the number of sources found in the *J*, *H* and *K*-bands of Two Micron All-Sky Survey (2MASS) with the number of sources found by 2MASS at the position of HD 101412. I then binned the sources in 200 bins, regularly ranging from 5 to 14.5 mag. I then chose the field, where the maximum discrepancy of the number of sources in any of the bins is minimal. To make sure we do not have issues with HD 101412 overshining too many sources, the discrepancies had to be minimal for FoVs of 90″ and 180″, i.e. making the effect of HD 101412 negligible. A finding was, that it was very important to have fields with a similar galactic latitude,

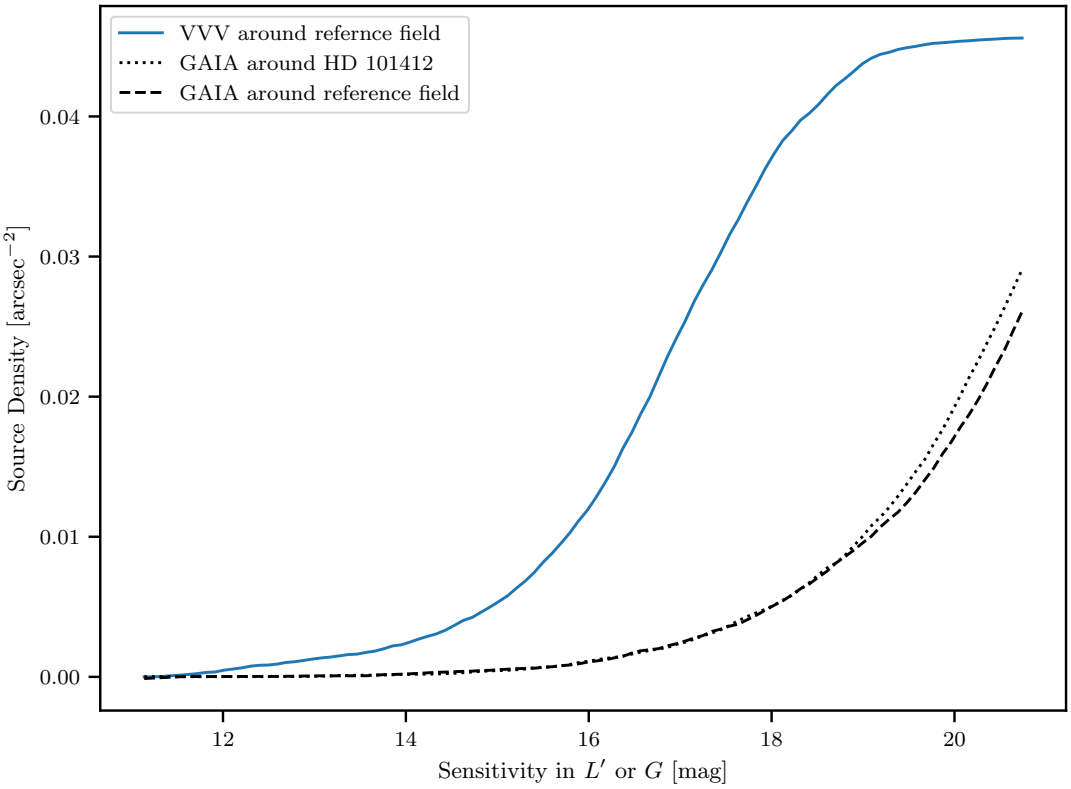

Figure 3.10: The source density of the VISTA Variables in the Via Lactea (VVV) survey around the reference field found to be the most similar to the one of HD 101412 based on 2MASS data. As comparison, the GAIA field around HD 101412 (dotted) and the reference field (dashed) is shown. Since most sources are of late spectral type and thus very red, GAIA finds much less sources in a brightness limited volume. The magnitude on the x-axis is L' for VISTA Variables in the Via Lactea (VVV) and GAIA's G band (similar to Johnson V) for GAIA.

whereas the longitude did not play a too big role. Thus, according to the described metric, the best field was the one with a very similar galacitic latitude. Its galactic coordinates are $l, b = 295.950°, 1.539\,47°$ (J2000). This is what I used as proxy for HD 101412's real field.

To then translate the Z, Y, J, H and Ks magnitudes of the VVV catalog to the needed L' magnitude, I used the VOSA service provided by Spanish Virtual Observatory (SVO)[8] (Bayo et al., 2008). This service fits stellar models to any given input, like spectra or photometric data and then translates the results into magnitudes for given filters. As input I gave any of the available Z, Y, J, H and Ks magnitudes of VVV data release 4 and as ouptut NaCo's L' filter, called `Paranal/NACO.Lp` in VOSA [9]. I further used the Kurucz ODFNEW/NOVER models (Castelli et al., 1997) with one additional parameter for the dereddening A_v, where I forced $0 \leq A_v \leq 3$. A_v is represents possible extinction and is described in Fitzpatrick & Massa (1999) and later improved by Indebetouw et al. (2005). The results of this fitting are shown in

[8] http://svo2.cab.inta-csic.es/theory/vosa/
[9] http://ivoa.net/documents/Notes/SVOFPS/index.html

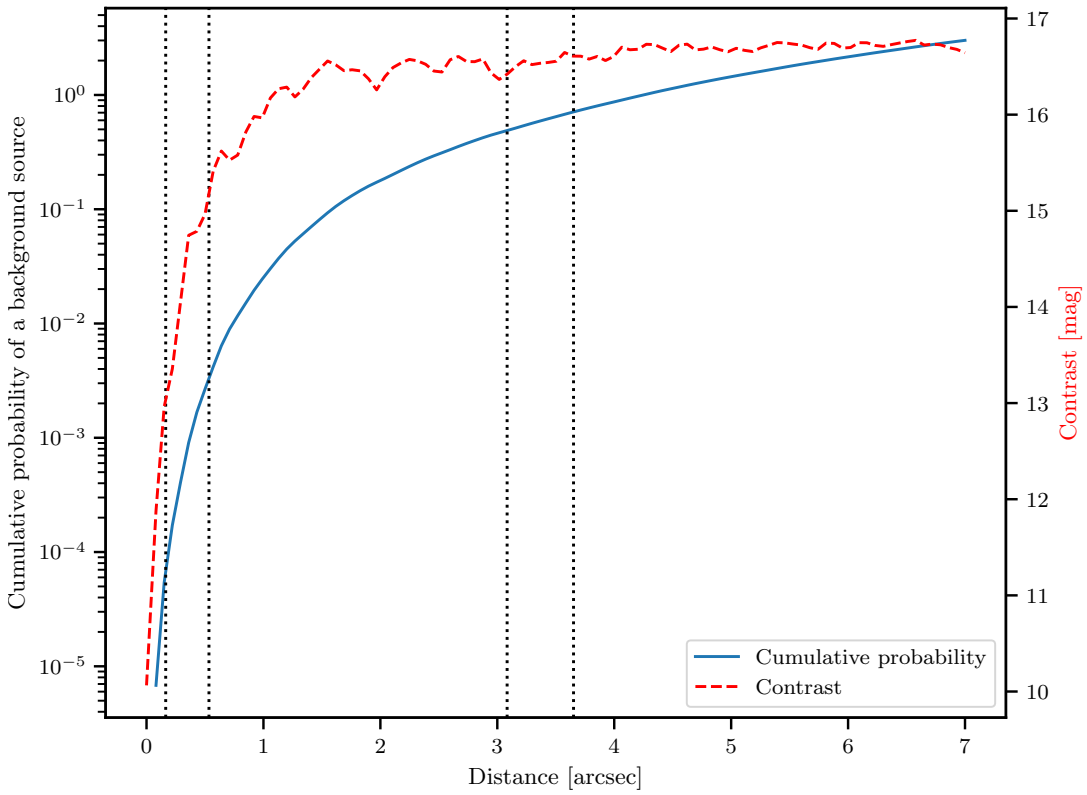

Figure 3.11: The blue lines denotes the likelyhood to find a Background source around HD 101412 as function of distance from the central star, based on the contrast curve (red dashed) and the background density presented in Fig. 3.10. The dotted black lines indicate the positions of the four sources found. Since we expect to find about the BG sources in our FoV, the outer two Companion Candidates (CCs) are considered BG sources and not followed up since they are also outside the FoV of GPI. The star's brightness is $L' = 5.7$ mag, which has to be subtracted from the right axis to get the stellar contrast limit.

Fig. 3.9. All sources that had measurements in at least three different bands were fitted and the L' magnitude extracted. Those were 3301 in total, and on average they show to be redder than Vega with $< Ks - L' >= 0.35$, where $<>$ denotes the average. This is expected since sources are either reddened by extinction or because most sources in the NIR are of late type in a magnitude limited sample. For the rest (1141), the closest available filter was used, which is mostly the *Ks* filter, since VVV DR4 has about 30 times more measurements in the *Ks* band than in any of the other bands.

After that, I simply counted the number of sources brighter than a given threshold in L' magnitude and divide by the search area of $\pi \cdot (180'')^2$ to obtain the BG density. The result is shown in Fig.3.10. As a consistency check, I compare the densities of HD 101412's field and the reference field with the now released GAIA DR2 densities in those fields . Up to ∼19th magnitude they are basically identical, hinting that our selection of the reference field was good, compare Fig. 3.10. However, the absolute number of sources is much lower in GAIA, since GAIA operates in the

CC #	Date [yyyy-mm-dd]	Sep. [mas]	ΔSep. [mas]	PA [deg]	ΔPA [deg]	mag [mag]	Δmag [mag]	Filter
b	2017-03-17	534.0	5.6	148.83	0.60	13.57	0.16	L'
c	2017-03-17	164.2	8.4	181.3	2.1	12.47	0.22	L'
d	2017-03-17	3084.6	12.7	230.24	0.26	13.77	0.17	L'
e	2017-03-17	3652.2	21.4	96.48	0.35	16.01	0.47	L'
b	2018-03-15	...	...	...	...	12.78	0.1	H
c	2018-03-15	...	...	...	...	13.99	0.1	H
b	2018-03-18	...	...	...	...	12.75	0.1	H
c	2018-03-18	...	...	...	...	14.06	0.1	H

Table 3.3: Positions and magnitudes of the four companions of the observations of the CCs around HD 101412. The nomenclature is the same as in Fig. 3.6. The errors of the magnitudes of the polarimetric measurements in the H-band are typical GPI uncertainties and should be an upper limit to the real error since the SNR is very high in the observations, compare Fig. 3.8 right side. However, all values of all GPI measurements are still work in progress and will be made available in a future publication.

visible where the most abundant M-type stars are very faint. This comparison nicely shows why it was so important to select a survey which operates at a similar wavelength as the NaCo-ISPY survey.

Finally a comparison with the contrast curve is made and the results are presented in Fig. 3.11. The contrast curve is also shown there for comparison. As mentioned we reach a background limit at almost $L' = 17$ mag, but in the inner regions out to about 1.5″ we are contrast limited. For the inner two CCs, the chances those are BG sources are 7.5×10^{-5} and 3.4×10^{-3} for the innermost and further source, respectively. Even accounting we observed roughly 100 stars in the NaCo-ISPY survey at that point, chances are extremely low we find two sources so close to the star – the only slightly realistic chance would maybe be a wide BG binary system. This is different for the two outer sources: Since HD 101412 is so close to the galactic plane, we expect to find about three sources in our entire FoV and at the positions of those two, chances are almost 50% to find some within their radius. And given we cannot confirm their nature neither with NaCo (no spectra), nor with GPI (FoV too small), we do not plan to follow them up. But for future investigation (e.g. with a sufficient baseline or SPHERE's IRDIS camera returning better photometric measurements than NaCo), I list their properties in Table 3.3.

3.1.5 Summary and Conclusion

Currently it is still unclear what the nature of the sources discovered around HD 101412 in the course of the NaCo-ISPY survey. We followed HD 101412 up with GPI, a high

contrast spectro-polarimetric instrument, currently located at GEMINI south (Macintosh et al., 2014). We chose H-band polarimetric observations (Fig. 3.8, right side) to seek a polarized scattered light detection from any extended portions of the circumstellar disk and complement the anticipated SPHERE spectroscopic data (see below). The GPI data showed no disk detection beyond 0.03″, the IWA of GPI in this band. Particularly around the companions no signal in the polarimetric data could be found. The companions' relative positions also appeared unchanged a year after the discovery, but that was expected given the very small (5.6 mas/yr) proper motion of HD 101412 and the ∼600 yr-long orbital period for the inner candidate assuming a face on orbit. Hence, we could in principle be seeing two unrelated background K giants. This is unlikely given their very small angular separations from HD 101412 (Fig. 3.11, Sect. 3.1.4) and their red $H - L'$ colors: 0.31 mag and 0.43 mag for the inner and outer companion, respectively. For a K0 giant $H - L' \approx 0.19$ mag and thus bluer. And from the GPI observations we know that there is no substantial amount of circumstellar dust at the companions' projected positions to redden them if they were background objects.

HD 101412 is thus almost certainly a rare massive planetary-like system: non-hierarchical, with multiple BD or low-mass stellar companions orbiting a single star. Only a few others systems with multiple substellar companions are known: HR 8799 (e.g. Zurlo & Bonnefoy, 2015), BD +20 2457 (Niedzielski et al., 2009), HD 1160 (Nielsen et al., 2012), HIP 73990 (Hinkley et al., 2015), and HD 87646 (Ma et al., 2016). Among these, HD 101412 is by far the youngest, and the only one at the < 5 Myr age when companions may be forming and growing through gravitational disk instability.

To conclude on the nature of the system, we obtained spectroscopic data in the Y- and J-bands, also using GPI. This data is currently being analyzed and planned to be published in the near future.

3.2 SPHERE's and NaCo's View of HD 191849

3.2.1 Introduction

On June 16th, 2017 we observed the only 6 pc distant (Gaia Collaboration et al., 2018) DD star HD 191849 in the course of the NaCo-ISPY program. Its properties are summarized in Table 3.4. Since the data was not of highest quality, the observations were repeated about one year later, on June 5th, 2018. In both data sets speckles at similar positions at about 2 λ/D could be identified. This corresponds to a physical distance of about 1 AU and would thus be by far the closest imaged planet, making it a very interesting science case. No appropriate archival data or reports in the literature could be found, where the same archives as the ones given in Sect. 3.5.1 were queried. Thus follow up observations with SPHERE were executed to conclude on the nature of the signals. No robust detection could be obtained.

Property	Value	Reference
Identifiers	HD 191849, HIP 99701, TYC 8392–2673–1	
	2MASS J20135335–4509506, SAO 230110	
SpT	M0 V	Gliese & Jahreiss (2015)
Distance	6.161 ± 0.002 pc	Gaia Collaboration et al. (2018)
Age	850 ± 400 Myr	Vican (2012)
RA (ICRS)	20:13:52.750	Gaia Collaboration et al. (2018)
DEC (ICRS)	−45:09:49.080	Gaia Collaboration et al. (2018)
pmRA*cos(DEC)	778.23 ± 0.074 mas/yr	Gaia Collaboration et al. (2018)
pmDEC	-159.74 ± 0.06 mas/yr	Gaia Collaboration et al. (2018)
Luminosity	0.0584 ± 0.0004 $L_\odot$	G. Kennedy (priv. comm., SED fitting)
Effective Temp.	$\sim 3849 \pm 7$ K	G. Kennedy (priv. comm., SED fitting)
L' luminosity	3.88 ± 0.35 mag	WISE interpolated (Cutri et al., 2013)
K luminosity	4.28 ± 0.024 mag	2MASS (Cutri et al., 2003)
Mass	0.51 ± 0.05 $M_\odot$	SpT-mass relation from Cox (2000)
I SPY priority	1	Reason: Proximity and Detection Space
I SPY Group	DEB	

Table 3.4: Basic properties of HD 191849.

3.2.2 Observations

We observed HD 191849 the first time on June 16th, 2017 in the L' band using the standard setup for stars brighter than about $L' \lesssim 6.5$ mag: Using the AGPM coronagraph and a DIT of 3.5 s. The conditions were relatively bad (seeing $\approx 1.4''$, coherence time $\tau \approx 1.8$ ms) and we obtained a field rotation of 98°. Additionally to the bad weather, there were centering problems with the AGPM reported in the night log each observer has to fill. With the PCA-based standard NaCo-ISPY data reduction pipeline (Cheetham et al., in prep.) using 10%, 20%, 30%, 40% and 50% of the maximally available principle components, we achieved a BG limit of 15.7 mag. Because of the bad conditions and the high priority, we re-observed the target almost one year later on June 5th, 2018. The conditions were better this time (seeing $\approx 0.67''$, coherence time $\tau \approx 2$ ms) and we obtained a field rotation of 114°. With this data we also achieved a significantly better BG limit of ~ 17.4 mag, compare Fig. 3.15.

In summer 2018, my granted observations of HD 101412 with SPHERE could not be executed anymore, since the star was already too low, compare Sect. 3.1.3. Since this happened to many scientists that applied for SPHERE data that semester, ESO offered to exchange granted but now unobservable targets to targets observable around September. Being a promising candidate, NaCo-ISPY decided to make use

of this offer and observe HD 191849. HD 191849 was then observed for 2 hrs (1:39 UT – 3:36 UT) of in the night of August 25th, 2018. We chose the coronagraphic IRDIFS_EXT mode of SPHERE, described in Sect. 1.3.4. It simultaneously takes a $R \approx 30$ spectrum from 0.95 - 1.35 µm and photometric observations in the $K1$- and $K2$-band filters. We used the standard setup for this mode. The DIT was 32 s for the IFS , and 2 s for IRDIS, as set by the night astronomer to avoid saturation. The weather was good (seeing $\approx$ 0.6 s, coherence time $\approx$ 4 ms) and we obtained a field rotation of about 40°.

3.2.3 Data Reduction

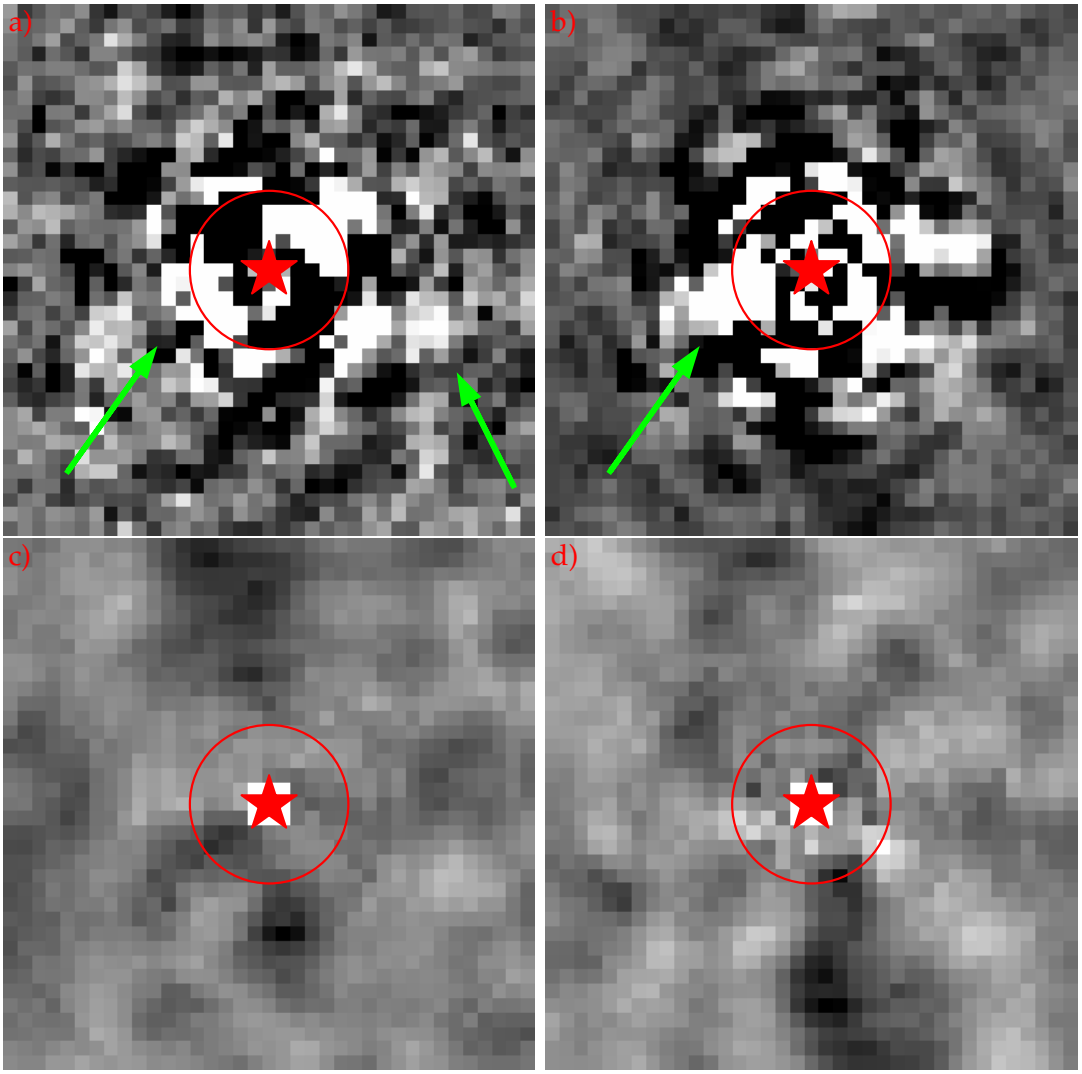

Figure 3.12: Reduced NaCo L'-band images of HD 191849 from June 2017 (a) and c)) and June 2018 (b) and d)). The top row shows the IDL based PCA reduction, where the arrows mark some suspicious speckles. The marked right speckle of panel a) could have moved either upwards or inwards in panel b). The bottom row shows the SNR map returned by TRAP. There no significant signal can be found. The star marks the stellar position and the circle 150 mas radius. North is up and east is left. All panels use linear scaling.

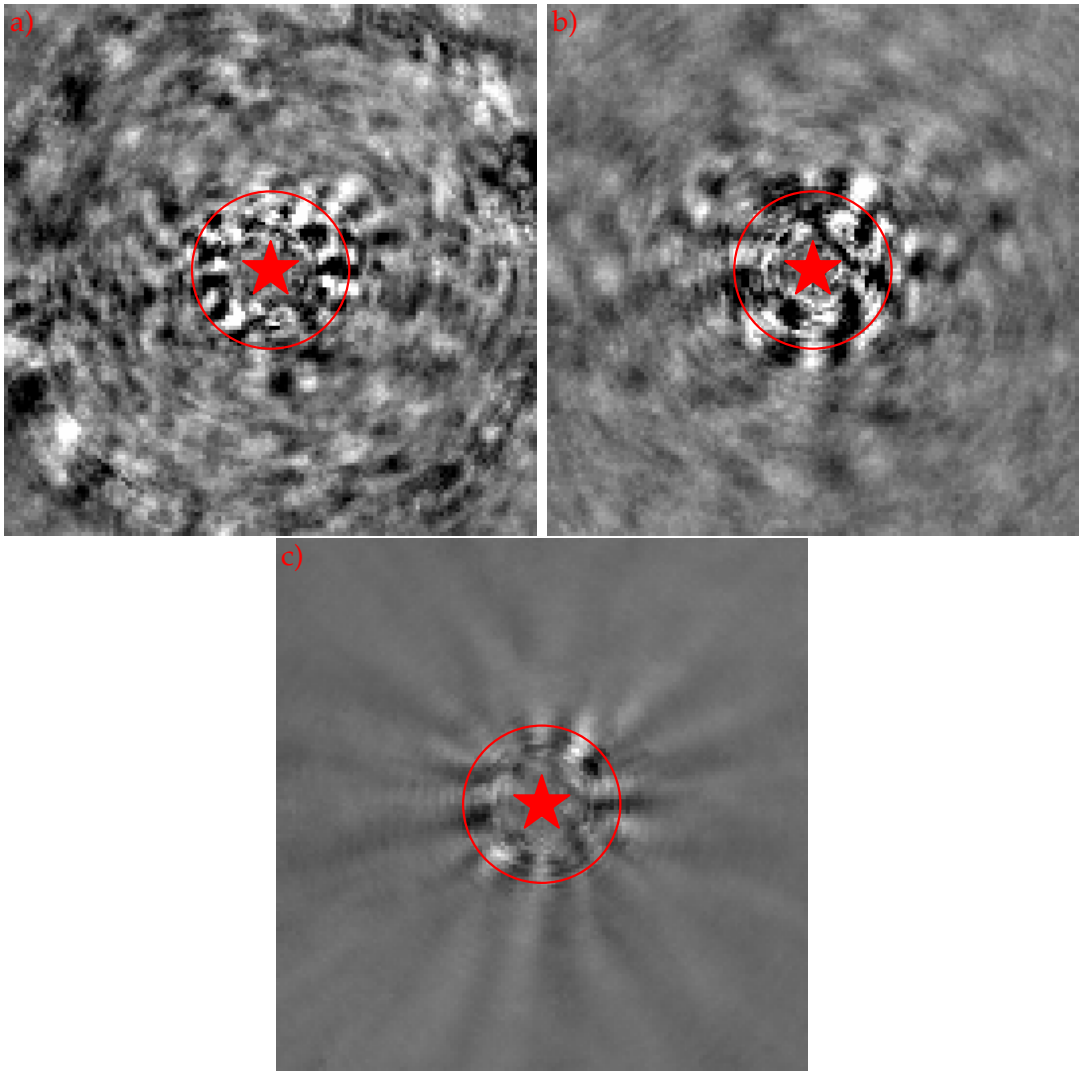

Figure 3.13: VIP-PCA reduced IFS of HD 191849 from August 2018. Panel a) shows the PCA reduced image at 0.96 µm (shortest wavelength), panel b) the same at 1.65 µm (longest wavlength). Panel c) shows all wavelength channels median combined. There is no significant detection: The only signal enhancements in the median combined image, bottom left and top right of the star, move out with increasing wavelength, compare panel a) and b). The star marks the stellar position and the circle 150 mas radius. North is up and east is left. All panels use linear scaling.

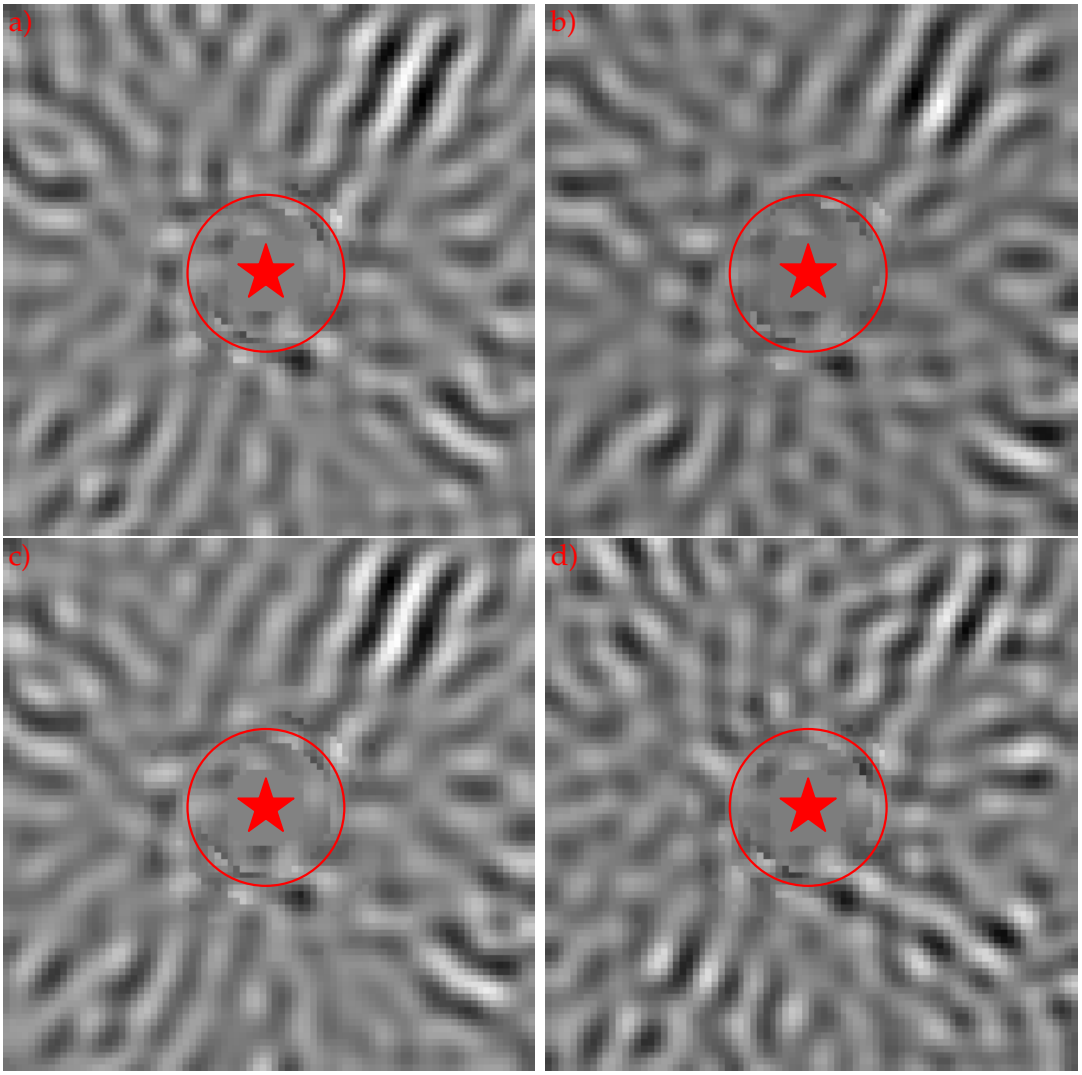

Figure 3.14: ANDROMEDA reduced IRDIS $K1$- and $K2$-band data of HD 191849 from August 2018. The panels show the normalized SNR maps returned by the ANDROMEDA code. There is no significant detection. The panels show the different filters and combinations described in the text: a) $K1$-band; b) $K2$ band; c) Combined (added) $K1$- and $K2$-bands; d) Subtracted (SADI) $K1$- and $K2$-bands.The radial structure comes from the normalization in annuli. The star marks the stellar position and the circle 150 mas radius. North is up and east is left. All panels use linear scaling.

Besides the official python-based NaCo-ISPY pipeline (Cheetham et al., in prep.), André Müller develops an IDL-based pipeline. With this pipeline experimental features and improvements as well as consistency checks are made. At the time of this analysis, the main difference was in the frame selection, being a bit more strict in the IDL pipeline. As is the standard procedure, we reduced both NaCo-ISPY data sets using both pipelines, varying the number of components used for the PCA reduction in steps from 10% to 50% of the maximal available components. The resulting images of the IDL pipeline are shown in Fig. 3.12 a) and b).

In March this year (2019), we re-reduced both NaCo-ISPY data sets using the now newly developed TRAP algorithm, specifically developed for the data analysis close to the IWA (Samland et al., in prep.; compare also Sect. 1.3.3). It has one free parameter, which is the number of principal components used for the model fitting. We kept the default of 30%. The image results are shown in Fig. 3.12 c) and d).

The SPHERE IRDIS and IFS data sets were reduced using the standard setup of the SPHERE Data Reduction Pipeline (DRP)[10] (Möller-Nilsson et al., 2010). It returns cosmetically reduced and aligned four dimensional data cubes: Two spatial dimensions, one time dimension and one wavelength dimension. The IFS data was reduced for each wavelength independently, using the `annular_pca` PCA routine from the VIP DI data reduction software package (Gonzalez et al., 2017). I chose a protection angle of 0.5 FWHM and an annular width of 3 FWHM. I varied the number of principle components between 3,7,12, 20 and 30. Finally I also collapsed the resulting spectral cube. The results for 12 components for two single wavelengths as well as the median collapsed image are shown in Fig. 3.13. The IRDIS $K1$- and $K2$-band data was reduced using ANDROMEDA (Cantalloube et al., 2015). A protection angle of 0.5 FWHM was chosen. ANDROMEDA offers multiple ways to combine the two spectral images: One can treat them separately, add them, or scale the $K2$ image by the wavelength ratio and subtract it from the $K1$ image. The idea of the latter is, besides standard SDI, that the planet's flux is strongly reduced in $K2$ because of the methane absorption pand at about 2.3 µm, compare the spectrum of 51 Eri in Fig. 1.7. We did all of the above combinations, and the results are shown in Fig. 3.14.

3.2.4 Results

The NaCo-ISPY observations from 2017 and 2018 showed speckles at similar positions out to 2 λ/D when the IDL based PCA reduction, see Fig. 3.12a and b. Reducing the data with the new TRAP algorithm, specialized on finding sources close to the IWA, nothing significant is detected, compare Fig. 3.12 c) and d).

The VIP reduced IFS data shows no signal of a source, but only wavelength dependent speckles, see Fig. 3.13.

[10] http://www.eso.org/sci/software/pipelines/sphere/sphere-pipe-recipes.html

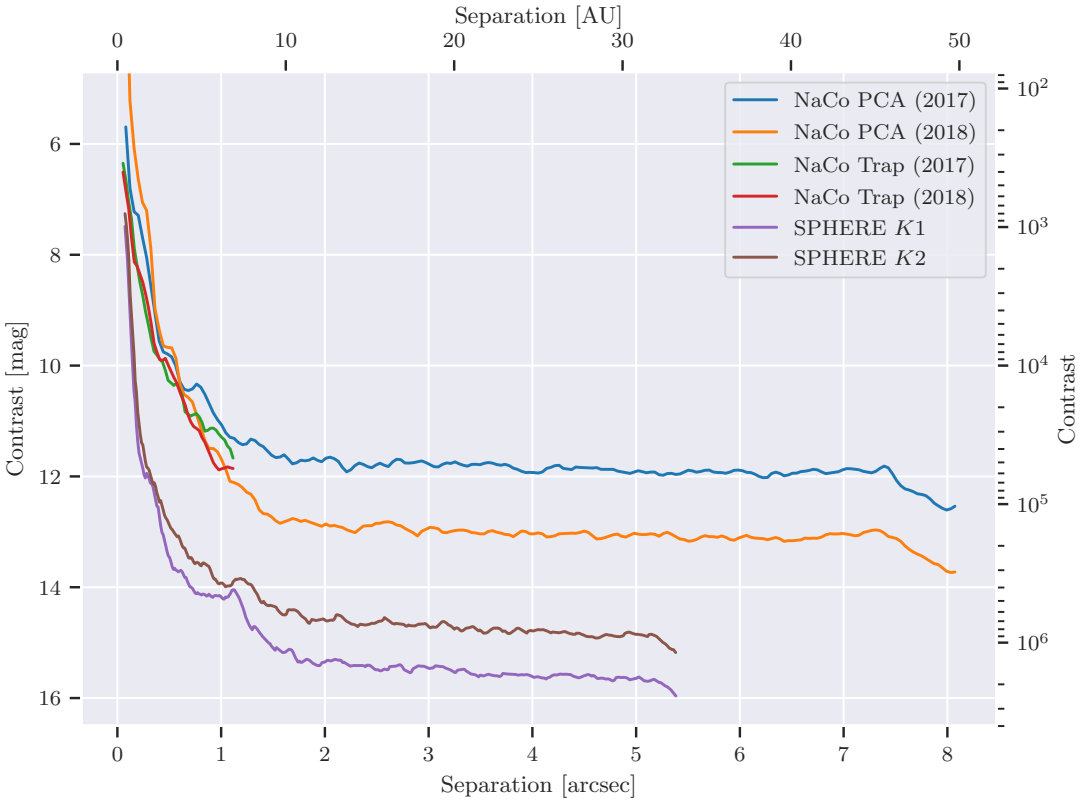

Figure 3.15: Comparison of the 5-σ contrast curves of the different observations and and analysis of HD 191849. With Trap only the inner region out to $\sim 1.1''$ was analyzed, for SPHERE the FoV is only $\sim 11''$. For the IFS data and the combined $K1$ and $K2$ filter no contrast is shown, since contrast curves for spectral combinations are very model dependent.

Also the ANDROMEDA reduced SPHERE-IRDIS $K1$- and $K2$-band data shows no significant signal in any of the four channel combinations, see Fig. 3.14.

Finally I also looked at the data from Gaia Data Release 2 (GAIA-DR2) (Gaia Collaboration et al., 2018). A massive planet around this close star with a period on the order of a year should be easily detected by GAIA. The GAIA-DR2 does only contain a 5 parameter fit and the individual measurements are not public yet. Thus no higher order model, including a companion, to the data can be derived directly. However, in GAIA-DR2 the parametrer `astrometric_excess_noise` gives a hint of the quality of the 5 parameter fit. For HD 191849 it is given as 0.0 ± 0.0 mas and thus insignificant.

3.2.5 Conclusion

No planet around HD 191849 could be found. Neither with NaCo, nor with SPHERE in various data reduction algorithms. Also GAIA-DR2 gives no hint towards a giant planet around this very close M0 V star. The "suspicious speckles" disappear in different analysis methods, and thus I conclude that the "suspicious speckles" are

almost certainly just speckles. In the $K1$- and $K2$-bands we can exclude any companion at a 5-σ level down to a contrast of $\sim$ 10 mag and 7.7 mag in the L'-band at 150 mas, see Fig. 3.15.

3.3 Does HD 58647 have a Companion?

Property	Value	Reference
Identifiers	HD 58647, HIP 36068, TYC 5408–4036–1	
	2MASS J07255610–1410435, SAO 152860	
SpT	B 9 IV	Houk (1978)
Distance	318.5 ± 4.3 pc	Gaia Collaboration et al. (2018)
Age	$\lesssim 10$ Myr	Because harbors a PPD
RA (ICRS)	07:25:56.099	Gaia Collaboration et al. (2018)
DEC (ICRS)	−14:10:43.549	Gaia Collaboration et al. (2018)
pmRA*cos(DEC)	-4.963 ± 0.062 mas/yr	Gaia Collaboration et al. (2018)
pmDEC	-3.274 ± 0.054 mas/yr	Gaia Collaboration et al. (2018)
Luminosity	$171 \pm 5\,L_\odot$	G. Kennedy (priv. comm., SED fitting)
Effective Temp.	7228 ± 5 K	G. Kennedy (priv. comm., SED fitting)
L' luminosity	3.85 ± 0.41 mag	WISE interpolated (Cutri et al., 2013)
ISPY priority	1	Reason: ProtoPlanetary Disk (PPD)
ISPY Group	PPD	

Table 3.5: Basic properties of HD 58647.

3.3.1 Observations and Data Reduction

CC #	**Date** [yyyy-mm-dd]	Sep. [mas]	ΔSep. [mas]	PA [deg]	ΔPA [deg]	mag [mag]	Δmag [mag]	Filter
1	2018-02-23	1635	6	31.33	0.142	−12.78	0.5	L'

Table 3.6: Positions and magnitudes of the identified foreground object in the NaCo-ISPY data for HD 58647. I use a platescale of 27.174 ± 0.070 and a true north of 0.571 ± 0.141, compare Sect. 2.4. The errors presented include those uncertainties.

On February 23rd, 2018 we observed the PPD star HD 58647 in the course of the NaCo-ISPY program. The conditions were very good (seeing $\approx 0.6''$, coherence time

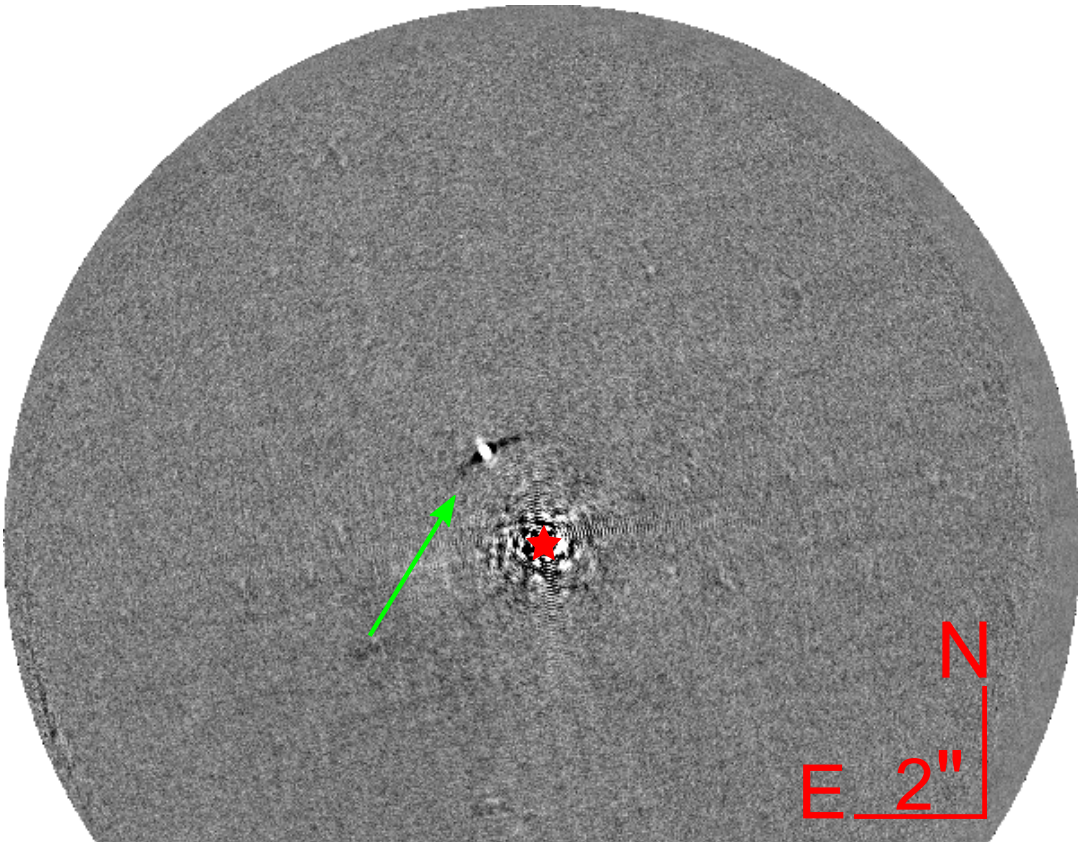

Figure 3.16: PCA reduced image of HD 58647 of the NaCo-ISPY observation taken on February 23rd, 2018

$\tau \approx 7.7$ ms) and we obtained a total field rotation of 127° . With the standard NaCo-ISPY data reduction pipeline (Cheetham et al., in prep.) we achieved a background limit of $\sim$ 16.7 mag, compare Fig. 3.1.

At a radial distance of about 1.6″ and a parallactic angle we found a source with a stellar contrast of about 1.98×10^{-4}, compare Fig. 3.16 and Table 3.6.

In order to confirm or discard this target via PM analysis, I routinely scanned the literature and archives of the same instruments as listed in Sect. 3.5.1. However, except for Sparse Aperture Masking (SAM) data from NaCo and NICR2, where the FoV is not sufficiently large, nothing useful is found. Thus no PM analysis or constraints on the color can be done.

3.3.2 Results

Since we only have one measurement in only one band of HD 58647, the only analysis we can do is to determine the precise position and magnitude of this companion. We then also compare it to BT-settl models, however, since the age is unknown, those properties are highly uncertain, even if the CC was bound.

In order to derive the positions and magnitude of the CC, the fake negative injection is used. A tool providing this fake injection for high contrast imaging the the VIP package (Gonzalez et al., 2017), where we used version 0.9.9 for python 3.

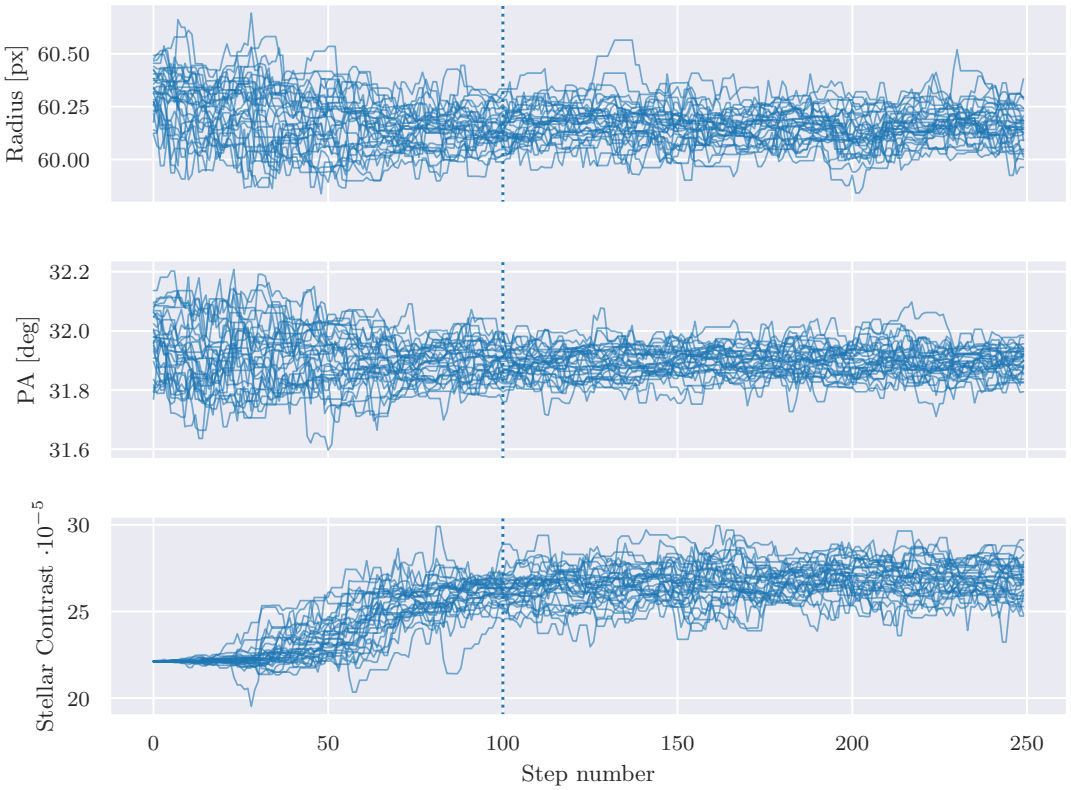

Figure 3.17: Walk plot of the results of the Marcov Chain Monte Carlo (MCMC) simulation of the CC around HD 58647 using the VIP pipeline 0.9.9 (Gonzalez et al., 2017). The blue dashed line marks the first 100 steps which are burnt (ignored) in the further analysis, because they were still part of the initialization process. The results are shown in a corner plot in Fig. 3.18.

The data cleaning, such as background subtraction, bad pixel correction, frame selection and centering was done by the standard NaCo-ISPY pipeline described in Cheetham et al. (in prep.). I then followed the tutorial for VIP[11]. There I normalized the flux frames routinely taken before and after each observing block using `vip.metrics.normalize_psf` and estimated the FWHM using the mean of the two components of `vip.var.fit_2dgaussian`. Then I am first guessing the rough ($\pm$1 px) position of the CC from the image shown in Fig. 3.16. A first guess of the flux is then achieved using a Nelder-Mead based optimization using the `vip.negfc.firstguess` routine. Here a negative fake planet with varying flux is injected at the rough position of the planet, PCA is applied and then the residuals are measured. The flux of the fake planet with the minimal flux is then used as a starting value.

Now with the starting position and a first guess of the flux, I started a MCMC chain using 30 walkers, each walking 250 steps using the `vip.negfc.mcmc_negfc_sampling` routine. To save computing time, only an annulus with a width of 3 FWHM was analyzed. The results are shown in Fig. 3.17 in form of a walk plot. One can see that the guess of the position was ok, but the flux was estimated by about 10 % in the

[11] https://nbviewer.jupyter.org/github/carlgogo/VIP_extras/blob/master/tutorials/01_adi_pre-postproc_fluxpos_ccs.ipynb

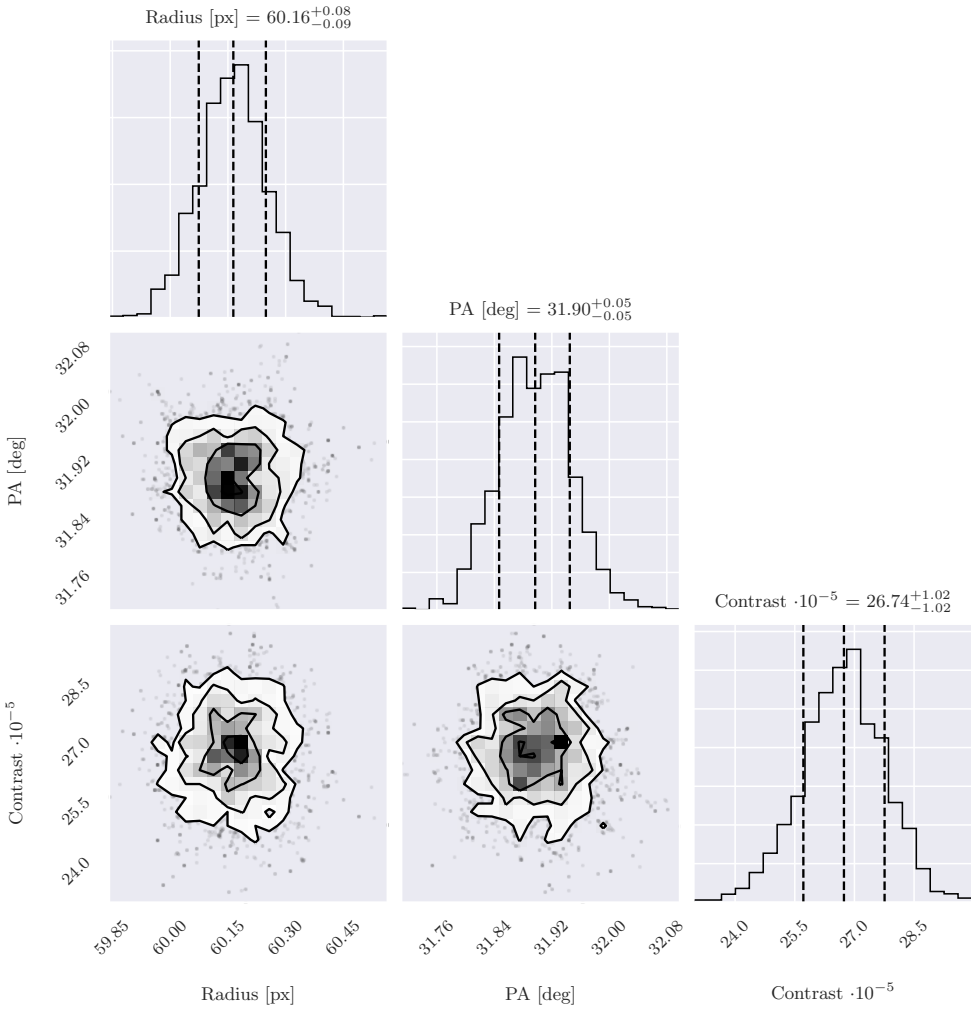

Figure 3.18: Corner plot of the results of the MCMC simulation of the CC around HD 58647. This cornerplot represents the results shown in Fig. 3.17 after burning the 100 initial steps. .

Nelder-Mead based approach compared to this more robust approach. However, that this values is slightly off is an expected behavior since only 15 planets with different fluxes were inserted to get a rough starting point. ince in the beginning the guesses were therefore off, I discarded the first 100 steps of each walker, which is the time until they stabilized. I then plotted remaining $150 \cdot 30$ points in a corner plot using the `corner` package (Foreman-Mackey, 2016). The results are presented in Fig. 3.18. Those values solely based on the pixels of the image, now need to be converted to physical properties. I therefore used a true north of $0.571(141)^\circ$, a platescale of 27.174 ± 0.070 mas/px (compare Sect. 2.4 and a stellar magnitude of $L' = 3.85 \pm 0.41$ mag (compare Table 3.5). Also note, that VIP uses a different convention of the PA, such that 90° need to be subtracted to come to standard east-of-west convention. The values and errors are presented in Table 3.6. Note that the biggest error in the L' magnitude arises from the uncertainty of the luminosity of the primary. Those values can then be used for future surveys to determine the properties of the CC.

Assuming the CC is bound, with the distance of 319 ± 4 pc as given in GAIA-DR2

Gaia Collaboration et al. (2018), the absolute magnitude can then be determined as $L' = 5.26 \pm 0.5$ Mag. Since the age is unknown, but we know the system needs to be relatively young since it still hosts its PPD, I give the best fitting BT-settl models (Allard, 2014) for three different ages: Assuming ages of 1, 5 and 10 Myr, the best gues BT-settl masses were about 0.055, 0.15 and 0.2 $M_{\odot}$, respectively. Thus, dependent on the age, the companion was either a high mass BD or a LMSO.

3.3.3 Conclusion

Usually CCs in DI are confirmed via the PM technique, compare Sect. 3.5.2. However, this requires a sufficiently large time span between the observation for the star to have moved sufficiently. In the case of NaCo-ISPY we require a movement of at least about 0.75 px or 20 mas. Given the PM of this HD 58647 is about 6 mas/yr, compare Table 3.5, a baseline of at least 3-4 yr would be needed. Since no archival data is available and our data is from 2018, one would have to wait at least until 2021 for a confirmation or rejection. By that time NaCo will be decomissioned such that this is not an option, so one would have to pick another instrument such as e.g. SPHERE (Beuzit et al., 2008). But as systematics between instruments might be present, an even longer baseline might be necessary.

Remains the possibility of spectrophotometric characterization, similar to HD 101412 in Sect. 3.1. Figure 3.4 shows at the example of HD 101412, that with NaCo it is basically impossible to discriminate between a BD and e.g. a background K-giant. Thus one would need an instrument with spectroscopic capabilities, such as GPI (Macintosh et al., 2014) or SPHERE. With those it would be possible, compare e.g. the example of HD 101412 in Fig. 3.5, where we obtained two spectroscopic and one photometric measurement to characterize two very close in CCs. However, given the relatively far distance of 1.6″ of the CC and a galactic latitude of only $+1.0°$, chances are very high that this is a BG object, compare Sect. 3.1.4. Thus the NaCo-ISPY consortium decided not to invest such large resources in this unpromising, but still possible candidate around HD 58647.

3.4 A foreground Object to HD 98922

3.4.1 Introduction

With the publication of the GAIA-DR2, I could confirm the assumption, that the CC to HD 98922 is indeed no companion. But as we typically find bright BG stars, in this case it is a somewhat dimmer FG star.

3.4.2 Observations and data reduction

Before the characterization this source, the NaCo-ISPY team did not routinely check the GAIA archive routinely. But with the release of GAIA DR2 on April 25th, 2018

Property	Value	Reference
Identifiers	HD 98922, HIP 55537, TYC 8617–657–1	
	2MASS J11223166–5322114, CD–52 4340	
SpT	B 9 V	Houk (1978)
Distance	690 ± 16 pc	Gaia Collaboration et al. (2018)
Age	0.01 Myr	Meeus et al. (2012)
RA (ICRS)	11:22:31.674	Gaia Collaboration et al. (2018)
DEC (ICRS)	−53:22:11.456	Gaia Collaboration et al. (2018)
pmRA*cos(DEC)	-8.655 ± 0.049 mas/yr	Gaia Collaboration et al. (2018)
pmDEC	0.819 ± 0.043 mas/yr	Gaia Collaboration et al. (2018)
Luminosity	$830 \pm 70\,L_{\odot}$	G. Kennedy (priv. comm., SED fitting)
Effective Temp.	8800 ± 600 K	G. Kennedy (priv. comm., SED fitting)
L' luminosity	2.9 ± 0.2 mag	WISE interpolated (Cutri et al., 2013)
I SPY priority	2	Reason: PPD but WDS-companion
I SPY Group	PPD	

Table 3.7: Basic properties of HD 98922.

Instrument	Date	Filter ([µm])	Total exposure Time [min]
NaCo	2006-02-11	*NB_2.12* (2.1)	11
NaCo	2006-02-27	*NB_2.12* (2.1)	11

Table 3.8: Archival data of HD 98922 found.

(Gaia Collaboration et al., 2018), and the very positive effect of this source, the NaCo-ISPY team now also checks the GAIA catalog to check the nature of CCs.

On February 22nd, 2018 we observed the extremely young (< 0.01 Myr (Meeus et al., 2012)) PPD star HD 98922 in the course of the NaCo-ISPY program. Under very good conditions (seeing $\approx$ 0.5″, coherence time $\tau \approx 8$ ms) and with a field rotation of 86.1 deg. Using the standard NaCo-ISPY data reduction (Cheetham et al., in prep.), we achieved a BG limit sensitivity of 16.9 mag, compare Fig. 3.1. In this BG we found a CC at 4.7". And assuming it was at the same distance and age as HD 98922, its L' magnitude would correspond to a BD objects according to BT-settl models (Baraffe et al., 2015).

Thus I scanned the archive and found two NaCo datasets from 2006, see Table 3.8. The observations were taken with the *NB_2.12* filter which operates at 2.12 µm. Even though the integration time was only 11 min and the field rotator was fixed in the jitter mode, we could identify the CC in both sequences.

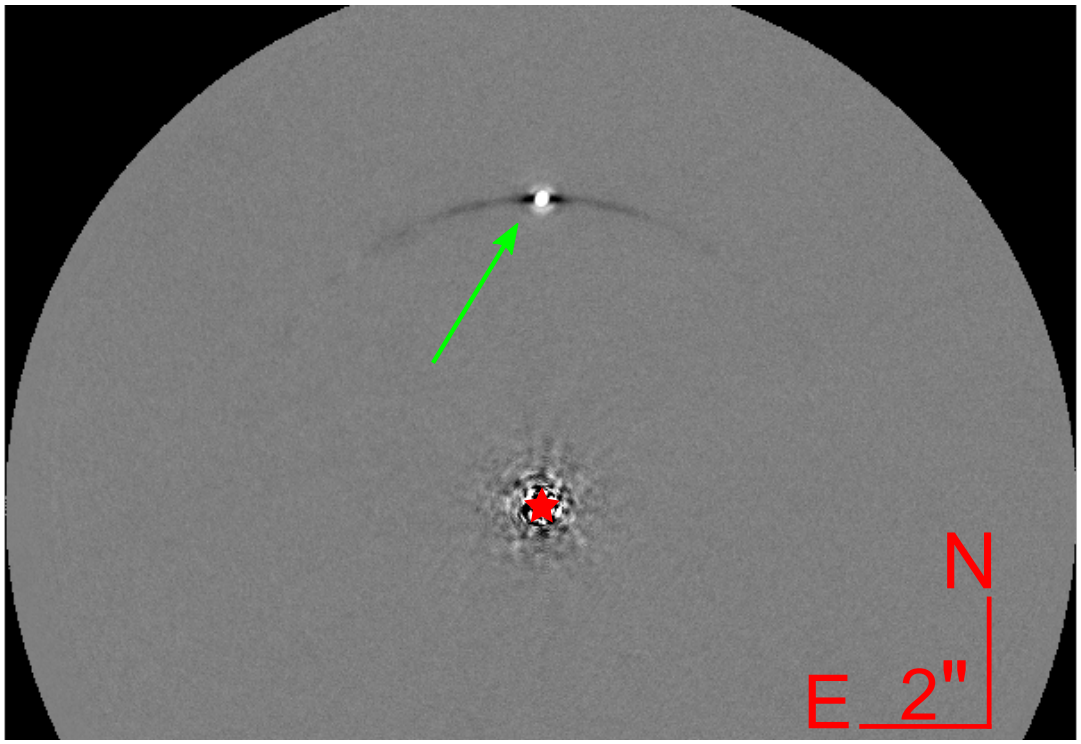

Figure 3.19: PCA reduced image of HD 98922 of the NaCo-ISPY observation taken on February 22nd, 2018

The data reduction for this archival data was done in the following way: From the nearest flats and darks I created a masterflat and masterdark images. I also created a BPM by 5-σ clipping the linear function which are fitted to the flatfield images for each pixel – after removing outliers in each pixel sequence. I then removed the dark, divided by the flatfield and replaced the bad pixels by the median of the four nearest good neighbors.

I then aligned the images by cutting an area around the star, upscaling it by a factor of 20 and cross correlating it to a randomly chosen, good frame. The aligned images are then median combined and relaigned to the median again.. To determine the positions of the CC and the stellar center, 2D-Gaussians are fitted. As a precision I assumed 2 px, which is a bit smaller than the FWHM of $\sim$2.5 px of the CC. As a pixel scale I used the official header value of 13.270 mas/px for the used S13 camera and assumed the true north was set correctly. The resulting images are shown in Fig. 3.20 and the positions of the CC are summarized in Table 3.9.

3.4.3 Common Proper Motion Analysis

When the source was observed in February 2018, the GAIA DR2 was not published yet and we did not think of it to become important for our analysis due to the typically very high contrast of the CC to the primary. Thus the PM analysis was done as usually. In Fig. 3.21a you can see the expected motion of the CC, if assuming the CC

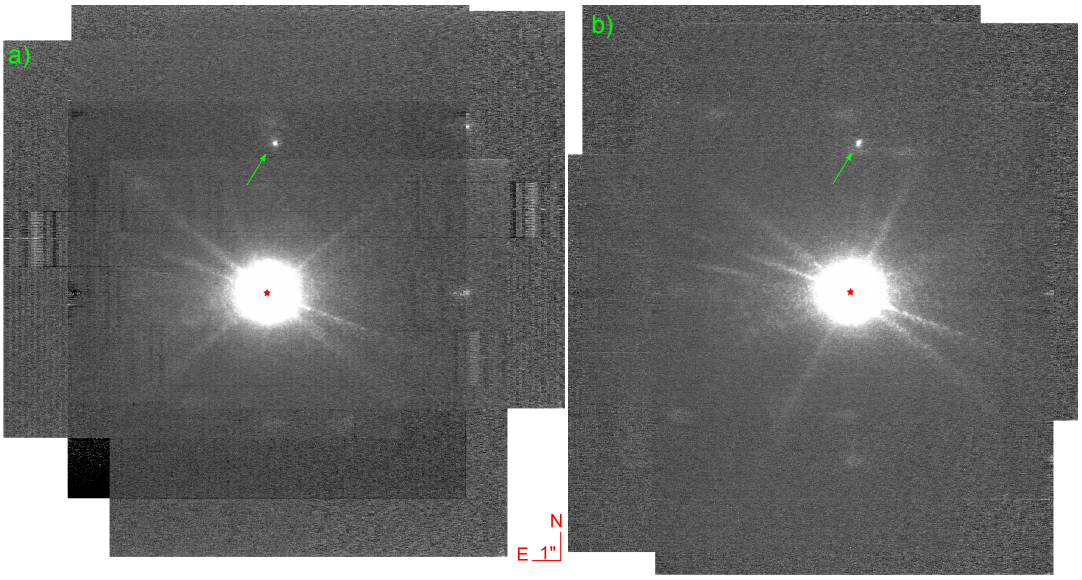

Figure 3.20: The archival, median combined NaCo images using the *NB_2.12* filter. The red stars denote the centers of the star, the green arrows the positions of the CC. a) From 2006-02-11 b) From 2006-02-27. North is up, east is left.

CC #	**Date** [yyyy-mm-dd]	Sep. [mas]	ΔSep. [mas]	PA [deg]	ΔPA [deg]	Filter
1	2006-02-11	5107	27	3.051	0.005	*NB_2.12*
1	2006-02-27	5103	27	3.065	0.005	*NB_2.12*
1	2018-02-22	4680	29	0.167	0.006	L'

Table 3.9: Positions and magnitudes of the identified foreground object in the NaCo-ISPY and archival data analyzed.

was a stationary BG object. Thus I tried to fit an orbit to this presumably BD object using imorbel[12] (Pearce et al., 2015). However, no stable solution was found.

After the release of GAIA DR2 in April 2018, the secondary source could be identified as GAIA-DR2 5348312633858300160 (I noted it was already in Gaia DR1 5348312633845243136, but with only the positional information). This source has a PM of pmRA*cos(DEC) $= 20.71 \pm 0.06$ mas/yr, pmDEC $= -35.68 \pm 0.05$ mas/yr. This is a faster motion than the one of HD 98922. This is plausible, since the distance is 304 ± 3 pc, and thus closer than HD 98922 with its 690 ± 16 pc. We thus have "discovered" a FG source. Unfortunately the age of this FG source is now unknown, and most likely much older than the 0.01 Myr Meeus et al. (2012) derived for HD 98922. Thus a first intuition that, due to its now even lower intrinsic brightness, it should be a free floating BD of even a free floating GP, cannot be confirmed. GAIA-DR2 gives its Temperature as 6000^{+1100}_{-600} K.

[12] http://drgmk.com/imorbel

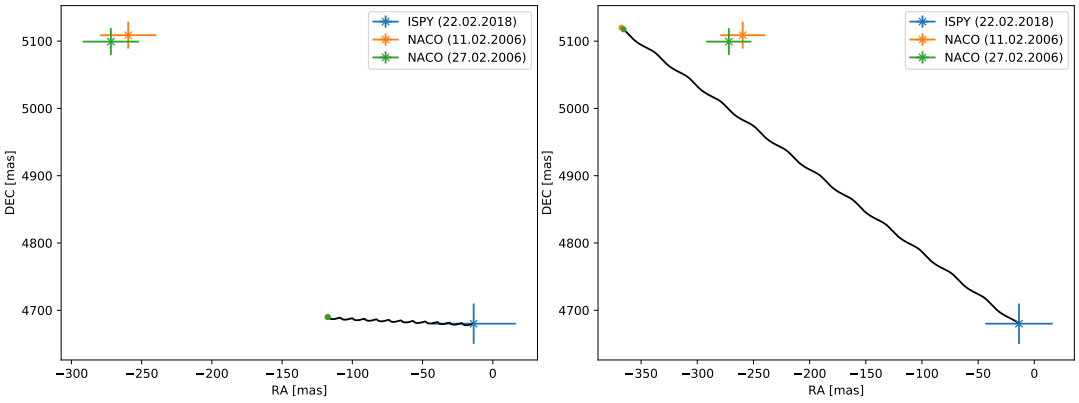

(a) (b)

Figure 3.21: Proper Motion (PM) analysis of HD 98922. The colored errorbars show the measured positions, the colored points the positions the Companion Candidate (CC) should have if a) only accounting for the PM of HD 98922 and b) accounting for the PM of HD 98922 and the CC (Gaia DR2 5348312633858300160). You can see that the measured positions are only roughly consistent with the measurements if accounting for the PM of the CC.

3.5 A background Object to HD 97048

3.5.1 Observations and Data Reduction

We observed the PPD star HD 97048 on May 2nd, 2016 and exactly one year later, on May 2nd 2017 with NaCo in L'. The field rotations were 68° and 48°, respectively. During the first epoch we discovered two CCs. Unfortunately the second run suffered from bad conditions, so neither of the two CCs is seen during the second epoch. You can find the positions and magnitudes of the CCs of the first run in Table 3.12.

In order to find out whether the CCs are bound, I queried the archives of NaCo[13], SPHERE[13] (Beuzit et al., 2008), FORS1[13] (Appenzeller et al., 1998), VISIR[13] (Lagage et al., 2004), NIRC2[14] (Xuan et al., 2018, e.g.), NICI[15] (Chun et al., 2008), GPI[15] (Macintosh et al., 2014), HiCIAO[16] (Suzuki et al., 2009), Hubble Space Telescope (HST)[17] and GAIA[18](Gaia Collaboration et al., 2016). Further I also searched the literature for more information. This is the standard approach are the standard archives queried by the NaCo-ISPY consortium if a CC is found.

Fortunately, due to its disk HD 97048 is a well studied system (e.g. van der Plas, G. et al. (2017) for ALMA data or Ginski et al. (2016) for SPHERE data). Thus I found a lot of archival data, where Table 3.11 lists the data which seemed promising and thus was analyzed in greater detail.

[13] http://archive.eso.org/eso/eso_archive_main.html
[14] https://koa.ipac.caltech.edu/cgi-bin/KOA/nph-KOAlogin
[15] https://archive.gemini.edu/searchform
[16] http://smoka.nao.ac.jp/fssearch.jsp
[17] http://hla.stsci.edu/hlaview.html
[18] https://gea.esac.esa.int/archive/

Property	Value	Reference
Identifiers	HD 97048, HIP 54413, TYC 9414–795–1	
	2MASS J11080329–7739174, CD–76 488	
SpT	A 0 V	Meeus et al. (2012)
Distance	185 ± 1.3 pc	Gaia Collaboration et al. (2018)
Age	6.5 ± 1 Myr	Meeus et al. (2012)
RA (ICRS)	11:08:03.318	Gaia Collaboration et al. (2018)
DEC (ICRS)	−77:39:17.490	Gaia Collaboration et al. (2018)
pmRA*cos(DEC)	-22.437 ± 0.061 mas/yr	Gaia Collaboration et al. (2018)
pmDEC	1.305 ± 0.059 mas/yr	Gaia Collaboration et al. (2018)
Luminosity	30.7 ± 6.1 $L_\odot$	Meeus et al. (2012)
Effective Temp.	6746 ± 200 K	Gaia Collaboration et al. (2018)
L' luminosity	4.47 ± 0.1 mag	WISE interpolated (Cutri et al., 2013)
I SPY priority	1	Reason: PPD
I SPY Group	PPD	

Table 3.10: Basic properties of HD 97048.

SPHERE reduction

The SPHERE polarimetric data was reduced by Matthias Samland using the official SPHERE DRP[10] (Möller-Nilsson et al., 2010). The resulting datacube was combined using cADI. More advanced algorithms like PCA require a full annulus visible in each frame and were not applicable here, because the CC "sits" in the corner of the detector. The outer CC cannot be seen at all due to the smaller FoV of SPHERE. The result is shown in Fig. 3.23 c).

HST Reduction

The HST observations were performed in RDI mode to observe the disk of this star under proposal ID 10425. The results of these observations and the disk detection are described in Doering et al. (2007). Unfortunately the images in this publication are cut and the only author who possessed the image (Ryan Doering) left astronomy, according to co-author Margaret Meixner. Thus I rewrote a RDI-pipeline, subtracting the reference star HD 80999 image from the target star HD 97048. The alignment of the images is done by upscaling the images by a factor 20 and then cross correlating them. Then I scaled the reference image such, that within within two FWHM of the PSF's radius, the enclosed flux is the same in both images. Fig. 3.22 shows the HST image of HD 97048 before and after the subtraction. The circle in the subtracted image marks the position of the inner CC, which, unfortunately, is not detected.

Instrument	Date	Filter ([µm])	Total exposure Time [min]
SPHERE	2016-02-21	K1+K2 (1.6 + 1.7)	90
NICI	2012-03-31	H20-Ice-L (3.9)	150
NICI	2012-03-31	L′ + CH4-H1S (1.6 + 3.8)	180
NICI	2012-04-01	H + K (2.2 + 1.7)	140
NaCo	2010-03-24	Ks (1.6)	40
NaCo	2010-03-25	Ks (1.6)	30
NaCo	2011-04-02	Ks (1.6)	70
VISIR	2005-06-19	PAH(4.8)	23
VISIR	2005-06-19	Q2 (18.7)	23
VISIR	2006-06-19	Q2 (18.7)	40
VISIR	2006-06-20	Q2 (18.7)	44
VISIR	2006-06-21	PAH2 (11.3)	35
VISIR	2006-06-22	PAH2 (11.3)	35
HST ACS/HRC	2005-07-16	F606W (0.6)	36.6

Table 3.11: Archival data analysed. The VISIR data does not show the Companion Candidates according to Dr. Wolfgang Brandner (priv. comm.). Also the archival NaCo data is not deep enough to show the Companion Candidates.

NICI Reduction

Since for NICI no official pipeline is available, I wrote my own pipeline to perform dark and sky subtraction, flat fielding, BPC, distortion correction and alignment of the images. The subtraction and flat fielding are standard procedures. For the BPC, a bad pixel mask was creating by finding 5-σ outliers in the flat field images. Bad pixels were corrected using the median of the four nearest, good neighbors. The distortion correction (including true north correction) follows the IDL-recipes provided in Hayward et al. (2014) for NICI. The alignment was done iteratively: First all images were upscaled by 20, cross correlated and shifted with respect to the the first image. Then the median of those images was taken and all images were cross correlated and shifted with respect to the median image. Finally the 70% best images were kept and used further. The best images were selected by the squared sum of the residuals, after the median was subtracted. The median of all remaining images was then subtracted from each image, the images were then derotated using Fast Fourier Transform (FFT) and median combined. This last step is know as classical Angular

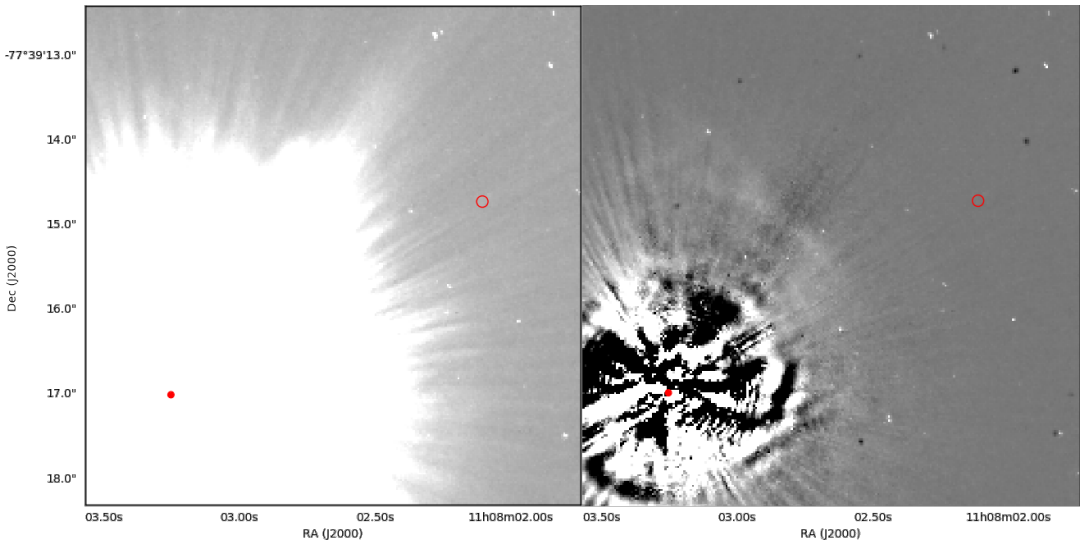

Figure 3.22: The HST image of HD 97048. The left image shows the image as taken from the Hubble Legacy Archive. The right shows the image with the scaled version of HD 80999 subtracted. The filled red dots mark the stellar centers and the red rings the position of the Companion Candidate as found in the NaCo-ISPY data. The dark points on the right images are background stars present in the reference image. The disk can be seen as in Doering et al. (2007), showing that the subtraction routing is performing well. North is up and east is left.

Differential Imaging (cADI) (e.g. Marois et al. (2006)). I also tried introducing protection angles and the PCA and LLSG (Local Low-rank plus Sparse plus Gaussian-noise decomposition) (Gomez Gonzalez, C. A. et al., 2016) algorithms provided by the Vortex Imaging Pipeline (VIP) pipeline (Gonzalez et al., 2017). However, since the CC is easily recovered using cADI and sits close to the corner and cADI has the biggest resulting FoV I stayed with cADI. The result is shown in Fig. 3.23.

3.5.2 Common Proper Motion Analysis

CC #	Date [yy-mm-dd]	Sep. [mas]	ΔSep. [mas]	PA [mas]	ΔPA [deg]	Mag [mag]	ΔMag [mag]	Filter µm
1	2016-05-02	4319	18	302.83	0.22	14.78	0.25	3.8
2	2016-05-02	6826	14	12.85	0.20	14.80	0.21	3.8
1	2012-04-01	4357	36	302.92	0.8	-	-	3.8
1	2016-02-20	4298	4.7	303.32	0.38	-	-	1.6
1	2016-02-20	4301	3.6	303.31	0.04	-	-	1.7

Table 3.12: Positions and magnitudes of the two identified Companion Candidates in the NaCo-ISPY and archival data analyzed. I used a platescale of 27.230 ± 0.07mas/px, and a true north of 0.59 ± 0.18 for the NaCo data. Further I used $L' = 4.47 \pm 0.1$ mag for HD 97048.

Since only the inner CC is visible in at least two epochs, we can only evaluate the common PM of this one companion. I used the GAIA-DR2 PM values for HD 97048 given in Table 3.10 and the NaCo-ISPY observation from 2016 as starting point. Fig. 3.25 shows that the NICI data rules out the possibility of a co-moving source. Thus no further analysis of the inner CC was done. To constrain the nature of the outer CC, a second epoch with NaCo or any other instrument with a large FoV would be necessary. But unfortunately neither of the CCs is visible in this second observation. But given the large separation of 6.63″, chances are very high this is a BG objects, and thus no third observation is scheduled. Still, the properties are listed in Table 3.12 for future analysis. The values for the out CC presented in this Table are derived using the same approach as for HD 58647, described in Sect. 3.3.2. The walkplot is omitted and the corresponding cornerplot shown in Fig. 3.24. For the NaCo-ISPY observations a platescale of 27.230 ± 0.07mas/px, and a true north of 0.59 ± 0.18 has been assumed.

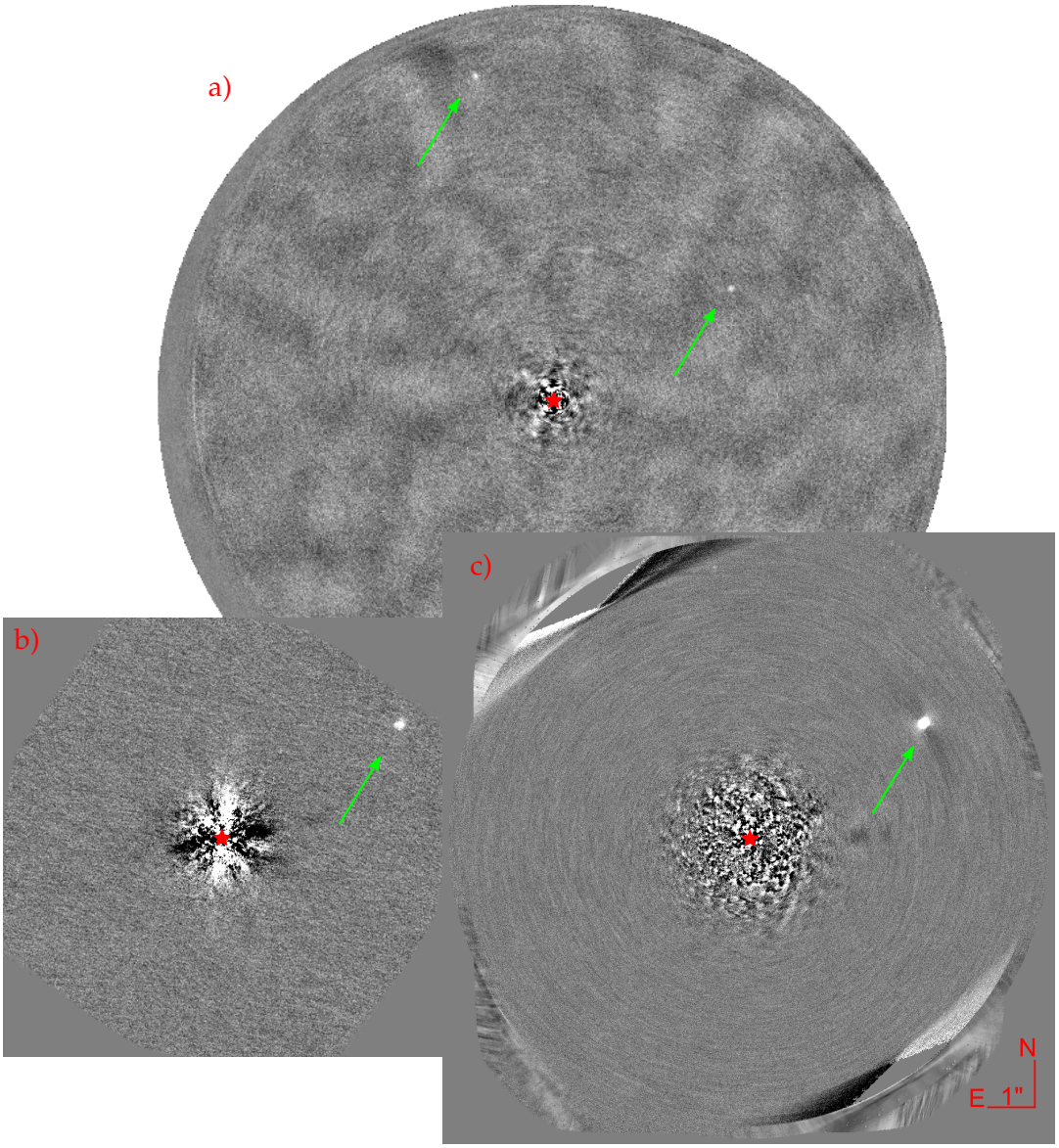

Figure 3.23: Images of HD 97048. a) PCA reduced NaCo-ISPY data from 2016. b) cADI reduced archival NICI data. c) cADI reduced archival SPHERE data in 1.6 µm. The Red stars denote the stellar centers, green arrows the positions of the CC. The scale is the same for bot images. The outer CC is outside the FoV of NICI and SPHERE and the inner one is only visible in the classical Angular Differential Imaging reductions.

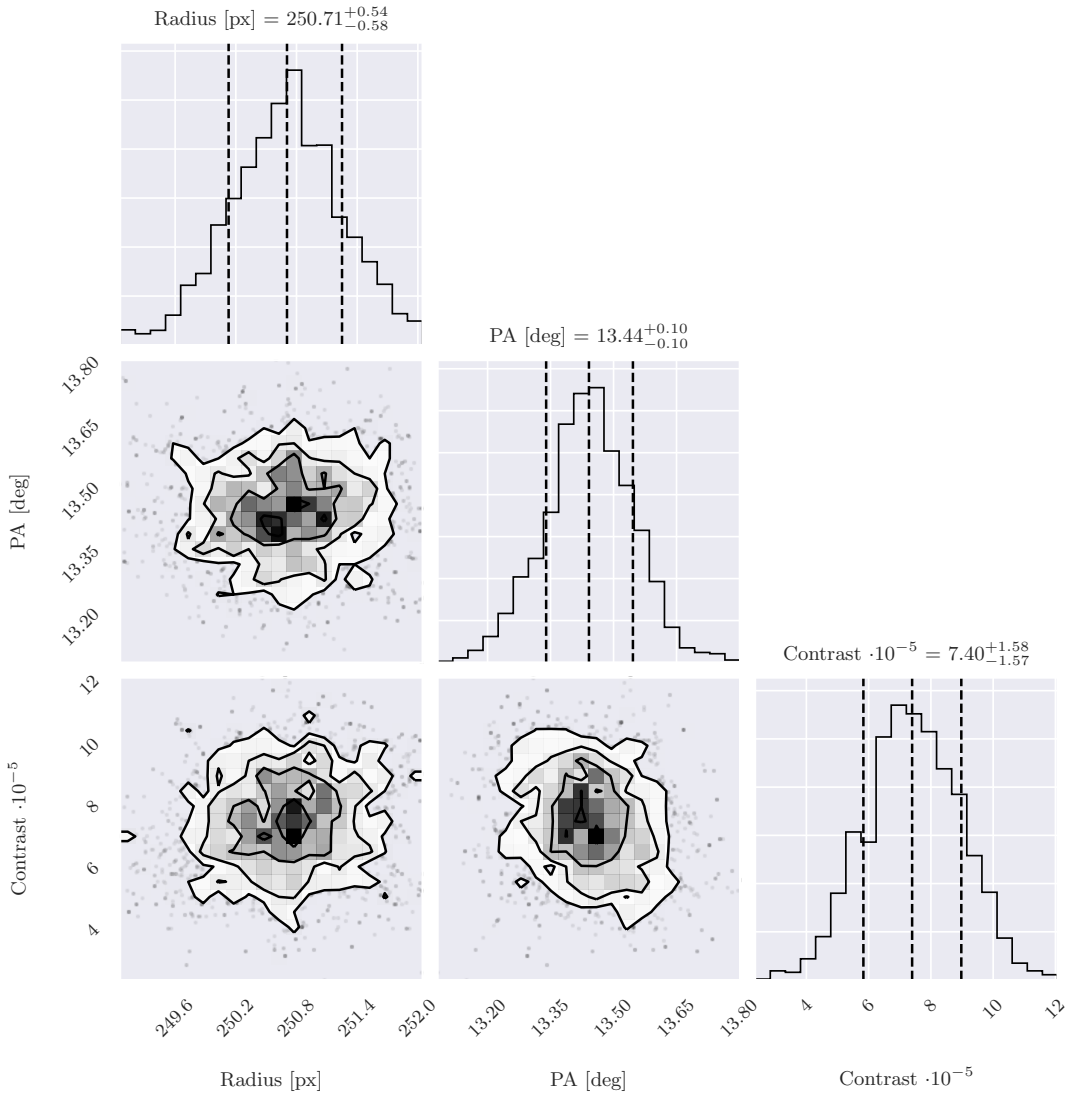

Figure 3.24: Cornerplot of the MCMC result of the outer CC around HD 97048.

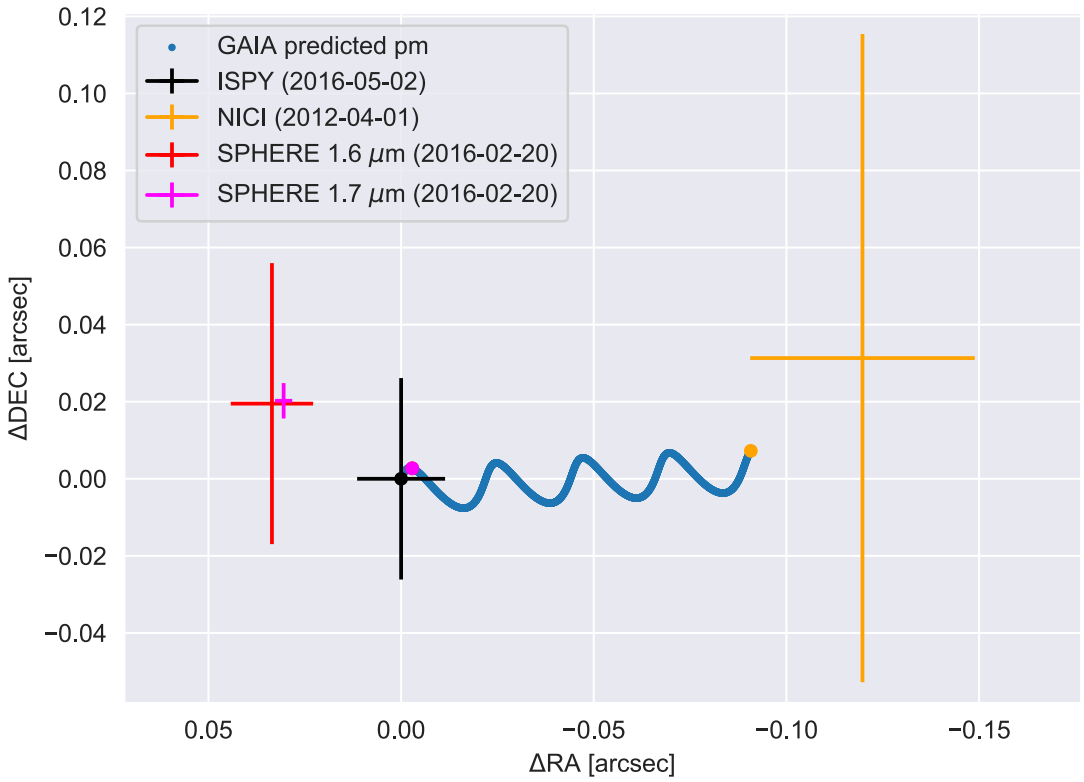

Figure 3.25: Proper Motion (PM) analysis for HD 97048. The errorbars denote the measured positions of the stars. The blue line shows the parallax plus PM of the Companion Candidate with respect to the NaCo-ISPY data, assuming it is a Background (BG) object. The colored points show the calculated positions of the epochs with respect to the NaCo-ISPY measurement.

Chapter 4

Radial Velocity Survey for Planets around Young stars

In addition to the NaCo Imaging Survey for Planets around Young stars (NaCo-ISPY) (see section 1.6.1), the idea arose to start a project searching also for closer-in planets around the same stars, but using Radial Velocity (RV) instead of Direct Imaging (DI). Thus in spring 2018, the first observations for the survey, now named Radial Velocity Survey for Planets around Young stars (RVSPY) with the FEROS instrument (Kaufer et al., 1999) at the MPG 2.2m telescope began.

The first section describes the motivation behind the project, section 4.2 the target selection and differences to the NaCo-ISPY targets. Section 4.3 describes the observing strategy and explains why we decided to focus on hot Jupiters. In Sect. 4.5 some early results are presented and briefly discussed.

4.1 Motivation and Previous Work

The basic idea behind the RVSPY project is quite simple: While DI is sensitive to far out planets with large periods, RV is best at finding planets close to their host stars. Thus, if one wanted to fully characterize a planetary system, those techniques perfectly complement each other to achieve this goal. Thus in principle one could fully characterize the system.

Unfortunately there is a big drawback: DI works best around young stars, where the planets are still hot from the formation process. The RV signal on the other hand is then dominated by the strong stellar activity those young stars have (e.g. Kjeldsen & Bedding (1995) and Chapt. 5). This is the reason why neither Weise (2010) nor Mohler-Fischer (2013) were able to find any planet when searching for them around young stars. And this is the reason why RVSPY together with NaCo-ISPY are the first surveys trying to achieve this goal. In fact after the analysis of the data (Chapt. 9 in Mohler-Fischer, 2013), Mohler-Fischer discussed what should be changed in future RV surveys focussing on young stars. Except for getting more and better data, she was not conclusive at all, since all indicators also have draw backs: E.g. if one selects stars with low $v \sin i$, one might get less active stars – but also gets biased

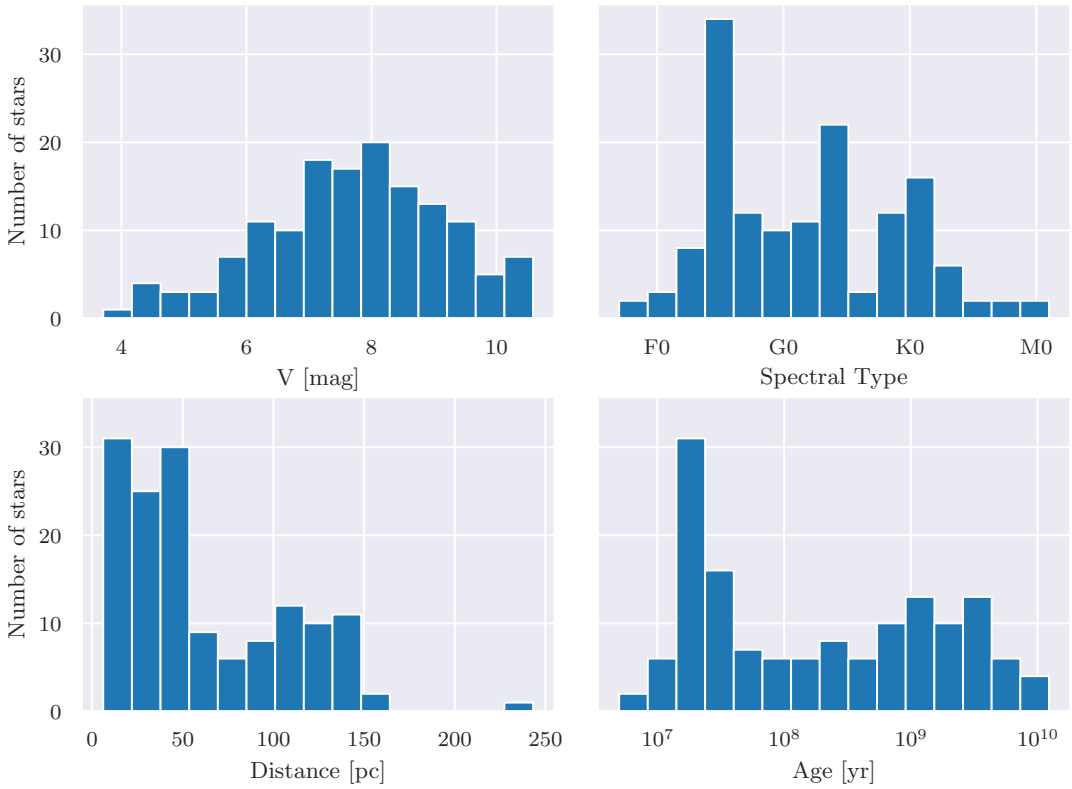

Figure 4.1: Key histograms of the 145 stars of the RVSPY targets. Even though it was no direct selection criterion, the stars are all relatively close ($\lesssim$ 150 pc). This is due to the magnitude limit and the fact that distance is a strong selection creterion in NaCo-ISPY, which is the basis of our target selection. Even though the stars are still quite young for RV surveys, we removed very young ($\lesssim$ 5 Myr) stars and addet older stars. One of the lessons learned from the survey lead by Mohler-Fischer (2013) and Weise, P. et al. (2010) as well as the stellar activity described in Chap. 5.

towards more inclined planetary systems. This is because for stars below a temperature of $\sim$ 6100 K, and thus the prime targets of RV surveys, the obliquity between star and planets seems to be close to zero (Winn & Fabrycky, 2015). Or selecting stars with a known photometric period might help to determine the rotation period and to distinguish stellar rotational effects from planetary lineshifts. However, if the stars are photometric variables, they probably are more active in general which complicates things again.

Having those complications in mind, it was decided that the potential win is worth some effort. Still we did not start the survey blindly, but adapted the target selection and the observations strategy accordingly by looking for hot Jupiters with strong RV (up to few 100 m/s) signals and excluding too young ($\lesssim$ 5 Myr) stars.

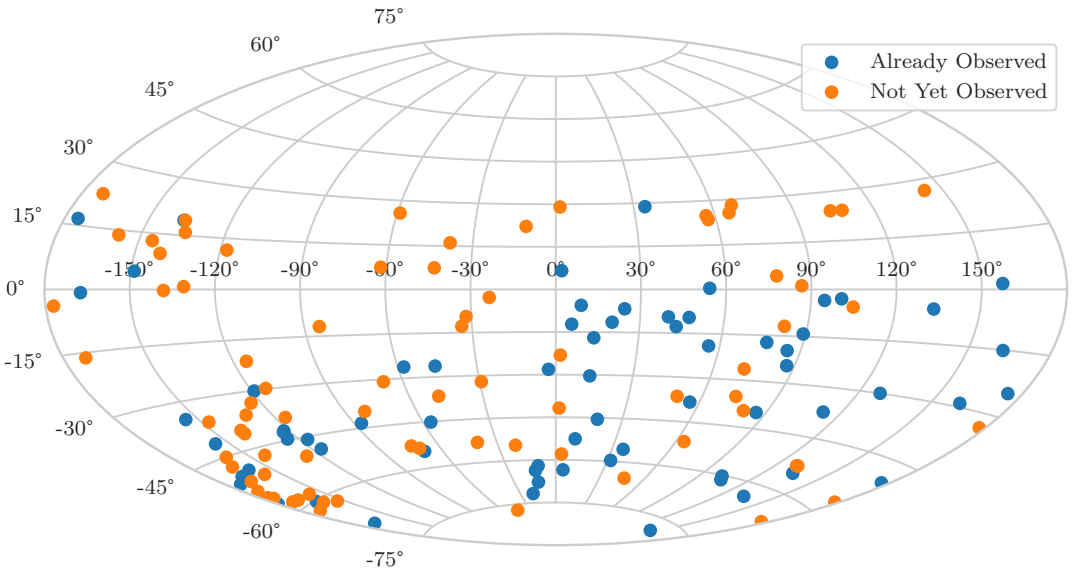

Figure 4.2: Sky distribution of the 145 stars part of the input catalog in the AITOFF projection. Color coded are the stars observed as of march 2019. One can see that a equal distribution in right ascension could be achieve, which is necessary for our observing plan of alternating observing times each night briefly described in Sec. 4.3.2.

4.2 Target Selection

As written in the previous section, the main challenge when working with young stars is to distinguish the planetary signals from the large stellar activity induced signals. This increase of stellar noise with youth has been shown in many different ways. Some examples are Meibom et al. (2015) using the $(B-V)_0$ photometric color index, Meléndez et al. (2016) using the $\mathrm{Log}R'_{HK}$ activity indicator or Booth et al. (2017) using the X-ray emission density of the star. Another study determining the age-lag-activity dependence is described in chapter 5. The main results in the latter are an extremely steep dependence of RV noise on age and an increase of stellar noise by about a factor of two when searching for signals of a few days period compared to those with a few weeks or months around young stars. In addition the planet's signal strength K increases like $K \propto P^{-\frac{1}{3}}$ towards shorter periods P. The consequences are to search for massive, short periodic planets, hot Jupiters around not too young ($\gtrsim$ 5 Myr) stars.

As explained in the motivation 4.1, it is not clear how to handle fast rotators. E.g. Saar et al. (1998, Fig. 2) or Gray (1999, Fig. 6) show how the achievable RV precision decreases with $v \sin i$. Lovis & Fischer (2010) describe the precision scales as Full Width Half Maximum (FWHM)$^{3/2}$ and since FWHM $\propto v \sin i$, it scales as $(v \sin i)^{3/2}$. They claim e.g. with $v \sin i \approx 25\,\mathrm{km\,s^{-1}}$, the achievable RV precision is $\approx 100\,\mathrm{m\,s^{-1}}$. Using CERES and ZASPE, we measured the formal RV error as function of $v \sin i$ for 145 stars of our sample, see Fig. 4.3. Based on this analysis and our requirement of a precision of about $50\,\mathrm{m\,s^{-1}}$, we discard stars with $v \sin i > 40\,\mathrm{km\,s^{-1}}$. The trade off is that this might bias us towards systems with low inclination.

Another limiting factor when finding planets is the Spectral Type (SpT). For stars earlier than about F5 ($T_{\rm eff} \gtrsim 7,000$ K) , the number of spectral lines decreases drastically in the visible and Near InfraRed (NIR). Since on first order the total RV precision depends on the square root of the number of lines present (compare Eq. (1.12), this leads to a drastic decrease in the overall achievable RV precision. We thus applied a soft cut for stars earlier than spectral type F5. Similarly, for very cool stars ($T_{\rm eff} \lesssim 3500$ K or SpT later than M3) where complex molecules are present, the spectral lines become densely packed so it is difficult to identify individual lines on which to measure the RV shifts (Lovis & Fischer, 2010). This again decreases the achievable RV precision. We thus did not include stars later than M3.

In order to keep integration times on FEROS short ($\lesssim 10$ min) and still get a Signal to Noise Ratio (SNR) of at least 100, no stars dimmer dimmer than $V = 10.5$ mag are considered in the survey.

Then the archives were searched, and stars excluded with too many ($\geq$ 120) already existing HARPS or FEROS observations. If more than 10 but less than 120 observations were found, it was decided case by case, dependent on the spacing of those observations. Observations with similar high cadence observations as ours (about one spectrum per day, see Sect. 4.3) were removed from the input target catalog. In order to facilitate this task, I created a plot for each star showing the spacing and integration times of the archival data, see Fig. 4.4

Now ideally one would like imaging and RV data of the very same star. Thus RVSPY focuses on stars of the NaCo-ISPY input list which either have already been observed or are high priority targets (priority 1 and 2) of NaCo-ISPY. In order to enlarge the survey, we extended the input list with targets similar to the NaCo-ISPY input catalog by replacing the constraint on the detectability as a complex function of distance, age and contrast, by a constraint on the apparent magnitude and the age cut only. The details about the selection of NaCo-ISPY are explained in section 1.6.1, but in short: Debris disk hosting star (DEB) from the Chen et al. (2014) catalog showing a significant InfraRed (IR) excess, meaning $L_{\rm IR}/L_* > 3 \times 10^{-6}$. They were then prioritized in order to maximize the physical detection space, e.g. prefer close over distant stars for simple geometric reasons. Since those geometric reasons do not apply to RV searches, the criteria were altered. Due to the alterations, more targets from Chen et al. (2014) and additionally from Cotten & Song (2016) were added to the target list. After all the selection criteria, with the exception of the $v \sin i$ criterion where the value is not a-priori known, were applied, we were left with 145 stars, as of March 2019. Their basic properties are shown in Fig. 4.1. A relatively equal sky distribution is needed to allow for the high cadence observing strategy throughout the year, see Sect. 4.3. Continuously taking test spectra of the stars without archival data to determine the $v \sin i$and the achievable precision, we are currently left with 113 stars which do fulfill all selection criteria. 102 of those are from Chen et al. (2014) and 11 are from Cotten & Song (2016). However, the final target selection is not fully completed yet and might be subject to small alterations, e.g. due to further test

spectra. For the final target list and more details, e.g. the names and properties of individual stars, I therefore refer to Zakhozhay 2019 (in prep.).

In summary. the selection criteria are:

- Accessible with FEROS: DEC < 30 deg
- Older than ~ 5 Myr
- Spectral type F5-M3
- $V < 10.5$ mag
- $v \sin i \leq 40$ km/s
- Less than 120 archival datasets
- Manual selection for 10 to 119 archival datasets
- Significant IR excess (selection criterion of the NaCo-ISPY survey)
- No known binary in the Washington Double Star catalog (WDS) (Mason et al., 2001) with less than about 2″ separation

4.3 Observing Strategy

4.3.1 Feasibility Study

As explained before and in more detail in Chapt. 5, finding planets around young stars using the RV technique is extremely challenging due to the high intrinsic stellar activity. Thus, a lot of discussions were made, how to optimize the observation strategy. Two options were discussed: Looking for planets with periods up to a few years or optimize the survey for hot Jupiters. The first approach tries to really "connect" the detection space of RV and DI. For RVSPY this would mean to search for planets with periods of up to a multiple years/semi major axis of at least a few AU. As explained in the motivation, this would certainly be a huge step in exoplanet sciences, since it would allow to fully characterize planetary systems and their planet occurrence rates above a certain mass threshold. Especially since most targets are young, we could put constraints on the migration timescales or formation regions. However, knowing that this is very challenging, Ralf Launhardt and me worked on simulating the feasibility of such a survey strategy: Since Ralf already developed a a Marcov Chain Monte Carlo (MCMC) based tool for NaCo-ISPY, he extended it for the capability to also simulate RV detection rates. The MCMC simulator requires two basic inputs: The planet occurrence rate and the detection completeness, both as functions of planetary mass and semi-major axis. The used occurrence rates of planets and Brown Dwarfs (BDs) are based on those given by Reggiani et al. (2016), and normalized by Galicher et al. (2016). Note that they do not have any pile up

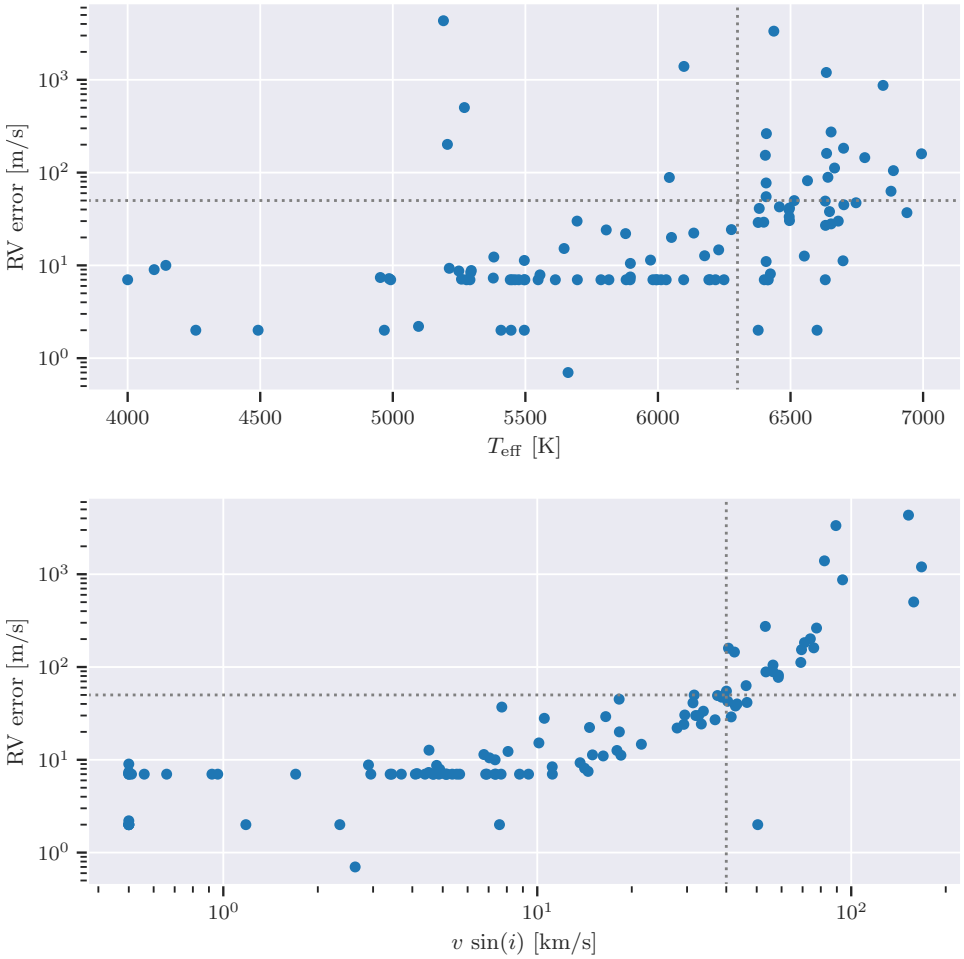

Figure 4.3: Dependence of RV precision on $T_{\rm eff}$ (top) and $v \sin i$ (bottom) for the 145 targets from the RVSPY target catalog. The RV error is the formal measurement uncertainty returned by CERES, whereas $T_{\rm eff}$ and $v \sin i$ are returned by ZASPE. The vertical dashed lines represent the soft cuts of 6300 K ($\sim$ SpT F5, top) and 40 km/s (bottom) applied to the target lists in order to achieve a precision of at least 50 m/s (horizontal dashed lines). The plateaus at 7 m/s and 1 m/s RV error are due to hardcoded limits in the CERES pipeline. We are currently discussing how we should handle them, e.g. if we should just remove the hard limit.

Taken from Zakhozhay et al. (in prep.)

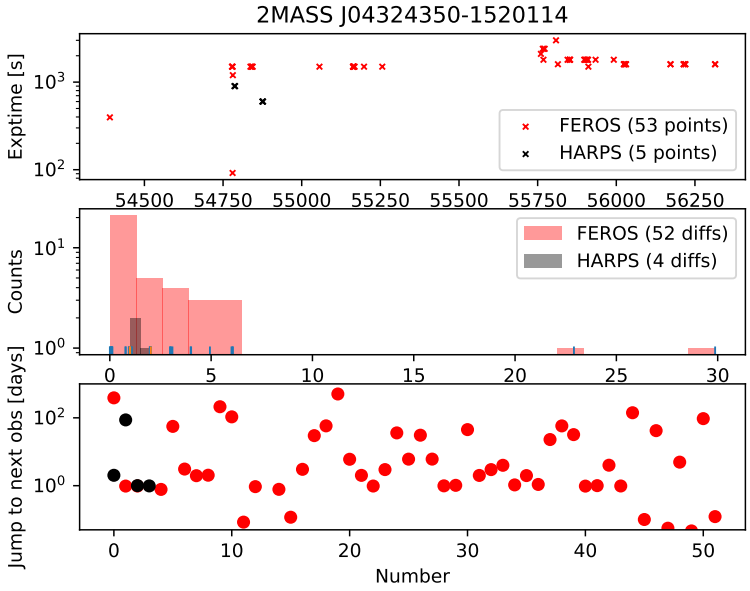

Figure 4.4: Example plot for 2MASS J04324350–1520114 as I created for every star in the input catalog. It gives an overview of the distribution of the observations. Black are HAPRS, red FEROS observations. The top panel shows a classic Barycentric Julian Date (BJD) plot with the exposuretime on the y-Axis. The central panel gives a histogram of the gaps between observations. The bottom panel shows the gap length (in days) between the observations, sorted as they were taken. Since this example has a lot of data taken on (almost) consecutive nights, it was not scheduled for further observations. However, it will still analyzed in a later stage.

of hot Jupiters included (see Fig. 4.5 left), which seems to be real (e.g. Seager et al., 2010). Thus more detections with short periodic planets might be possible. Then we needed the NaCo-ISPY detection limit, which is calculated routinely for each observation as a function of luminosity and projected separation. With the newest BT-settl models (Allard, 2014) and the distance measured by Gaia Data Release 2 (GAIA-DR2) (Gaia Collaboration et al., 2016, 2018), those can be converted a mass and physical separation threshold. Since at that time there were no RVSPY observations yet, we used the detection limits given by Mohler-Fischer (2013) in Table 4.4 she computed using fake RV signal injection. Her RV survey was a continuation and deeper analysis of the survey started by Patrick Weise and is described in Weise, P. et al. (2010)[1].

Now we had all the input parameters. We then simulated 100,000 combined NaCo-ISPY and RVSPY surveys, where the planets were randomly generated according to the assumed planet occurrence rate and random orbital orientations and phases. We also assumed to observe 158 stars with NaCo-ISPY and 111 of those with RVSPY. Those numbers were the sizes of the target catalogs at the time the

[1]We used this RV survey as a reference, since it also used the FEROS instrument and focused on young stars typically younger than 10 Myr

Survey	Planets	Brown Dwarfs
NaCo-ISPY	1.8 ± 1.3	3.9 ± 1.8
RVSPY	0.4 ± 0.6	0.4 ± 0.6

Table 4.1: Results of the MCMC simulation of the expected outcome of the two exoplanet hunting surveys described in Sect. 4.3.1. Especially for RVSPY, it was clear we had to adapt the observing strategy and we could not overlap the detection spaces from RV and DI.

analysis was performed in late 2017. The results are visualized in Fig. 4.5 and the key numbers are given in Table 4.1. According to this simulation RVSPY would find only 0.4 ± 0.6 Planets – a very discouraging result and the reason that RVSPY mainly gave up on "connecting" the RV and DI detection space.

4.3.2 Conclusion

The feasibility study presented in the previous section shows that an overlap of both detection methods, RV and DI, can currently not be achieved. We thus decided to maximize the detection rate of RVSPY. As for short periodic planets the RV signal K is significantly stronger ($K \propto P^{-\frac{1}{3}}$, P is the Period of the companion) and additionally the stellar noise is reduced by rouhly two (see chapter 5), we decided to focus on hot Jupiters. This means we try to get at least one spectrum per night for about 10 days. In order to minimize the one day aliasing, it is tried to observe the star at a different time during each night. Additionally we add one night of three observations or two nights of two observations for each target to further suppress aliasing and gain sensitivity for planets with periods below about two days. We call this high cadence observations. As aforementioned this observing strategy, a possibly homogeneous distribution of the targets is necessary. Otherwise swapping the time cannot be done properly if e.g. all targets are observable only towards the end of the night.

We deviate from this mode for potential follow ups where we suspect a longer periodic signal, or to get one test spectrum to derive the $v \sin i$ and then decide whether we want to keep or remove that target, as described in the target selection, Sect. 4.2 where we put a limit of $v \sin i \lesssim 40$ km/s.

4.4 Data Reduction

In order to reduce all data including the archival data, I created a small python 3 based tool that automatically downloads and sorts all the science files and needed calibration files for a given list of targets. The output is done in a way so the files can be directly reduced with the CERES (Brahm et al., 2017) pipeline to return RV data. This section is dedicated to explain the main features of the tool, as well as explain how to use it, since it is also meant for other scientists that need to download and reduce data from FEROS. Due to its modular design, it is also possible to extend it

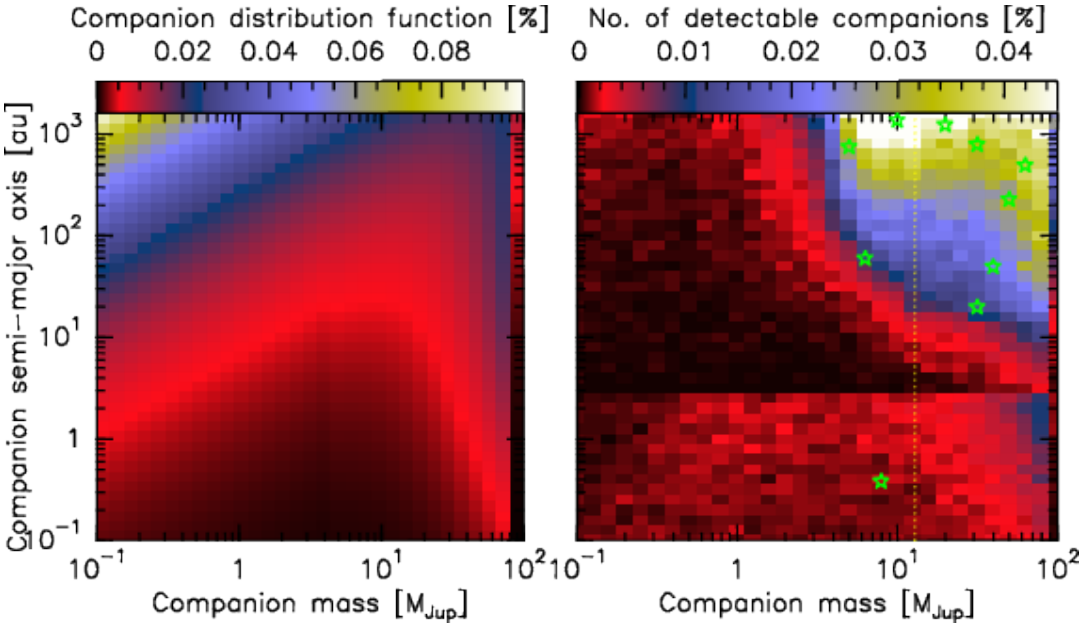

Figure 4.5: *Left*: Occurrence rates of companions as given in Reggiani et al. (2016) and normalized using Galicher et al. (2016) as used for the MCMC simulation. *Right*: Outcome of the simulation, where black means very unlikely detection and white means likely detection. The green stars denote the result of one typical simulation, the vertical dashed line marks the 13 M_{Jup}limit. The absolute values are defined such, that the integral along mass and semi-major axis returns the total number of found companions. This integral is equal to the expected number of 6.5 found companions for both surveys combined.

relatively easy to any other ESO instrument, where the main work is to modify the calibration module, that checks and downloads the calibration files for a given night. The code is publicly available on github[2].

The main function to call is `down_reduce.py`. It has two functions: `download` and `reduce`. The `reduce` function is basically a wrapper for CERES, which handles the files structure with optional, self-explanatory keywords to pass to it or to edit in the below mentioned `config.py` file. The only additional feature worth mentioning is the automatized selection of the binary mask and the Proper Motion (PM) used for the CERES pipeline based on the default values returned by SIMBAD for the respective target. The binary masks selected for the automatic selection are:

- M2 for stars of SpT M0 or later
- K5 for stars of later than K0 but earlier than M0
- G2 for any earlier star (this is also the default mask of CERES, if nothing else is selected)

[2] `https://github.com/sbrems/FEROS`. This module requires the modules `starclass` and `misc`, bot also openly available on my github.

Alternatively one can manually provide the input file for CERES (referred to as `reffile` in the CERES manual), where the parameters of the mask to use, the coordinates, the PM and the $v \sin i$ have to be given. For science results it is mandatory to check if the automatic determination was appropriate and provide the file with the proper parameters else. I refer to the the CERES quick start tutorial[3] for more information about this configuration file file.

The `download` method has one keyword (`store_pwd`), which sets if your ESO password shall be stored or not. Apart from that there is a list called `targets` which needs to hold the targets to download. Additional parameters are set in the config-file. Those parameters are e.g. the ESO username, the folders where to save and if and how to organize the data (e.g. sort targets in different folders) and the logs, the `query_radius` as well as an optional earliest date (`default_startdate`) of which files should be downloaded. Also here the names and the comments in the `config.py` file are self-explanatory.

Process overview The first step of the routine is to query the ESO archive for SCIENCE files for the selected target, instrument and in the selected date range. The target is resolved using SIMBAD (Wenger et al., 2000). Since often the target names are not set properly in the data archives, querying by coordinates is the only useful way to perform this task. Therefore the `query_radius` has to be selected such that only the right targets are found, but still all observations are within the `query_radius`. For FEROS 8′ have proven as a good value and are the default. But it needs to be checked later manually that the downloaded files indeed correspond to the required target.

Afterwards all nights are collected in which science data is present. For each night the calibration files are collected by calling the `get_calib` routine for each night. Here it is checked, that for FEROS at least 5 `BIAS`, 10 `FLAT` and 6 or 12 `WAVE_CALIB` files have been taken, either at the afternoon before, or the morning after the observation. The standard daily calibration creates those files every day as as consecutive files. And in most cases those files are present. The routine is robust against multiple, even aborted calibration sequences, as long as one sequence has finished with the standard output, meaning those 21 or 27 files were created consecutively. However, sometimes it happens that before and after the night the calibrations fail and no full, consecutive calibration set is present. If this happens, no calibration data will be downloaded and the routine will just continue with the next night. The nights where no calibration data was downloaded will be written in the `log_dir` in the file `failed_calib.txt`. This file is never deleted automatically, but the dates are always appended, additionally noting the date of the query as well as the target that required this calibration data is written to avoid later confusion. How to proceed with those nights, is up to the user. We noted that often a large part of the calibration had been finished and only a few files are missing, so that one can

[3] https://github.com/rabrahm/ceres

still use those. If, however, this is not the case, another alternative is to take other calibration data closest in time or to discard the data.

So far no data has been downloaded, but only the ESO file-IDs collected that are needed. Thus the next step is to download all the data. Therefore the ESO-login is required, also to access proprietary data. Proprietary data that could not be downloaded will be stored in the `log_dir` under `failed_download.txt`. Stored is which file (ESO-ID containing date and time) could not be downloaded, and when this happened and for which target. The files are downloaded into the `astroquery_dir`, which should contain sufficient space, even though the data is stored only in compressed form in this directory.

Finally the files are copied to the `default_science_dir` and by default distributed into folders sorted by date only. Note that the files are not sorted by target by default, since this would require the calibration files of one night to be stored multiple times if multiple targets of this night are present. Also the CERES pipeline would need to perform the analysis of the calibration files for each target. Since this takes several hours ($\sim$ 3 h) on multiple ($\sim$ 5) cores for each night, one might want to run this not more often than necessary.

4.5 Early Results

RVSPY is a quite young and still ongoing survey and most of the work has been dedicated in the observations and target selection so far. Still some early data analysis was performed for all the targets and four examples are presented here. Besides parameters to characterize the star (such as $v \sin i$ or $T_{\rm eff}$), the analysis so far consists of: a) Archival data search b) Extraction of all RV values c) Generating a Generalized Lomb Scargle diagram (GLS) diagram which is scanning for significant sinusoidal signals in the RV data (VanderPlas, 2017; Zechmeister & Kürster, 2018) d) Looking for correlations between the Bisector Span (BIS) and RV value as both are returned by CERES (Brahm et al., 2017). Based on this analysis, so far (March 2019) five stars have been selected for follow up observations with many more candidates. In the following, four examples are presented of the different cases encountered during the analysis, where for the nomenclature the internal numbering "RVSPY N" is used for the $N^{\rm th}$ star.

RVSPY 36 shows signs of a periodic signal with a period of about 10 days and a semi amplitude of about 300 m/s. It has a false alarm probability of about 0.02 and therefore is a good example for what RVSPY is looking for. However, the BIS shows a clear correlation with RV. The origin of this correlation is unknown, since star spots (all: cold and hot, optically thin and thick) would cause an anticorrelation as seen in the case of RVSPY 51. Investigation is ongoing, including analysis of other activity indicators and correlations with those.

RVSPY 51 has a very significant period of 2 days. The Cross Correlation Function (CCF) does not show anything peculiar. However, the BIS span clearly anticorrelates with RV, making this a textbook example for variation a stellar spot induces.

RVSPY 69 represents most of our targets. No significant periodic signal has been found by the GLS. The spread of the RV data points is larger than expected based on the formal error bars representing the measurement precision. This hints towards stellar activity. Since the precise origin is unknown, the overshoot in stellar activity is simply referred to as stellar jitter.

RVSPY 80 is a clear case of a spectroscopic (close) binary of similar brightness. This certainty comes from the CCF, showing peaks at different RV values (spectroscopic binary). The time series of the CCF is shown in Fig. B.1 confirms this suspicion and also explains the jump: At the beginning three older datasets with no counterpart in Fig. 4.9 show a similar RV resulting in a double peaked CCF and the huge BIS. Then, around Barycentric Julian Date (BJD) 2358330 the two stars are most aligned with respect to our line of sight (opposition). Afterwards the two peaks in the CCF start to separate again and from BJD 2458339 the RV signals are so far apart, that CERES only fits one of the peaks, resulting in the jump seen in the RV data. Since the CCFs around Julian Date (JD)$\approx$ 2458251 and JD$\approx$ 2458337 cover the system in the same phase, the period of the binary can already be estimated to be around $\sim$ 86 days. However, further analyzes is needed.

In order to analyze this data, a first quick step would be to fit two gaussians to the CCF instead of one to get the RV signals of both of the stars. Keplerian fits should then already give a good hint about the orbit of the binary system. To increase precision, second step would then be to correlate the spectrum not with one binary mask, but with two binary masks simultaneously. Finally, to further characterize the stellar companions, e.g. determine their SpT/$T_{\rm eff}$, log$g$, metallicity and mass, the spectrum needs to be analyzed similar to what ZASPE does, but by analyzing both stars simultaneously. Here it might help that the RV of both components has been determined before. With this the total mass of the system can be determined and therewith the orbit constrained further. This can then be used to analyze the effects of the binary on the disk of the system, similar to (e.g. Müller, A. et al., 2018, Musso Barcucci, accepted).

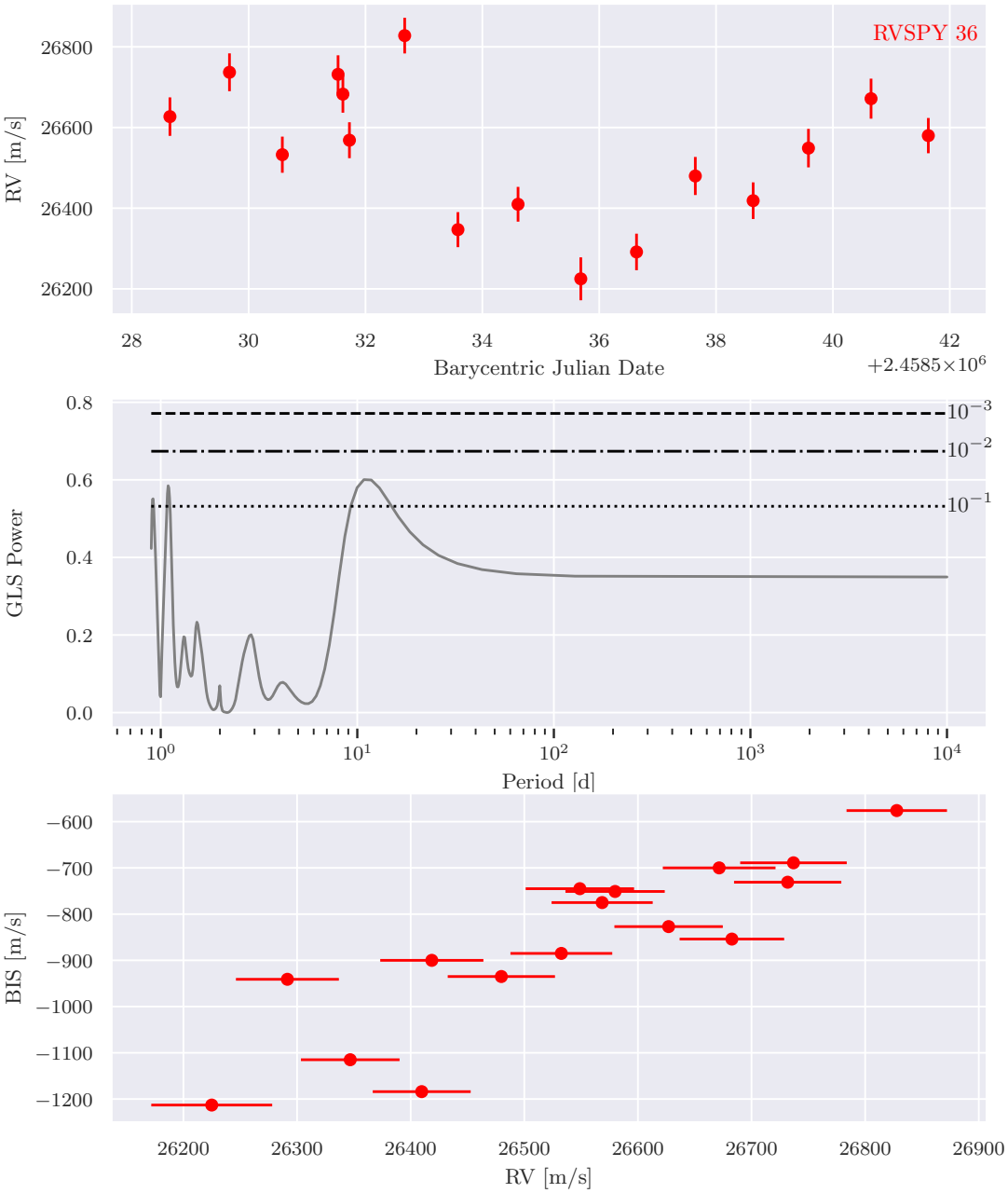

Figure 4.6: Analysis of the radial velocity and bisector span of RVSPY 36. The RV curve shows a sinusoidal signal with a period of about 10 days, which has also been picked up by the GLS diagram (center) with a of about 0.02 (dashed and dotted horizontal lines). The origin of the correlation of the points is unknown and will be investigated.

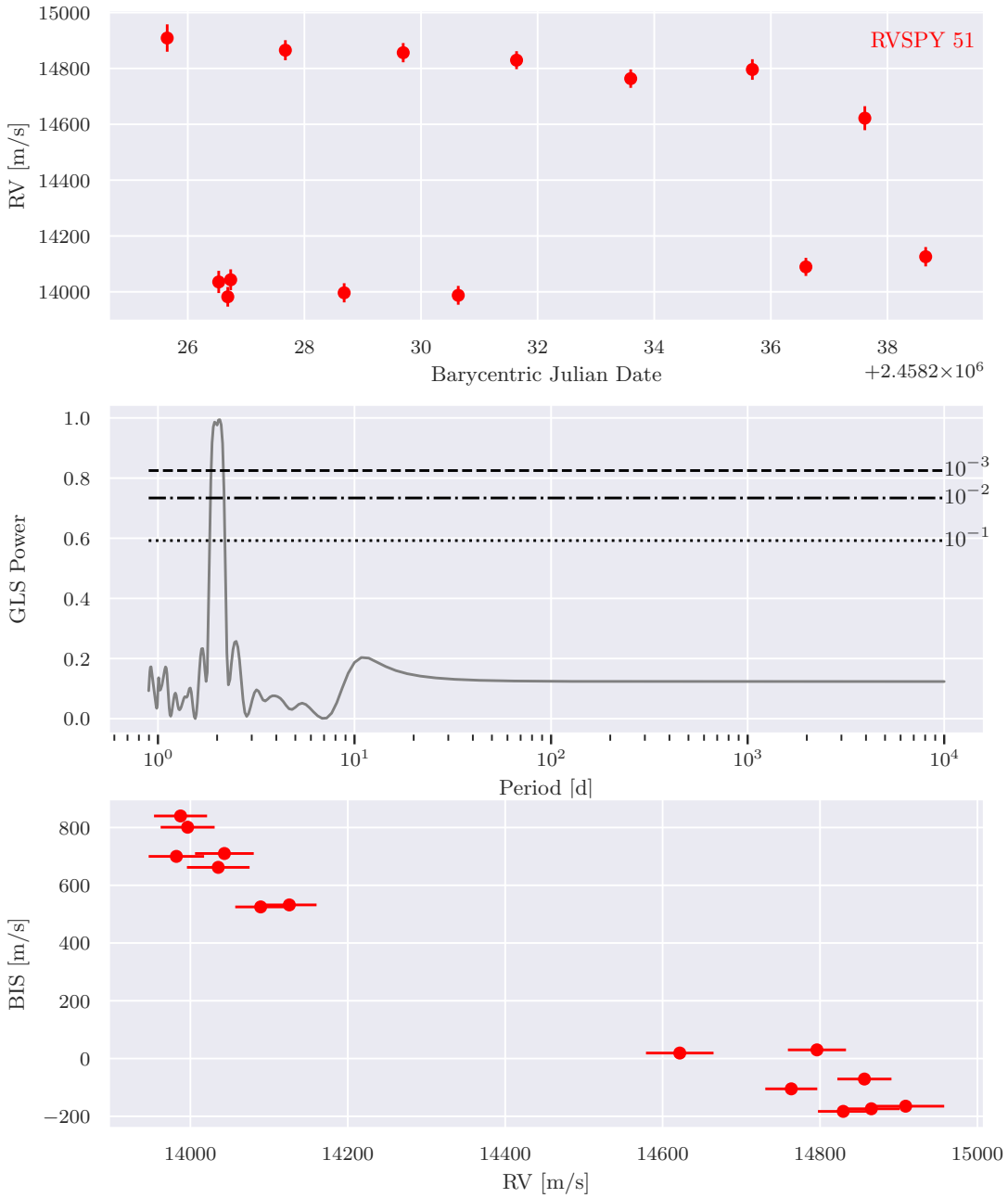

Figure 4.7: Same as Fig. 4.6, but for RVSPY 51. The periodic signal of about two days is very likely caused by a stellar spot, since the BIS clearly anticorrelates with the RV.

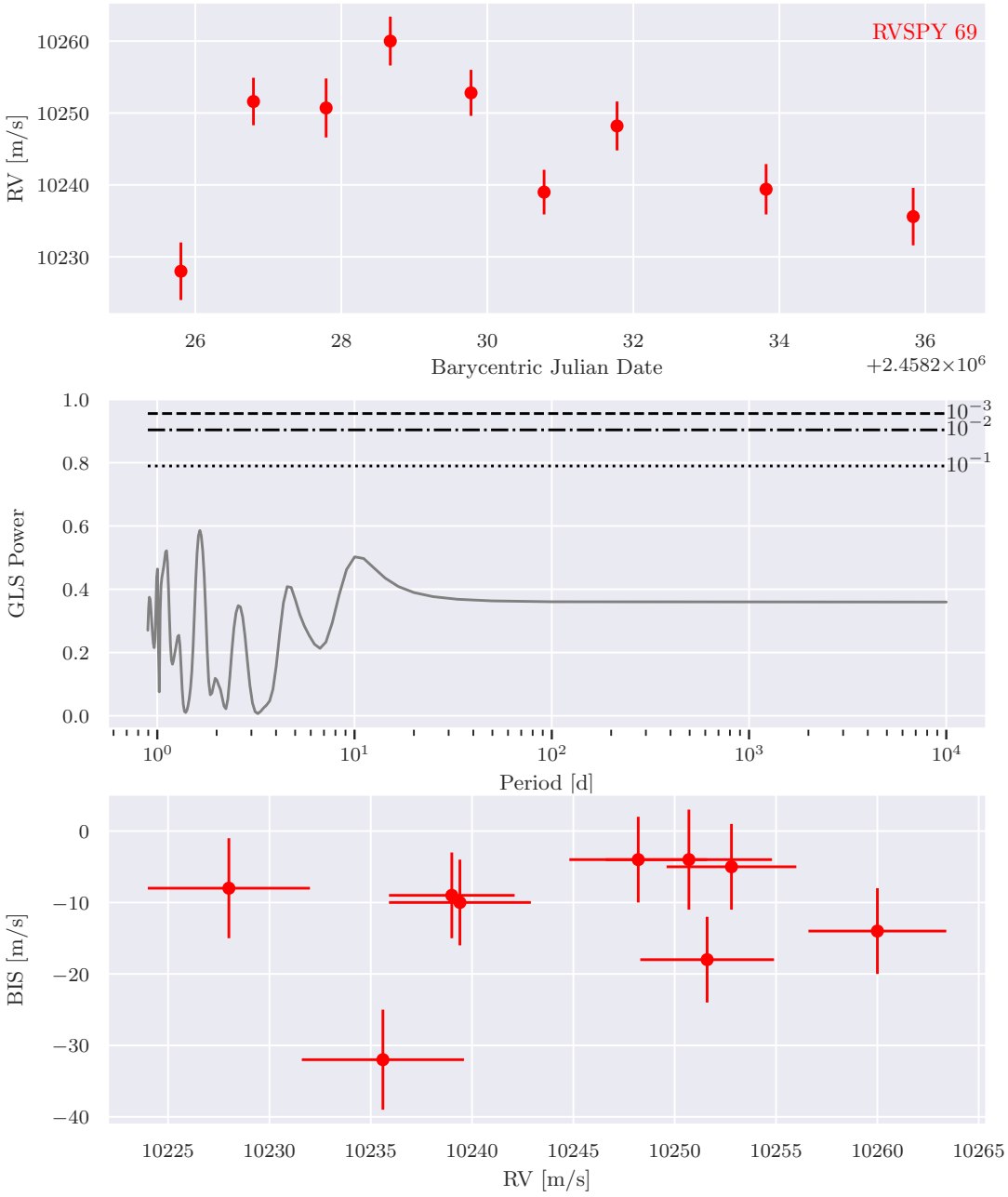

Figure 4.8: Same as Fig. 4.6, but for RVSPY 69. An example of how most observed RV sequences look: The GLS does not show hints of any periodicity and also the BIS does not show a correlation. The scatter is slightly larger than the formal error bars on the RV data suggests, hinting towards stellar activity. Since the origin is unknown, it is simply referred to as stellar jitter.

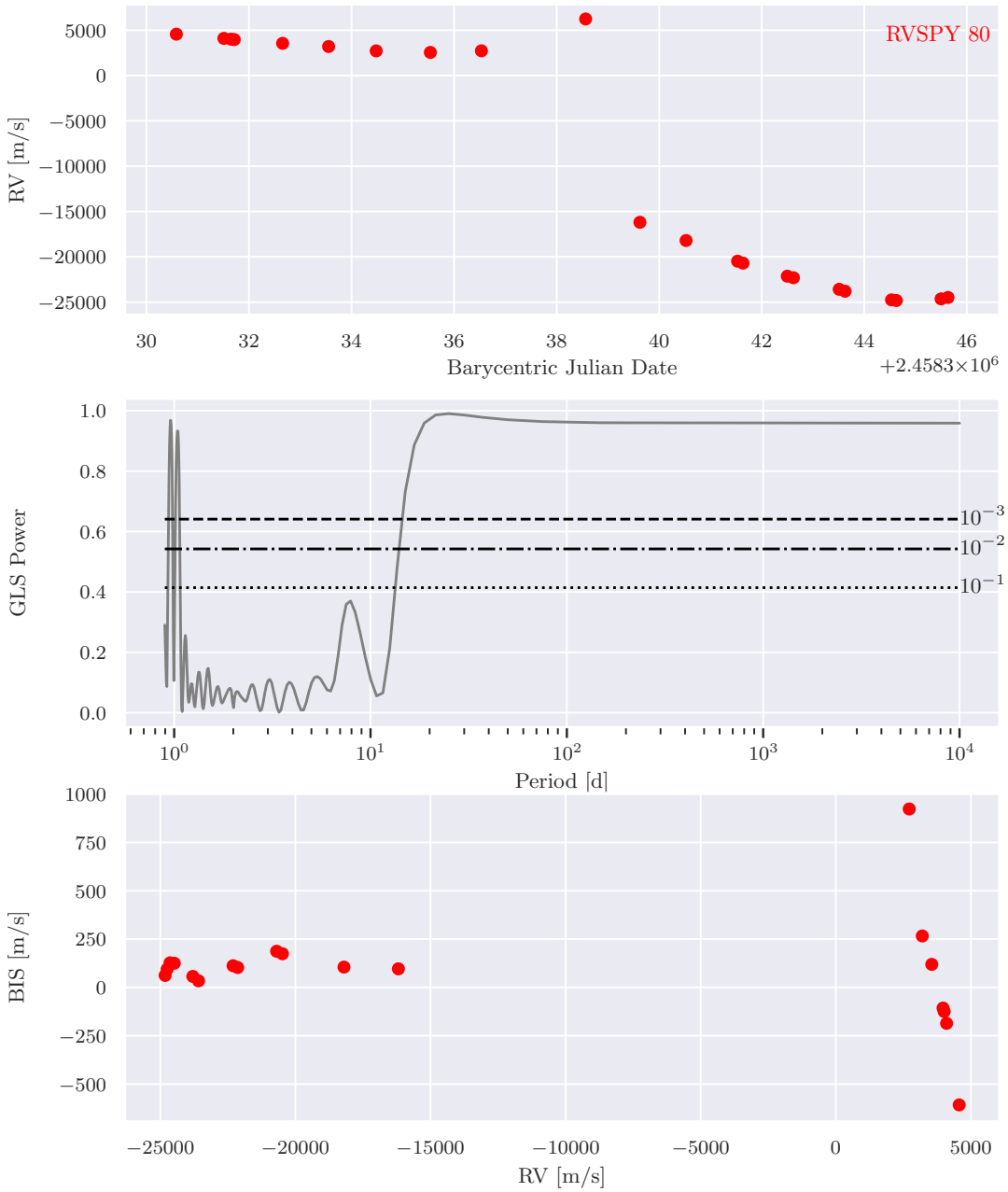

Figure 4.9: Same as Fig. 4.6, but for RVSPY 80. The RV shows a shape as for an eccentric binary or massive planetary system. The jump an the strange shape can be explained by a close binary system. The CCF time series shown in Fig. B.1 strengthens this assumption.

Chapter 5

Radial Velocity Jitter of Stars as a Function of Observational Timescale and Stellar Age

The research of this chapter has been submitted in an almost identical version to Astronomy and Astrophysics.

5.1 Introduction

Many of the almost 4000 known exoplanets were found using the Radial Velocity (RV) method. However, according to the NASA exoplanets archive[1], only three of them (V830 Tau b, Donati et al. 2016; K2-33 b, David et al. 2016 and TAP 26 b, Yu et al. 2017) are younger than 100 Myr. The main reason for this is the strong stellar activity of young stars, which makes it hard to find the subtle planetary signal in the large stellar variations. This is unfortunate for two reasons: First, planet formation takes place in young systems and at least gas giants need to form before the disk dissipates after less than a few 10 Myr, see Sect. 1.2.2 or Ercolano & Pascucci (2017). Second, planets at large orbital distances are almost exclusively detected via Direct Imaging (DI), which is best applicable to young systems where the planets are still hot from their formation. Thus, in order to discover all planets in a system, one either needs to image old stars – which seems currently impossible given the already low detection rate around young stars – or try to minimize the impact of the stellar activity of young stars, see Fig. 1.3. A lot has been done to understand and characterize stellar activity (e.g. Dumusque, 2018) or to correct for it in the analysis of the spectrum, see Sect. 1.4.1. But since the RV signal is what we measure, knowledge about the typical RV variability is important, e.g. for developing and testing RV activity models or planning RV surveys. In this Chapt., we thus derive a model free, analytic relation between stellar jitter, stellar age and lag, where lag denotes the timescale on which the jitter is measured.

[1] https://exoplanetarchive.ipac.caltech.edu/index.html, as on March 10th, 2019

In order to derive this relation, we systematically analyze precise Doppler measurements from FEROS (Kaufer et al., 1999) and HARPS (Mayor et al., 2003) using the Pooled Variance (PV) technique.

This paper is organized as follows: In Sec. 5.2 we introduce the input target list as well as target selection and data cleaning. Section 5.3 explains the PV technique, the activity modeling for individual stars as well as the uncertainty estimation. Section 5.4 presents two analytic activity-age-lag functions to the pooled data of all stars. In Sec. 5.5 we discuss the strengths, weaknesses and limits of this analysis and give example values of the empirical activity-age-lag function. Sect. 5.6 then concludes on the main findings of this paper.

5.2 Target sample

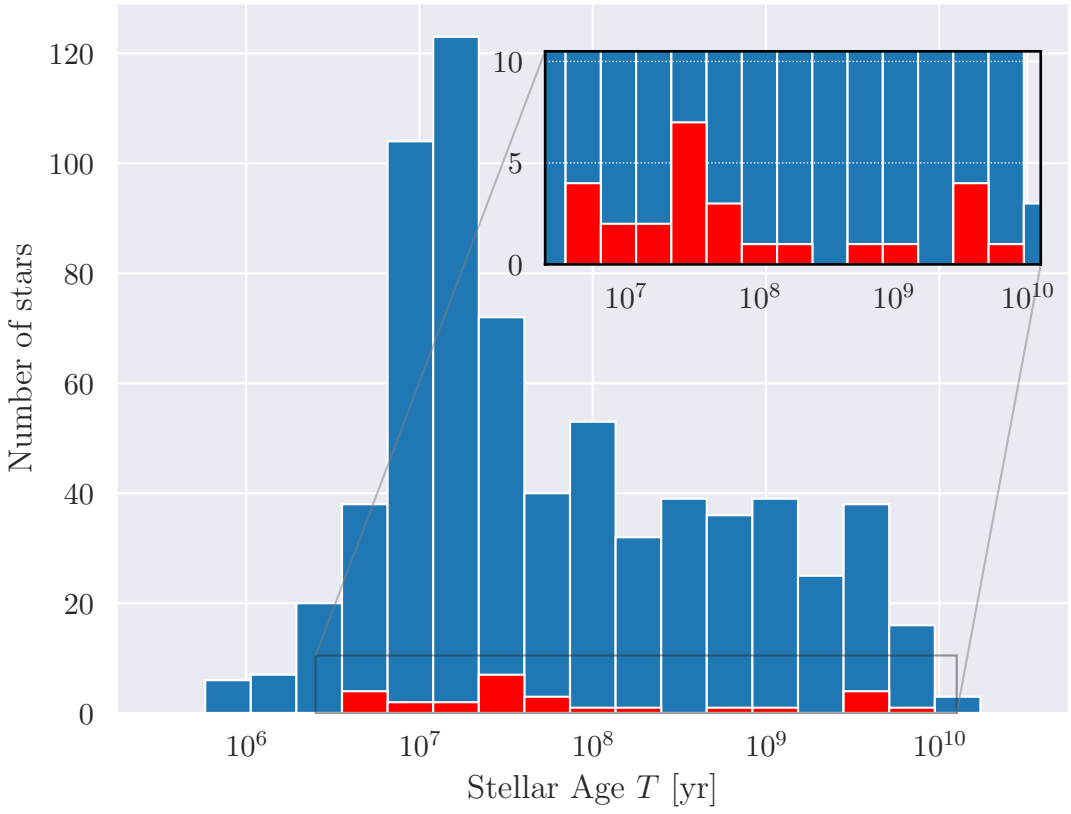

Figure 5.1: Age distribution of the stars in the input catalog (blue) and the remaining 27 stars (red) after applying the selection criteria described in the text. The remaining sample has a relatively evenly spread age distribution. Young stars ($\leq$ 100 Myr) are especially important for this analysis and are in general rarely observed in Radial Velocity surveys.

Our goal is to characterize RV jitter as function of stellar age and probed timescale. Thus we need to put together a sample of young and old stars with known ages that have been part of RV monitoring programs.

Main ID	RA	DEC	SpT	Age [Myr]	Instrument	Surv.	Age ref.
ζ Tuc	00:20:01.910	–64:52:39.440	F9 V	3950	HARPS	1	4
CD–78 24	00:42:20.300	–77:47:40.000	K3V	15 ± 10	FEROS	2	5
CD–37 1123	03:00:46.900	–37:08:02.000	G9V	30 ± 15	FEROS	2	5
TYC 8870–372–1	03:31:48.900	–63:31:54.000	K0V	25 ± 15	FEROS	2	5
HD 25457	04:02:36.660	–00:16:05.920	F7 V	50 ± 15	Both	1, 2, 3	5
2MASS J04324350–1520114	04:32:43.509	–15:20:11.268	G4V	10 ± 5	FEROS	2	5
CD–36 1785	04:34:50.800	–35:47:21.000	K1V	20 ± 15	FEROS	2	5
58 Eri	04:47:36.210	–16:56:05.520	G1.5 V	45 ± 10	HARPS	1, 3	6
α Men	06:10:14.200	–74:45:09.100	G5 V	7244 ± 3226	HARPS	1	7
HD 45184	06:24:43.880	–28:46:48.420	G2 V	4420.0	HARPS	3	8
HD 51062	06:53:47.400	–43:06:51.000	G5V	200 ± 50	FEROS	2	5
HD 51797	06:56:23.500	–46:46:55.000	K0V	30 ± 15	FEROS	2	5
CD–84 80	07:30:59.500	–84:19:28.000	G9V	30 ± 15	FEROS	2	5
V479 Car	09:23:35.000	–61:11:36.000	K1V	8 ± 3	FEROS	2	5
CD–39 5833	09:47:19.900	–40:03:10.000	K0V	25 ± 10	FEROS	2	5
HD 96064	11:04:41.580	–04:13:15.010	G5	90 ± 10	FEROS	2	5
CD–56 4581	12:39:38.000	–57:31:41.000	G9V	25 ± 10	FEROS	2	5
TYC 9034-968-1	15:33:27.500	–66:51:25.000	K2V	30 ± 15	FEROS	2	5
KW Lup	15:45:47.600	–30:20:56.000	K2V	5 ± 2	FEROS	2	9
SZ 77	15:51:47.000	–35:56:43.000	M0	5 ± 3	FEROS	2	5
SR 9	16:27:40.286	–24:22:04.030	K7	5 ± 3	FEROS	1, 2	5
HD 154577	17:10:10.270	–60:43:48.740	K0 V	4800	HARPS	3	8
V702 CrA	19:02:02.000	–37:07:44.000	G5	5 ± 2	FEROS	2	9
HD 191849	20:13:52.750	–45:09:49.080	M0 V	850 ± 400	HARPS	1, 3	4
HD 199260	20:56:47.331	–26:17:46.960	F6 V	3460	HARPS	1, 3	10
HD 202628	21:18:27.269	–43:20:04.750	G5 V	604 ± 445	HARPS	1, 3	11
CD–52 10232	22:39:30.300	–52:05:17.000	K0V	60 ± 15	FEROS	2	5

Table 5.1: Properties of the 27 stars that qualified for the further analysis. Surv. denotes the survey the star was taken from, where multiple entries are possible.

References. (1): ISPY Launhardt et al. (in prep.); (2): Mohler-Fischer (2013) and Weise, P. et al. (2010); (3): RV SPY Zakhozhay et al. (in prep.).; (4) Vican (2012); (5) Weise, P. et al. (2010); (6) Maldonado et al. (2010); (7) Lachaume et al. (1999); (8) Chen et al. (2014); (9) Weise (2010); (10) Ibukiyama & Arimoto (2002); (11) Tucci Maia et al. (2016)

We assemble our input target list from three different surveys which all focus on young stars in the southern hemisphere:

1. The ongoing NaCo-ISPY[2] direct imaging survey (Launhardt et al., in prep.; 443 targets)
2. The recently started FEROS RV survey RV SPY (Zakhozhay et al., in prep.; 180 targets)
3. The RV survey to find planets around young stars from Weise (2010) and Mohler-Fischer (2013; 214 targets)

Since there are duplicates in the catalogs, we end up with 699 targets. Figure 5.1 shows the age distribution of those stars. One can see that most stars in the input catalog are younger than 100 Myr. Almost all of the older stars come from the RV SPY survey, which also included older stars to avoid the issues of young and active stars as RV targets.

We searched the archives for public data from the ESO-instruments HARPS (Mayor et al., 2003) and FEROS (Kaufer et al., 1999) for all 699 stars in our input catalog. The RVs were derived using the CERES pipeline (Brahm et al., 2017) for FEROS and the SERVAL pipeline (Zechmeister et al., 2018) for HARPS data. We removed bad observations with formal errors above 20 m/s and 50 m/s for HARPS and FEROS respectively, and via iterative 10 σ-clipping on all data of a star simultaneously. In order to qualify for our final analysis, the remaining data need to be sufficiently evenly distributed for each star and instrument. We ensured this by requiring a minimum of 30 observations, at least two year baseline, no gap larger than 50% and a maximum of two gaps larger than 20% of the baseline. Since HARPS underwent a major intervention, including a fiber change, in June 2015 (Lo Curto et al., 2015), these criteria needed to be fulfilled for any of the data sets before or after the intervention.

Finally stars with known companions (stellar or substellar) listed in the Washington Double Star catalog (Mason et al., 2001), the Spectroscopic Binary Catalog (9th edition Pourbaix, D. et al., 2004) or the NASA Exoplanet Archive[1]were also removed. This is done so we can make the assumption that we are left only with stellar noise.

After this selection we were left with 27 stars: 9 with sufficient HARPS data and 19 with sufficient FEROS data, where HD 25457 had good data from both instruments. Table 5.2 lists their basic properties and Fig. C.1 shows the RV data for all 27 stars.

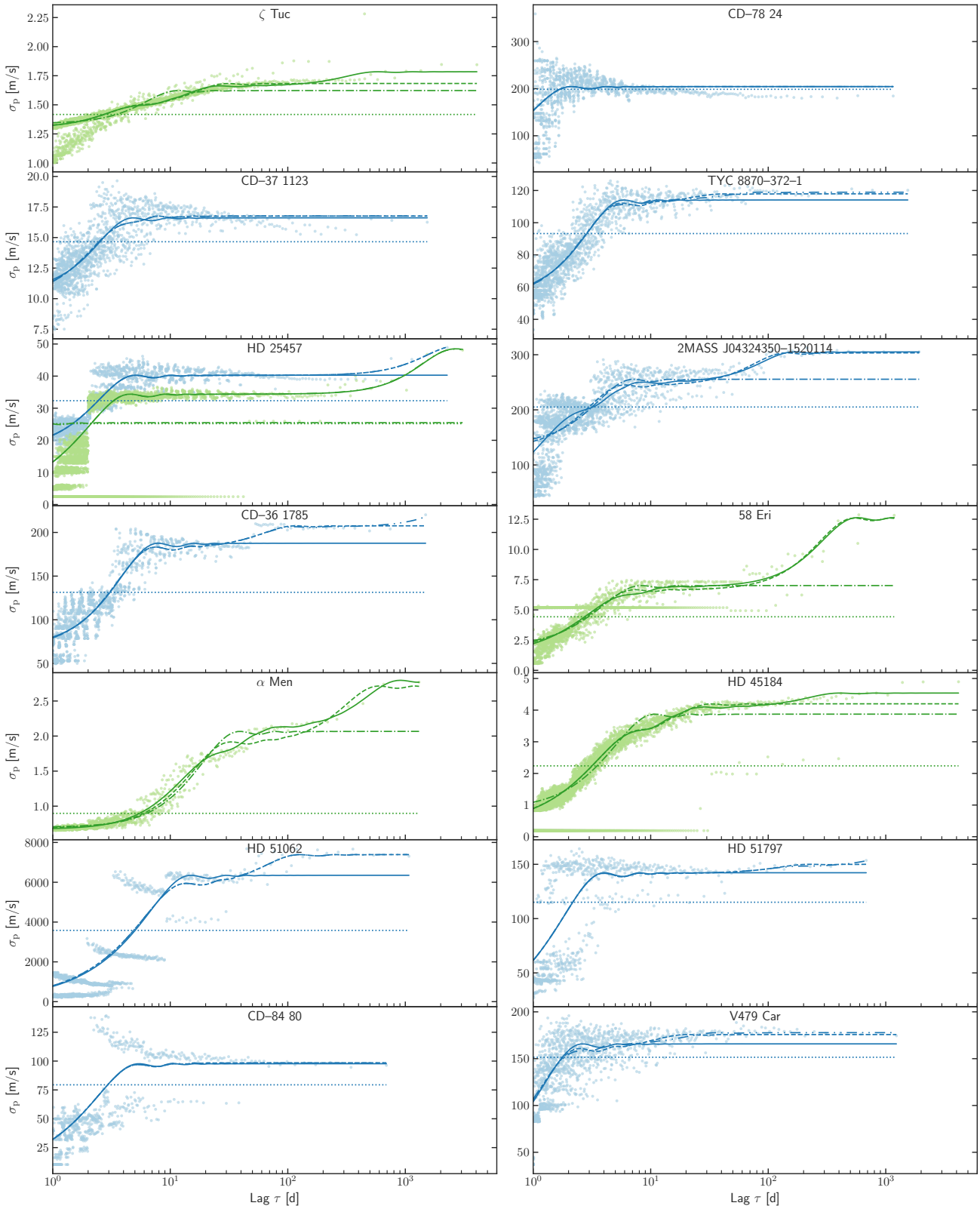

Figure 5.2: Pooled results for the 27 qualified stars. Blue symbols denote FEROS data and green symbols HARPS data. The lines show the best fits for the different number of sinusoidal signals fitted: Dotted: 0 (constant), dash-dotted: 1 signal, dashed: 2 signals, dash-dot-dotted: 3 signals. The solid line replaces the line which qualified as best fit, using the F-test described in Sect. 5.3.3. The model parameters are shown in Table 5.2. Note that σ_p and not σ_p^2 is shown.

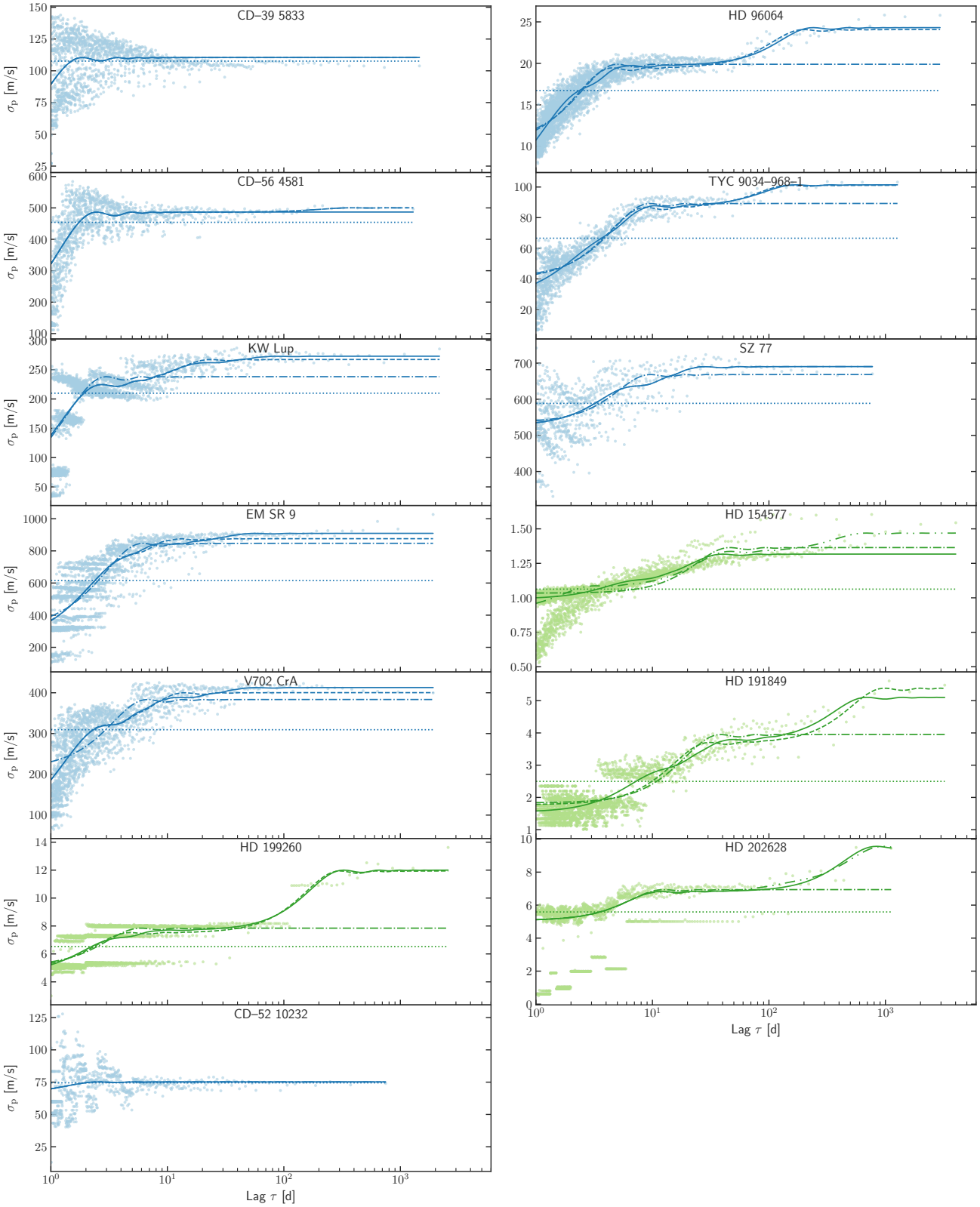

Figure 5.2: Continued.

5.3 Method

5.3.1 Models

In order to determine the typical RV scatter over different observing timescales (lags), several methods were applied.

1. Variogram or structure function (Hughes et al., 1992), using different estimators as described in Rousseeuw & Croux (1993) and Eyer & Genton (1999).
   The idea here is to create all possible differences between the measured RV datapoints. Then those points are sorted by the time differences (lag) and compared to theoretical predictions of a sinusoidal signal.

2. Self created, automated block-finding algorithms with random selection of single observation in clustered observations.
   The algorithm identifies clustered observations on different timescales. For clusters shorter than an arbitrarily chosen fraction of the lag probed, one random observation will be picked, while longer blocks will be split into subblocks of the according size. For each block the variance is determined and used as the typical variance for that timescale.

3. Consecutive binning: Bin the observations on the timescale chosen.
   Similar to the method before, but there is no upper limit on the block size and one takes the mean instead of a random representative of that bin. This is done for all lags to be probed.

4. Pooled Variance (PV)

Since only the latter one turned out to be robust enough to identify signals in sparse and irregularly sampled data, we used it for our analysis. The remainder of this section is dedicated to describing the method in more detail. We use the method of PV or Pooled Variance Diagram (PVD), which was first introduced for the analysis of time series of astronomical data by Dobson et al. (1990) to analyze the CaII emission strength of active late-type stars. Dobson et al. (1990), Donahue et al. (1995), Donahue & Dobson (1996), Donahue et al. (1997a,b) and Kürster et al. (2004) demonstrated the capability of this technique to detect time scales pertaining to stellar activity such as

1. The stellar rotation period,

2. The typical time scale of active region reconfiguration,

3. The stellar activity cycle.

The PV is a combined variance estimate from k different sets of measurements $y_{i,j}$, $i = 1, \ldots, N_j$, $j = 1, \ldots, k$ each of which has a different mean $\overline{y_j}$. If it can be assumed that

[2] http://www.mpia.de/NACO_ESPRI_GTO

all the individual sets of measurements have the same variance (despite the different mean), then the PV σ_{p} is defined as

$$\begin{aligned}\sigma^2_{\mathrm{p},k} &:= \frac{(N_1-1)\sigma_1^2+\cdots+(N_k-1)\sigma_k^2}{(N_1-1)+\cdots+(N_k-1)} \\ &= \frac{\sum_{i=1}^{N_1}(y_{i,1}-\overline{y_1})^2+\cdots+\sum_{i=1}^{N_k}(y_{i,k}-\overline{y_k})^2}{N_1+\cdots+N_k-k},\end{aligned} \tag{5.1}$$

with $\sigma_{\mathrm{p},j}$ being the variance of the jth data set, i.e. the PV is the weighted mean of the variances of the individual data sets.

In this paper we will make the assumption of (on average) equal RV variances in spite of different mean RV for data sets that were obtained within time intervals of equal length. In particular we assume this to be true for the data taken by HARPS before and after the intervention in June 2015 (Lo Curto et al., 2015). For these data sets the PV can be calculated and is used as an estimate of the true variance for this time scale. As long as the lag probed is shorter than the observational baseline, the PV is more precise than the variance of a single data set due to the larger number of measurements as several data sets are combined. If the length of the time intervals differs we expect in general different variances.

5.3.2 Block Sizes

As the integer k to split our observations in smaller blocks is arbitrary, we run $k = 1,\ldots,B$, where B is the number of days covered by the observations. In other words: We split our data in blocks, starting from one block having the full baseline length, to B blocks with a length of 1 day each. We define the lag $\tau := B/k$, which corresponds to the length of each bin in days for a given k. For each value of k, or equivalent lag τ, we then obtain a different variance $\sigma^2_{\mathrm{p},k}$ as defined in Eq. 5.1. Note: Due to the HARPS fiber change in June 2015 (Lo Curto et al., 2015), we removed HARPS data taken during this procedure (2457173.0 – 2457177.0 JD) and did not allow blocks to combine data taken before and after the intervention. Thus we had two data sets with shortened baselines. After applying the PV, we then treat the two datasets as one again.

It is difficult to assign absolute error bars to each pooled data point, as the formal RV precision (few m/s) is typically much smaller than the pooled variance (few 100 m/s). We therefore decided to assign a weight w_k to each measurement $\sigma_{\mathrm{p},k}$. In contrast to errors, weights only have a relative meaning and thus do not need to be calibrated absolutely. Since more points yield in general a more significant result , we use the square root of the number of individual points minus the number of filled boxes that were used to compute this point. We subtract the number of filled

boxes because each box takes one degree of freedom (the mean) :

$$\mathrm{w}_k := \sqrt{\frac{n_k - \tilde{k}}{2}} \quad , \tag{5.2}$$

where $n_k := N_1 + \cdots + N_{\tilde{k}}$ is the number of individual data points contributing, and $\tilde{k}$ is the number of blocks where the variance could be calculated, i.e. the number of boxes with at least two measurements. This formula, and especially the subtraction of $\tilde{k}$, are further motivated by the relative uncertainty of the variance estimator for N points, which is $\sqrt{\frac{2}{N-1}}$ (e.g. Squires, 2001, p. 22). Thus, under the assumption of k independent blocks with N/k measurements in each block, the uncertainty is

$$\sqrt{\frac{2}{N/k-1}} \cdot \frac{1}{\sqrt{k}} = \sqrt{\frac{2}{N-k}} \equiv w_k^{-1} \tag{5.3}$$

for k independent blocks with N/k measurements in each block (compare also Brown & Levine, 2007).

5.3.3 Activity Modeling

Now that we know the variance on different timescales, we want to find the periods P and amplitudes K of the underlying modulations. Under the assumption of an underlying, infinitely sampled sinusoidal signal $y(t) = K \sin\left(\frac{2\pi}{P}t - \delta\right)$ with semi-amplitude K, period P and phase δ, the analytic PV for timescale τ is given in equation C.8, which is independent of δ.

Since there might be no, one or multiple such periodic signals, we fit 4 different curves to each PV data of a star:

$$\sigma_{\mathrm{p}}^2(\tau) = A^2 + \sum_{i=1}^{m} K_i^2 \left[\frac{1}{2} + \frac{\cos(2\pi\tau/P_i) - 1}{(2\pi\tau/P_i)^2}\right] \quad , \tag{5.4}$$

where $m \in [0, 1, 2, 3]$ is the number of sinusoidal signals and τ is the timescale, or lag, probed. In other words: Only white noise or white noise plus up to three underlying sinusoidal signals are fitted, using χ^2-minimization, where the formal squared errors are given by 1/weight from Eq. 5.2. Note that the models have $2m+1$ free parameters. In order to decide how many signals are significant, we used an F-test (Rawlings et al., 1998), often used in nested models. Note that number of independent measurements required in this test is the number of observations and not the number of points in the PVD. This approach has one value α to be chosen arbitrarily. This α acts as a threshold on the significance of the additional parameter and is typically chosen to be around $\alpha \approx 0.01 - 0.05$. The larger it is, the more favorable is the model with more parameters. We select $\alpha = 0.05$ since we rather want to wrongly identify a signal than miss an increase of jitter.

5.3.4 Uncertainty Estimation

Finally we want to assign confidence intervals to each of the $2m + 1$ parameters we found for each star to best describe its activity. We tried different methods:

1. Marcov Chain Monte Carlo (MCMC) on the raw data;
2. Marcov Chain Monte Carlo (MCMC) on the pooled data;
3. Monte Carlo (MC)-like on the pooled data: we removed the modeled signal from the pooled data, binned e.g. 7 neighboring data points and determined their mean and variance. This mean and variance are then used to create 7 new, random data points, assuming a Gaussian distribution. Then we re-added the modeled signal and re-performed the fitting routine;
4. Bootstrap resampling the original data;
5. Bootstrap resampling the pooled data.

Quantifying these methods not only by eye, but also by using artificially generated data where we knew the true periods and amplitudes of the underlying signals, we found the last method to give the most realistic results.

More specifically: We pooled the data using Eq. (5.1) as described in Sects. 5.3.1 and 5.3.2, resulting in k pairs of lag τ and variance σ_{p}^2. Afterwards we determined the model to best describe the data using the F-test, see Sect. 5.3.3. We randomly redrew k pairs of lag τ and variance σ_{p}^2 with putting back. This is the method known as *bootstrapping*. Fixing the model to the one found for the original data, we fit this model to the new data. Repeating the last two steps 5000 times yields an estimate of the robustness of the model parameters. The original fit is used as the best fit and the standard deviations left and right of that return the asymmetric error bars. An example of this distribution for HD 45184 is shown in Fig. C.2 (bottom left), where the lines indicate the best fits and confidence intervals. However, bootstrapping assumes the underlying data points to be mutually independent and well sampled. Since the statistical independence of the PVs is not fulfilled here and additional systematics might be present, the errors should be seen as lower limits to the real uncertainties.

5.4 Results

We derived an analytic activity-lag-function for the 27 stars that were selected by the criteria described in Sect. 5.2. The analytic function fitted to the PV data of each star is given by Eq. (5.4). This equation describes constant noise plus up to three independent, sinusoidal signals as they would show up in the Pooled Variance Diagram (PVD) in the case of infinite sampling. It has one free parameter for the constant plus two more for each signal identified. Those parameters represent the period and amplitude of the assumed underlying sinusoid. As it was integrated over

Main ID	N sines	Baseline	#Obs	A	K_1	P_1	K_2	P_2	K_3	P_3
		d		$\mathrm{m\,s^{-1}}$	$\mathrm{m\,s^{-1}}$	d	$\mathrm{m\,s^{-1}}$	d	$\mathrm{m\,s^{-1}}$	d
ζ Tuc	3	4725	3222	$1.30^{0.00}_{0.00}$	$0.95^{0.00}_{0.02}$	$5.14^{0.01}_{0.19}$	$1.11^{0.01}_{0.03}$	$26.31^{0.16}_{2.02}$	$0.92^{0.07}_{0.07}$	$580.97^{99.26}_{181.46}$
CD–78 24	1	1157	44	$33.89^{42.48}_{31.67}$	$285.13^{3.96}_{20.02}$	$2.11^{0.09}_{0.06}$	…	…	…	…
CD–37 1123	1	1536	54	$10.58^{0.17}_{0.19}$	$18.11^{0.21}_{0.20}$	$4.85^{0.18}_{0.17}$	…	…	…	…
TYC 8870–372–1	1	1541	62	$54.81^{0.94}_{1.01}$	$141.54^{0.82}_{0.81}$	$5.92^{0.12}_{0.12}$	…	…	…	…
HD 25457	1	2273	45	$17.54^{0.33}_{0.35}$	$51.29^{0.27}_{0.25}$	$5.08^{0.09}_{0.09}$	…	…	…	…
HD 25457	2	4089	78	$0^{+0.00}_{-0.00}$	$48.63^{0.05}_{0.05}$	$4.57^{0.03}_{0.03}$	$48.39^{26.77}_{12.81}$	$2683.90^{2297.09}_{896.58}$	…	…
2MASS J04324350–1520114	3	1924	51	$0^{+0.00}_{-0.00}$	$248.41^{5.02}_{4.68}$	$2.43^{0.06}_{0.05}$	$251.86^{4.58}_{4.84}$	$8.51^{0.60}_{0.46}$	$247.06^{3.99}_{4.27}$	$168.18^{13.36}_{13.32}$
CD–36 1785	1	1489	48	$69.75^{1.63}_{1.66}$	$246.37^{1.33}_{1.35}$	$7.90^{0.18}_{0.17}$	…	…	…	…
58 Eri	3	1963	135	$1.38^{0.15}_{0.24}$	$7.91^{0.40}_{0.73}$	$5.99^{0.40}_{0.58}$	$5.43^{0.82}_{0.50}$	$16.51^{17.81}_{2.93}$	$14.94^{2.11}_{1.86}$	$575.51^{166.61}_{110.79}$
α Men	3	1309	213	$0.67^{0.00}_{0.00}$	$2.06^{0.01}_{0.07}$	$24.46^{0.17}_{1.12}$	$1.95^{0.05}_{0.02}$	$83.38^{4.74}_{3.57}$	$2.59^{0.19}_{0.12}$	$907.66^{111.60}_{61.39}$
HD 45184	3	4751	312	$0.44^{0.02}_{0.03}$	$4.33^{0.04}_{0.04}$	$7.33^{0.09}_{0.10}$	$3.79^{0.05}_{0.04}$	$27.95^{1.10}_{0.87}$	$2.77^{0.42}_{0.19}$	$407.08^{273.35}_{73.41}$
HD 51062	1	1074	47	$0^{+0.00}_{-0.00}$	$8981.18^{121.44}_{124.71}$	$15.01^{0.78}_{0.67}$	…	…	…	…
HD 51797	1	682	48	$0^{+0.00}_{-0.00}$	$201.15^{1.23}_{3.42}$	$4.04^{0.23}_{0.13}$	…	…	…	…
CD–84 80	1	690	35	$0^{+0.00}_{-0.00}$	$138.19^{1.76}_{1.88}$	$5.42^{0.30}_{0.24}$	…	…	…	…
V479 Car	1	1232	56	$0^{+0.00}_{-0.00}$	$234.48^{0.85}_{8.25}$	$2.63^{0.17}_{0.04}$	…	…	…	…
CD–39 5833	0	1458	49	$107.62^{0.38}_{0.39}$	…	…	…	…	…	…
HD 96064	3	2946	124	$2.05^{2.80}_{1.96}$	$20.41^{0.32}_{0.42}$	$2.36^{0.24}_{0.08}$	$18.87^{0.49}_{0.94}$	$6.35^{0.46}_{0.24}$	$20.01^{0.70}_{0.74}$	$240.25^{28.09}_{25.59}$
CD–56 4581	1	1290	70	$0^{+0.00}_{-0.00}$	$688.53^{1.60}_{1.62}$	$2.47^{0.03}_{0.03}$	…	…	…	…
TYC 9034–968–1	3	1269	92	$27.83^{3.23}_{13.27}$	$62.68^{5.12}_{2.53}$	$3.55^{0.71}_{0.64}$	$99.43^{2.70}_{5.03}$	$10.46^{0.97}_{0.54}$	$72.25^{2.40}_{2.65}$	$171.35^{25.49}_{20.62}$
KW Lup	2	2167	63	$0^{+0.00}_{-0.00}$	$315.04^{1.13}_{1.10}$	$2.69^{0.04}_{0.04}$	$209.07^{3.09}_{3.02}$	$23.59^{1.55}_{1.34}$	…	…
SZ 77	1	774	51	$535.81^{5.28}_{5.82}$	$565.18^{11.45}_{10.87}$	$9.67^{1.32}_{0.94}$	…	…	…	…
EM SR 9	2	1910	100	$248.62^{23.29}_{45.49}$	$937.34^{50.14}_{62.33}$	$4.45^{0.40}_{0.42}$	$729.75^{71.21}_{64.91}$	$12.72^{6.21}_{1.73}$	…	…
HD 154577	2	4797	743	$0.99^{0.00}_{0.00}$	$0.69^{0.01}_{0.01}$	$7.07^{0.16}_{0.10}$	$1.01^{0.01}_{0.01}$	$40.15^{1.56}_{0.81}$	…	…
V702 CrA	2	1914	76	$0^{+0.00}_{-0.00}$	$434.00^{4.84}_{5.00}$	$2.80^{0.05}_{0.05}$	$363.52^{5.80}_{5.57}$	$14.03^{1.01}_{0.83}$	…	…
HD 191849	3	3229	39	$1.54^{0.01}_{0.01}$	$2.95^{0.12}_{0.06}$	$11.83^{0.70}_{0.38}$	$3.87^{0.12}_{0.10}$	$47.80^{5.97}_{2.36}$	$4.86^{0.59}_{0.39}$	$693.70^{380.18}_{136.43}$
HD 199260	2	2570	51	$4.91^{0.08}_{0.09}$	$8.06^{0.10}_{0.09}$	$4.84^{0.24}_{0.22}$	$13.12^{0.58}_{0.50}$	$304.08^{39.66}_{26.81}$	…	…
HD 202628	1	1819	109	$5.08^{0.02}_{0.03}$	$6.69^{0.11}_{0.10}$	$12.54^{0.61}_{0.51}$	…	…	…	…
CD–52 10232	0	748	37	$74.48^{0.36}_{0.37}$	…	…	…	…	…	…

Table 5.2: Parameters and formal errors of the 27 stars, where HD 25457 has sufficient data in HARPS and FEROS. *N sines* refers to the number of periods fitted, *Baseline* to the baseline the observations are spanning and *#Obs* the number of good Radial Velocity (RV) measurements.

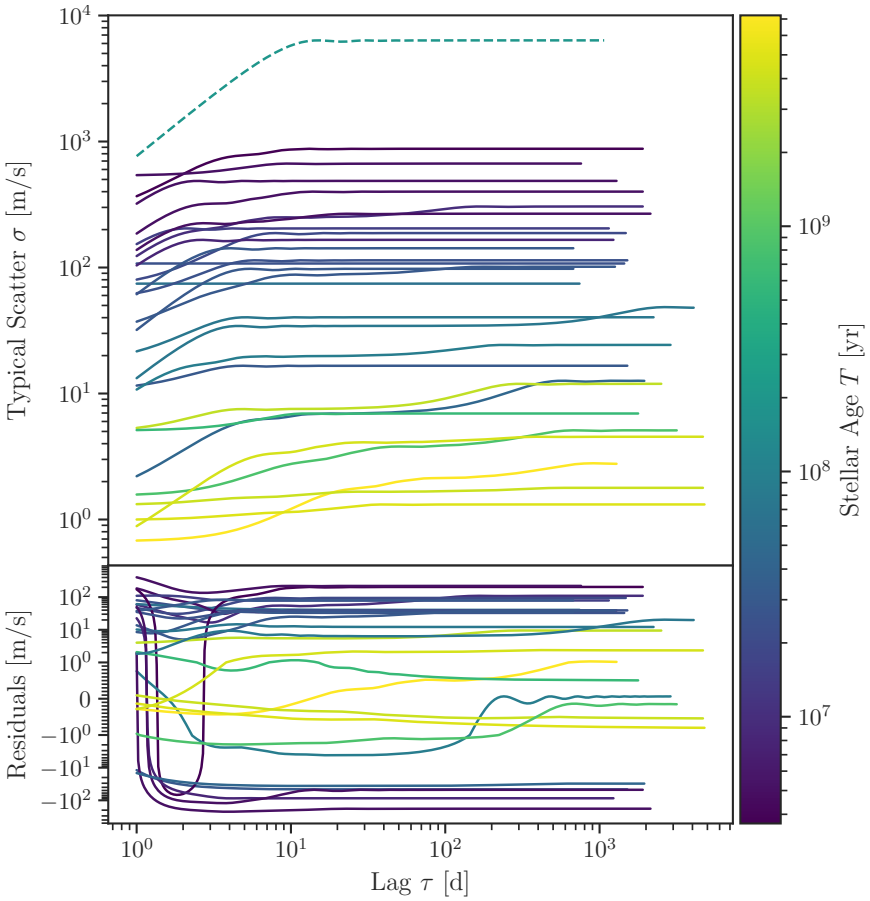

Figure 5.3: Top: Fitted RV jitter of the 28 RV datasets of the 27 stars using the procedure described in Sect. 5.3.3. The color indicates the age of the star, showing a clear correspondence of RV jitter and age. The dashed line corresponds to HD 51062 which is a known photometrically variable star. It is ignored in any further analysis. Bottom: The residuals of the above from the more complex age-lag-activity model b) described in Sect. 5.4, Eq. (5.6), excluding HD 51062.

the phase and we assume all phases to be covered roughly equally, no parameter for the phase or potential phase jumps is needed, see appendix C.2. The results of the fits are presented in Table 5.2. Figure 5.2 shows those fits graphically as well as the PV for all stars and Fig. 5.3 then compares those to the age of the stars. With the exception of HD 51062 (dashed line), a known rotationally variable star (Kiraga, 2012), a clear correlation between age and RV scatter σ is found. We thus excluded HD 51062 from our further analysis. As shown in Table 5.3, on average there were 1.7 independent signals with periods between 2.1 and 2683 days identified. These lead to an increase of the stellar variance by a factor of about 2 when probing longer timescales – or lags τ. This means that if one is looking for planetary signals, not only does the planet's signal's amplitude $K_{\rm pl}$ decrease with $K_{\rm pl} \propto P^{-1/3}$, but also does the underlying noise double when probing months instead of days.

In order to quantify this further and to make it possible for surveys to predict the amount of RV jitter *before* starting the observations, we fitted an empirical model, now adding a dependence on age to the model. Since the systematics are much

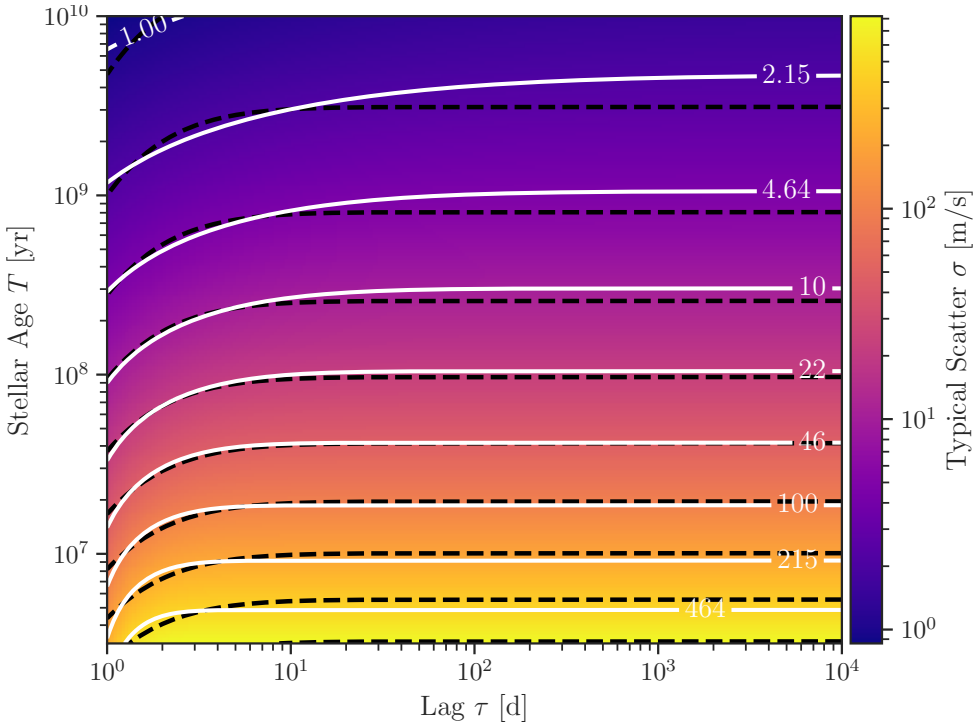

Figure 5.4: Fitted activity model to the Pooled Variance (PV) data excluding HD 51062. This model has been subtracted in Fig. 5.3. The color code and white solid lines with contour levels show the more complex model b) of Eq. (5.6). As expected, the most important parameter is age. It also shows the increase of significant activity timescales with age: 99% of the final activity are reached after $\sim$ 5 d for a 10 Myr old star, but only after $\sim$ 30 yr for a 10 Gyr old star. The black dashed lines show the simpler model a) of Eq. (5.5) where the timescales are forced to be the same for all ages.

larger than the formal errors on the curves, we did not account for those errors, nor for the uncertainties of the ages. Instead we reused the weights for each point derived earlier, but normalized them such that the sum of the weights equals one for each star. This procedure ensures that each star gets assigned the same weight, but it still downweights points in the PVD generated only with a few points. We used a shifted and stretched error function, loosely motivated by Eq. (C.8) as our model. It is analytically described by

$$\sigma_m^2(\hat{T},\hat{\tau}) = K_{\mathrm{m0}} \cdot \left(\hat{T}^{K_{\mathrm{m1}}}\right)^2 \cdot \left[\mathrm{erf}\left(P_{\mathrm{m0}} + \frac{\hat{\tau}}{\hat{T}^{d_m}}\right)\right] - c_{\mathrm{m}} \quad , \tag{5.5}$$

where $\hat{T}$ and $\hat{\tau}$ are the decadic logarithms of the stellar age T in years and lag τ in days, respectively. K_{m0}, K_{m1}, P_{m0}, d_{m} and c_{m} are free parameters of the model and erf is defined by $\mathrm{erf}(x) := \frac{1}{\sqrt{(\pi)}} \int_{-x}^{x} \mathrm{e}^{-t^2} \mathrm{d}t$. The respective $K_{\mathrm{m}i}$ and $P_{\mathrm{m}i}$ describe amplitude and period of the model, similar to K_i and P_i of the one dimensional case given in Eq. (5.4). The parameter d describes how steeply the noise σ_{m} increases with lag τ, and c is a simple offset since the error function goes through the origin. We call this model a), and the fitted parameter values and errors are given in Table 5.3, the

Mod.	K_{m0} [m^2/s^2]	K_{m1}	P_{m0}	P_{m1}	d_m	c_m [m^2/s^2]
a)	-12.7	-0.91	1.19	...	0.02	2.38
	± 0.26	± 0.01	± 0.01	...	± 0.01	± 0.05
b)	-11.48	-0.86	1.15	59k	5.35	2.29
	± 0.24	± 0.01	± 0.01	± 26k	± 0.22	± 0.05

Table 5.3: Least square fit results of the simple model a) from Eq. (5.5) and the slightly more complex model b) described in Eq. (5.6) to the data of 26 stars (excluding HD 51062). The first row gives the parameter values, the second the corresponding formal errors.

contours of the 2D-function are plotted in Fig. 5.4 as black dashes. The most striking feature is the more than exponential dependence of the RV scatter on stellar age. Although this behavior was known qualitatively before, to the authors' knowledge the dependence is quantified for the first time here. In addition, the stellar noise increases when going to longer baselines: A factor of 3.5 for stars with an age of 3 Myr years, and 2 for stars with an age of 10 Gyr. With this model, this increase happens on average such that 99% of the maximum activity are reached after 20 d. Thus, especially for young stars, the already very high noise level is more than tripling when probing signals on longer timescales compared to shorter timescales.

Additionally it is interesting to know whether younger stars typically have longer or shorter periodic signals than older stars. To answer this, another free parameters P_{m1} was introduced, slightly changing Eq. (5.5) to

$$\sigma_m^2(\hat{T},\hat{\tau}) = K_{m0}\cdot\left(\hat{T}^{K_{m1}}\right)^2\cdot\left[\mathrm{erf}\left(P_{m0}+\frac{\hat{\tau}\cdot P_{m1}}{\hat{T}^{d_m}}\right)\right]-c_m \quad , \tag{5.6}$$

which we now refer to as model b). As shown in Table 5.3, we derive a value of $P_{m1} = 59,000 \pm 26,000$. The positive value of P_{m1} means, that younger stars have shorter activity timescales than older ones, as can clearly be seen in the 2D-function with white contours shown in Fig. 5.4. With this dependence, 99% of the maximum activity will be reached after 3 d for 3 Myr old stars and after 5 d, 20 d, 225 d and 30 yr for 10 Myr, 100 Myr, 1 Gyr and 10 Gyr old stars, respectively.

5.5 Discussion

Without making use of any stellar models, we were able to determine the Radial Velocity (RV) jitter as function of lag for 27 stars and to describe it with an analytic function for all of those using Pooled Variance (PV). However, since the assumption of statistical independence is violated in the pooled points, the F-test used to determine the number of sinusoidal signals identified is strictly speaking not applicable.

Thus, even though the results look convincing, one cannot put numbers on the significance of an identified signal, one of the original plans to characterize stars even further. Consequently, the errors determined using bootstrapping need to be considered as lower limits, because of this lack of statistical independence. For the future a Monte Carlo (MC) simulation on the original data with scaled error bars would perhaps return more realistic errors. But since we neither make use of the number of signals identified nor of the errors, we did not pursue this further.

Since the ages of all stars are known, we could determine an empirical but still analytic model of the age-lag-activity relation. This model shows that the typical RV jitter of a star depends more strongly than exponentially on the age of the star. This makes the age a crucial parameter for the presence of RV jitter. The strength of the increase of the RV jitter with lag depends on the age: The maximum stellar RV jitter of 3 million year old stars is 820 m/s, and reduces to 199 m/s, 23 m/s and 4.8 m/s and 1.5 m/s for stars with ages of 10 Myr, 100 Myr, 1 Gyr and 10 Gyr, respectively. When considering a time scale of only 1 d the RV jitter is smaller by roughly a factor of 3.5 for stars with ages of 3 Myr and a factor of 2 for stars with an age of 1 Gyr. How fast this jitter then increases with lag strongly depends on the age of the stars: 99% of the maximum RV jitter will be reached after 3 d, 5 d, 19 d, 225 d and 30 yr for stars with an age of 3 Myr, 10 Myr, 100 Myr, 1 Gyr and 10 Gyr, respectively. Note that the maximum baseline of our measurements is about 13 yr, so that we cannot say anything about the contribution of activity cycles that operate on even longer timescales.

Keeping the timescale of this increase to be the same for all stars (model a)), we find that 99% of the maximum RV jittter will be reached with a lag of 20 days, whereas the relative increase and the maximum values of the RV jitter do not change significantly.

This means that e.g. for RV exoplanet hunting surveys using state of the art instruments, one should be aware that for stars younger than a few 100 Myr the limit is set by the stellar jitter and not by instrumental precision and the age is a crucial parameter. For example, the RV SPY survey excludes stars younger than about 5 Myr although its goal is finding planets around young stars. Additionally RV SPY focuses on searching hot Jupiters, where the stellar jitter is slightly smaller and the planet's signal is larger than for longer periodic planets (Zakhozhay et al., in prep.).

5.6 Conclusions

In this paper we have shown that the Pooled Variance (PV) can be used to model and determine stellar activity timescales and amplitudes and applied it to 28 data sets of 27 different stars. We find an empirical relation between Radial Velocity (RV) scatter, stellar age and lag τ. We found a steeper than exponential dependence of RV jitter on age. Further, the RV scatter roughly doubles with the lag τ when probing months instead of a few days.

This relation is not only important for stellar modeling, but also for developing an observing strategy for RV exoplanet surveys, especially if young stars are involved. E.g. in searches for hot Jupiters, dense sampling has an about two times higher sensitivity compared to long term, random sampling. A survey making use of the findings in this paper is the RV SPY survey with FEROS, which aims at finding hot Jupiters around young stars (Zakhozhay et al., in prep.).

Chapter 6

Summary and Outlook

6.1 Summary

My thesis was mainly concerned with the detection of new exoplanets using the Direct Imaging (DI) and Radial Velocity (RV) methods. In this thesis I described the different surveys I took and take part in, as well as their current status and results. I presented methods to identify and reject candidates using the above mentioned techniques. I also presented the current highlights of the NaCo-ISPY survey, as well as the RVSPY survey, with a focus on the systems I worked on. Whilst the surveys I was involved in produced no new planetary discoveries, many other valuable scientific results were obtained, e.g. NaCo-ISPY provided the L'-band measurement to the spectacular discovery of PDS 70 b (Keppler et al., 2018). My analysis of how stellar RV jitter depends on age and observational timescale, resulted in one paper which has been submitted to *Astronomy & Astrophysics* and I presented in Chapter 5. I also began the analysis of HD 101412, an A0V star with two possible sub-stellar companions. I will summarize the individual chapters below:

In Chapt. 2 I described the astrometric calibration of the *L*27 camera used by the NaCo-ISPY survey. I described the regularly executed observations to obtain the data needed for those calibrations. In Sect. 2.3 I then presented and explained the software I developed to analyze these observations automatically. I presented the results in Sect. 2.4, which are in good agreement with NaCo-ISPY's main astrometric calibration pipeline, and show the same slight ($\sim 0.6°$) offset in the orientation with respect to the values provided by the instrument's output.

In Chapter 3 I described individual results of the NaCo-ISPY survey. Section 3.1 described the aforementioned system HD 101412 which likely is host to a Low Mass Stellar Object (LMSO) and a Brown Dwarf (BD). I described the efforts taken to characterize the system, as well as the results at the current status. I also described the results to be expected from the recently obtained spectroscopic data with the GPI instrument. In Sect. 3.2 I described the system HD 191849, where the NaCo-ISPY data was compatible with a Giant Planet (GP) at about 1 AU. I described the follow up observations and data analysis, leading to the exclusion of such a companion with high certainty. Section 3.3 showed an example of a Companion Candidate (CC) that can neither be confirmed as a Background (BG) object nor as a bound object. I also

explained why the chances are low for it to be bound, resulting in the discontinuation of observations by NaCo-ISPY. In Sects. 3.4 and 3.5 I showed examples of CCs that could be identified as foreground and BG sources and are thus of no further interest to the NaCo-ISPY survey.

The RV survey RVSPY was introduced in Chapt. 4. The original idea of RVSPY was to "connect" the detection space of DI and RV observations. I described my contributions to change observing strategy, which now has the detection of hot Jupiters as its primary goal and the overlap of detection space changing to a secondary goal. I further presented some early results from the first year of this survey.

The main reason for RVSPY to look for hot Jupiters instead of longer periodic planets, is the large scatter of RV measurements. This increase in the RV scatter is due to increased activity of young stars. This motivated the research presented in Chapt. 5: I analyzed the dependence of RV scatter as function of stellar age and observational timescale. The result is a greater than exponential dependence of the RV jitter on stellar age, and an increase by about a factor of 2 when probing timescales of years instead of hours or days. This work has also been submitted to *Astronomy & Astrophysics* for publication.

6.2 Outlook

The most immediate task is certainly to continue the characterization of HD 101412 and its two probable companions, presented in Sect. 3.1. Therefore I will analyze the recently taken GPI Y- and J-band spectroscopic data and the even more recently taken NaCo K-band data (April 13th). This data, combined with the previously derived L'- and H-band magnitudes, will then be used to characterize the companions' nature. This includes answering questions about the possible formation mechanism (cold start vs. hot start), as well as spectral type, effective temperature, pressure scale, cloud layers or the surface gravity. I also plan to use petitCODE, tool specifically dedicated to determine these parameters (Mollière et al., 2015).
In addition to the above, relative astrometry of the two CCs will help to determine if they are bound or not. With the typical precision of $\sim$ 0.2 px (2.9 mas) provided by GPI for relative astrometry, it could be seen whether the companions have moved with respect to each other. If the motion is large ($\sim$ 5 mas), this can only be explained if at least one of the companions was unbound, whereas no or small relative motion would give first constraints about their orbital motion, if both are found to bound.

Of the four exoplanet surveys I worked on during my PhD – NaCo-ISPY, LIStEN, RVSPY and LEECH – the first three are still ongoing and thus require ongoing analysis of the data. NaCo-ISPY has 28 more full nights to observe, with its last observations scheduled in August this year (2019). The instrument will be decommissioned shortly afterwards. Thus any remaining and newly obtained, not yet thoroughly analyzed data needs to be analyzed immediately to decide whether follow ups are

necessary or not, before NaCo's decommissioning. This will include analysis similar to the examples given in Chapt. 3.

The future of LIStEN is currently uncertain, but we expect about three more target observations in the current semester 2019A. These, as well as a handful of old data sets, need to be analyzed to decide about follow up observations and publications.

So far RVSPY has obtained RV measurements of 70 stars where the data has been analyzed in parts, but more rigorous analysis for some companions needs to be performed, including one planetary candidate. E.g. for RVSPY 36 it is still unclear what causes the correlation of the bisector span with the RV signal, see Sect. 4.5. Multiple companions also show a long term trend, spanning at least one year. This could be caused by a longer periodic planet. However, a non-expected trend is also observed in the standard calibrator stars which we regularly observe with FEROS. We currently suspect that this trend is in close connection with the burn through of FEROS' calibration lamp at the end of last year. I am working with the collaborators on resolving this immediate issue, so we can than decide which targets need to be followed up with what sampling.

The next steps for RV and DI driven discoveries and characterizations of exoplanets seem relatively clear. With ESPRESSO and CARMENES, the RV community just recently received two powerful instruments, helping to find and characterize new exoplanets. Besides instruments with even higher resolving power, the need to disentangle intrinsic stellar signals from planetary signals is immediate. This can, for example be done by simultaneously analyzing the RV data with photometric data, e.g. from the recently launched TESS satellite.

For DI we need larger, more stable instruments to probe planets closer to the Inner Working Angle (IWA). These necessities will be tackled by multiple upcoming instruments: VLT's upcoming ERIS instrument, first light is planned for 2020, the hopefully soon to be launched James Webb Space Telescope (JWST) and the 39 m E-ELT, planned for 2025. Further post-processing algorithms are continuously improved. Besides the new developments presented in Sect. 1.3.3, new ideas include the use of machine learning as well as meta data, e.g. from the Adaptive Optics (AO), to further disentangle the planetary and stellar signal.

Appendix A

Individual measurements of the Astrometric Correction

MJD	AGPM	Field	N_{stars}	Pixelscale [mas/px]	σ Pixelscale [mas/px]	TN [deg]	σ TN [deg]
57374.3130	True	Trapezium	10	27.224	0.017	0.563	0.041
57374.3289	False	Trapezium	6	27.187	0.034	0.622	0.037
57374.3296	False	Trapezium	6	27.201	0.031	0.631	0.042
57374.3302	False	Trapezium	9	27.057	0.066	0.460	0.139
57374.3307	False	Trapezium	8	27.131	0.027	0.577	0.035
57374.3552	False	Trapezium	13	27.164	0.034	0.496	0.067
57374.3557	False	Trapezium	13	27.140	0.036	0.500	0.069
57375.1252	False	47tuc	34	27.220	0.017	0.579	0.034
57375.1255	False	47tuc	15	27.191	0.027	0.619	0.058
57375.1259	False	47tuc	35	27.228	0.014	0.574	0.029
57375.1261	False	47tuc	21	27.243	0.023	0.536	0.048
57375.1265	False	47tuc	16	27.183	0.029	0.538	0.072
57375.1268	False	47tuc	14	27.163	0.032	0.532	0.078
57375.1268	False	47tuc	14	27.163	0.032	0.532	0.078
57438.1888	False	Trapezium	6	27.189	0.021	0.653	0.031
57438.1894	False	Trapezium	7	27.171	0.018	0.648	0.030
57539.4387	True	47tuc	5	27.195	0.065	1.433	0.212
57540.3854	False	47tuc	7	27.201	0.066	0.649	0.147
57540.3860	False	47tuc	8	27.199	0.056	0.651	0.124
57540.4048	True	47tuc	11	27.157	0.077	0.558	0.193
57540.4088	False	47tuc	13	27.172	0.045	0.485	0.118
57540.4093	False	47tuc	14	27.191	0.027	0.539	0.080
57540.4093	False	47tuc	14	27.191	0.027	0.539	0.080
57600.4054	False	47tuc	25	27.161	0.020	0.619	0.041
57601.4383	True	47tuc	21	27.179	0.029	1.149	0.065
57601.4408	True	47tuc	26	27.189	0.025	1.152	0.058
57601.4423	True	47tuc	24	27.189	0.026	1.149	0.060

57701.0090	True	47tuc	34	27.184	0.023	0.517	0.056
57701.0107	True	47tuc	33	27.179	0.023	0.506	0.052
57732.0446	True	47tuc	11	27.187	0.041	1.163	0.135
57733.0087	False	47tuc	36	27.155	0.016	0.615	0.033
57733.0092	False	47tuc	35	27.161	0.017	0.624	0.035
57830.0225	False	Trapezium	4	27.176	0.032	0.744	0.039
57830.0229	False	Trapezium	5	27.185	0.017	0.726	0.043
57830.0249	False	Trapezium	6	27.183	0.021	0.705	0.035
57830.0253	False	Trapezium	5	27.171	0.020	0.732	0.038
57830.0303	True	Trapezium	4	27.462	0.039	0.466	0.076
57892.4183	False	47tuc	49	27.167	0.013	0.453	0.026
57892.4188	False	47tuc	49	27.173	0.013	0.458	0.026
57892.4307	True	47tuc	24	27.202	0.033	0.944	0.070
57921.4146	False	47tuc	14	27.170	0.031	0.596	0.063
57921.4152	False	47tuc	11	27.166	0.039	0.652	0.087
57922.4141	True	47tuc	17	27.204	0.035	1.050	0.071
57922.4183	False	47tuc	40	27.168	0.015	1.025	0.030
57922.4188	False	47tuc	44	27.175	0.014	1.036	0.028
57948.4137	False	47tuc	41	27.167	0.015	0.488	0.031
57948.4141	False	47tuc	42	27.168	0.015	0.492	0.031
57948.4146	False	47tuc	42	27.173	0.016	0.489	0.031
57948.4151	False	47tuc	41	27.169	0.015	0.489	0.031
57948.4156	False	47tuc	45	27.168	0.015	0.491	0.030
57948.4250	False	47tuc	41	27.157	0.015	0.559	0.029
57948.4255	False	47tuc	36	27.158	0.016	0.568	0.032
57948.4260	False	47tuc	22	27.154	0.022	0.613	0.047
57948.4265	False	47tuc	40	27.161	0.015	0.575	0.029
57948.4269	False	47tuc	40	27.157	0.015	0.569	0.029
57948.4367	True	47tuc	4	27.039	0.272	0.472	0.417
57948.4370	True	47tuc	9	27.267	0.059	1.125	0.117
57948.4373	True	47tuc	11	27.254	0.041	1.107	0.080
57948.4376	True	47tuc	12	27.220	0.062	1.135	0.093
57948.4379	True	47tuc	12	27.215	0.062	1.125	0.092
57948.4471	True	47tuc	20	27.249	0.033	0.368	0.078
57948.4474	True	47tuc	25	27.236	0.029	0.379	0.067
57948.4477	True	47tuc	26	27.230	0.027	0.399	0.059
57948.4480	True	47tuc	25	27.245	0.029	0.373	0.062
57948.4483	True	47tuc	31	27.231	0.024	0.413	0.053
57995.4260	False	47tuc	3	27.317	0.031	0.201	0.036
57995.4265	False	47tuc	2	27.289	0.000	0.013	0.000
57995.4270	False	47tuc	2	27.424	0.000	1.426	0.000
57995.4275	False	47tuc	2	27.439	0.000	1.150	0.000

57995.4275	False	47tuc	2	27.439	0.000	1.150	0.000
58056.9993	True	47tuc	4	27.018	0.067	1.030	0.243
58056.9996	True	47tuc	4	27.004	0.064	0.970	0.234
58056.9996	True	47tuc	4	27.004	0.064	0.970	0.234
58056.9996	True	47tuc	4	27.004	0.064	0.970	0.234
58057.0006	True	47tuc	2	27.018	0.000	-0.842	0.000
58057.0102	False	47tuc	7	27.204	0.067	1.065	0.103
58057.0107	False	47tuc	6	27.235	0.070	1.028	0.109
58057.0112	False	47tuc	9	27.189	0.054	1.091	0.105
58057.0116	False	47tuc	11	27.206	0.043	1.064	0.089
58057.0121	False	47tuc	10	27.216	0.046	1.004	0.094
58057.0121	False	47tuc	10	27.216	0.046	1.004	0.094
58057.9957	True	47tuc	4	27.132	0.600	1.202	0.666
58057.9960	True	47tuc	2	27.606	0.000	0.766	0.000
58057.9964	True	47tuc	3	26.446	0.866	1.125	0.669
58057.9964	True	47tuc	3	26.446	0.866	1.125	0.669
58058.0008	True	47tuc	3	27.726	0.057	1.150	0.094
58058.0011	True	47tuc	4	26.896	0.518	0.469	1.028
58058.0014	True	47tuc	3	27.334	0.098	0.774	0.230
58058.0018	True	47tuc	4	27.475	0.156	0.741	0.283
58058.0018	True	47tuc	4	27.475	0.156	0.741	0.283
58058.0018	True	47tuc	4	27.475	0.156	0.741	0.283
58058.0018	True	47tuc	4	27.475	0.156	0.741	0.283
58058.0162	False	47tuc	31	27.172	0.016	0.508	0.035
58058.0167	False	47tuc	39	27.167	0.014	0.497	0.029
58058.0172	False	47tuc	41	27.192	0.014	0.493	0.029
58174.0533	False	Trapezium	12	27.164	0.019	0.560	0.039
58174.0537	False	Trapezium	14	27.170	0.015	0.588	0.032
58174.0542	False	Trapezium	14	27.172	0.015	0.583	0.033
58174.0547	False	Trapezium	14	27.171	0.015	0.584	0.032
58174.0551	False	Trapezium	12	27.163	0.019	0.567	0.038
58174.0551	False	Trapezium	12	27.163	0.019	0.567	0.038
58174.0781	True	Trapezium	7	27.225	0.039	1.201	0.063
58174.0781	True	Trapezium	7	27.225	0.039	1.201	0.063
58174.0781	True	Trapezium	7	27.225	0.039	1.201	0.063
58174.0781	True	Trapezium	7	27.225	0.039	1.201	0.063
58179.0115	False	Trapezium	17	27.177	0.013	0.619	0.026
58179.0120	False	Trapezium	17	27.173	0.013	0.621	0.027
58179.0125	False	Trapezium	18	27.170	0.013	0.604	0.027
58179.0129	False	Trapezium	17	27.173	0.013	0.617	0.026
58179.0134	False	Trapezium	18	27.155	0.026	0.530	0.057
58179.0249	True	Trapezium	8	27.148	0.024	1.219	0.042

58179.0252	True	Trapezium	9	27.163	0.025	1.230	0.046
58179.0255	True	Trapezium	9	27.162	0.025	1.232	0.045
58179.0259	True	Trapezium	9	27.162	0.026	1.228	0.047
58179.0262	True	Trapezium	9	27.157	0.027	1.228	0.047
58276.4131	True	47tuc	28	27.221	0.027	1.018	0.059
58276.4134	True	47tuc	28	27.215	0.026	1.051	0.051
58276.4138	True	47tuc	31	27.213	0.024	1.042	0.048
58276.4141	True	47tuc	36	27.217	0.022	1.020	0.046
58276.4145	True	47tuc	33	27.227	0.024	1.014	0.049
58276.4504	True	47tuc	29	27.238	0.025	0.445	0.053
58276.4508	True	47tuc	31	27.242	0.026	0.424	0.056
58276.4511	True	47tuc	24	27.238	0.028	0.451	0.055
58276.4515	True	47tuc	34	27.245	0.024	0.434	0.051
58276.4518	True	47tuc	35	27.242	0.023	0.435	0.049
58290.4020	True	47tuc	33	27.218	0.029	1.022	0.057
58290.4024	True	47tuc	35	27.228	0.030	1.008	0.059
58290.4027	True	47tuc	32	27.227	0.030	1.018	0.059
58290.4031	True	47tuc	34	27.227	0.028	1.030	0.057
58290.4034	True	47tuc	32	27.219	0.025	1.014	0.049
58290.4080	False	47tuc	52	27.176	0.012	1.063	0.026
58290.4085	False	47tuc	52	27.182	0.012	1.065	0.025
58290.4090	False	47tuc	46	27.174	0.013	1.067	0.028
58290.4094	False	47tuc	48	27.181	0.014	1.065	0.028
58290.4099	False	47tuc	47	27.176	0.013	1.065	0.027
58291.4197	True	47tuc	8	27.080	0.101	0.593	0.273
58291.4200	True	47tuc	14	27.095	0.068	0.703	0.185
58291.4204	True	47tuc	24	27.211	0.027	0.988	0.058
58291.4207	True	47tuc	17	27.205	0.036	0.950	0.075
58291.4210	True	47tuc	30	27.214	0.024	0.974	0.052
58291.4254	False	47tuc	50	27.170	0.012	1.024	0.026
58291.4259	False	47tuc	49	27.173	0.013	1.031	0.026
58291.4264	False	47tuc	49	27.169	0.013	1.032	0.027
58291.4268	False	47tuc	48	27.171	0.013	1.024	0.027
58291.4273	False	47tuc	46	27.172	0.013	1.030	0.028
58317.4152	True	47tuc	11	27.242	0.042	1.068	0.092
58317.4156	True	47tuc	12	27.259	0.041	1.107	0.073
58317.4159	True	47tuc	12	27.257	0.040	1.094	0.072
58317.4162	True	47tuc	17	27.237	0.034	1.135	0.061
58317.4166	True	47tuc	12	27.259	0.041	1.103	0.071
58317.4217	False	47tuc	38	27.172	0.011	1.140	0.025
58317.4222	False	47tuc	39	27.181	0.012	1.165	0.027
58317.4227	False	47tuc	40	27.176	0.012	1.161	0.027

58317.4231	False	47tuc	40	27.171	0.014	1.177	0.031
58317.4236	False	47tuc	39	27.170	0.014	1.179	0.031
58350.4131	False	47tuc	53	27.188	0.013	0.590	0.028
58350.4135	False	47tuc	57	27.177	0.012	0.594	0.026
58350.4140	False	47tuc	59	27.186	0.012	0.594	0.025
58350.4145	False	47tuc	60	27.184	0.012	0.598	0.025
58350.4149	False	47tuc	59	27.184	0.012	0.594	0.026
58350.4260	True	47tuc	33	27.215	0.025	1.127	0.054
58350.4264	True	47tuc	36	27.214	0.022	1.145	0.048
58350.4268	True	47tuc	31	27.219	0.026	1.113	0.056
58350.4271	True	47tuc	34	27.220	0.022	1.150	0.047
58350.4274	True	47tuc	33	27.227	0.022	1.149	0.048
58351.3800	False	47tuc	42	27.155	0.015	0.695	0.029
58351.3805	False	47tuc	39	27.166	0.015	0.698	0.030
58351.3809	False	47tuc	35	27.157	0.017	0.720	0.034
58351.3814	False	47tuc	36	27.167	0.017	0.706	0.033
58351.3819	False	47tuc	40	27.168	0.015	0.705	0.031
58351.3980	True	47tuc	28	27.225	0.025	1.182	0.052
58351.3983	True	47tuc	25	27.226	0.029	1.150	0.066
58351.3987	True	47tuc	26	27.224	0.026	1.188	0.056
58351.3990	True	47tuc	29	27.225	0.023	1.175	0.048
58351.3994	True	47tuc	16	27.216	0.038	1.185	0.080
58363.4066	True	47tuc	12	27.152	0.035	1.212	0.084
58363.4070	True	47tuc	11	27.197	0.034	1.207	0.084
58363.4073	True	47tuc	18	27.205	0.030	1.118	0.071
58363.4077	True	47tuc	19	27.200	0.028	1.132	0.070
58363.4080	True	47tuc	14	27.209	0.029	1.196	0.068
58363.4177	False	47tuc	16	27.232	0.031	0.672	0.059
58363.4182	False	47tuc	28	27.196	0.019	0.713	0.041
58363.4186	False	47tuc	36	27.183	0.017	0.726	0.036
58363.4191	False	47tuc	38	27.196	0.016	0.731	0.034
58363.4196	False	47tuc	38	27.189	0.016	0.721	0.033
58364.3944	False	47tuc	48	27.178	0.013	0.713	0.027
58364.3949	False	47tuc	40	27.182	0.015	0.716	0.032
58364.3954	False	47tuc	43	27.172	0.014	0.716	0.029
58364.3958	False	47tuc	45	27.178	0.014	0.712	0.029
58364.3963	False	47tuc	47	27.184	0.013	0.713	0.028
58364.4054	True	47tuc	33	27.228	0.027	1.130	0.071
58364.4057	True	47tuc	32	27.233	0.024	1.187	0.049
58364.4061	True	47tuc	34	27.229	0.023	1.208	0.048
58364.4064	True	47tuc	33	27.225	0.024	1.203	0.049
58364.4068	True	47tuc	34	27.230	0.023	1.199	0.048

58376.3818	True	47tuc	13	27.204	0.040	1.141	0.091
58376.3821	True	47tuc	23	27.231	0.038	1.169	0.075
58376.3825	True	47tuc	16	27.226	0.037	1.175	0.087
58376.3828	True	47tuc	30	27.251	0.029	1.195	0.058
58376.3831	True	47tuc	29	27.241	0.029	1.183	0.058
58376.3916	False	47tuc	48	27.157	0.014	0.665	0.027
58376.3921	False	47tuc	46	27.167	0.014	0.666	0.027
58376.3925	False	47tuc	48	27.165	0.014	0.667	0.027
58376.3930	False	47tuc	48	27.166	0.014	0.666	0.026
58376.3935	False	47tuc	47	27.171	0.014	0.665	0.026
58377.3981	True	47tuc	11	27.266	0.050	1.278	0.119
58377.3984	True	47tuc	4	27.107	0.102	0.690	0.343
58377.3988	True	47tuc	2	27.743	0.000	-0.653	0.000
58377.3991	True	47tuc	5	27.138	0.063	1.141	0.248
58377.3995	True	47tuc	10	27.232	0.055	1.211	0.129
58377.4087	False	47tuc	31	27.178	0.018	0.769	0.037
58377.4091	False	47tuc	22	27.163	0.021	0.730	0.041
58377.4096	False	47tuc	30	27.158	0.020	0.778	0.040
58377.4101	False	47tuc	36	27.174	0.016	0.766	0.032
58377.4105	False	47tuc	37	27.159	0.016	0.764	0.033
58377.4137	False	47tuc	40	27.176	0.015	0.754	0.031
58377.4142	False	47tuc	36	27.164	0.016	0.758	0.033
58377.4146	False	47tuc	33	27.170	0.018	0.768	0.036
58377.4151	False	47tuc	31	27.167	0.019	0.770	0.039
58377.4156	False	47tuc	35	27.174	0.017	0.750	0.034
58410.1894	True	47tuc	5	27.319	0.076	1.146	0.102
58410.1897	True	47tuc	8	27.302	0.072	1.205	0.100
58410.1901	True	47tuc	9	27.222	0.057	0.994	0.113
58410.1904	True	47tuc	4	27.208	0.098	1.238	0.389
58410.1908	True	47tuc	25	27.203	0.028	1.104	0.058
58410.2018	False	47tuc	34	27.172	0.017	0.622	0.032
58410.2023	False	47tuc	42	27.168	0.014	0.625	0.029
58410.2028	False	47tuc	39	27.177	0.015	0.633	0.029
58410.2032	False	47tuc	42	27.168	0.015	0.635	0.029
58410.2037	False	47tuc	46	27.177	0.013	0.632	0.027
58449.0232	False	47tuc	49	27.165	0.014	0.497	0.027
58449.0237	False	47tuc	54	27.168	0.012	0.492	0.024
58449.0241	False	47tuc	57	27.161	0.012	0.487	0.024
58449.0246	False	47tuc	55	27.175	0.012	0.486	0.024
58449.0251	False	47tuc	54	27.167	0.013	0.490	0.025
58449.0370	False	47tuc	56	27.160	0.013	0.497	0.025
58449.0374	False	47tuc	61	27.167	0.012	0.502	0.023

58449.0379	False	47tuc	56	27.165	0.012	0.505	0.025
58449.0384	False	47tuc	61	27.169	0.012	0.498	0.023
58449.0389	False	47tuc	58	27.167	0.012	0.498	0.024
58449.0512	True	47tuc	18	27.200	0.029	1.083	0.065
58449.0515	True	47tuc	18	27.208	0.030	1.068	0.066
58449.0519	True	47tuc	27	27.219	0.024	1.054	0.052
58449.0522	True	47tuc	16	27.209	0.033	1.098	0.072
58450.3644	False	Trapezium	16	27.154	0.028	0.575	0.058
58450.3649	False	Trapezium	15	27.176	0.016	0.636	0.033
58450.3653	False	Trapezium	15	27.178	0.017	0.634	0.034
58450.3658	False	Trapezium	16	27.168	0.024	0.591	0.051
58450.3663	False	Trapezium	15	27.162	0.016	0.625	0.033
58450.3764	True	Trapezium	8	27.155	0.035	1.212	0.059
58450.3767	True	Trapezium	10	27.190	0.030	1.214	0.049
58450.3771	True	Trapezium	8	27.174	0.033	1.234	0.056
58450.3774	True	Trapezium	9	27.173	0.032	1.213	0.052
58450.3778	True	Trapezium	9	27.173	0.031	1.224	0.054
58501.0261	False	47tuc	17	27.153	0.029	0.645	0.067
58501.0265	False	47tuc	27	27.155	0.022	0.618	0.046
58501.0270	False	47tuc	34	27.154	0.018	0.624	0.038
58501.0275	False	47tuc	20	27.178	0.029	0.666	0.066
58501.0279	False	47tuc	35	27.181	0.018	0.615	0.036
58501.0389	True	47tuc	24	27.232	0.031	1.087	0.068
58501.0393	True	47tuc	18	27.221	0.039	1.032	0.082
58501.0396	True	47tuc	23	27.243	0.032	1.100	0.073
58501.0400	True	47tuc	26	27.219	0.032	1.075	0.069
58501.0403	True	47tuc	20	27.240	0.036	1.038	0.076
58502.1394	False	Trapezium	11	27.135	0.040	0.545	0.077
58502.1398	False	Trapezium	11	27.129	0.041	0.500	0.081
58502.1403	False	Trapezium	9	27.126	0.056	0.508	0.107
58502.1408	False	Trapezium	10	27.112	0.048	0.520	0.092
58502.1412	False	Trapezium	11	27.123	0.042	0.500	0.084
58502.1520	True	Trapezium	6	27.240	0.044	0.660	0.075
58502.1523	True	Trapezium	6	27.236	0.043	0.657	0.071
58502.1527	True	Trapezium	6	27.233	0.038	0.678	0.067
58502.1530	True	Trapezium	7	27.240	0.039	0.658	0.074
58502.1534	True	Trapezium	7	27.248	0.038	0.647	0.072

Table A.1: Results of the individual astrometric measurements. *N* stars denotes the number of stars matched with stars in the catalog and used for the calibration.

Appendix B

Cross Correlation Function Time Series of RVSPY 80

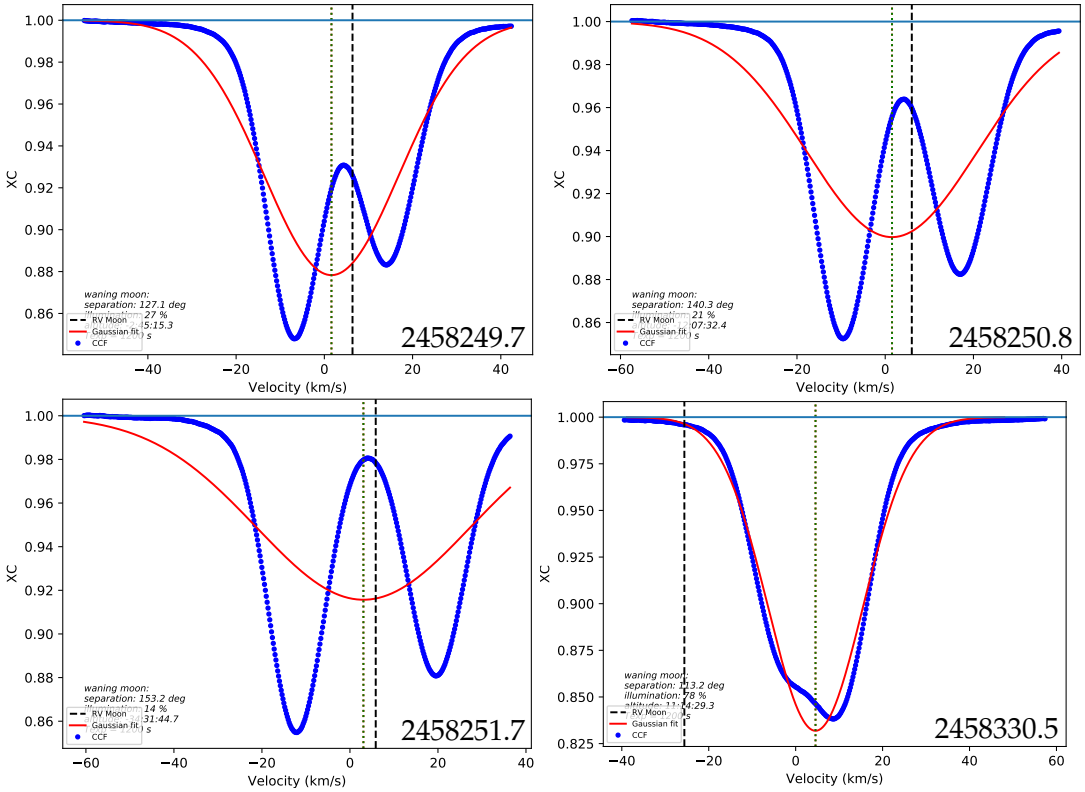

Figure B.1: Time series of the Cross Correlation Function (CCF) of RVSPY 80 shown as blue lines as returned by CERES. The red line represents a fit of a Gaussian to the data. The center of which is marked with a vertical dotted line and represents the measured RV value. The dotted dashed curve is the lunar RV not fitted for here since it did not contribute significantly. The Barycentric Julian Date (BJD) is given in the bottom right of each panel. The contribution of the secondary companion can be clearly seen "moving in" and out again, explaining the behavior of the RVs and Bisector Span (BIS) in Fig. 4.9. Note that the first three panels shown here have no counterpart in Fig. 4.9.

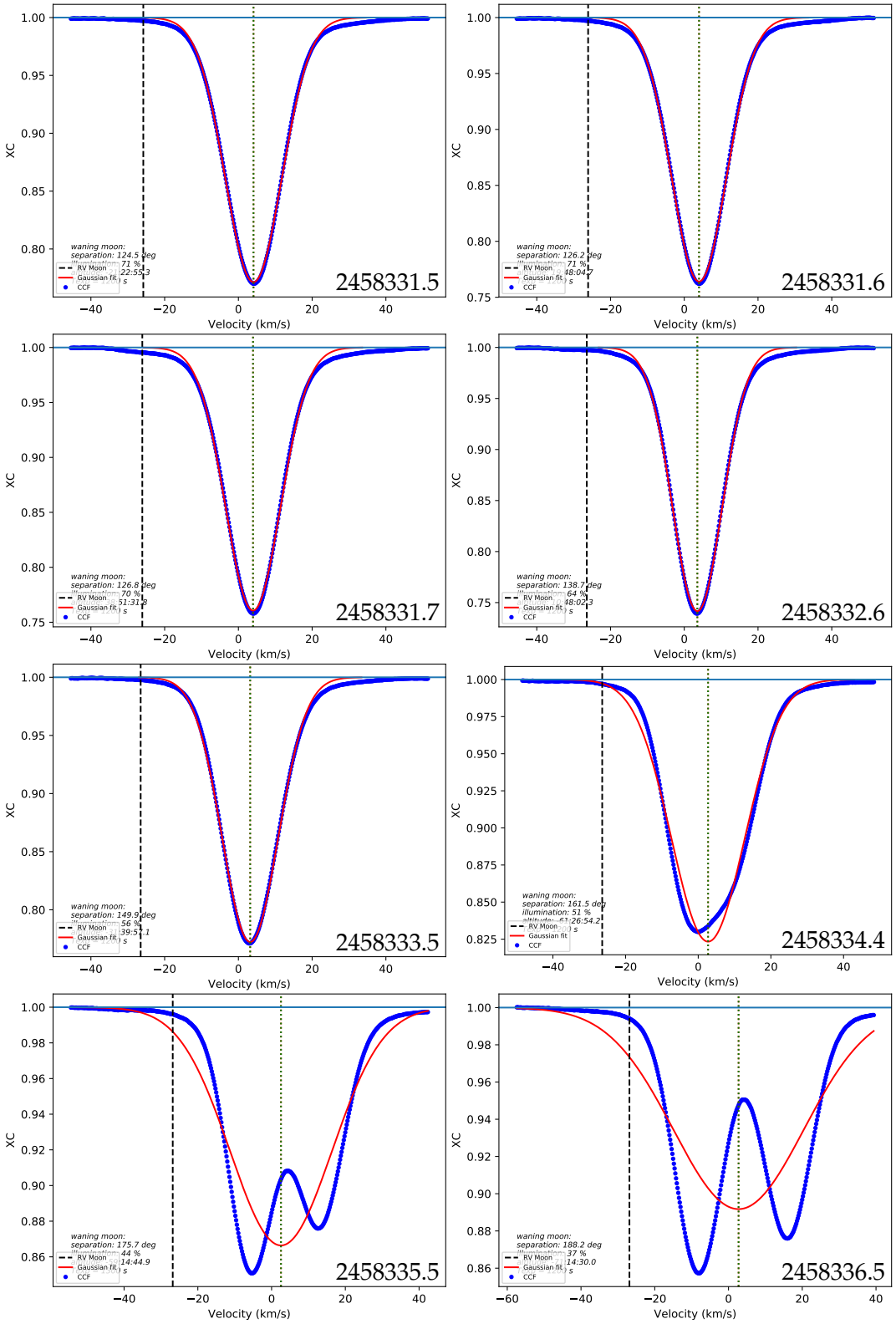

Figure B.1: Continued.

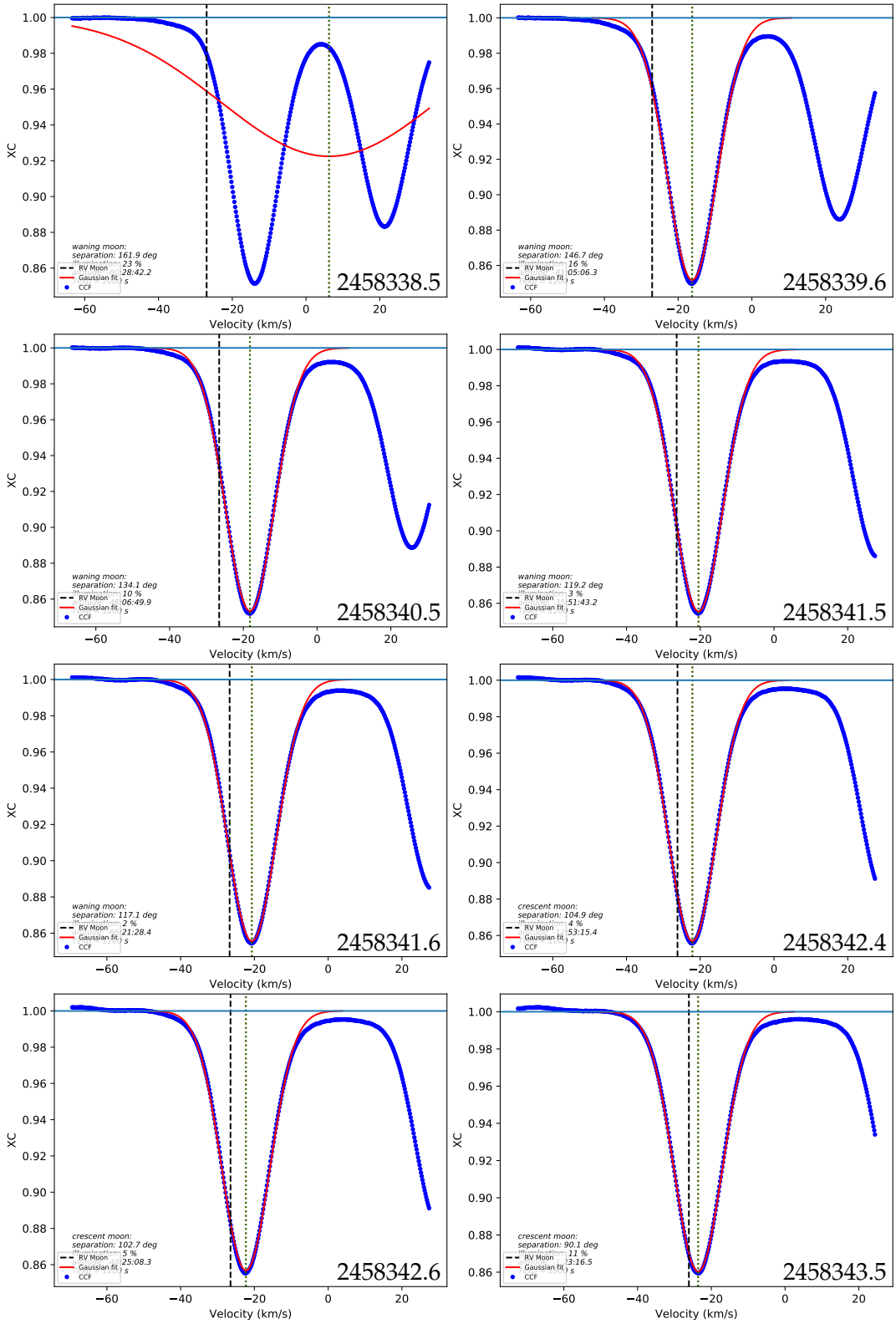

Figure B.1: Continued.

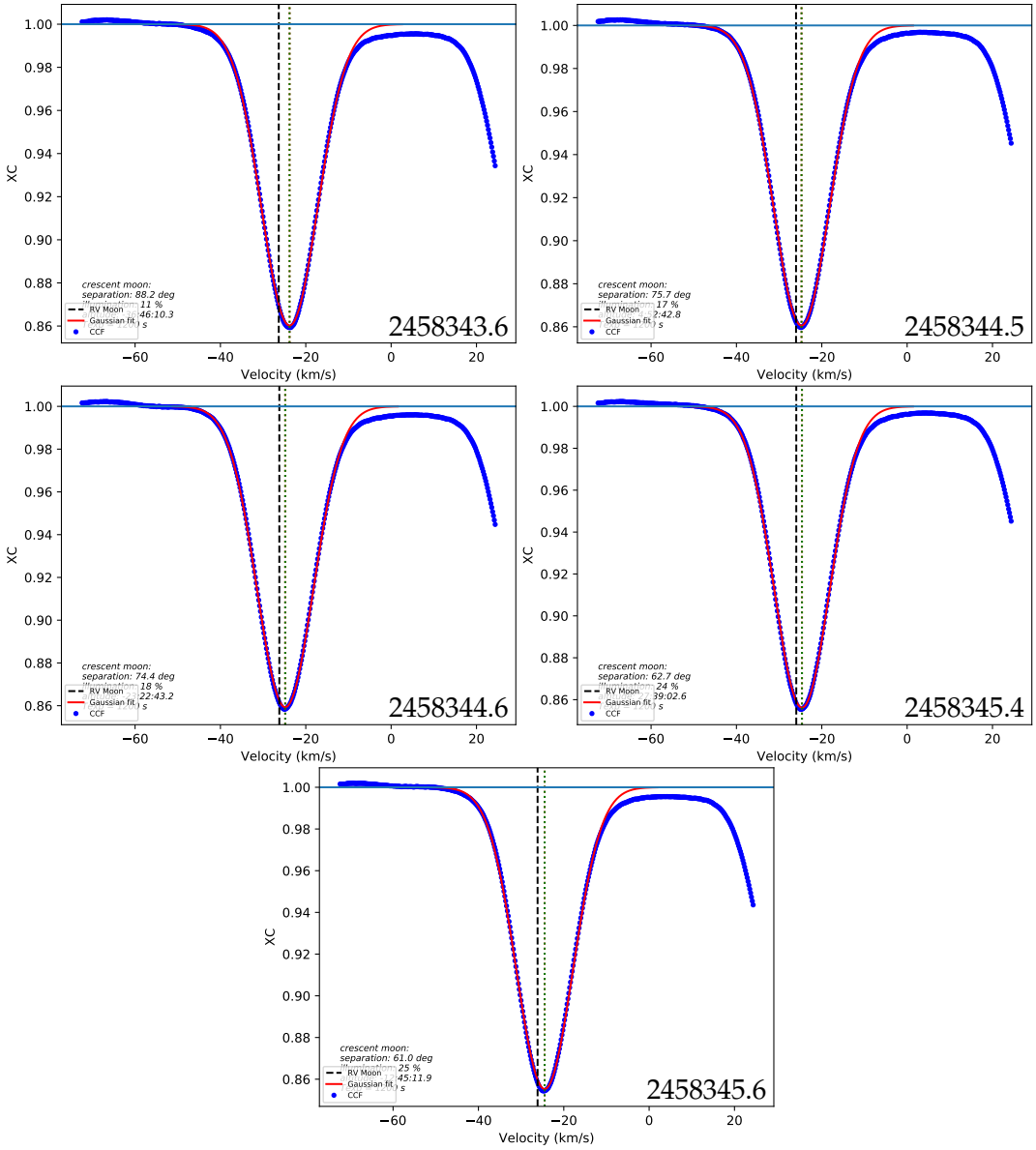

Figure B.1: Continued.

Appendix C

Supplementary Material of Chapter 5

C.1 Analytic description of the PV

The variance of a data set $y_i = 1, \ldots, n$ is given by

$$\sigma^2(n) = \frac{1}{n-1} \sum_{i=1}^{n} (y_i - \overline{y})^2 \tag{C.1}$$

where $\overline{y} = \frac{1}{n} \sum_i = 1^n y_i$. For sufficiently large n, we have

$$\sigma^2 \approx \frac{1}{n} \sum_{i=1}^{n} (y_i - \overline{y})^2 = \overline{y^2} - \overline{y}^2 \tag{C.2}$$

where $\overline{y^2} = \frac{1}{n} \sum_{i=1}^{n} y_i^2$.

In the limit of equidistant and infinitely dense sampling of the data, we can replace the sums by integrals; then Eq. C.2 becomes

$$\sigma^2(\tau) = \frac{1}{\tau} \int_0^\tau y^2(t)\, \mathrm{d}t - \left(\frac{1}{\tau} \int_0^\tau y(t)\, \mathrm{d}t \right)^2 \tag{C.3}$$

where τ is the time scale over which the variance is to be evaluated.

As we will see below, for periodic functions the shape of $\sigma^2(\tau)$ depends strongly on the phase of the periodic function. In practice, however, the phase of a signal is often sampled repeatedly in a random fashion, and some interesting signals are also variable in phase even if periodic otherwise. Therefore, we consider the phase-averaged variance, with $\delta \in [0, 2\pi)$ the phase of the signal $y(\delta)$

$$\overline{\sigma^2}(\tau) = \frac{1}{2\pi} \int_0^{2\pi} \sigma^2(\tau, \delta)\, \mathrm{d}\delta \tag{C.4}$$

Note that we take averages over the signal $\overline{y}$ with respect to the selected time scale τ, whereas we take the average over the variance $\overline{\sigma^2}$ with respect to the phase of the signal δ.

In the analytic case (infinitely dense sampling) the Pooled Variance (PV) of a data set is given by inserting Eq. C.3 into Eq. C.4. In reality one might see effects of transient oscillations if the signal is not sampled densely at all phases. To minimize the influence of those effects, the selection criteria for the sampling described in Sect. 5.2 were applied.

C.2 Analytic PV of sinusoids

As an example we consider the PV of a sine wave:

$$y(t) = K \sin\left(\frac{2\pi}{P}t - \delta\right) \tag{C.5}$$

where K is the (semi-) amplitude, P is the period and $\delta \in [0, 2\pi)$ the phase.

Evaluating Eq. C.3 for the sine function of Eq. C.5 yields the scaled variance

$$\begin{aligned}\omega^2(\theta) = \frac{1}{2} &- \frac{\sin(2\theta - 2\delta) + \sin(2\delta)}{4\theta} \\ &- \left[\frac{\cos\delta - \cos(\theta - \delta)}{\theta}\right]^2\end{aligned} \tag{C.6}$$

where $\omega^2 := \sigma^2/K^2$ and $\theta = 2\pi\tau/P$.

Inserting Eq. C.6 into Eq. C.4 yields the normalized, analytic PV of a sine wave

$$\overline{\omega^2}(\theta) = \frac{1}{2} + \frac{\cos\theta - 1}{\theta^2} \tag{C.7}$$

or

$$\overline{\sigma^2}(\tau) = K^2\left[\frac{1}{2} + \frac{\cos(2\pi\tau/P) - 1}{(2\pi\tau/P)^2}\right] \tag{C.8}$$

We have $\lim_{\tau\to 0}\overline{\sigma^2}(\tau) = 0$ and $\overline{\sigma^2}(\tau) = K^2/2$ for $\tau = P$ and also for $\tau \gg P$.

C.3 Radial Velocity Data

See next page.

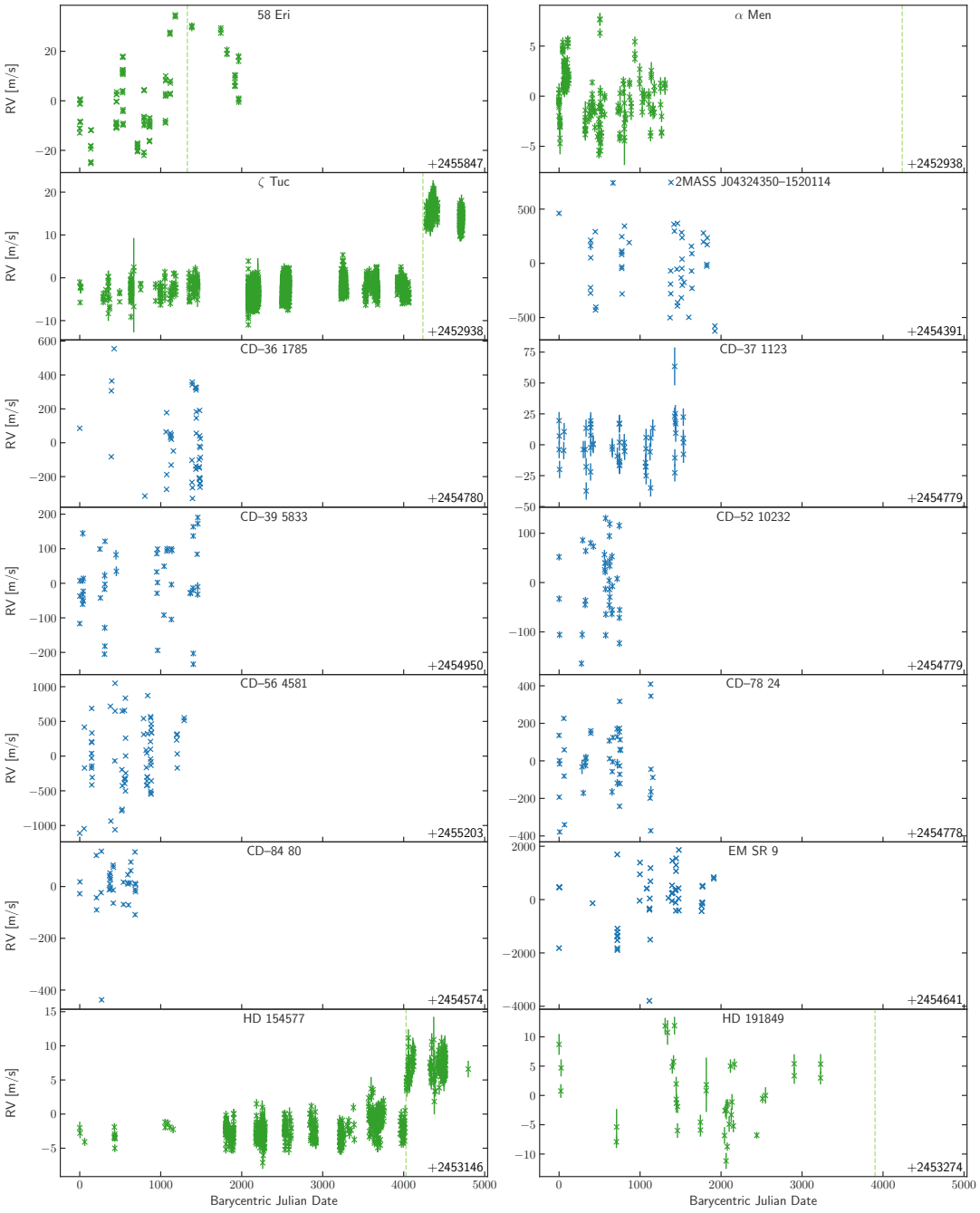

Figure C.1: Radial velocity data for all 27 stars after removing the bad data as described in Sect. 5.2 and subtracting the mean of each data set. Green symbols is HARPS and blue symbols denote FEROS data. In the bottom right of each plot the offset of the Julian Date on the x-axis is given. The green, vertical lines denote the fiber change of HARPS where the data sets were split. You can see how some data show clear jumps there while others do not. That is why we decided to split the data. Jumps in the pooled variance diagram in Fig. 5.2 like in HD 51062 or HD 25457 can be explained by clustered (e.g. HD 25457) or relatively sparse (e.g. HD 51062) data.

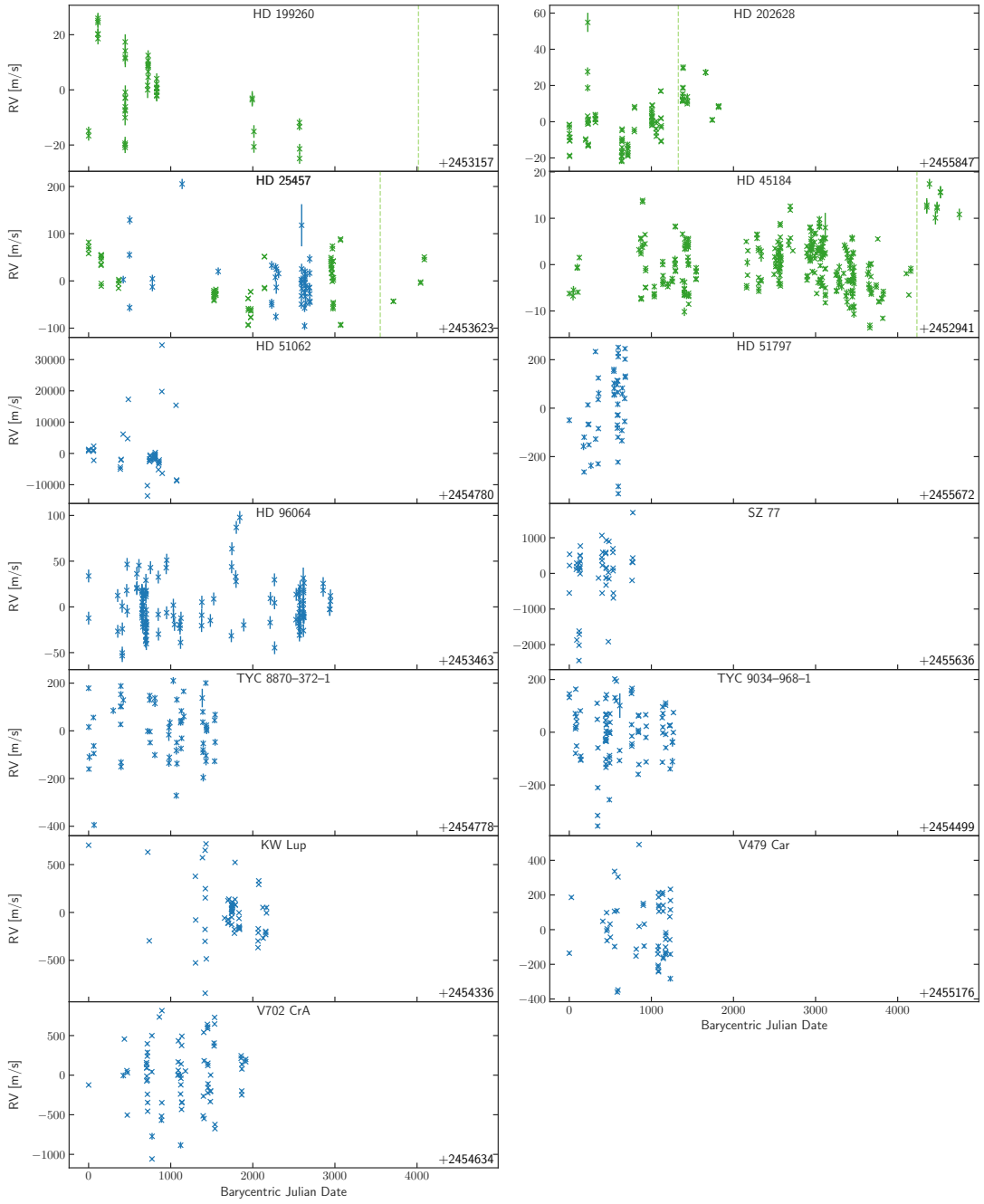

Figure C.1: Continued.

C.4 Pooled Variance fits

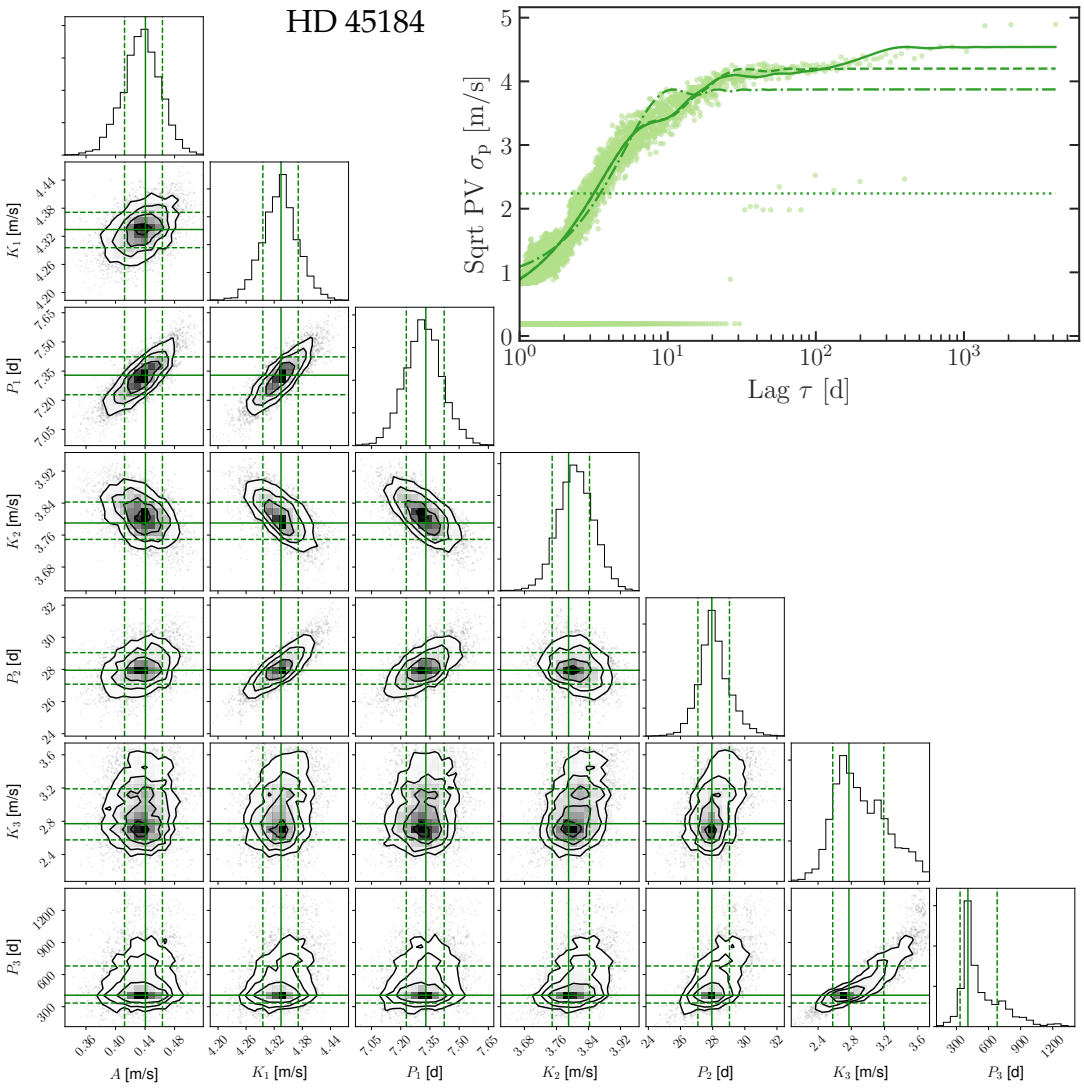

Figure C.2: Bottom left: Results of the bootstrapping procedure shown as an example for HD 45184. Shown is a corner plot using the Foreman-Mackey (2016) python package. A denotes the offset wheres K_i and P_i show the amplitudes and periods of the ith signal, as defined in equation 5.4. The solid green bars denote the fit to the original data, whereas the dashed lines denote the 1 σ-confidence levels. In the case of HD 45184, 3 signals were identified as significant by the F-test, which is shown here. Top right: Pooled Variance (PV) plot: The points mark the results of the PV and the curves the fits with different numbers of sinusoidal signals modeled: Dotted: 0 (constant), dash-dotted: 1 sinusoid, dashed: 2 sinusoids, solid: 3 sinusoids (best fit). The flat line of points at the bottom are due to the sparse sampling after the HARPS intervention, where only two times two observations are taken within less than 20 days. And those were respectively taken in the same nights, see Fig. C.1. But since they are down-weighted anyway and to be consistent, we keep them.

Bibliography

Absil, O., Milli, J., Mawet, D., et al. 2013, A&A, 559, L12

Agol, E., & Fabrycky, D. C. 2018, Transit-Timing and Duration Variations for the Discovery and Characterization of Exoplanets, 7

Albrecht, S., Winn, J. N., Johnson, J. A., et al. 2012, The Astrophysical Journal, 757, 18

Allard, F. 2014, in IAU Symposium, Vol. 299, IAU Symposium, ed. M. Booth, B. C. Matthews, & J. R. Graham, 271–272

Amara, A., & Quanz, S. P. 2012, Monthly Notices of the Royal Astronomical Society, 427, 948

Andrews, S. M., Huang, J., Pérez, L. M., et al. 2018, ApJ, 869, L41

Appenzeller, I., Fricke, K., Fürtig, W., et al. 1998, The Messenger, 94, 1

Avenhaus, H., Quanz, S. P., Garufi, A., et al. 2018, ArXiv e-prints, arXiv:1803.10882

Babcock, H. W. 1953, Publications of the Astronomical Society of the Pacific, 65, 229

Bailey, V. P., Hinz, P. M., Puglisi, A. T., et al. 2014, in Proc. SPIE, Vol. 9148, Adaptive Optics Systems IV, 914803

Baraffe, I., Homeier, D., Allard, F., & Chabrier, G. 2015, A&A, 577, A42

Batygin, K., & Brown, M. E. 2016, AJ, 151, 22

Baudoz, P., Boccaletti, A., Lacour, S., et al. 2014, in Society of Photo-Optical Instrumentation Engineers (SPIE) Conference Series, Vol. 9147, Ground-based and Airborne Instrumentation for Astronomy V, 91479E

Bayo, A., Rodrigo, C., Barrado Y Navascués, D., et al. 2008, A&A, 492, 277

Bedell, M., Hogg, D. W., Foreman-Mackey, D., Montet, B. T., & Luger, R. 2019, arXiv e-prints, arXiv:1901.00503

Bertin, E., & Arnouts, S. 1996, A&AS, 117, 393

Beuzit, J.-L., Feldt, M., Dohlen, K., et al. 2008, in Proc. SPIE, Vol. 7014, Ground-based and Airborne Instrumentation for Astronomy II, 701418

Beuzit, J. L., Vigan, A., Mouillet, D., et al. 2019, arXiv e-prints, arXiv:1902.04080

Bitsch, B., Lambrechts, M., & Johansen, A. 2015, A&A, 582, A112

Booth, R. S., Poppenhaeger, K., Watson, C. A., Silva Aguirre, V., & Wolk, S. J. 2017, MNRAS, 471, 1012

Borucki, W. J., Koch, D., Basri, G., et al. 2010, Science, 327, 977

Bottom, M., Muirhead, P. S., Johnson, J. A., & Blake, C. H. 2013, Publications of the Astronomical Society of the Pacific, 125, 240

Brahm, R., Jordán, A., & Espinoza, N. 2017, PASP, 129, 034002

Brandl, B. R., Absil, O., Agócs, T., et al. 2018, in Society of Photo-Optical Instrumentation Engineers (SPIE) Conference Series, Vol. 10702, 107021U

Brandner, W., Rousset, G., Lenzen, R., et al. 2002, The Messenger, 107, 1

Brown, L. D., & Levine, M. 2007, Ann. Statist., 35, 2219

Cantalloube, F. 2016, Theses, Université Grenoble Alpes

Cantalloube, F., Mouillet, D., Mugnier, L. M., et al. 2015, A&A, 582, A89

Carlotti, A., Hénault, F., Dohlen, K., et al. 2018, in Society of Photo-Optical Instrumentation Engineers (SPIE) Conference Series, Vol. 10702, 107029N

Cassan, A., Kubas, D., Beaulieu, J. P., et al. 2012, Nature, 481, 167

Castelli, F., Gratton, R. G., & Kurucz, R. L. 1997, A&A, 318, 841

Chabrier, G. 2003, PASP, 115, 763

Chambers, J. E. 2009, Annual Review of Earth and Planetary Sciences, 37, 321

Chauvin, G., Lagrange, A.-M., Dumas, C., et al. 2004, A&A, 425, L29

Chauvin, G., Desidera, S., Lagrange, A.-M., et al. 2017, in SF2A-2017: Proceedings of the Annual meeting of the French Society of Astronomy and Astrophysics, ed. C. Reylé, P. Di Matteo, F. Herpin, E. Lagadec, A. Lançon, Z. Meliani, & F. Royer, 331–335

Cheetham, A. C., Samland, M., Brems, S. S., et al. 2019, A&A, 622, A80

Chen, C. H., Mittal, T., Kuchner, M., et al. 2014, The Astrophysical Journal Supplement Series, 211, 25

Chun, M., Toomey, D., Wahhaj, Z., et al. 2008, in Proc. SPIE, Vol. 7015, Adaptive Optics Systems, 70151V

Claudi, R. U., Turatto, M., Gratton, R. G., et al. 2008, in Proc. SPIE, Vol. 7014, Ground-based and Airborne Instrumentation for Astronomy II, 70143E

Clenet, Y., Kasper, M. E., Ageorges, N., et al. 2004, in Proc. SPIE, Vol. 5490, Advancements in Adaptive Optics, ed. D. Bonaccini Calia, B. L. Ellerbroek, & R. Ragazzoni, 107–117

Close, L. M., Puglisi, A., Males, J. R., et al. 2012, ApJ, 749, 180

Copernicus, N. 1543, D revolutionibus orbium coelestium

Cotten, T. H., & Song, I. 2016, The Astrophysical Journal Supplement Series, 225, 15

Cox, A. N., ed. 2000, Allen's astrophysical quantities, 4th edn. (New York: AIP Press), XVIII, 719 S., literaturangaben

Crepp, J. R., & Johnson, J. A. 2011, ApJ, 733, 126

Cugno, G., Quanz, S. P., Launhardt, R., et al. 2019, arXiv e-prints, arXiv:1902.04092

Cunha, D., Santos, N. C., Figueira, P., et al. 2014, A&A, 568, A35

Cunha, J. V., Silva, F. E., & Lima, J. A. S. 2018, MNRAS, 480, L28

Cutri, R. M., Skrutskie, M. F., van Dyk, S., et al. 2003, VizieR Online Data Catalog, II/246

Cutri, R. M., Wright, E. L., Conrow, T., et al. 2013, Explanatory Supplement to the AllWISE Data Release Products, Tech. rep., IPAC/California Institute of Technology

Czekala, I., Mandel, K. S., Andrews, S. M., et al. 2017, ApJ, 840, 49

Dalton, G. B., Caldwell, M., Ward, A. K., et al. 2006, in Proc. SPIE, Vol. 6269, Society of Photo-Optical Instrumentation Engineers (SPIE) Conference Series, 62690X

Danielski, C., Baudino, J.-L., Lagage, P.-O., et al. 2018, AJ, 156, 276

David, T. J., Hillenbrand, L. A., Petigura, E. A., et al. 2016, Nature, 534, 658

de Zeeuw, T., Tamai, R., & Liske, J. 2014, The Messenger, 158, 3

Defrère, D., Absil, O., Hinz, P., et al. 2014, in Society of Photo-Optical Instrumentation Engineers (SPIE) Conference Series, Vol. 9148, Adaptive Optics Systems IV, 91483X

Desidera, S., Covino, E., Messina, S., et al. 2015, A&A, 573, A126

Dobson, A. K., Donahue, R. A., Radick, R. R., & Kadlec, K. L. 1990, in Astronomical Society of the Pacific Conference Series, Vol. 9, Cool Stars, Stellar Systems, and the Sun, ed. G. Wallerstein, 132–135

Doering, R. L., Meixner, M., Holfeltz, S. T., et al. 2007, AJ, 133, 2122

Dohlen, K., Langlois, M., Saisse, M., et al. 2008, in Proc. SPIE, Vol. 7014, Ground-based and Airborne Instrumentation for Astronomy II, 70143L

Dominik, C., & Decin, G. 2003, ApJ, 598, 626

Donahue, R. A., & Dobson, A. K. 1996, in Astronomical Society of the Pacific Conference Series, Vol. 109, Cool Stars, Stellar Systems, and the Sun, ed. R. Pallavicini & A. K. Dupree, 599

Donahue, R. A., Dobson, A. K., & Baliunas, S. L. 1995, in Bulletin of the American Astronomical Society, Vol. 27, American Astronomical Society Meeting Abstracts #186, 843

Donahue, R. A., Dobson, A. K., & Baliunas, S. L. 1997a, Sol. Phys., 171, 191

—. 1997b, Sol. Phys., 171, 211

Donati, J. F., Moutou, C., Malo, L., et al. 2016, Nature, 534, 662

Dong, R., Li, S., Chiang, E., & Li, H. 2018, ApJ, 866, 110

Dong, R., Zhu, Z., & Whitney, B. 2015, ApJ, 809, 93

Dong, R., Rafikov, R., Zhu, Z., et al. 2012, ApJ, 750, 161

Dullemond, C. P., Birnstiel, T., Huang, J., et al. 2018, ApJ, 869, L46

Dumusque, X. 2018, A&A, 620, A47

Einstein, A. 1905, Annalen der Physik, 322, 891

Emerson, J., McPherson, A., & Sutherland, W. 2006, The Messenger, 126, 41

Ercolano, B., & Pascucci, I. 2017, Royal Society Open Science, 4, 170114

Espinoza, N., Rackham, B. V., Jordán, A., et al. 2019, MNRAS, 482, 2065

Eyer, L., & Genton, M. G. 1999, A&AS, 136, 421

Figueira, P., Adibekyan, V. Z., Oshagh, M., et al. 2016, A&A, 586, A101

Fitzpatrick, E. L., & Massa, D. 1999, ApJ, 525, 1011

Forbrich, J., Preibisch, T., & Menten, K. M. 2006, A&A, 446, 155

Foreman-Mackey, D. 2016, The Journal of Open Source Software, 24, doi:10.21105/joss.00024

Fried, D. L. 1966, J. Opt. Soc. Am., 56, 1372

Fusco, T., Rousset, G., Sauvage, J.-F., et al. 2006, Optics Express, 14, 7515

Gaia Collaboration, Prusti, T., de Bruijne, J. H. J., et al. 2016, A&A, 595, A1

Gaia Collaboration, Brown, A. G. A., Vallenari, A., et al. 2018, A&A, 616, A1

Galicher, R., Marois, C., Macintosh, B., et al. 2016, A&A, 594, A63

Gardner, J. P., Mather, J. C., Clampin, M., et al. 2006, Space Sci. Rev., 123, 485

Gáspár, A., Rieke, G. H., & Balog, Z. 2013, ApJ, 768, 25

Gaudi, B. S. 2010, arXiv e-prints, arXiv:1002.0332

Gerard, B. L., & Marois, C. 2016, in Proc. SPIE, Vol. 9909, Adaptive Optics Systems V, 990958

Ginski, C., Stolker, T., Pinilla, P., et al. 2016, A&A, 595, A112

Gliese, W., & Jahreiss, H. 2015, VizieR Online Data Catalog, V/35

Goldreich, P., & Ward, W. R. 1973, ApJ, 183, 1051

Gomez Gonzalez, C. A., Absil, O., Absil, P.-A., et al. 2016, A&A, 589, A54

Gonzalez, C. A. G., Wertz, O., Absil, O., et al. 2017, The Astronomical Journal, 154, 7

Gonzalez, J.-F., Laibe, G., Maddison, S. T., Pinte, C., & Ménard, F. 2015, MNRAS, 454, L36

Gordon, I. E., Rothman, L. S., Tan, Y., Kochanov, R. V., & Hill, C. 2017, in 72nd International Symposium on Molecular Spectroscopy, TJ08

Gould, A., Udalski, A., Shin, I. G., et al. 2014, Science, 345, 46

Gravity Collaboration, Abuter, R., Accardo, M., et al. 2017, A&A, 602, A94

Gravity Collaboration, Abuter, R., Amorim, A., et al. 2018, A&A, 615, L15

Gray, D. F. 1999, in Astronomical Society of the Pacific Conference Series, Vol. 185, IAU Colloq. 170: Precise Stellar Radial Velocities, ed. J. B. Hearnshaw & C. D. Scarfe, 243

Günther, M. N., Queloz, D., Gillen, E., et al. 2018, MNRAS, 478, 4720

Guyon, O., Pluzhnik, E. A., Kuchner, M. J., Collins, B., & Ridgway, S. T. 2006, ApJS, 167, 81

Hatzes, A. P. 1996, PASP, 108, 839

Hauschildt, P. H., Allard, F., & Baron, E. 1999, ApJ, 512, 377

Hayashi, C. 1981, Progress of Theoretical Physics Supplement, 70, 35

Hayward, T. L., Biller, B. A., Liu, M. C., et al. 2014, Publications of the Astronomical Society of the Pacific, 126, 1112

Heinze, A. N., Hinz, P. M., Sivanandam, S., et al. 2010, The Astrophysical Journal, 714, 1551

Hill, J. M. 2010, Applied optics, 49, D115

Hinkley, S., Oppenheimer, B. R., Soummer, R., et al. 2007, ApJ, 654, 633

Hinkley, S., Kraus, A. L., Ireland, M. J., et al. 2015, ApJ, 806, L9

Hinz, P. M., Defrère, D., Skemer, A., et al. 2016, in Proc. SPIE, Vol. 9907, Optical and Infrared Interferometry and Imaging V, 990704

Houk, N. 1978, Michigan catalogue of two-dimensional spectral types for the HD stars

Houk, N., & Cowley, A. P. 1975, University of Michigan Catalogue of two-dimensional spectral types for the HD stars. Volume I. Declinations -90_ to -53_0.

Hsu, D. C., Ford, E. B., Ragozzine, D., & Ashby, K. 2019, arXiv e-prints, arXiv:1902.01417

Huélamo, N., Figueira, P., Bonfils, X., et al. 2008, A&A, 489, L9

Hughes, P. A., Aller, H. D., & Aller, M. F. 1992, ApJ, 396, 469

Hummel, W., Lidman, C., Devillard, N., et al. 2002, in Society of Photo-Optical Instrumentation Engineers (SPIE) Conference Series, Vol. 4844, Observatory Operations to Optimize Scientific Return III, ed. P. J. Quinn, 417–427

Ibukiyama, A., & Arimoto, N. 2002, A&A, 394, 927

Indebetouw, R., Mathis, J. S., Babler, B. L., et al. 2005, ApJ, 619, 931

Johansen, A., Blum, J., Tanaka, H., et al. 2014, Protostars and Planets VI, 547

Johansen, A., & Youdin, A. 2007, ApJ, 662, 627

Kalas, P., Graham, J. R., Chiang, E., et al. 2008, Science, 322, 1345

Kasper, M., Apai, D., Janson, M., & Brandner, W. 2007, A&A, 472, 321

Kasting, J., Traub, W., Roberge, A., et al. 2009, in astro2010: The Astronomy and Astrophysics Decadal Survey, Vol. 2010, 151

Kaufer, A. 2018, Very Large Telescope: NaCo User Manual, p102 edn., ESO

—. 2019, SPHERE User manual, p104 edn.

Kaufer, A., Stahl, O., Tubbesing, S., et al. 1999, The Messenger, 95, 8

Kenworthy, M. A., Snik, F., Keller, C. U., et al. 2018, in Society of Photo-Optical Instrumentation Engineers (SPIE) Conference Series, Vol. 10702, 1070246

Keppler, M., Benisty, M., Müller, A., et al. 2018, A&A, 617, A44

King, J. R., Villarreal, A. R., Soderblom, D. R., Gulliver, A. F., & Adelman, S. J. 2003, AJ, 125, 1980

Kiraga, M. 2012, Acta Astron., 62, 67

Kjeldsen, H., & Bedding, T. R. 1995, A&A, 293, 87

Klahr, H. 2008, New A Rev., 52, 78

Klüter, J., Bastian, U., Demleitner, M., & Wambsganss, J. 2018, A&A, 620, A175

Konopacky, Q. M., Rameau, J., Duchêne, G., et al. 2016, ApJ, 829, L4

Kramer, M. 2018, Pulsar Timing as an Exoplanet Discovery Method, 5

Kraus, S., Hofmann, K. H., Malbet, F., et al. 2009, A&A, 508, 787

Kürster, M., Endl, M., Els, S., et al. 2004, in IAU Symposium, Vol. 202, Planetary Systems in the Universe, ed. A. Penny, 36

Lachaume, R., Dominik, C., Lanz, T., & Habing, H. J. 1999, A&A, 348, 897

Lacour, S., Nowak, M., Wang, J., et al. 2019, VizieR Online Data Catalog, J/A+A/623/L11

Lada, C. J., & Wilking, B. A. 1984, ApJ, 287, 610

Lafrenière, D., Marois, C., Doyon, R., & Barman, T. 2009, ApJ, 694, L148

Lafrenière, D., Marois, C., Doyon, R., Nadeau, D., & Artigau, É. 2007, ApJ, 660, 770

Lagage, P. O., Pel, J. W., Authier, M., et al. 2004, The Messenger, 117, 12

Langlois, M., Dohlen, K., Augereau, J. C., et al. 2010, in Society of Photo-Optical Instrumentation Engineers (SPIE) Conference Series, Vol. 7735, Ground-based and Airborne Instrumentation for Astronomy III, 77352U

Lannier, J., Delorme, P., Lagrange, A. M., et al. 2016, A&A, 596, A83

Larkin, J. E., Chilcote, J. K., Aliado, T., et al. 2014, in Proc. SPIE, Vol. 9147, Ground-based and Airborne Instrumentation for Astronomy V, 91471K

Lenzen, R., Hartung, M., Brandner, W., et al. 2003, in Proc. SPIE, Vol. 4841, Instrument Design and Performance for Optical/Infrared Ground-based Telescopes, ed. M. Iye & A. F. M. Moorwood, 944–952

Levison, H. F., Thommes, E., & Duncan, M. J. 2010, AJ, 139, 1297

Liu, M. C., Wahhaj, Z., Biller, B. A., et al. 2010, in Proc. SPIE, Vol. 7736, Adaptive Optics Systems II, 77361K

Lo Curto, G., Pepe, F., Avila, G., et al. 2015, The Messenger, 162, 9

Loinard, L., Torres, R. M., Mioduszewski, A. J., & Rodríguez, L. F. 2008, in IAU Symposium, Vol. 248, A Giant Step: from Milli- to Micro-arcsecond Astrometry, ed. W. J. Jin, I. Platais, & M. A. C. Perryman, 186–189

Lovis, C., & Fischer, D. 2010, Radial Velocity Techniques for Exoplanets (The University of Arizona Press), 27–53

Low, C., & Lynden-Bell, D. 1976, MNRAS, 176, 367

Lyne, A. G., & Bailes, M. 1992, Nature, 355, 213

Lyot, B. 1939, MNRAS, 99, 580

Ma, B., Ge, J., Wolszczan, A., et al. 2016, The Astronomical Journal, 152, 112

Maaskant, K. M., Honda, M., Waters, L. B. F. M., et al. 2013, A&A, 555, A64

Macintosh, B., Graham, J. R., Ingraham, P., et al. 2014, Proceedings of the National Academy of Sciences, http://www.pnas.org/content/early/2014/05/08/1304215111.full.pdf

Macintosh, B., Graham, J. R., Barman, T., et al. 2015, Science, 350, 64

Maire, A. L., Skemer, A. J., Hinz, P. M., et al. 2015a, A&A, 576, A133

—. 2015b, A&A, 579, C2

Maldonado, J., Martínez-Arnáiz, R. M., Eiroa, C., Montes, D., & Montesinos, B. 2010, A&A, 521, A12

Mamajek, E. E., & Hillenbrand, L. A. 2008, ApJ, 687, 1264

Marigo, P., Girardi, L., Bressan, A., et al. 2017, ApJ, 835, 77

Marois, C., Lafrenière, D., Doyon, R., Macintosh, B., & Nadeau, D. 2006, The Astrophysical Journal, 641, 556

Martinache, F. 2019, arXiv e-prints, arXiv:1904.02087

Mason, B. D., Wycoff, G. L., Hartkopf, W. I., Douglass, G. G., & Worley, C. E. 2001, The Astronomical Journal, 122, 3466

Masset, F. S., & Papaloizou, J. C. B. 2003, ApJ, 588, 494

Mawet, D. 2013, Caltech Messenger, 152, 8

Mawet, D., Riaud, P., Absil, O., & Surdej, J. 2005, ApJ, 633, 1191

Mayor, M., & Queloz, D. 1995, Nature, 378, 355

Mayor, M., Pepe, F., Queloz, D., et al. 2003, The Messenger, 114, 20

McLaughlin, D. B. 1924, ApJ, 60, doi:10.1086/142826

McLaughlin, D. E., Anderson, J., Meylan, G., et al. 2006, The Astrophysical Journal Supplement Series, 166, 249

Meeus, G., Waters, L. B. F. M., Bouwman, J., et al. 2001, A&A, 365, 476

Meeus, G., Montesinos, B., Mendigutía, I., et al. 2012, A&A, 544, A78

Meibom, S., Barnes, S. A., Platais, I., et al. 2015, Nature, 517, 589

Meléndez, J., Santos, L. A. d., & Freitas, F. C. 2016, Proceedings of the International Astronomical Union, 12, 274–281

Menu, J., van Boekel, R., Henning, T., et al. 2015, A&A, 581, A107

Mesa, D., Bonnefoy, M., Gratton, R., et al. 2019, arXiv e-prints, arXiv:1902.02536

Meshkat, T., Kenworthy, M. A., Reggiani, M., et al. 2015, ArXiv e-prints, arXiv:1508.00565

Meyer, M. R., & Wilking, B. A. 2009, PASP, 121, 350

Miller, G. E., & Scalo, J. M. 1979, ApJS, 41, 513

Milli, J., Banas, T., Mouillet, D., et al. 2016, in Society of Photo-Optical Instrumentation Engineers (SPIE) Conference Series, Vol. 9909, Adaptive Optics Systems V, 99094Z

Milli, J., Hibon, P., Christiaens, V., et al. 2017, A&A, 597, L2

Milli, J., Kasper, M., Bourget, P., et al. 2018, in Society of Photo-Optical Instrumentation Engineers (SPIE) Conference Series, Vol. 10703, Adaptive Optics Systems VI, 107032A

Minniti, D., Lucas, P. W., Emerson, J. P., et al. 2010, New A, 15, 433

Mohler-Fischer, M. 2013, PhD thesis, University of Heidelberg

Möller-Nilsson, O., Pavlov, A., & Feldt, M. 2010, in Society of Photo-Optical Instrumentation Engineers (SPIE) Conference Series, Vol. 7740, Software and Cyberinfrastructure for Astronomy, 774022

Mollière, P., van Boekel, R., Dullemond, C., Henning, T., & Mordasini, C. 2015, The Astrophysical Journal, 813, 47

Morbidelli, A., & Nesvorny, D. 2012, A&A, 546, A18

Mordasini, C., Klahr, H., Alibert, Y., Benz, W., & Dittkrist, K.-M. 2010, arXiv e-prints, arXiv:1012.5281

Mordasini, C., Marleau, G.-D., & Mollière, P. 2017, A&A, 608, A72

Morton, T. D., Bryson, S. T., Coughlin, J. L., et al. 2016, ApJ, 822, 86

Müller, A., Keppler, M., Henning, Th., et al. 2018, A&A, 617, L2

Mustill, A. J., Davies, M. B., & Johansen, A. 2018, MNRAS, 478, 2896

Niedzielski, A., Nowak, G., Adamów, M., & Wolszczan, A. 2009, ApJ, 707, 768

Nielsen, E. L., Liu, M. C., Wahhaj, Z., et al. 2012, ApJ, 750, 53

Nielsen, E. L., De Rosa, R. J., Macintosh, B., et al. 2019, arXiv e-prints, arXiv:1904.05358

Ormel, C. W., & Klahr, H. H. 2010, A&A, 520, A43

Otten, G. P. P. L., Snik, F., Kenworthy, M. A., Miskiewicz, M. N., & Escuti, M. J. 2014, Optics Express, 22, 30287

Papaloizou, J. C. B., Nelson, R. P., Kley, W., Masset, F. S., & Artymowicz, P. 2007, Protostars and Planets V, 655

Patience, J., Macintosh, B., Graham, J. R., et al. 2015, in AAS/Division for Extreme Solar Systems Abstracts, Vol. 3, AAS/Division for Extreme Solar Systems Abstracts, 202.01

Pawellek, N., & Krivov, A. V. 2015, MNRAS, 454, 3207

Pearce, T. D., Wyatt, M. C., & Kennedy, G. M. 2015, Monthly Notices of the Royal Astronomical Society, 448, 3679

Perrin, M. D., Duchene, G., Millar-Blanchaer, M., et al. 2015, ApJ, 799, 182

Perryman, M. 2018, The Exoplanet Handbook, 2nd edn. (Cambridge University Press), doi:10.1017/9781108304160

Pinte, C., Price, D. J., Ménard, F., et al. 2018, The Astrophysical Journal Letters, 860, L13

Pollack, J. B., Hubickyj, O., Bodenheimer, P., et al. 1996, Icarus, 124, 62

Pourbaix, D., Tokovinin, A. A., Batten, A. H., et al. 2004, A&A, 424, 727

Poyneer, L., van Dam, M., & Véran, J.-P. 2009, Journal of the Optical Society of America A, 26, 833

Poyneer, L. A., De Rosa, R. J., Macintosh, B., et al. 2014, in Proc. SPIE, Vol. 9148, Adaptive Optics Systems IV, 91480K

Quanz, S. P., Amara, A., Meyer, M. R., et al. 2015, The Astrophysical Journal, 807, 64

Quirrenbach, A., Amado, P. J., Caballero, J. A., et al. 2014, in Proc. SPIE, Vol. 9147, Ground-based and Airborne Instrumentation for Astronomy V, 91471F

Rackham, B. V., Pinhas, A., Apai, D., et al. 2019, arXiv e-prints, arXiv:1903.06152

Raettig, N., Klahr, H., & Lyra, W. 2015, ApJ, 804, 35

Ragazzoni, R., & Farinato, J. 1999, A&A, 350, L23

Rameau, J., Follette, K. B., Pueyo, L., et al. 2017, AJ, 153, 244

Rameau, J., Chauvin, G., Lagrange, A.-M., et al. 2013, A&A, 553, A60

Rantakyrö, F. T., Bailey, V. P., Quiroz, C., et al. 2018, in Society of Photo-Optical Instrumentation Engineers (SPIE) Conference Series, Vol. 10702, 1070240

Rawlings, J. O., Pantula, S. G., & Dickey, D. A. 1998, Applied regression analysis, 2nd edn., Springer texts in statistics (New York ; Berlin ; Heidelberg ; Barcelona ; Budapest ; Hong Kong ; London ; Milan ; Paris ; Santa Clara ; Singapore ; Tokyo: Springer), XVIII, 657 S., literaturverz. S. 635 - 646

Reggiani, H., Meléndez, J., Yong, D., Ramírez, I., & Asplund, M. 2016, A&A, 586, A67

Reiners, A.and Zechmeister, M., Caballero, J. A., Ribas, I., et al. 2018, A&A, 612, A49

Ricker, G. R., Winn, J. N., Vanderspek, R., et al. 2014, in Society of Photo-Optical Instrumentation Engineers (SPIE) Conference Series, Vol. 9143, Space Telescopes and Instrumentation 2014: Optical, Infrared, and Millimeter Wave, 914320

Roddier, F. 1981, Progess in Optics, 19, 281

Roddier, F., Roddier, C., & Roddier, N. 1988, in Society of Photo-Optical Instrumentation Engineers (SPIE) Conference Series, Vol. 976, Statistical optics, ed. G. M. Morris, 203–209

Rodrigues, M., Capone, J., Earle, A., et al. 2018, in Society of Photo-Optical Instrumentation Engineers (SPIE) Conference Series, Vol. 10702, 107029M

Rossiter, R. A. 1924, ApJ, 60, doi:10.1086/142825

Rousseeuw, P. J., & Croux, C. 1993, Journal of the American Statistical Association, 88, 1273

Rousset, G., Fontanella, J.-C., Kern, P. Y., et al. 1990, in Society of Photo-Optical Instrumentation Engineers (SPIE) Conference Series, Vol. 1237, Amplitude and Intensity Spatial Interferometry, ed. J. B. Breckinridge, 336–344

Rousset, G., Lacombe, F., Puget, P., et al. 2003, in Proc. SPIE, Vol. 4839, Adaptive Optical System Technologies II, ed. P. L. Wizinowich & D. Bonaccini, 140–149

Ruane, G., Ngo, H., Mawet, D., et al. 2019, AJ, 157, 118

Saar, S. H., Butler, R. P., & Marcy, G. W. 1998, ApJ, 498, L153

Sahlmann, J., Triaud, A. H. M. J., & Martin, D. V. 2015, MNRAS, 447, 287

Salpeter, E. E. 1955, Physical Review, 97, 1237

Samland, M. 2015, Master's thesis, University of Heidelberg

Samland, M., Mollière, P., Bonnefoy, M., et al. 2017, A&A, 603, A57

Schlieder, J. E., Skemer, A. J., Maire, A.-L., et al. 2016, ApJ, 818, 1

Schmid, H. M., Bazzon, A., Roelfsema, R., et al. 2018, A&A, 619, A9

Schwarz, R., Funk, B., Bazso, A., & Zechner, R. 2016, in International Conference "The Astrophysics of Planetary Habitability

Seager, S., Dotson, R., & Institute, L. 2010, Exoplanets, Space Science Series (University of Arizona Press)

Setiawan, J., Weise, P., Henning, T., et al. 2007, ApJ, 660, L145

Shack, R. V., & Platt, B. C. 1971, J. Opt. Soc. Am., 61, 656

Simon, K. P., & Sturm, E. 1994, A&A, 281, 286

Skemer, A. J., Hinz, P., Esposito, S., et al. 2014, in Society of Photo-Optical Instrumentation Engineers (SPIE) Conference Series, Vol. 9148, Adaptive Optics Systems IV, 91480L

Skemer, A. J., Morley, C. V., Zimmerman, N. T., et al. 2016, ApJ, 817, 166

Skrutskie, M. F., Cutri, R. M., Stiening, R., et al. 2006, AJ, 131, 1163

Snik, F., Otten, G., Kenworthy, M., et al. 2012, in Society of Photo-Optical Instrumentation Engineers (SPIE) Conference Series, Vol. 8450, Modern Technologies in Space- and Ground-based Telescopes and Instrumentation II, 84500M

Sparks, W. B., & Ford, H. C. 2002, ApJ, 578, 543

Squires, G. L. 2001, Practical physics, 4th edn. (Cambridge [u.a.]: Cambridge University Press), XI, 212 S.

Stamatellos, D. 2013, EPJ Web of Conferences, 47, 08001

Stamatellos, D., & Whitworth, A. P. 2008, A&A, 480, 879

Stolker, T., Bonse, M. J., Quanz, S. P., et al. 2019, A&A, 621, A59

Stone, J. M., Skemer, A. J., Kratter, K. M., et al. 2016, ArXiv e-prints, arXiv:1601.03377

Stone, J. M., Skemer, A. J., Hinz, P. M., et al. 2018, AJ, 156, 286

Suriano, S. S., Li, Z.-Y., Krasnopolsky, R., & Shang, H. 2017, MNRAS, 468, 3850

Suzuki, R., Tamura, M., Suto, H., et al. 2009, in American Institute of Physics Conference Series, Vol. 1158, American Institute of Physics Conference Series, ed. T. Usuda, M. Tamura, & M. Ishii, 293–298

Takahashi, S. Z., & Inutsuka, S.-i. 2014, ApJ, 794, 55

Takami, M., Bailey, J., & Chrysostomou, A. 2003, A&A, 397, 675

Tamura, M. 2016, Proceeding of the Japan Academy, Series B, 92, 45

Teague, R., Bae, J., Bergin, E. A., Birnstiel, T., & Foreman-Mackey, D. 2018, ApJ, 860, L12

The, P. S., de Winter, D., & Perez, M. R. 1994, A&AS, 104, 315

Tokovinin, A., & Kornilov, V. 2007, MNRAS, 381, 1179

Traub, W. A., & Oppenheimer, B. R. 2010, Direct Imaging of Exoplanets, ed. S. Seager (University of Arizona Press), 111–156

Tucci Maia, M., Ramírez, I., Meléndez, J., et al. 2016, A&A, 590, A32

van der Marel, N., Verhaar, B. W., van Terwisga, S., et al. 2016, A&A, 592, A126

van der Plas, G., Wright, C. M., Ménard, F., et al. 2017, A&A, 597, A32

van Leeuwen, F. 2010, Space Sci. Rev., 151, 209

VanderPlas, J. T. 2017, ArXiv e-prints, arXiv:1703.09824

Vican, L. 2012, The Astronomical Journal, 143, 135

Vigan, A., Moutou, C., & Langlois, M. 2008, in SF2A-2008, ed. C. Charbonnel, F. Combes, & R. Samadi, 81

Vigan, A., Moutou, C., Langlois, M., et al. 2010, in In the Spirit of Lyot 2010, E48

Vigan, A., Patience, J., Marois, C., et al. 2012, A&A, 544, A9

Voigt, H.-H. 1956, ZAp, 40, 157

Wade, G. A., Drouin, D., Bagnulo, S., et al. 2005, A&A, 442, L31

Waelkens, C., Bogaert, E., & Waters, L. B. F. M. 1994, in Astronomical Society of the Pacific Conference Series, Vol. 62, The Nature and Evolutionary Status of Herbig Ae/Be Stars, ed. P. S. The, M. R. Perez, & E. P. J. van den Heuvel, 405

Wahhaj, Z., Cieza, L. A., Mawet, D., et al. 2015, A&A, 581, A24

Wakeford, H. R., Sing, D. K., Kataria, T., et al. 2017, Science, 356, 628

Wang, J. J., Graham, J. R., Dawson, R., et al. 2018, AJ, 156, 192

Ward, W. R. 1997, Icarus, 126, 261

Weidenschilling, S. J. 1977, Ap&SS, 51, 153

Weise, P. 2010, PhD thesis, University of Heidelberg

Weise, P., Launhardt, R., Setiawan, J., & Henning, T. 2010, A&A, 517, A88

Wenger, M., Ochsenbein, F., Egret, D., et al. 2000, A&AS, 143, 9

Wilson, J. C., Hinz, P. M., Skrutskie, M. F., et al. 2008, in Proc. SPIE, Vol. 7013, Optical and Infrared Interferometry, 70133A

Winn, J. N. 2010, Exoplanet Transits and Occultations, ed. S. Seager, 55–77

Winn, J. N., & Fabrycky, D. C. 2015, ARA&A, 53, 409

Wold, S., Esbensen, K., & Geladi, P. 1987, Chemometrics and Intelligent Laboratory Systems, 2, 37 , proceedings of the Multivariate Statistical Workshop for Geologists and Geochemists

Wolszczan, A., & Frail, D. A. 1992, Nature, 355, 145

Wong, K. W. K., Berti, E., Gabella, W. E., & Holley-Bockelmann, K. 2019, MNRAS, 483, L33

Wyatt, M. C. 2008, ARA&A, 46, 339

Xuan, W. J., Mawet, D., Ngo, H., et al. 2018, AJ, 156, 156

Yu, L., Donati, J.-F., Hébrard, E. M., et al. 2017, MNRAS, 467, 1342

Zechmeister, M., & Kürster, M. 2018, GLS: Generalized Lomb-Scargle periodogram, Astrophysics Source Code Library, ascl:1807.019

Zechmeister, M., Reiners, A., Amado, P. J., et al. 2018, A&A, 609, A12

Zellem, R., Lewis, N., A. Knutson, H., et al. 2014, The Astrophysical Journal, 790, doi:10.1088/0004-637X/790/1/53

Zhang, K., Blake, G. A., & Bergin, E. A. 2015, ApJ, 806, L7

Zurlo, A., & Bonnefoy, M. 2015, in AAS/Division for Extreme Solar Systems Abstracts, Vol. 47, 202.05

Bibliography of own Publications

This chapter lists all publications where I am either author or co-author. Papers I cited in the thesis but which are not submitted yet, are not listed.

Bibliography of first-author papers used in this thesis

Brems, S. S.; Kürster, Martin; Trifonov, T.; Reffert, S.; Quirrenbach, A., *Radial Velocity Jitter of Stars as a Function of Observational Timescale and Stellar Age*, submitted to A&A

Bibliography of first-author papers not cited in this thesis

Brems, S. S.; Schäfer, Björn Malte; Bucciantini, Niccolò et al. 2018, *The Dark Universe - Exercises and Proceedings from the German-Italian WE Heraeus Summer School held in 2017 in Heidelberg*, arXiv e-prints, arXiv:1808.07551

Bibliography of co-author papers cited in this thesis

Musso Barcucci, A.; Launhardt, R.; Kennedy, G. M. et al., *ISPY - NaCo Imaging Survey for Planets around Young stars. Discovery of an M-dwarf in the gap between HD 193571 and its debris ring*, accepted for publication in A&A

Cugno, G., Quanz; S. P., Launhardt; R. et al. 2019, including Brems, S. S., *ISPY - NaCo Imaging Survey for Planets around Young stars. A young companion candidate embedded in the R CrA cloud*, A&A, 624, A29

Cheetham, A. C.; Samland, M.; Brems, S. S. et al. 2019, *Spectral and orbital characterisation of the directly imaged giant planet HIP 65426 b*, A&A, 622, A80

Stone, Jordan M.; Skemer, Andrew J.; Hinz, Philip M. et al. 2018, *The LEECH Exoplanet Imaging Survey: Limits on Planet Occurrence Rates under Conservative Assumptions*, AJ, 156, 286

Keppler, M.; Benisty, M.; Müller, A. et al. 2018, *Discovery of a planetary-mass companion within the gap of the transition disk around PDS 70*, A&A, 617, A44

Bibliography of co-author papers not cited in this thesis

Trifonov, Trifon; Kürster, Martin; Reffert, Sabine et al. 2018, *New HARPS and FEROS Observations of GJ 1046*, Research Notes of the American Astronomical Society, 2, 180

Barragán, O.; Gandolfi, D.; Smith, A. M. S. et al. 2018, *K2-139 b: a low-mass warm Jupiter on a 29-d orbit transiting an active K0 V star*, MNRAS, 475, 1765

Gandolfi, Davide; Barragán, Oscar; Hatzes, Artie P. et al. 2017, *The Transiting Multiplanet System HD 3167: A 5.7 $M_\oplus$ Super-Earth and an 8.3 $M_\oplus$ Mini-Neptune*, AJ, 154, 123

Trifonov, T.; Kürster, M.; Zechmeister, M. et al. 2017, *Three planets around HD 27894. A close-in pair with a 2:1 period ratio and an eccentric Jovian planet at 5.4 AU*, A&A, 602, 8

Unless stated differently, the online resources were last accessed on April 22nd, 2019.

List of Figures

1.1 Discovery image of 2M 1207 b . . . 2
1.2 Exoplanet detections per year . . . 3
1.3 Mass vs semi-major axis diagram of all known exoplanets. . . . 4
1.4 Schematic overview of planet and star formation. . . . 5
1.5 ALMA images of disks from the DSharp survey. . . . 8
1.6 Simulation of gas and dust in a disk only showing gaps in the dust . . 10
1.7 Spectrum of the Giant Planet 51 Eri b obtained using Direct Imaging . 13
1.8 The Sun's brightness compared to Earth's and Jupiter's. . . . 14
1.9 Examples of first light coronagraphs for the European Extremely Large Telescope . . . 19
1.10 Schematic of how the RV method works. . . . 27
1.11 Demonstration of the chromatic index in RV data. . . . 30
1.12 Measuring the RV signal on individual lines. . . . 31
1.13 Schmatics of the microlensing technique and the lightcurve of HD 209458 showing the primary and secondary transits of a hot Jupiter. . . . 33
1.14 Sky distribution of the NaCo-ISPY and LIStEN targets showing how they complement each other covering the whole sky. . . . 37
1.15 Reduced images of the planet discovered around PDS 70 b. . . . 40
1.16 Histograms of Age, Distance and Spectral Type of the LEECH observed targets . . . 40

2.1 Examples of images taken with NaCo for the astrometric calibration. . 48
2.2 Extracted sources matched with the input catalog. . . . 52
2.3 Astrometric calibration for all possible combinations between individual stars. . . . 55
2.4 Platescale and true north calibration of NaCo-ISPY . . . 58

3.1 Contrast curves of the five NaCo-ISPY systems . . . 59
3.2 SED fit to HD 101412 using stellar models and BBs. . . . 62
3.3 Predicted contrast of HD 101412 to for different filters. . . . 63
3.4 Simulated color-color diagram for the inner CCs around HD 101412 as seen by NaCo and the comparison to Background K giants. . . . 64
3.5 Simulated possible results for the CCs around around HD 101412 as seen by GPI and the comparisons of real BD spectra and a K0 III spectrum. . . . 65

3.6 I SPY detection image showing all 4 companion candidates around HD 101412 . . . 67
3.7 Centering problems of the HD 101412 data taken on March 12, 2018 with GPI's polarimetric mode . . . 68
3.8 I SPY and GPI images of the inner 2 companion candidates around HD 101412 . . . 69
3.9 Magnitude comparison of stars in a reference field for HD 101412 . . . 70
3.10 Source density around HD 101412 with GAIA and VVV . . . 71
3.11 Likelyhood for the identified sources around HD 101412 to be Background (BG) sources . . . 72
3.12 PCA and Reduced NaCo . . . 76
3.13 VIP-PCA reduced IFS data of HD 191849. . . . 77
3.14 ANDROMEDA reduced IRDIS data of HD 191849. . . . 78
3.15 5-σ contrast curves of the different observations and and analysis of HD 191849. . . . 80
3.16 PCA reduced image of HD 58647 of the NaCo-ISPY observation taken on February 23rd, 2018 . . . 82
3.17 Walk plot of the properties of the CC around HD 58647. . . . 83
3.18 Corner plot of the properties of the CC around HD 58647. . . . 84
3.19 PCA reduced image of HD 98922 of the NaCo-ISPY observation taken on February 22nd, 2018 . . . 87
3.20 Archival NaCo images of HD98922 . . . 88
3.21 Proper motion analysis of HD 98922. . . . 89
3.22 HST image of HD 97048 before and after subtracting the reference image. . . . 92
3.23 Reduced NaCo-ISPY, NICI and SPHERE data of HD 97048 . . . 94
3.24 Cornerplot of the MCMC result of the outer CC around HD 97048. . . . 95
3.25 Proper motion analysis of HD 97048 . . . 96

4.1 Key histograms of the 145 stars of the RVSPY targets. . . . 98
4.2 Sky distribution of the 145 RVSPY targets. . . . 99
4.3 Dependence of the radial velocity precision on $T_{\rm eff}$ and $v \sin i$. . . . 102
4.4 Example of the distribution of the archival RV measurements of 2MASS J04324350–1520114 . . . 103
4.5 Simulated return of the ISPY and RVSPY surveys if executed as originally planned. . . . 105
4.6 Analysis of the radial velocity and bisector span of RVSPY 36 . . . 109
4.7 Analysis of the radial velocity and bisector span of RVSPY 51 . . . 110
4.8 Analysis of the radial velocity and bisector span of RVSPY 69 . . . 111
4.9 Analysis of the radial velocity and bisector span of RVSPY 80 . . . 112

5.1 Age distribution of the stars of the stellar activity analysis. . . . 114
5.2 Pooled results for the 27 qualified stars of the stellar activity analysis. . . 117

5.3 Fitted radial velocity jitter for the 28 individual stars of the stellar activity analysis. 124
5.4 Fitted activity model showing radial velocity scatter as function of stellar age ant lag. 125

B.1 Time series of the Cross Correlation Function of RVSPY 80 141

C.1 Radial velocity data for all 27 stars of the stellar activity analysis. . . . 147
C.2 Results of the bootstrapping procedure for the fit to the pooled variance of HD 45184. 149

List of Tables

1.1 Comparison of key aspects of NaCo, SPHERE and GPI 24
1.2 Overview of large Direct Imaging Surveys 45

2.1 Coordinates and number of measurements that lead to a result for the astrometric calibrators. 48
2.2 Astrometric Calibration: Comparing use of median image or single images 54

3.1 Basic properties of HD 101412. 61
3.2 Overview of high contrast observations for HD 101412 66
3.3 Overview of the positions and Magnitudes of the Companion Candidates around HD 101412 73
3.4 Basic properties of HD 191849. 75
3.5 Basic properties of HD 58647. 81
3.6 Position and magnitude of the identified foreground object around HD 58647 81
3.7 Basic properties of HD 98922. 86
3.8 Archival data of HD 98922 86
3.9 Positions and magnitudes of the identified foreground object around HD 98922 88
3.10 Basic properties of HD 97048. 90
3.11 Analyzed archival data of HD 97048 91
3.12 Positions and magnitudes of the two identified Companion Candidates around HD 97048 92

4.1 Results of the Marcov Chain Monte Carlo simulation of the outcome of NaCo-ISPY and RVSPY 104

5.1 Stellar properties of the 27 stars analyzed in the activity analysis 115
5.2 Parameters and formal errors of the fits to the pooled variances. 123
5.3 Results of the two dimensional age-lag-activity fit to stellar jitter. . . . 126

A.1 Results of the individual measurements of the astrometric calibration. 139

Acronyms

Symbols

2MASS Two Micron All-Sky Survey.

A

ADI Angular Differential Imaging.

AGPM Annular Groove Phase Mask.

ANDROMEDA ANgular Differential OptiMal Exoplanet Detection Algorithm.

AO Adaptive Optics.

APLC Apodized Pupil Lyot Coronagraph.

B

BB Black Body.

BD Brown Dwarf.

BG Background.

BIS Bisector Span.

BJD Barycentric Julian Date.

BPC Bad Pixel Correction.

BPM Bad Pixel Map.

C

cADI classical Angular Differential Imaging.

CARMENES Calar Alto high-Resolution search for M dwarfs with Exoearths with Near-infrared and optical Échelle Spectrographs.

CC Companion Candidate.

CCF Cross Correlation Function.

CONICA COudé Near Infrared CAmera.

D

DD Debris Disk.

DEB Debris disk hosting star.

DI Direct Imaging.

DIT Detector Integration Time.

DM Deformable Mirror.

DRP Data Reduction Pipeline.

DRS Data Reduction Software.

E

E-ELT European Extremely Large Telescope.

F

FFT Fast Fourier Transform.

FG Foreground.

FIR Far Infrared.
FoV Field of View.
FPM Focal Plane Mask.
FPP False Positive Probability.
FWHM Full Width Half Maximum.

G
GAIA-DR2 Gaia Data Release 2.
GLS Generalized Lomb Scargle diagram.
GP Giant Planet.
GPI Gemini Planet Imager.
GPIES GPI Exoplanet Search.
GTO Guaranteed Time Observations.
gvAPP grating vector Apodizing Phase Plate.

H
HCI High Contrast Imaging.
HST Hubble Space Telescope.

I
IFS Integral Field Spectrograph.
IR InfraRed.
IRDIS InfraRed Dual-band Imager and Spectrograph.
IWA Inner Working Angle.

J
JD Julian Date.
JWST James Webb Space Telescope.

L
LBT Large Binocular Telescope.
LBTI LBT Interferometer.
LEECH LBTI Exozodi Exoplanet Common Hunt.
LIStEN L-band Imaging Survey to find Exoplanets in the North.
LMIRcam L/M-band InfraRed Camera.
LMSO Low Mass Stellar Object.
LSS Longs Slit Spectroscopy.

M
MC Monte Carlo.
MCMC Marcov Chain Monte Carlo.
MIR Mid Infrared.
MMSN Mimimum Mass Solar Nebula.

N
NaCo Naos Conica.
NaCo-ISPY NaCo Imaging Survey for Planets around Young stars.
NAOS NAsmyth Adaptive Optics System.
NIR Near InfraRed.

P

PA Parallactic Angle.

PCA Principal Components Analysis.

PM Proper Motion.

PPD ProtoPlanetary Disk.

PSD Power Spectral Density function.

PSF Point Spread Function.

PV Pooled Variance.

PVD Pooled Variance Diagram.

R

RA-VVC Ring Apodized Vector Vortex Coronagraph.

RDI Reference Differential Imaging.

RV Radial Velocity.

RVSPY Radial Velocity Survey for Planets around Young stars.

S

SAM Sparse Aperture Masking.

sb9 Spectroscopic Binary Catalog 9th edition.

SDI Spectral Differential Imaging.

SED Spectral Energy Distribution.

SERVAL SpEctrum Radial Velocity AnaLyser.

SExtractor Source Extractor.

SNR Signal to Noise Ratio.

Spaxel Spectral Pixel.

SPHERE Spectro-Polarimetric High-contrast Exoplanet REsearch.

SpT Spectral Type.

SVO Spanish Virtual Observatory.

T

TESS Transiting Exoplanet Survey Satellite.

V

VIP Vortex Imaging Pipeline.

VIS Visible.

VLT Very Large Telescope.

VVV VISTA Variables in the Via Lactea.

W

WDS Washington Double Star catalog.

WFS Wavefront Sensor.

Acknowledgements

There were so many people supporting me throughout my PhD, that it is impossible to list them all. However, I will give a try to mention at least some of them.

First of all, I would like to thank my supervisors Andreas Quirrenbach, Sabine Reffert and Wolfgang Brandner for all their advices and the confidence they had in me, as well as to provide me with the opportunity to make all the experiences in and around astronomy and science. I could always rely on their expertise and their help when I had any questions. Furthermore I would like to thank Ralf Launhardt, the leader of the ISPY project, Olga Zakhhay, the leader of the RVSPY project, and Martin Kürster for all their support and good discussions concerning ISPY, RVSPY and stellar activities. I want to thank the whole crew of all three projects for their support. In particular André Müller, Anthony Cheetham, Arianna Musso Barcucci, Trifon Trifonov, Stanimir Metchev[1] and Sascha Quanz for helping me with various issues in and around those projects. I would also like to thank Davide Gandolfi for his support during my first year as a PhD student. Also I would like to thank Hubert Klahr for agreeing to be the second referee of this thesis, as well as Björn Malte Schäfer and Ulrich Uwer for agreeing to be my further examiners.

Furthermore I would like to thank all of the MPIA and LSW staff (yes, I mean everyone), making me feel at home at both institutes. I was invited to join multiple MPIA outings – even at these times when the ~~wall~~ fence between the institutes keeps growing. In particular I would like to thank my amazing Stef[2] office as well as all the other students making every day unique and always being up for a coffee, drone flight, running session, cake, beer or simple gossip. And science discussions, of course. Here I think in particular of Steffi, Rob, Marcelo, Stephan, Paul, Sepideh, Vera, Hotti, Christina, Theo, Katja, Mauricio, Olga, Dorit, Felix, Dane, Kai, and many more.

Also I would like to thank Steffi Yen, Robert Harris, Florian Dinger, Matthias Samland, Clemens Hassel, and Faustine Cantalloube for offering to read parts of my thesis and providing useful comments and/or content.

Des Weiteren möchte ich mich natürlich auch allen meinen Unterstützern und Mitfieberern oder Zeitvertreibern im Familien- und Freundeskreis bedanken. Es wäre unmöglich gewesen, meine Arbeit ohne die Rückendeckung zu schreiben, welche es mir ermöglicht hat wochenlang in die Atacamawüste oder auf Konferenzen zu verschwinden. Dies gilt zum einen meinen Eltern: Meinem Papa, da dieser bereits im Kindesalter mein Interesse an den Naturwissenschaften weckte und bis heute weiter aktiv befeuert. Und meiner Mama, die es sich nicht hat nehmen lassen, beinahe jede Woche das Ländle per Bahn zu durchqueren, um ihre Donnerstage mit meinem Sohn Phileas zu verbringen, damit ich neue Welten entdecken kann. Und natürlich geht ein großes Dankeschön an meine Patentante Doris als ihre würdige

[1] He started Astronomy on Tap in Heidelberg during one of his visits. So I think we should all thank him.

Vertretung, falls die anderen Enkel doch auch Aufmerksamkeit benötigten. Zum anderen Danke ich herzlich meinen Schwiegereltern Gertrud und Clemens Storz, sowie meiner Schwägerin Teresa. Auch sie haben einen großen Beitrag geleistet, indem sie jeden Mittwoch Türme, Züge oder Burgen mit Phileas bauten, damit Papa in Ruhe forschen kann.

Schlussendlich möchte ich mich ganz besonders meiner Frau Franzi und meinem Sohn Phileas danken, dass sie ein mir Zuhause sind, an dem man seinem Ärger Luft machen kann und trotzdem darauf vertrauen darf, am nächsten Tag wieder nach allen Kräften unterstützt zu werden. Außerdem danke an Phileas, dass er nie nachtragend war wenn ich Abends wieder länger arbeiten war und insbesondere, dass ich an seinem ersten Geburtstag in die Sterne geschaut habe statt mit ihm zu feiern.

Declaration of Authorship

I, Stefan Sebastian BREMS, declare that this thesis titled, "Stellar Imaging and Spectroscopy for the Discovery of Extrasolar Planets" and the work presented in it are my own. I confirm that:

- This work was done wholly or mainly while in candidature for a research degree at this University.
- Where any part of this thesis has previously been submitted for a degree or any other qualification at this University or any other institution, this has been clearly stated.
- Where I have consulted the published work of others, this is always clearly attributed.
- Where I have quoted from the work of others, the source is always given. With the exception of such quotations, this thesis is entirely my own work.
- I have acknowledged all main sources of help.
- Where the thesis is based on work done by myself jointly with others, I have made clear what was done by others and what I have contributed myself.

Signed:

_____

Date:

_____